

EXPANDING THE LIMITS OF
MAGNETIC RESONANCE FORCE MICROSCOPY

A Dissertation

Presented to the Faculty of the Graduate School

of Cornell University

in Partial Fulfillment of the Requirements for the Degree of

Doctor of Philosophy

by

Neil Edward Jenkins

January 2007

© 2006 Neil E. Jenkins

ALL RIGHTS RESERVED

EXPANDING THE LIMITS OF
MAGNETIC RESONANCE FORCE MICROSCOPY

Neil Edward Jenkins, Ph.D.

Cornell University 2007

The first half of this dissertation details a procedure for the batch fabrication and characterization of ultrasensitive silicon cantilevers with integrated submicron-scale magnetic tips. The fabrication of these magnetic-tipped cantilevers is essential for detecting the small forces experienced in magnetic resonance force microscopy (MRFM). Cantilevers with spring constants as small as 10^{-5} N/m were fabricated with quality factors as high as 35,000 and a force sensitivity as low as 64×10^{-18} N Hz $^{-1/2}$ at room temperature in vacuum. At cryogenic temperatures, quality factors increased to around 200,000 with a force sensitivity of 14×10^{-18} N Hz $^{-1/2}$. Polycrystalline nickel tips were fabricated on the ends of the cantilevers using lithographic techniques and studied by cantilever magnetometry, proving that the magnets were not oxidized and suitable for use in MRFM experiments.

In an effort to broaden the applicability of MRFM to more general samples, the second half of this dissertation describes the detection of electron spins in samples with short spin-lattice relaxation times (T_1) as a force gradient. When the electron spins in a sample of diphenylpicrylhydrazyl (DPPH) were exposed to unmodulated, resonant radiofrequency radiation in the presence of a low magnetic gradient, we observed a change in the resonance frequency of the cantilever predicted by the

derivative of the force. Surprisingly, a small increase in the gradient from $\sim 80\text{T/m}$ to 300 T/m caused the shape of the signal to change dramatically and unexpectedly. To explain this anomalous spring constant shift in the presence of a higher gradient, we have considered electron and nuclear spin diffusion, the possibility of dynamic nuclear polarization, the differences in the average power experienced by the sample during the two experiments, and the glue used to attach the sample to the cantilever tip. This protocol allows samples with spin-lattice relaxation times shorter than 10 ms to be studied with force gradient MRFM techniques for the first time. Finally, we propose an MRFM protocol using parametric amplification to detect small spring constant shifts. We describe control experiments where small parametric amplification gain factors, on par with those expected in MRFM experiments, are measured using ultrasensitive cantilevers.

BIOGRAPHICAL SKETCH

Neil Edward Jenkins was born April 27, 1978 in Lumberton, NC to Raybon and Frances Jenkins at the height of strawberry season. Neil grew up in the simple, bucolic confines of Chadbourn, NC, about an hour west of Wilmington. He was raised, along with his younger brother Grant, by two elementary school educators who emphasized learning and caring for others above all else. Most of Neil's formative years were spent playing little league baseball, video games, and Magic: The Gathering, while finding plenty of time to swim, ski, read, and collect everything from baseball cards to comics. In school, Neil typically excelled in all topics that did not require speaking in a foreign language and enjoyed summers at various math and science camps, such as the North Carolina Governor's School. Upon graduating from West Columbus High School at the top of his class, Neil matriculated to Wake Forest University where he developed an interest in the physical sciences and fraternity life. After receiving a B.S. in Chemistry and a B.A. in Physics, he decided to put off the real world for another six years (more or less) and attend graduate school at Cornell University in Ithaca, NY. While working towards his Ph.D. in Chemistry under the supervision of Prof. John Marohn, Neil found a wife, Amy, and a son, Noah, who shares his love of games and comics. Noah described Neil's thesis research in a 2005 classroom assignment as follows: "He deals with action and reaction physics. He works really hard, sometimes from 10:00 in the morning to 4:00 the next morning. It's weird how long he can stay up all night." Having finally abandoned his dream of being doused in chemicals after a lightning strike and obtaining super speed, Neil has decided to leave research science and pursue a career in national security, working with the Center for Naval Analyses in Alexandria, VA.

”I heard the jury’s still out on Science.”

— George Oscar (GOB) Bluth

ACKNOWLEDGEMENTS

First and foremost, I have to thank my lovely wife, Amy. Without you, I would never have been able to finish this. Coming home to you everyday has been a true joy, and I have never been happier than when we watch TV together or take those long car trips. Thank you for marrying me and making me the happiest man alive. You have made the terrible winters in Ithaca worth it.

Thanks also to my son, Noah. You don't know how much it means to me to help raise you to be the man you will become. You are a blessing. Thanks for helping to keep me young by making my addiction to comics and games look normal to the adults around me, despite the gray hairs that you give me.

Mom and Dad, thank you for your constant love and support. You have done everything in your power to make me happy and raising me to understand the importance of family and being happy. My greatest hope is that Amy and I do as good of a job raising our children as you have. I love you.

Thanks also to my little brother, Grant. I'm proud of you and love you. Continue to make the best choices in life.

Thanks and gratitude go to my boss, John Marohn. You have given me an excellent opportunity here at Cornell, and I greatly appreciate it. You have given me a fantastic background that will certainly help me in the future, even though I'm not going to be in the lab. It was a pleasure working for you.

Thanks to my committee members, Melissa Hines and Ben Widom. You were always willing to answer questions, help out, and write those letters, and I appreciate it.

Many thanks to the members of the Marohn Group that helped me through everything from circuitry to theory to liquid helium fills: Sean, Bill, Tina, Seppe,

Erik, Jahan, Lauren, Jack, and Jim. I enjoyed the conversations and the fact that there really were no bad times. Good luck in the future.

Thanks to the friends that made Cornell worthwhile: Jenny, Maloney, Scott, Witinski, British Mark, and Dan. I'll never forget the parties, the camping out, the late night D.P. Dough, and the quiet nights at Green St. Unfortunately, I'll never forget the smell of Dunbar's, either.

Thanks to the friends that became an integral part of my later life at Cornell: Tammy and Chris, Scott and Julie, and Angela. Thanks for coming over to mooch off our cable, our food, and talk about "Lost", "Project Runway", and "The Apprentice". Amy and I appreciate it and we'll miss you guys badly. Best of luck in the future.

Thanks to the staff and users of the CNF: Daron Westly, Jerry Comeau, Jim Clair, Meredith Metzler, Lidija Sekaric, and everyone else that made the cantilever fabrication possible. Couldn't have done it without you.

TABLE OF CONTENTS

1	Introduction to Magnetic Resonance Force Microscopy	1
1.1	The MRFM Experiment	3
1.2	Measuring Small Forces in MRFM	8
1.3	Survey of MRFM Milestones	11
1.4	Summary and Outline of the Dissertation	18
2	Cantilever Engineering and Sensitivity	20
2.1	Introduction	20
2.1.1	Equation of motion and cantilever response	20
2.2	Derivation of Cantilever Properties	22
2.2.1	The bending moment	22
2.2.2	Deriving k and f_0	25
2.3	Minimum Detectable Force	30
2.3.1	Quantitative derivation of F_{\min}	32
2.4	Cantilever Design	34
2.4.1	An alternative approach: high f_0 oscillators	36
2.5	Cantilever Magnetometry	40
2.6	Summary and Conclusions	42
3	Cantilever Fabrication and Characterization	43
3.1	Introduction	43
3.2	Fabrication Process	44
3.3	Cantilever Characterization	50
3.3.1	Characterization apparatus and fiber-optic interferometry . .	50
3.3.2	Characterization results	54
3.4	Cantilever Magnetometry	62
3.5	Sharp Cantilevers	66
3.6	Phatlevers	69
3.7	Summary and Conclusions	78
4	Force Gradient Detected Electron Spin Resonance	82
4.1	Introduction	82
4.2	MRFM Techniques	84
4.2.1	Cyclic saturation ESR	84
4.2.2	OSCAR	87
4.2.3	CERMIT	95
4.2.4	Motivations	99
4.3	Experimental Apparatus and Sample	100
4.3.1	Overview	100
4.3.2	RF coil and circuit	101
4.3.3	Positive feedback	103
4.3.4	Magnetic particle	105

4.3.5	Sample preparation	110
4.4	Experimental Details	113
4.5	Results	119
4.5.1	The low gradient case	119
4.5.2	The high gradient case	122
4.6	Discussion	126
4.6.1	The low gradient force signal	126
4.6.2	The high gradient force signal	130
4.6.3	Saturation of the force and force gradient signals	132
4.6.4	The low gradient Δk signal: simulations	141
4.6.5	The low gradient Δk signal: physical picture	149
4.6.6	The high gradient Δk signal: simulations	152
4.6.7	The anomalous CERMIT signal	154
4.6.8	Investigating the anomaly: The spin diffusion paradox	159
4.6.9	Investigating the anomaly: Dynamic nuclear polarization	164
4.7	Investigating the anomaly: Comparing average rf power	168
4.8	Summary and Conclusions	173
5	Parametric Amplification of Ultrasensitive Cantilevers	179
5.1	Introduction	179
5.2	Parametric Amplification: Background and Theory	181
5.2.1	Derivation of Parametric Amplification in a Simple Harmonic Oscillator	182
5.2.2	Parametric amplification and MRFM	186
5.3	Experimental Aspects	190
5.3.1	Changing the spring constant by a capacitive force	190
5.3.2	Description of the experiment	193
5.4	Results	201
5.4.1	Confirming parametric amplification	202
5.4.2	Measuring a small gain factor	207
5.4.3	Parametric amplification with positive feedback	209
5.5	Summary and Conclusions	212
A	Peak Separation in the Low Gradient Regime	215
B	Derivation of the Spin Diffusion Length	219
References		222

LIST OF TABLES

1.1	Significant Milestones in MRFM	13
2.1	Comparison of Oscillator S_F Values	36
3.1	Cantilever characterization parameters.	61
4.1	Cantilever parameters for force and force gradient ESR.	114
4.2	Experimental parameters for the force and force gradient experiments.	114
4.3	Results of the low gradient force and force gradient experiments. .	121
4.4	Results of the high gradient force and force gradient experiments. .	125
4.5	Magnetic particle parameters inferred from simulations of the spring constant shift data.	146
5.1	Cantilever and experimental parameters for parametric amplification control experiments.	194

LIST OF FIGURES

1.1	The MRFM Experiment.	4
1.2	A comparison of small forces	9
2.1	Bending moment	23
2.2	Cantilever dimensions	29
3.1	Process flow for fabricating ultrasensitive cantilevers with magnetic tips.	45
3.2	SEM image of Magnetic-tipped Cantilevers	49
3.3	Graph of cantilever mean-squared displacement as a function of temperature.	55
3.4	Lock-in demodulated cantilever ring-down	56
3.5	An across-wafer comparison of measured and expected spring constants.	58
3.6	An across-wafer comparison of measured and expected resonance frequencies.	59
3.7	Setup for cantilever magnetometry	63
3.8	Cantilever frequency shift, in parts per million, versus applied magnetic field.	65
3.9	Dissipation of blunt and sharp cantilevers versus distance above an evaporated gold surface	67
3.10	Sharp cantilevers fabricated using electron beam lithography	68
3.11	SAM-MRFM with Phatlevers	71
3.12	SEM micrographs of fabricated phatlevers	73
3.13	Dimensions for phatlevers used for k approximation.	75
4.1	Magnetization behavior and the force in Cyclic Saturation ESR . .	86
4.2	The OSCAR Experiment	89
4.3	The CERMIT Experiment.	96
4.4	Experimental setup overview.	102
4.5	Positive feedback circuit	104
4.6	Probe placement for saturation and experiment	109
4.7	Photograph of ESR probe	112
4.8	Block diagram of the cyclic saturation ESR experiment	116
4.9	Block diagram of the force gradient ESR experiment	118
4.10	Force and force gradient results for the low gradient experiment. .	120
4.11	Force and force gradient results for the high gradient experiment .	123
4.12	Power broadening in the low gradient force experiment	133
4.13	Force and magnetic moment saturation curves for the low gradient case	135
4.14	Power broadening and saturation in the high gradient force experiment	137

4.15	Power broadening and saturation in the high gradient force gradient experiment.	139
4.16	Comparison of the saturation behavior with respect to output and average power.	140
4.17	Comparison of the simulated force gradient to the experiment	145
4.18	Typical hysteresis curve for the magnetic particle	148
4.19	Pictorial representation of the sensitive slice as it moves through the sample	149
4.20	Direction of movement for the sensitive slice compared to the sign of the force gradient.	150
4.21	Comparison of the simulated force gradient to the experiment in the high gradient case	153
4.22	Anomalous Δk shift, 500 mW rf power	156
4.23	Anomalous Δk at several rf powers	158
4.24	Spin diffusion in the high gradient case	162
4.25	Comparing force and force gradient signals at different rf powers	170
4.26	Anomalous CERMIT signal based on the comparison of force and force gradient experiments performed at different powers.	171
5.1	General behavior of X_{on} and Y_{on} versus phase for parametric amplification.	185
5.2	Spring constant shift versus DC voltage for a capacitive driving force.	192
5.3	Block diagram for the parametric amplification experiment.	195
5.4	Circuit diagram for the custom-built phase shifter.	196
5.5	Circuit diagram for the custom-built frequency doubler.	198
5.6	Lock-in demodulated X and Y versus time in the parametric amplification experiment for different phases.	203
5.7	X_{on} and Y_{on} versus phase for the parametric amplification experiment	204
5.8	Gain and residuals versus phase for data from Figure 5.7	206
5.9	Gain and residuals versus phase at $V_{\text{AC}} = 1 \text{ V}$ and $V_{\text{AC}} = 0.1 \text{ V}$	208
5.10	Gain, X_{on} , and Y_{on} versus phase with positive feedback	211
A.1	Changing the coil constant	216
B.1	Spin magnetization density at steady state with spin diffusion.	220

CHAPTER 1

INTRODUCTION TO MAGNETIC RESONANCE FORCE MICROSCOPY

Magnetic resonance techniques have vastly changed the fields of organic chemistry and medicine over the last fifty years. Commercially available nuclear magnetic resonance (NMR) spectrometers in chemistry laboratories make it possible to identify the products of synthesis reactions within minutes. Magnetic resonance imaging (MRI) is used in hospitals all over the world to diagnose cancer, measure neural activity in the brain, or determine ligament damage to the knee or other joints safely and noninvasively.

Ideally, one would like to use a chemically informative technique like magnetic resonance imaging to obtain the structure of *individual* biological molecules, such as proteins. Structure determination allows for a better understanding of protein function, and eventually could lead to drugs designed specifically to target protein binding sites in order to cure or prevent disease. Theoretically, this would require that the structure be determined with angstrom-level resolution and single hydrogen nucleus sensitivity.

Conventional NMR techniques, such as two dimensional nuclear Overhauser enhancement spectroscopy (NOESY) and correlated spectroscopy (COSY), have been used to obtain the structure of proteins by determining the relative position of the protons in the sample [1]. The 2002 Nobel Prize in Chemistry was awarded to Kurt Wuthrich “for his development of nuclear magnetic resonance spectroscopy for determining the three-dimensional structure of biological macromolecules in solution” [2]. Unfortunately, magnetic resonance techniques are notoriously insensitive and require concentrated, homogeneous samples, making them ill-suited

for studying single biomolecules. Additionally, magnetic resonance imaging techniques have been used to obtain images of biological cells [3]. However, as many as 10^{12} nuclear spins are needed to obtain an image with a spatial resolution of about 1 mm^3 [4], which is many orders of magnitude larger than the angstrom level resolution needed to image protein binding sites. Detection of smaller volumes using conventional MRI will only become more difficult as the signal-to-noise decreases, and imaging single proteins is likely impossible.

X-ray crystallography has also been used to determine the structure of a significant number of proteins. According to the Research Collaboratory for Structural Bioinformatics (RCSB) Protein Database, approximately 34,000 protein structures have been determined by x-ray crystallography, compared to the 5,900 structures determined by NMR techniques, as of November 2006 [5]. Unfortunately, x-ray crystallography is limited in that it requires homogenous, ordered crystals, which can take months or years to isolate [6]. Some proteins do not form crystals at all. Unlike magnetic resonance techniques, x-ray crystallography cannot be used to determine protein structure in solution and therefore is not able to study the protein in its native environment. X-ray crystallography and NMR spectroscopy have long been considered complementary techniques for protein structure determination [7]. However, neither technique is able to study individual, non-crystallizing proteins. Development of a technique that could image any individual biological molecule with single proton sensitivity could revolutionize medicine and drug design.

Magnetic resonance force microscopy, or MRFM, is an emerging technique that could eventually be used to image single nuclear spins in individual protein molecules, nondestructively, with angstrom-scale spatial resolution. MRFM was proposed in 1991 as a way to image biological molecules by measuring the

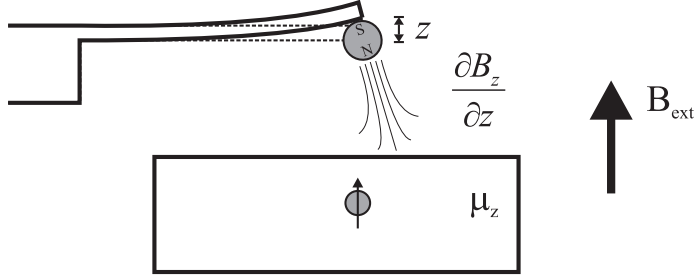
magnetic moment of the nuclear spin as a deflection in a small, magnetic-tipped oscillator [8, 9]. This imaging technique seeks to combine the chemical characterization of magnetic resonance techniques with the scanning capabilities of atomic force microscopy, while also incorporating subsurface imaging. Since this proposal, MRFM has been used to detect a single electron spin [10] and as few as 500 nuclear spins [11]. In this chapter, the basic MRFM experiment will be described, followed by a discussion of the small forces that must be detected using this technique. This chapter will conclude with a brief survey of the most important MRFM milestones to date and an outline for the remainder of this dissertation.

1.1 The MRFM Experiment

In MRFM, the magnetic moment of an ensemble of sample spins is measured as a deflection in a cantilever beam. An idealized, single-spin MRFM experiment is depicted in Figure 1.1. A cantilever with a small magnet attached to the end is brought near a sample with a single spin (electron or nucleus) directly below the tip. A large external field is applied in the z direction and the spin orients itself along this field preferentially. A force between the magnetic dipole of the spin and the gradient from the magnet on the cantilever tip causes a deflection of the cantilever beam, as seen in Figure 1.1(a). Depending on the polarization of the magnet and the spins, the force can be attractive or repulsive. This interaction is functionally similar to the force between two macroscale, “refrigerator-style” magnets brought close to each other.

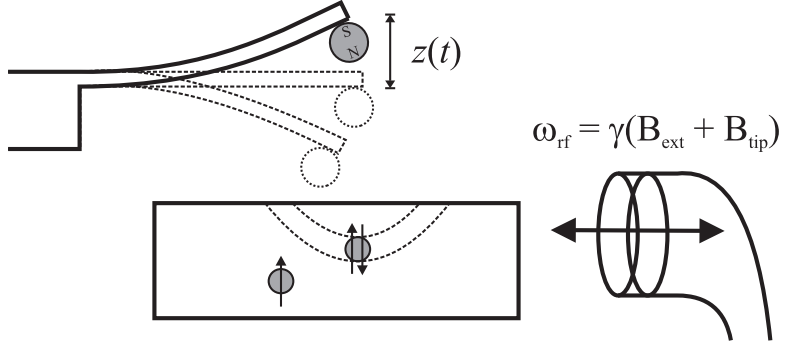
What is the size of the force and how large of a deflection will it cause? The force on the cantilever is the product of the magnetic moment of the spin and the

(a)



$$F_z = \mu_z \frac{\partial B_z}{\partial z}$$

(b)



$$F_z(t) = \mu_z(t) \frac{\partial B_z}{\partial z}$$

Figure 1.1: The MRFM Experiment. In (a), the force, F_z , between the sample spin (μ_z) and the gradient from the magnetic particle ($\partial B_z / \partial z$) causes a small DC deflection in the cantilever, determined by Hooke's law. The magnetic moment of the spin is modulated by an rf field from a nearby coil in (b). Modulating the spin magnetization at the cantilever resonance frequency results in a large, time dependent cantilever amplitude that is proportional to the quality factor of the cantilever, $z = QF/k$. Cantilever deflections are not to scale.

field gradient from the particle

$$F_z = \mu_z \frac{\partial B_z}{\partial z} \quad (1.1)$$

where the magnetic moment (μ) and the gradient ($\partial B_z / \partial z$) are taken to be along the direction of the cantilever motion (z). In this example, the spin is a proton with a magnetic moment of $\mu_p = 1.41 \times 10^{-26}$ J/T. To increase the magnitude of the force, it is necessary to maximize the gradient. The gradient from a spherical particle is

$$\frac{\partial B_z}{\partial z} = 2B_s \frac{r^3}{(r + d)^4} \quad (1.2)$$

where d is the distance from the surface of the magnet to the spin, r is the radius of the magnet, and B_s is the saturation magnetization of the particle. Based on Eq. 1.2, a small magnet, positioned as close as possible to the spin, should give a large gradient. Assume that the magnetic particle is made of iron ($B_s = 2.15$ T) and has a radius of $r = 15$ nm. The tip-sample distance is set by the cantilever position, and we imagine that it is possible to approach the spin to within $d = 5$ nm with no ill effect on the cantilever. The resulting gradient at the spin is large: 9.1×10^7 T/m. Note that according to Eq. 1.2, the gradient will be maximized when the tip-sample distance is zero. This is experimentally untenable since the cantilever would be touching the sample and no deflection would occur. Instead, the distance d is set to a small value and a magnet radius is chosen that maximizes the gradient at this distance. In this case, it is easy to prove that the gradient will be at a maximum when $r = 3d$, as is the case above.

The force on the cantilever, using Eq. 1.1 and the gradient is therefore $F_z = 1.3 \times 10^{-18}$ N or 1.3 aN. This small force causes a deflection in the cantilever proportional to the cantilever's stiffness, measured by the spring constant k . The

cantilever deflection in the z direction is calculated using Hooke's law, $F = -kz$, where the negative sign indicates that this is a restoring force. If the cantilever is extremely soft with a spring constant on the order of 10^{-5} N/m, the displacement from equilibrium will be 1.3×10^{-13} m or 1.3 mÅ. This is approximately one thousand times smaller than the diameter of an atom! Using typical detection techniques, it is highly unlikely that we would ever be able to measure this small deflection.

Fortunately, the size of the deflection can be enhanced by changing the direction of the magnetic moment at a specific frequency. By applying radio frequency (rf) radiation from a nearby coil, the direction of the magnetization of the spins can be flipped from along the external magnetic field to against the field, changing the force on the cantilever from attractive to repulsive. Flipping these spins at the cantilever resonance frequency modulates the force on the cantilever and results in a quality factor enhanced cantilever amplitude

$$z = \frac{F}{k}Q \quad (1.3)$$

The quality factor, Q , is directly proportional to the amount of time it takes for an oscillator to “ring-down” to its equilibrium oscillations after being excited. If the Q of our cantilever is large, say 25,000, the oscillation amplitude in our single nuclear spin example becomes approximately 3 nm and is easily detectable using a fiber-optic interferometer and a lock-in amplifier. The large cantilever oscillations due to on-resonance force modulation are depicted in Figure 1.1(b).

Controlling the direction of the spin magnetic moment not only enables us to enhance the cantilever detection, but it also allows us to use MRFM as an imaging technique. The only spins that contribute to the cantilever deflection are the ones

in the region of space where the equality

$$\omega_{\text{rf}} = \gamma(B_{\text{ext}} + B_{\text{tip}}) \quad (1.4)$$

is satisfied. The frequency of the rf radiation, ω_{rf} , is the Larmor precession frequency of the spins and is equivalent to the frequency of energy needed to flip the spins. The region of space where Eq. 1.4 is satisfied is shaped like a bowl, seen in Figure 1.1(b), due to the shape of the field from the magnetic particle, B_{tip} . Only the spins in this bowl, known as the sensitive slice, will be affected by the rf radiation. Spins above the slice experience a tip field that is too high to satisfy Eq. 1.4, whereas those below the slice experience a tip field which is too weak.

By changing either ω_{rf} or the external magnetic field, B_{ext} , the position of the sensitive slice in the sample will change and a different set of spins will be addressed by the rf. As the slice is scanned, the deflection of the cantilever changes depending on the spin density in the slice, mapping out the sample spin density in one dimension as a force on the cantilever. This technique can be extended to three dimensions by scanning the cantilever in the x and y directions. This is similar to the techniques used in MRI, where magnetic field gradients cause the protons in body tissue to resonate at different frequencies depending on their location. The sensitive slice moves through the body by scanning the frequency of the applied rf pulse and an image is reconstructed from the inductively coupled NMR signal [12].

It should be noted that many early MRFM experiments, including those discussed later in this dissertation, were performed in the sample-on-cantilever geometry. In this geometry, the sample, rather than the magnet, is affixed to the cantilever tip. The cantilever is positioned near a large magnetic particle, which provides the gradient. This geometry is formally identical to the magnet-on-cantilever geometry discussed above and is useful for control experiments because it is easier

to align the sample on the cantilever to a large particle than it is to align the cantilever to a sample surface.

1.2 Measuring Small Forces in MRFM

As calculated above, the magnetic moment of a single nuclear spin causes a force on the cantilever as small as a single attonewton, or 10^{-18} N in the presence of a small magnet close to the spin. This is an incredibly small force, and it will be difficult to create gradients much larger than 9×10^7 T/m. Therefore, in order to image a biological molecule with single spin sensitivity, we must be able to measure a force as small as an attonewton.

Figure 1.2 allows the reader to compare the force expected in the single spin NMR-MRFM experiment to small forces experienced in the physical world that may be more familiar. At the larger end of the spectrum, we find that the gravitational force on Newton's apple falling from a tree is approximately 0.5 N, assuming an average apple size. The force required to break a covalent chemical bond has been measured by anchoring one end of a molecule to a surface and the other to an atomic force microscopy cantilever. The cantilever pulls on the bond until it breaks, and the force required to break the bond is measured by the cantilever displacement. This force was determined to be approximately 1 nN (nanonewtons) or 10^{-9} N [13], a billion times larger than the forces we would like to measure. The forces from molecular motors have been measured using optical methods. An individual fiber of myosin, the molecular motor responsible for the contraction of muscles, was found to exert 4 pN (piconewtons) or 4×10^{-12} N of static force [14], a million times larger than our target. Finally, the repulsive Coulomb force between two electrons 1 μ m apart is 230 aN, two orders of magnitude larger than the force

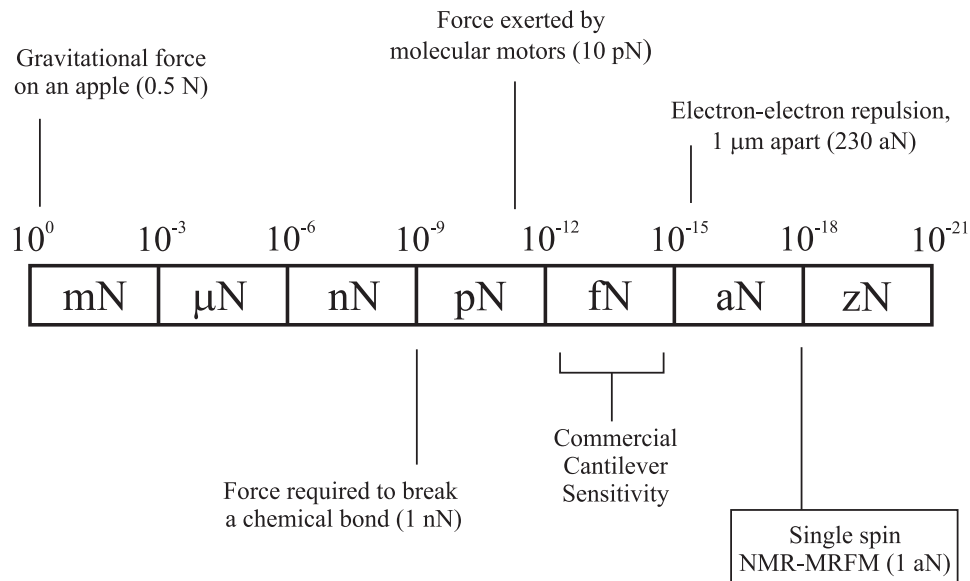


Figure 1.2: A comparison of small forces. The sensitivity limit of commercially available cantilevers is approximately 10^{-15} N, one thousand times larger than the force expected in the single spin NMR-MRFM experiment.

in the single-spin NMR-MRFM experiment.

Measuring forces above a femtonewton (10^{-15} N) is possible using commercially available atomic force microscope cantilevers. The commercial cantilever used by Marohn, *et al.* (Digital Instruments model ESP) exhibited a minimum detectable force of approximately 1 fN in a 1 Hz bandwidth at room temperature and in vacuum [15]. Unfortunately, cantilevers with force sensitivities below this threshold cannot be purchased “off the shelf” and must instead be custom fabricated, requiring an extensive knowledge of microfabrication techniques and a clean room facility. Achieving attonewton force sensitivity is crucial to the success of MRFM and has been achieved by several MRFM-focused research groups that custom fabricate silicon cantilevers with thicknesses less than 1 μm [16–19].

However, this is not the only stringent requirement. Recall that the 1 aN force

described above is based on an incredibly small magnetic particle ($r = 15\text{ nm}$) 5 nm away from the sample spin. In the magnet-on-cantilever geometry, this requires that a small magnet be attached to the end of the small cantilever. In most experiments, small magnets with dimensions in the hundreds of nanometers are evaporated one by one onto the end of the cantilever using a shadow mask, or more commonly, glued to the end of the cantilever *by hand*. The magnets are then shaped by ion beam milling to obtain dimensions on the nanometer scale. This is, to say the least, a difficult and tedious process. If MRFM is to become a characterization technique on the scale of NMR, MRI, or X-ray crystallography, a fabrication procedure that incorporates a nanoscale magnet on the tip of the cantilever in a batch process must be realized.

Many other factors must also be considered in order to measure small forces. MRFM experiments must be performed in high vacuum since the quality factor of the cantilever is larger in the absence of ambient gas. A high quality factor ensures that the cantilever oscillations will be large (Eq. 1.3) and also decreases the intrinsic force sensitivity of the oscillator. Cryogenic temperatures, typically 4 K or below, are necessary in order to reduce the Brownian motion noise of the cantilever, improving cantilever sensitivity. Working at low temperatures and high external magnetic fields improves the sample polarization and the resulting signal strength in samples with many spins. A great deal of engineering expertise must be used to build these cryogenic, high vacuum MRFM probes, which contain many small parts that must be spaced microns apart and stay aligned when cooled. A working knowledge of electronics, circuitry, and optics is a necessity in order to manipulate cantilever oscillation and position, create modulated rf signals, and detect cantilever motion. Thus, the measurement of small forces requires an

intimate knowledge of physics, chemistry, and engineering that must be brought together to produce a working magnetic resonance force microscope.

1.3 Survey of MRFM Milestones

MRFM was first proposed by John Sidles, a professor in the Department of Orthopaedics at the University of Washington, in 1991 as a method for imaging single biological molecules that could not be identified using conventional imaging techniques [8]. Sidles proposed that a single nuclear spin could be detected as a force between the spin magnetic moment and the gradient from a magnetic particle attached to a piezoelectric, tuning fork oscillator. The amplitude of the tuning fork would be enhanced to a measurable level using a threefold resonance technique. The tuning fork was imagined to have a resonance frequency equal to the precession frequency of the spin in the megahertz range. When the oscillator is driven into resonance and brought near the sample, which is also oscillating at the precession frequency, the fluctuating field from the magnetic particle changes the magnetization of the sample spin, creating a time dependent force on the oscillator. Since this proposal, MRFM techniques have been simplified somewhat, as evidenced in the example experiment in Section 1.1. This section presents a brief survey of the major MRFM milestones reached over the last 15 years. This survey is not intended as a complete overview of the technique, but should provide the reader with the general roadmap that the community has followed in attempting to reach single nuclear spin sensitivity.

According to Sidles, MRFM sensitivity has doubled every 3.1 months between 1992 and 2004, “a rate of progress unequalled by any sensor technology in history” [20]. Initial MRFM experiments studied electrons, which give a larger force

signal than nuclei due to their larger magnetic moment ($\mu_e \sim 650\mu_p$). The first force detection of electron spin resonance was performed by Dan Rugar at IBM's Almaden Research Center in 1992 [21], approximately one year after the original proposal. Rugar glued a sample of diphenylpicrylhydrazyl (DPPH) to the end of a commercial AFM cantilever and produced a signal at room temperature by modulating the sample magnetization at half the cantilever resonance frequency in the presence of an applied magnetic field from an rf coil. The peak force in this experiment was 14 fN, slightly larger than the force sensitivity of the commercial cantilever. Rugar's group used this same technique and sample-on-cantilever geometry one year later to demonstrate the first successful imaging of electron spins using MRFM [22, 23]. In this experiment, the magnetic particle was placed on a piezoelectric transducer and scanned in the x and y direction, while the sensitive slice was moved through the sample in z by varying the distance between the tip and the sample. The resulting magnetic resonance force maps of the DPPH sample were deconvoluted using a reconstruction technique to recover the spin density from the force maps with a resolution in the z direction of about 1 μm .

In 1994, Rugar demonstrated the first detection of nuclei using force detection. A custom fabricated silicon nitride cantilever, 900 Å thick was used to measure the magnetic moment of 10^{13} protons in ammonium nitrate at room temperature [24]. The magnetization was modulated by cyclic adiabatic inversion, whereby the spin magnetization is flipped at the cantilever resonance frequency rather than saturated. Ammonium nitrate was chosen for this technique because of its high proton density and long relaxation time in the rotating frame, $T_{1\rho} > 1$ s, allowing the sample magnetization to follow the rf field for many cantilever oscillations. Three-dimensional imaging of ammonium nitrate was observed two years later in the

Table 1.1: Significant Milestones in MRFM, listed by publication year.

Year	Milestone	Reference
1992	Force Detection of Electrons	[21]
1993	3-D Imaging of Electrons	[22]
1994	Force Detection of ^1H	[24]
1996	3-D Imaging of ^1H	[25]
	Force Detection of FMR	[26]
	Low Temperature NMR-MRFM (^{19}F)	[27]
1997	Fabrication of aN Sensitive Cantilevers	[16]
1998	Cyclic Adiabatic Inversion ESR-MRFM	[28]
	Magnet-on-Cantilever MRFM	[29, 30]
2001	OSCAR Demonstrated, 100 Electron Sensitivity	[31]
2003	i-OSCAR Demonstrated, 10 Electron Sensitivity	[32]
2004	Single spin ESR-MRFM	[10]
	Batch Fabrication of Magnetic-Tipped Cantilevers	[19]
	CERMIT Demonstrated, 500,000 ^1H Sensitivity	[33]
2005	2,000 ^1H Sensitivity, First Protein Studied by MRFM	[34]
2006	Cyclic CERMIT Demonstrated, 500 ^{19}F Sensitivity	[11]

sample-on-cantilever geometry [25]. As before, the magnetic tip was scanned in x and y , but the sensitive slice was scanned by changing the rf frequency, not the actual z position of the particle. Zhang and Hammel demonstrated the first observation of ferromagnetic magnetic resonance (FMR) by MRFM in a yttrium iron garnet sample later in that year [26].

NMR-MRFM was performed at low temperature by Wago, *et al.* in an attempt to improve sensitivity [27]. As will be proven later, decreasing the temperature lowers the thermal vibration noise of the cantilever and improves force sensitivity. The fluorine nuclei (^{19}F) in a sample of CaF_2 were detected at 6 K with a force sensitivity of 80 aN using a commercial cantilever. To further improve sensitivity, Stowe, *et al.* fabricated aN sensitive ultrathin cantilevers for use in MRFM in 1997 [16]. Cantilevers were developed with thicknesses as small as 60 nm and spring constants of $6.5 \times 10^{-6} \text{ N/m}$ to attain force sensitivities as low as 5.6 aN at 4 K, just above the force calculated for the single nuclear spin experiment.

Before 1998, ESR-MRFM techniques commonly used the cyclic saturation technique, which requires spin ensembles where the polarization is governed by Boltzmann statistics and the Curie law. To detect the signal from smaller and smaller electron spin ensembles where the number of polarized spins decreases drastically, it was necessary to use cyclic adiabatic inversion, which does not require a large polarization. Unfortunately, this technique does require a long $T_{1\rho}$ compared to the cantilever oscillation period. Nuclear samples with long $T_{1\rho}$ are readily available, but it is difficult to find electron samples that meet this requirement. Wago, *et al.* demonstrated a cyclic adiabatic inversion technique with electrons by creating a sample with favorably long relaxation times at low temperatures [28]. Gamma irradiation of silica results in dangling silicon bonds, which leave a single electron

in the orbital of a silicon atom, known as an E' center [35, 36]. These E' centers have relaxation times as long as several seconds at cryogenic temperatures and are perfectly suited for these experiments. In this experiment, the sample was glued to the end of the cantilever, and cyclic inversions were used to measure the sample T_1 by nutation and perform spin-echo experiments. The amount of γ irradiation could be decreased to reduce the density of unpaired electrons in the silica sample and tailor the number of spins in the sensitive slice.

The gradients used in the sample-on-cantilever experiments described above are consistently smaller than ~ 600 T/m, five orders of magnitude smaller than the gradient necessary to obtain a force of 1 aN in the single nuclear spin experiment. Unfortunately, increasing the gradient, which is inversely proportional to the thickness of the sensitive slice decreases the total force on the cantilever, making it difficult to resolve the signal. As the gradient increases, the slice becomes thinner, fewer spins will be in resonance at once, and the total force decreases. However, the force *per spin* increases with the gradient. In order to reach single spin sensitivity, the gradient must be increased despite the resulting loss in total force.

A large gradient for MRFM was first produced by inverting the orientation of the experiment to the magnet-on-cantilever geometry, allowing for the use of smaller magnetic particles close to the sample. A gradient of 1,000 T/m was used to image a sample of DPPH by hand-gluing a 110 μm diameter nickel sphere to the end of a cantilever [29]. A grid of $64 \times 64 \times 33$ points was imaged at 0.9 s per point, requiring 1.4 days to complete. In the same year, Bruland, *et al.* also demonstrated a magnet-on-tip geometry with a gradient of 250,000 T/m using a 7 μm diameter samarium cobalt sphere approximately 500 nm from the sample [30].

In 2001, Stipe, *et al.* detected ESR-MRFM from 100 net electron spins with a gradient larger than 10^5 T/m using the oscillating cantilever-driven adiabatic reversals technique, known as OSCAR [31]. OSCAR is the first MRFM technique to detect the spin magnetization as a change in the spring constant of the cantilever resulting from an oscillatory interaction force. In 2003, a modulated OSCAR (interrupted OSCAR, or i-OSCAR) was used to study the \sqrt{N} statistical polarization of order 10 spins by Mamin, *et al.* [32]. In each of these experiments the magnet-on-cantilever geometry detected the electrons in the E' centers of γ -irradiated silica, where the spin concentration was reduced by decreasing the amount of irradiation. OSCAR and i-OSCAR will be described in much more detail later in this dissertation.

In 2004, Rugar, *et al.* achieved single electron spin detection, a long-standing goal and the most significant MRFM accomplishment to date [10]. Rugar used i-OSCAR to measure a few millihertz frequency shift from a single electron in a frequency noise of 25 mHz (SNR = 0.06) by signal averaging for 13 hours per point. This required 19 days to obtain a full scan of the sample. The experiment was performed at 1 K with a thin, magnetic-tipped cantilever oriented perpendicular to the sample surface. This orientation allows the magnetic tip to be brought within nanometers of the sample surface without the chance of “snap-in” to the surface due to electrostatic forces encountered in the traditional parallel geometry.

Two significant advances were also published in 2004 by the Marohn group at Cornell University. The first batch fabrication of magnetic-tipped ultrasensitive cantilevers was developed by Jenkins, *et al.* [19] (the subject of the first half of this dissertation). This fabrication protocol eliminates the need for tedious methods to position magnets on the tips of cantilevers individually and may allow

for the eventual use of the technique as a general characterization tool. Garner, *et al.* demonstrated the cantilever-enabled readout of magnetic-inversion transients (CERMIT) protocol for detecting homogenous distributions of spins below a perpendicularly-oriented cantilever tip [33]. It can be imagined that when the cantilever is perpendicular to the sample surface, the force below the tip will be zero by symmetry. To avoid this problem, CERMIT creates an inhomogeneous distribution of spins directly below the tip and detects this as a change in the cantilever spring constant. A nuclear spin sensitivity of 500,000 ^1H was achieved using this protocol. CERMIT will be discussed in further detail in a later chapter of this dissertation.

Since 2004, the Rugar group has refocused its efforts on single nuclear spin detection. In 2005, the detection of the \sqrt{N} statistical polarization in nuclear spin ensembles was demonstrated. Mamin, *et al.* studied ensembles of order $\sqrt{N} = 10^4$ net spins with a sensitivity of roughly 2000 net spins by averaging for 2.5 hours in CaF_2 [34]. The nuclear spins in PMMA (poly(methyl methacrylate)) and the protein collagen, the first biological sample detected by MRFM, were also studied. The spin densities of all three samples were in the range of $4 - 6 \times 10^{22}$ spins/cm³, and the statistical polarization was studied by working at small external fields, reducing the Boltzmann polarization. Using a cyclic CERMIT protocol, the Rugar group demonstrated the current state-of-the-art sensitivity of 500 nuclear spins, discussed at the 2006 Kavli Institute at Cornell University Summer School in MRFM [11]. Interestingly, this record sensitivity was achieved by returning to the sample-on-cantilever geometry. A thin layer of CaF_2 was evaporated onto the end of a thin cantilever and then scanned perpendicularly over an array of nanofabricated pyramidal FeCo magnets. These tiny pyramids

produce gradients of 1.4×10^6 T/m, seven times larger than the gradient in the single electron experiment.

1.4 Summary and Outline of the Dissertation

Great progress has been made towards single nuclear spin sensitivity, which may eventually allow for angstrom-level resolution imaging of single biomolecules. Unfortunately, with the exception of collagen, no biological samples have been studied using MRFM. The OSCAR technique requires a long correlation time, τ_m , which is related to $T_{1\rho}$, in order to force the spins to coherently follow the cantilever oscillations. For example, the τ_m of the typical E' centers used in the most sensitive ESR-MRFM experiments are as long as several seconds, whereas τ_m is approximately 100 ms for collagen [34]. This value is expected to be quite short for most other samples as well, casting doubt on the real world applicability of the OSCAR technique.

Furthermore, the CERMIT experiment is limited by the spin-lattice relaxation time of the sample (T_1), which must be longer than several cantilever oscillations. Since T_1 is generally longer than $T_{1\rho}$ at cryogenic temperatures for most samples, the CERMIT limitation is less restrictive than the OSCAR limitation. However, the CERMIT technique may not be adaptable to samples with T_1 's below about 10 ms, based on the period of typical audio frequency cantilevers (i.e., cantilevers with a resonance frequency in the range of approximately 50Hz to tens of kilohertz).

In order for MRFM to become a useful characterization tool for the scientific community, it is necessary to develop force sensors that are capable of measuring incredibly small forces with nanoscale magnetic tips batch fabricated at the end of the cantilever. Additionally, techniques must be developed to expand the types

of samples that can be characterized with MRFM by reducing the dependence on long spin coherence times. It is the purpose of this thesis to describe progress towards meeting these goals.

Chapter 2 of this thesis will describe the theoretical and practical considerations in the design of attonewton sensitive force detectors. The minimum detectable force and the scaling law for fabricating ultrasensitive cantilevers will be derived, and characterization of magnetic tips will be discussed.

Chapter 3 will detail the fabrication and characterization procedure of ultra-sensitive, magnetic-tipped silicon cantilevers with low spring constants and high quality factors. We will also consider designs for cantilevers that can be used in the perpendicular geometry with reduced non-contact friction and in MRFM studies of self-assembled monolayers.

Chapter 4 will outline a new MRFM detection protocol for detecting electron spins as a change in the cantilever spring constant, the first direct observation of a force gradient detected ESR signal. Unexpectedly, we find that the shape of the signal depends on the size of the gradient produced by the magnetic particle.

Chapter 5 will describe control experiments for a technique that could be used to detect small spring constant shifts in MRFM experiments without the need for signal averaging. The theory of parametric amplification will be described and results will show that spring constant changes, on par with those expected in MRFM experiments, are easily detectable using parametric amplification.

CHAPTER 2

CANTILEVER ENGINEERING AND SENSITIVITY

2.1 Introduction

Development of sensitive cantilevers with integrated magnetic tips able to detect forces as small as 10^{-18} N is a formidable challenge. This chapter will focus on the design requirements and properties of these force sensors. We will begin with the equation of motion for the cantilever, and the relevant cantilever properties important to force sensitivity will be defined. A derivation of the form of these properties in terms of the cantilever length, width, and height will follow, along with derivations for the minimum detectable force. The results of this work will motivate our fabrication requirements for developing ultrasensitive cantilevers. The chapter will conclude with a brief discussion of cantilever magnetometry as a characterization method for the magnetic tips.

2.1.1 Equation of motion and cantilever response

The equation of motion for a damped harmonic oscillator is

$$m\ddot{x} + \Gamma\dot{x} + kx = F \quad (2.1)$$

where x is the cantilever position, \dot{x} is the cantilever velocity, \ddot{x} is the cantilever acceleration, m is the mass of the oscillator, Γ is the cantilever dissipation, k is the cantilever spring constant, and F is the applied force. It is useful to divide this equation by the mass to obtain the canonical equation of motion

$$\ddot{x} + \frac{\omega_0}{Q}\dot{x} + \omega_0^2x = \frac{F\omega_0^2}{k} \quad (2.2)$$

where

$$\frac{\omega_0}{Q} = \frac{\Gamma}{m} \quad \text{and} \quad \omega_0^2 = \frac{k}{m} \quad (2.3)$$

Q is the quality factor of the cantilever, and ω_0 is the resonance frequency in rad/s. The quality factor is inversely proportional to the damping term, and is a ratio of the energy stored in the oscillator to the energy lost through dissipation per cycle. The quality factor is also a measure of the time required for the oscillator to “ring-down” from an excited amplitude. The larger the Q , the longer the ring-down.

If the oscillator is driven with a cosinusoidal force at a frequency ω

$$F = F_0 \cos \omega t \quad (2.4)$$

then the solution to the canonical equation of motion will describe the cantilever response at steady-state. The cantilever response will be periodic and of the form

$$x(t) = x_c \cos \omega t + x_s \sin \omega t = z_0 e^{i\omega t} \quad (2.5)$$

where x_c is the in-phase cantilever response, and x_s is the out-of-phase response. To make the math easier, $x(t)$ is rewritten in terms of a complex number z_0 where the real part of z_0 is the in-phase cantilever response and the imaginary part of z_0 is the out-of-phase response. When $x(t)$ is substituted into Eq. 2.2, the form of z_0 is determined to be

$$z_0 = \frac{F_0}{k} \frac{\omega^2}{(\omega_0^2 - \omega^2) + \frac{i\omega\omega_0}{Q}} \quad (2.6)$$

Based on Eq. 2.6, the cantilever response to an on-resonance force ($\omega = \omega_0$) is

$$z_0 = -\frac{iQF_0}{k} \quad (2.7)$$

Therefore, the cantilever responds out-of-phase with the driving force at an amplitude of QF_0/k , and there is no in-phase response. If the force is small, as in

an MRFM experiment, it is advantageous to oscillate the force at the resonance frequency in order to amplify the signal by a factor of Q . If Q is large, small oscillating forces will result in large, easily measured cantilever displacements.

2.2 Derivation of Cantilever Properties

In this section, the cantilever spring constant and resonance frequencies will be derived in terms of the cantilever dimensions from an engineering prospective, based on Kinsler's *Fundamentals of Acoustics* [37]. The general solution for the fourth order differential equation for the bending in a floating beam will be determined, and then used for the case of a cantilever, fixed at one end.

2.2.1 The bending moment

In order to determine the form of the cantilever parameters, we must first define the bending moment, or the internal torque, of a beam under stress. We consider an internal segment of a straight beam of length l , having uniform cross section S . The segment of the beam, which is the hatched portion of Figure 2.1(a), has a length dx . The dotted line represents the neutral axis which is the section of the beam that does not change length when the bar is bent. Sections above the neutral axis are stretched longer than normal under bending, and sections above the neutral axis are compressed. Figure 2.1(b) shows the segment of length dx under a bending force. When the bar is bent, the length of the shaded portion of Figure 2.1(b) changes by an amount δx . The shaded portion is a distance r from the neutral axis and the bending of the segment is measured by the radius of curvature R .

When the beam is bent, a longitudinal force df lengthens the shaded portion.

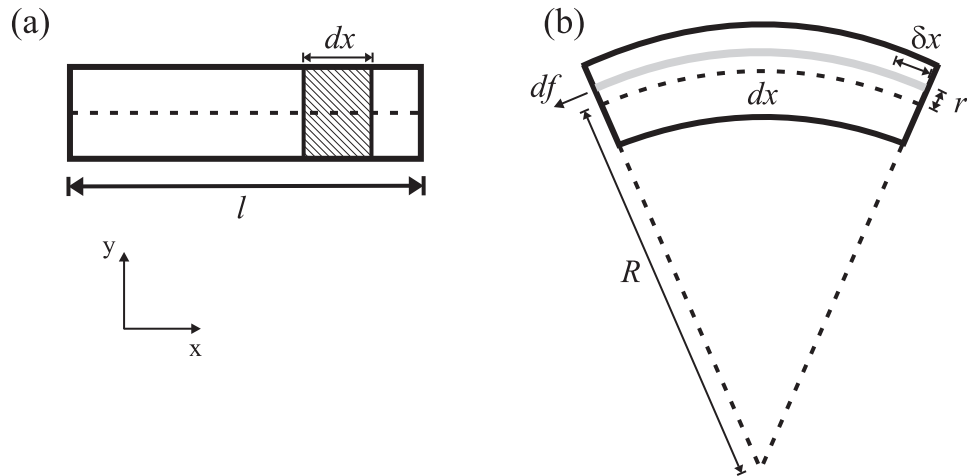


Figure 2.1: Determining the bending moment of a beam under stress. The beam of length l and cross section S is depicted in (a). The dotted line represents the neutral axis of the beam, which does not change length when the bar is stressed. We consider a small section of the beam of length dx , which is shaded in (a). The beam is flexed, and the segment is bent with a radius of curvature R in (b). The shaded portion of the segment a distance r from the neutral axis is stretched by a longitudinal force df a distance δx .

The longitudinal force is defined as

$$df = -EdS \frac{\delta x}{dx} \quad (2.8)$$

where E is the Young's modulus of the material (a measure of a material's stiffness), dS is the cross-sectional area of the shaded portion, and $\delta x/dx$ is the ratio of the change in length to the original length, otherwise known as the strain. The sign of df is negative because the force is a tension.

It is more convenient to define the force in terms of the radii. Based on the geometry of the arc defined by the curvature of radius, the ratio of the arc lengths and radii for the neutral axis is the same as that for the shaded segment

$$\frac{dx}{R} = \frac{dx + \delta x}{R + r} \quad (2.9)$$

which can be rewritten as

$$\frac{\delta x}{dx} = \frac{r}{R} \quad (2.10)$$

This is substituted into Eq. 2.8

$$df = -\left(\frac{E}{R}\right) r dS \quad (2.11)$$

Since the forces above the neutral axis are canceled by the forces below the axis, the total longitudinal force will be zero. However, a bending moment M is present in the bar, and it is defined as

$$M = \int r df = -\frac{E}{R} \int r^2 dS \quad (2.12)$$

If we define the radius of gyration, κ , as

$$\kappa^2 = \frac{1}{S} \int r^2 dS \quad (2.13)$$

then we can write the bending moment as

$$M = -\frac{ES\kappa^2}{R} \quad (2.14)$$

For a bar of thickness t , the radius of gyration is $\kappa = t/\sqrt{12}$.

If displacements of the segment in the y direction are limited to small values,

$\partial y/\partial x \ll 1$ and

$$R = \frac{[1 + (\partial y/\partial x)^2]^{3/2}}{\partial^2 y/\partial x^2} \approx \frac{1}{\partial^2 y/\partial x^2} \quad (2.15)$$

resulting in a bending moment of

$$M = -ES\kappa^2 \left(\frac{\partial^2 y}{\partial x^2} \right) \sim [\text{N} \cdot \text{m}] \quad (2.16)$$

which has units of torque, as expected.

2.2.2 Deriving k and f_0

We now consider the shear forces acting on the bent beam segment that occur along with the bending moments. A shear force F_y acts on the left end of the segment in the upward direction, which is positive. The force acting on the right side of the beam ($F_y(x+dx)$) must be downward and is negative. On the left side of the beam, the bending moment is $M(x)$, and on the right side, it is $-M(x+dx)$. These shear forces put an additional torque on the beam. Recall that a torque is the product of the force and the distance that the force is acting from the end (i.e., the distance of the lever arm), $\vec{\tau} = \vec{r} \times \vec{F}$, where \vec{r} represents the lever arm.

When a bar is in a state of static equilibrium, the torques and the shear forces acting on any segment must produce no net moment, thus $\sum \vec{M} + \sum \vec{r} \times \vec{F} = 0$. The total moments and torques in the segment are thus

$$M(x) - M(x+dx) - F_y(x+dx) dx = 0 \quad (2.17)$$

There is no torque from the force $F_y(x)$ since the lever arm of the segment at the end of the beam would be zero. We now assume that the segment length dx is

small and expand $M(x + dx)$ and $F_y(x + dx)$ in Taylor expansions about x out to first terms and Eq. 2.17 becomes

$$M(x) - \left(M(x) + \frac{\partial M}{\partial x} dx \right) - \left(F_y(x) + \frac{\partial F_y}{\partial x} dx \right) dx = 0 \quad (2.18)$$

If dx is small, then $(dx)^2$ is also small, and Eq. 2.18 simplifies to

$$F_y = -\frac{\partial M}{\partial x} = -ES\kappa^2 \left(\frac{\partial^3 y}{\partial x^3} \right) \quad (2.19)$$

using Eq. 2.16. The net upward force dF_y acting on the segment dx is thus

$$dF_y = F_y(x) - F_y(x + dx) = \left(\frac{\partial F_y}{\partial x} \right) dx = -ES\kappa^2 \left(\frac{\partial^4 y}{\partial x^4} \right) dx \quad (2.20)$$

We can now write an equation of motion associated with this force dF_y . The force will give the mass of the segment an upward acceleration by Newton's second law $dF_y = m\partial^2 y / \partial t^2$. The mass of the beam (m) is the product of the density (ρ) and the volume (Sdx). Using this and Eq. 2.20, we are left with

$$\frac{\partial^2 y}{\partial t^2} = -(\kappa c)^2 \frac{\partial^4 y}{\partial x^4} \quad (2.21)$$

where $c^2 = E/\rho$.

This fourth order differential equation of motion can be solved using separation of variables. The complex transverse displacement is

$$y(x, t) = \Psi(x)e^{-i\omega t} \quad (2.22)$$

We take the derivatives and substitute them into Eq. 2.21, resulting in

$$\frac{\partial^4 \Psi}{\partial x^4} = \left(\frac{\omega}{\nu} \right)^4 \Psi \quad (2.23)$$

where $\nu^2 = \omega(\kappa c)$, which has units of velocity. We assume a solution of the form $\Psi = e^{\gamma x}$ which is valid when $\gamma = \pm g$ and $\pm ig$, where $g = \omega/\nu$. This leads to

$$\Psi(x) = Ae^{gx} + Be^{-gx} + Ce^{igx} + De^{-igx} \quad (2.24)$$

where A , B , C , and D are arbitrary complex constants that will depend on the boundary conditions of the beam. The actual solution of Eq. 2.21 is the real part Eq. 2.22:

$$y(x, t) = [A \cosh gx + B \sinh gx + C \cos gx + D \sin gx] \cos(\omega t + \phi) \quad (2.25)$$

This is the general solution to Eq. 2.21. To determine the spring constant and resonance frequency in terms of the cantilever parameters, we must define four boundary conditions for a beam fixed at one end and determine the four coefficients.

At the fixed end of the cantilever beam, the displacement and the slope should be zero

$$y(0, t) = 0 \quad \text{and} \quad \frac{\partial y}{\partial x}(0, t) = 0 \quad (2.26)$$

When we apply the first of these boundary conditions to Eq. 2.25, we find that $A = -C$. Similarly, the second boundary condition results in $B = -D$. Combining these results gives a general solution of

$$y(x, t) = [A(\cosh gx - \cos gx) + B(\sinh gx - \sin gx)] \cos(\omega t + \phi) \quad (2.27)$$

To find the form of A and B , we need two additional boundary conditions. At the free end of the cantilever ($x = l$ where l is the cantilever length), there can be no externally applied torque (i.e., bending moment)

$$M = -ES\kappa^2 \left(\frac{\partial^2 y}{\partial x^2} \right) = 0 \quad (2.28)$$

and there can be no shear force

$$F_y = ES\kappa^2 \left(\frac{\partial^3 y}{\partial x^3} \right) = 0 \quad (2.29)$$

Thus the final two boundary conditions are

$$\frac{\partial^2 y}{\partial x^2}(l, t) = 0 \quad \text{and} \quad \frac{\partial^3 y}{\partial x^3}(l, t) = 0 \quad (2.30)$$

Applying these two boundary conditions to Eq. 2.27 results in two equations

$$A(\cosh gl + \cos gl) = -B(\sinh gl + \sin gl) \quad (2.31)$$

$$A(\sinh gl - \sin gl) = -B(\cosh gl + \cos gl) \quad (2.32)$$

$$(2.33)$$

By finding the frequencies at which these two equations are both simultaneously true, we find the resonance frequency and the frequencies of the higher cantilever modes. First divide Eq. 2.31 by Eq. 2.32 and simplify with trigonometric identities

$$\cosh gl \cos gl = -1 \quad (2.34)$$

Numerical techniques can be used to determine the allowed values of gl that satisfy the above equation

$$gl = \frac{\omega l}{\nu} = (1.194, 2.988, 5, 7, \dots) \frac{\pi}{2} \quad (2.35)$$

Each coefficient represents a different cantilever mode. The fundamental mode is represented by 1.194, and the second mode is represented by 2.988, and so on. Notice that the higher modes are not harmonics of the fundamental mode for a cantilever beam.

The resonance frequency can be written in terms of cantilever length, l , and thickness, t , using the first coefficient of Eq. 2.35, $\omega = 2\pi f$, $\nu = \sqrt{\omega\kappa c}$, $c^2 = E/\rho$, and $\kappa = t/\sqrt{12}$,

$$f_0 = \frac{3.518}{2\pi} \frac{t}{l^2} \left(\frac{E}{12\rho} \right)^{1/2} \sim [\text{Hz}] \quad (2.36)$$

Thus, we see that the resonance frequency of the cantilever is proportional to the thickness of the beam, and inversely proportional to the square of the length.

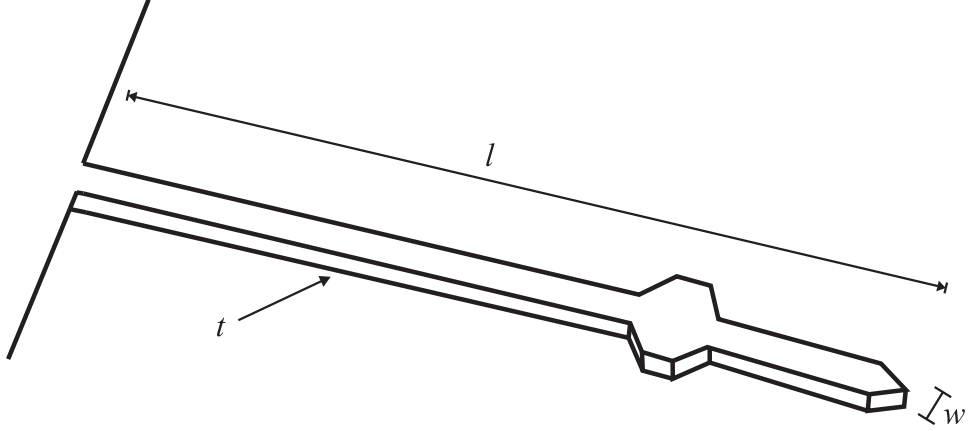


Figure 2.2: Typical cantilever with thickness t , length l , and thickness t .

The fiber-optic interferometer used to detect cantilever motion is aligned to the octagonal paddle.

Higher f_0 cantilevers are short and thick, and lower f_0 cantilevers are long and thin.¹

The spring constant is determined using $\omega_0^2 = k/m_{\text{eff}}$, from the equation of motion for the simple harmonic oscillator, where m_{eff} is the effective mass, ($m_{\text{eff}} = 0.25m_{\text{beam}}$). The mass of the beam, m_{beam} , is determined using the density (ρ) and the volume, $V = lwt$, where w is the width of the beam. Thus the spring constant is

$$k = 1.030 \frac{1}{4} \frac{Ewt^3}{l^3} \sim \left[\frac{\text{N}}{\text{m}} \right] \quad (2.37)$$

The cantilever spring constant is proportional to the cantilever width and the cube of the thickness, and inversely proportional to the length.

¹The simplification used to determine Eq. 2.36 matches an expression for f_0 used in internal group documents. The most intuitive simplification results in a numerical prefactor of $1.194^2\pi/8$ for the fundamental frequency, and is equivalent to the prefactor in Eq. 2.36.

2.3 Minimum Detectable Force

During an experiment, many sources of noise may exist that can spuriously drive the cantilever and limit the size of the force that can be detected, including ambient vibrations in the room or noise from the detector. These external sources of noise can be limited by vibration damping and through the use of ultrasensitive detection techniques. However, a source of noise inherent to the thermal fluctuations of the cantilever still exists and will ultimately limit the detection capabilities of the cantilever. These thermal fluctuations arise from the coupling of the cantilever to the environment through the equipartition theorem [38].

Consider a harmonic oscillator in equilibrium with its surroundings. The Hamiltonian of this oscillator will be the sum of its kinetic and potential energies

$$\mathcal{H} = \frac{p^2}{2m} + \frac{1}{2}kx^2 \quad (2.38)$$

where p is the momentum of the oscillator, and x is the cantilever displacement. The average value of a quadratic term in the Hamiltonian is equal to $k_B T/2$ according to the equipartition theorem. This allows us to link the fluctuations of the cantilever, x , to the temperature of the thermal bath, T ,

$$\frac{1}{2}k_B T = \frac{1}{2}k\langle x^2 \rangle \quad (2.39)$$

where $\langle x^2 \rangle$ is the average of the squared rms displacement and is equivalent to the area under the power spectrum. By accurately measuring the temperature and $\langle x^2 \rangle$, it is possible to determine the spring constant if all other sources of noise are adequately removed.

We can determine the minimum detectable force of the cantilever qualitatively by considering the power spectrum of the cantilever displacement. The

Fourier transform of the cantilever displacements due to thermal noise results in a Lorentzian lineshape with a peak at the cantilever resonance frequency. The square of the average Fourier transform is the power spectrum of the cantilever displacement as a function of frequency, $P_x(f)$, which has units of m²/Hz. Recall that when a cantilever is driven through its resonance frequency, the displacement has a peak amplitude of $x = QF/k$ at f_0 . Similarly, the peak in $P_x(f)$ occurs at f_0 and is equal to

$$P_x(f_0) = \frac{Q^2}{k^2} P_F(f_0) \quad (2.40)$$

where $P_F(f_0)$ is the force power spectral density at f_0 , which has units of N²/Hz. The full width at half maximum (FWHM) of this peak is f_0/Q .

We can now use the equipartition theorem (Eq. 2.39) and the fact that the area under the power spectrum is equal to $\langle x^2 \rangle$ to relate the cantilever fluctuations to the dissipation. We assume that the peak can be approximated as a triangle with a base of approximately twice the FWHM and a height of $Q^2 P_F(f_0)/k^2$. The area of the triangle is equal to $k_B T/k$ by the equipartition theorem

$$\frac{k_B T}{k} \approx \frac{f_0}{Q} \frac{Q^2}{k^2} P_F(f_0) \quad (2.41)$$

This is the fluctuation-dissipation theorem where the fluctuations in the cantilever ($k_B T/k$) are shown to be coupled to the dissipations (Q). Solving for the force power spectral density at f_0 results in

$$P_F(f_0) \approx \frac{k k_B T}{f_0 Q} \sim \left[\frac{\text{N}^2}{\text{m}} \right] \quad (2.42)$$

The signal is detected in a bandwidth b , and the minimum detectable force of the cantilever is approximately

$$F_{\min} \approx \left(\frac{k k_B T b}{f_0 Q} \right)^{1/2} \sim [\text{N}] \quad (2.43)$$

As will be seen in the following section, this qualitative approach to the minimum detectable force correctly predicts the general behavior of F_{\min} with respect to the cantilever parameters.

2.3.1 Quantitative derivation of F_{\min}

The minimum detectable force for a cantilever will now be derived quantitatively using the mechanical transfer function, $\chi(f)$, and the force noise spectral density, P_F , which is assumed to be frequency independent (white noise). The area under the power spectrum can be written as

$$\langle x^2 \rangle = \int_0^\infty P_x(f) df = \int_0^\infty |\chi(f)|^2 P_F(f) df \quad (2.44)$$

We will ultimately determine F_{\min} by determining the form of $P_F(f)$ and multiplying by the bandwidth.

We must first find the form of the mechanical transfer function. The force on an oscillator can be written as $F(t) = F(\omega)e^{i\omega t}$ and the resulting cantilever amplitude response is $z(t) = z(\omega)e^{i\omega t}$, where z is the complex cantilever displacement. The oscillatory force $F(\omega)$ is related to the response $z(\omega)$ using the mechanical transfer function $\chi(\omega)$

$$z(\omega) = \chi(\omega)F(\omega) \quad (2.45)$$

The transfer function can be used to convert the force to a displacement or vice versa. The form of the transfer function can be determined by substituting $z(t)$ into the equation of motion for the harmonic oscillator (Eq. 2.2). This results in

$$z(\omega) = F(\omega) \frac{\omega_0^2/k}{(\omega_0^2 - \omega^2) + i\frac{\omega\omega_0}{Q}} \quad (2.46)$$

and the transfer function is thus

$$\chi(\omega) = \frac{\omega_0^2/k}{(\omega_0^2 - \omega^2) + i\frac{\omega\omega_0}{Q}} \sim \left[\frac{m}{N} \right] \quad (2.47)$$

When $\omega = \omega_0$, the transfer function becomes $\chi(\omega_0) = -iQ/k$, and we see the familiar cantilever response to an on-resonance force (Eq. 2.7).

The transfer function can now be used to evaluate the integral in Eq. 2.44, where we have set $\omega = 2\pi f$

$$\langle x^2 \rangle = P_F \int_0^\infty \left[\frac{f_0^2/k}{(f_0^2 - f^2) + i\frac{ff_0}{Q}} \right] \left[\frac{f_0^2/k}{(f_0^2 - f^2) - i\frac{ff_0}{Q}} \right] df \quad (2.48)$$

After some simplification, it is advantageous to make the change of variables $f = f_0 F$ and $df = f_0 dF$. This results in

$$\langle x^2 \rangle = P_F \frac{f_0}{k^2} Q \int_0^\infty \frac{Q dF}{Q^2 (F^2 - 1)^2 + F^2} \quad (2.49)$$

This integral is evaluated using Mathematica and found to have a value of $\pi/2$.

We can now use the equipartition theorem to solve for P_F

$$P_F = \frac{2kk_B T}{\pi f_0 Q} \sim \left[\frac{N^2}{Hz} \right] \quad (2.50)$$

When detecting the signal in a bandwidth b , the minimum detectable force is

$$F_{min} = S_F \sqrt{b} = \sqrt{\frac{2kk_B Tb}{\pi Q f_0}} \sim [N] \quad (2.51)$$

where $S_F = P_F^{1/2}$ is the force fluctuation spectral density in units of $N/\text{Hz}^{1/2}$. Typically, the cantilever sensitivity is reported in terms of S_F to allow comparisons of cantilevers independent of bandwidth, which may be different from experiment to experiment.

Based on Eq. 2.51, it becomes clear that force sensitivity is directly proportional to the square root of the spring constant and the temperature and inversely

proportional to the square root of the resonance frequency and the quality factor. The engineering requirements necessary to satisfy these conditions are discussed in the following section.

2.4 Cantilever Design

Upon initial inspection of Eq. 2.51, it would be advantageous to fabricate cantilevers with a large resonance frequency and a low spring constant while maintaining a high quality factor. Unfortunately, the equations that govern k and f_0 make this difficult. Thin and long cantilevers have low k , and low f_0 ; thick and short cantilevers have high f_0 and high k .

To determine which parameters are most important, the spring constant and resonance frequency can be substituted into the minimum detectable force to show how the cantilever dimensions influence F_{\min} . Using Eqs. 2.36, 2.37 and Eq. 2.51, we find

$$F_{\min} = \left(\frac{k_B T}{Q} \right)^{1/2} t \left(\frac{w}{l} \right)^{1/2} \sqrt{b} (E\rho)^{1/4} \quad (2.52)$$

This equation illuminates the strategy used in this work to engineer ultrasensitive cantilevers. In order to detect forces in the attonewton (10^{-18} N) range, cantilevers are fabricated to be thin, narrow, and long while maintaining a large quality factor. Of these dimensions, it is most important to make the cantilevers thin, since F_{\min} is proportional to thickness, whereas it is proportional to the square root of the width to length ratio. The Young's modulus and the density scale with F_{\min} to the 1/4 power, and thus are not as important as the cantilever dimensions.

Maximizing the quality factor of the oscillator is critical to improve sensitivity. However, this can be difficult when fabricating thin cantilevers. At the nanoscale, surface chemistry of oscillators becomes extremely important since the surface

area to volume ratio is much larger than normal. For example, Q is known to be highly dependent on surface effects for sub-micron thick resonators [39]. As the thickness of the oscillator decreases, dissipation is enhanced by surface defects in the atomic lattice and thin layers of surface contamination. For example, oxidation of the cantilever surface in atmosphere is known to lower the Q by promoting dissipation of energy to the surroundings. It has been shown that the quality factor for small oscillators can be improved chemically by hydrogenating the surface or covering it with a self-assembled monolayer (SAM) [40–42]. This can prevent or delay the onset of oxidation, increasing and stabilizing the Q . Additionally, dissipation of energy to the cantilever base by clamping losses can be minimized during fabrication by adding a ledge to the cantilever base [43].

Based on the design constraints from Eq. 2.52, we chose to fabricate low spring constant cantilevers from single-crystal silicon. Single-crystal silicon has a high Young's modulus ($E = 1.3 \times 10^{11}$ N/m²) and density ($\rho = 2.3 \times 10^3$ kg/m³) compared to silicon nitride, another popular oscillator material. However, the low internal stress of single-crystal silicon relative to other materials allows thin, long, and narrow oscillators to be formed without curling. Single-crystal silicon also has a low mechanical loss due to few defects and impurities in the crystal structure, leading to a higher quality factor.

Single-crystal silicon cantilevers developed in this work are less than 500 nm thick and have resonance frequencies in the audio range ($\sim 1 - 20$ kHz) with spring constants as low as 10^{-5} N/m. Quality factors can be as high as 5×10^4 at room temperature, and 2-3 times larger at 4 K.² These parameters result in S_F 's in the

²Note that Q actually decreases between 70 – 170 K, possibly related to surface imperfections, oxidation, or adsorbed contaminants [39]. This has also been observed in the laboratory when performing experiments in liquid nitrogen (77 K).

Table 2.1: Comparison of various parameters for different of MEMS and NEMS oscillators at several temperatures.

Oscillator	f_0 (kHz)	k (mN/m)	Q	S_F (aN/Hz $^{1/2}$)
Thin Si Cantilever, 300 K [19]	2.6	0.13	31,700	64
Thin Si Cantilever, 4 K [32]	8.6	0.60	50,000	7.0
Thin Si Cantilever, 110 mK [18]	5.0	0.26	150,000	0.820
Piezoresistive Si Cantilever, 10 K [47]	66	2.3	10,000	17
Doubly Clamped Nanotube, 300 K [48]	55,000	0.40	80	20
SiN Doubly Clamped Beam, 25 mK [49]	20,000	5,000	150,000	0.600

low attonewton per root hertz range at cryogenic temperatures [44, 45] and as low as 60 aN/Hz $^{1/2}$ at room temperature [19, 46].

Table 2.1 compares the spring constant, resonance frequency, quality factor, and S_F for several types of oscillators at different temperatures, fabricated in this work and elsewhere. The first three entries are for different ultrathin, low spring constant cantilevers [18, 19, 32]. As expected, the f_0 is typically in the low kilohertz range, and k is $\sim 10^{-4}$ N/m. The quality factor of each individual cantilever is high, and the general trend of higher quality factors at low temperature is observed. The cantilever in Jenkins, *et al.* shows record sensitivity at room temperature for an ultrathin cantilever. Thanks to the use of a dilution refrigerator to obtain temperatures of 110 mK, Mamin, *et al.* observed the smallest recorded force sensitivity for a cantilever beam of 820×10^{-21} N or 820 zN (zeptonewtons).

2.4.1 An alternative approach: high f_0 oscillators

Ultrasensitive oscillators can also be designed by maximizing the resonance frequency while maintaining a large quality factor. Typically, this is accomplished

by shrinking the dimensions of the oscillator to the nanoscale. For example, short, thick cantilevers can be designed with relatively high f_0 values in the hundreds of kilohertz. Other types of oscillators, such as doubly clamped beams have been fabricated with submicron dimensions, resulting in f_0 's in the megahertz range. These devices are often referred to as NEMS, or nanoelectromechanical systems (as opposed to MEMS, or microelectromechanical systems, like cantilevers).

Despite the dimensional scaling in Eq. 2.52, high f_0 oscillators may have advantages over low spring constant cantilevers in MRFM applications. The original MRFM proposal by Sidles envisioned using radio frequency (MHz) oscillators to detect and oscillate the spin magnetization [8, 50], eliminating the need for an external oscillatory transverse field from a coil or a stripline which can deleteriously heat the sample. Additionally, high frequency oscillators may exhibit less dissipation when brought into close contact with a surface than audio range cantilevers [51]. This is important in current, state-of-the-art MRFM applications where it is necessary to operate the magnetic-tipped cantilever near a surface to maximize the gradient.

Doubly clamped beams, nanowires, and paddles have been the focus of several applied physics groups interested in MRFM and general attonewton-sensitivity force detection techniques. Doubly-clamped silicon nanowires have been routinely fabricated with widths as small as 45 nm and resonance frequencies in the hundreds of megahertz. Typical quality factors of these wires are in the 10^3 range at room temperature [52]. Recently, high tensile stress radio frequency silicon nitride nanowires were developed with quality factors as high as 200,000 [53]. Doubly clamped silicon paddles with torsional resonance frequencies in the megahertz range generally have room temperature quality factors ranging from 1,000 for met-

allized devices [54] to 60,000 for oscillators with methyl-terminated surfaces [42]. Doubly clamped GaAs beams have also been fabricated with $f_0 = 116$ MHz and a Q of 1,700 at 30mK that can achieve a displacement sensitivity of $2 \times 10^{-15} \text{ m}/\sqrt{\text{Hz}}$, which is only a factor of 100 larger than the quantum limit [55].

Decreasing the size of an oscillator, however, makes it much more difficult to detect the motion [56]. The motion of relatively large structures, such as thin cantilevers, can be detected using fiber-optic interferometry to convert the motion to a voltage change (this will be discussed in more detail in Section 3.3). Unfortunately, the size of high f_0 devices limits the use of interferometry since the device size begins to approach the wavelength of the laser and diffraction becomes a problem. Electronic detection techniques also become problematic when using smaller oscillators due to stray electric couplings resulting from the reduced dimensions.

The final three entries in Table 2.1 give examples of NEMS oscillators that use alternate detection methods while still providing excellent force sensitivity. The fourth entry in the table is a piezoresistive silicon cantilever developed by Michael Roukes' group [47]. The resonance frequency is small compared to the final two oscillators ($f_0 = 66$ kHz), but the motion is detected piezoelectrically. When the cantilever bends, the voltage in the legs changes proportionally. This couples the motion of the cantilever to a voltage signal, and no interferometer is necessary. A force sensitivity of $17 \text{ aN}/\text{Hz}^{1/2}$ is measured at 10 K. Piezoelectric cantilevers are advantageous since the interferometer, which can misalign at cryogenic temperatures, is no longer present. However, the force sensitivity must be improved by an order of magnitude before approaching single spin sensitivity.

The final two entries in Table 2.1 describe megahertz oscillators whose motion is transduced via methods designed *in situ* with the oscillator. The first oscillator

in this group is a carbon nanotube suspended over a trench, which acts as a transistor. This was developed in the McEuen group via “bottom-up” fabrication techniques [48]. When the nanotube is driven by an AC voltage between the source and the drain, the capacitive force between the nanotube and the gate can be measured, and the size of the force is dependent on the distance between the tube and the gate. Despite a Q of only 80, the force sensitivity at room temperature is $20\text{aN}/\text{Hz}^{1/2}$, thanks to the large f_0 of 55MHz and a spring constant of $4\times 10^{-4}\text{N/m}$.

Keith Schwab’s group has developed a silicon nitride doubly clamped beam with an $f_0 = 20$ MHz where the motion is coupled to a superconducting single-electron transistor (SSET) [49]. At millikelvin temperatures, the Q is large, overcoming the large spring constant ($k = 5$ N/m), resulting in a force sensitivity of 600 zN at millikelvin temperatures [57]. The movement of the charged oscillator causes a change in the charge of the gate electrode of the SSET fabricated beside the oscillator, which can be measured as a change in conductance [58].

Several other techniques, such as magnetomotive detection, path stabilized Michelson interferometry, and Fabry-Perot interferometry have also been used to detect the motions of small oscillators [56]. There is no question that these high f_0 devices are extremely sensitive to small forces and rival the sensitivity of ultrathin cantilevers currently used in the most sensitive MRFM experiments. However, the schemes required to detect the motion of these oscillators make them ill-suited to current MRFM detection techniques that require bringing the oscillator close to a sample surface. The prospect of scanning the sample surface is also difficult when using a doubly clamped beam rather than a cantilever. It is conceivable that high frequency cantilevers could ultimately detect small forces in MRFM experiments, but only after several engineering and detection requirements are met.

2.5 Cantilever Magnetometry

So far, this discussion has focused on designing the most sensitive cantilevers possible. It is also important to place a small magnet near the end of the cantilever to provide the gradient for the force in the MRFM experiment. In this section, we discuss cantilever magnetometry, a method for characterizing small magnetic particles that can be used in MRFM experiments [44, 59].

Cantilever magnetometry is able to characterize the tip magnetization over a large range (for example, from -6 T to $+6$ T) and quantify small-angle magnetic fluctuations. In these experiments, the magnetic-tipped cantilever is placed in an external magnetic field, directed along the cantilever length, with the long axis of the rectangular magnet parallel to the length. At zero external field, the cantilever spring constant is k_0 , and can be measured by analyzing the Brownian motion prior to the experiment. The cantilever is then oscillated by positive feedback while the external field is increased. At high external fields, the cantilever stiffness will change due to the increased interaction between the magnetic particle and the field. The magnetic axis of the particle will want to stay along the field, and this increases the effective spring constant of the cantilever (k_{eff}), which is expressed as

$$k_{\text{eff}}(B) = k_0 + k_{\text{mag}} \quad (2.53)$$

where k_{mag} is the spring constant stiffening due to the external field. This stiffening is a function of the external field B and the magnetic moment of the tip μ [60]

$$k_{\text{mag}} = \left(\frac{\alpha}{l}\right)^2 \left\{ \mu B \frac{\mu_0 \mu (N_t - N_l)}{BV + \mu_0 \mu (N_t - N_l)} \right\} \quad (2.54)$$

where $\alpha = 1.377$ for a cantilever beam, μ_0 is the permittivity of free space, V is the tip volume, and $N_t - N_l$ is the difference in the tip's demagnetization factors

along the direction of the cantilever's thickness and length. By scanning the field, the magnetic moment of the tip can be determined and a hysteresis loop can be inferred [59]. Magnetic moment resolution better than $10^4 \mu_B$ has been achieved using cantilever magnetometry [44].

The change in the cantilever stiffness is measured as a change in the cantilever resonance frequency. Recall that

$$f_0 = \frac{1}{2\pi} \sqrt{\frac{k_0}{m}} \quad (2.55)$$

It follows that a change in the spring constant k_{mag} can be expressed in terms of a change in the resonance frequency f_m

$$\frac{f_m}{f_0} = \sqrt{\frac{k_{\text{eff}}}{k_0}} = \sqrt{1 + \frac{k_{\text{mag}}}{k_0}} \quad (2.56)$$

This can be expanded in a Taylor series, and the change in the frequency becomes

$$\frac{\Delta f}{f_0} = \frac{1}{2} \frac{k_{\text{mag}}}{k_0} \quad (2.57)$$

This expression will be used in several experiments in this dissertation to convert frequency shifts to spring constant shifts. Note that k_{mag} is a spring constant change Δk .

The minimum detectable magnetic moment in cantilever magnetometry can be determined using Eq. 2.54. In the high field limit, $B \gg \mu_0 \mu (N_t - N_l)/V$, k_{mag} becomes

$$k_{\text{mag}} = \left(\frac{\alpha}{l}\right)^2 \mu M_s (N_t - N_l) \quad (2.58)$$

where we have made the substitution $M_s = \mu_0 \mu / V$. The minimum detectable magnetic moment μ_{min} that can be detected is thus directly proportional to the minimum detectable spring constant shift k_{min} . Since $k_{\text{min}} = F_{\text{min}} / \sqrt{2}x_{0p}$, where

x_{0p} is the zero-to-peak amplitude of the cantilever oscillations, the minimum detectable magnetic moment can be expressed in terms of the cantilever parameters

$$\mu_{\min} \propto t w^{1/2} l^{3/2} \times \frac{1}{\sqrt{Q}} \quad (2.59)$$

Therefore, in order to detect the small μ from a nanoscale magnetic tip, the cantilever should be short, thin, and narrow. This is slightly different than the minimum detectable force case where the cantilevers should be long, thin, and narrow. In order to characterize the small magnets deposited during the fabrication process, it is advantageous to make some cantilevers short solely for magnetometry sensitivity considerations. The experimental methods and results of the cantilever magnetometry experiments will be discussed in Chapter 3.

2.6 Summary and Conclusions

In this chapter, the engineering requirements for fabricating ultrasensitive cantilevers have been discussed. Cantilevers with force sensitivities in the aN/\sqrt{Hz} range can be developed by making the cantilevers long, thin, and narrow. In order to characterize the magnetic tips of these magnets, some cantilevers should be made that are short, thin, and narrow to detect small magnetic moments.

In the following chapter, a batch fabrication process for magnetic-tipped ultrasensitive cantilevers will be discussed. Methods for determining the spring constant, resonance frequency, and quality factor will also be explained. Cantilevers fabricated using these engineering requirements have record force sensitivities at room temperature and have been used to detect electron and nuclear spins in MRFM experiments.

CHAPTER 3

CANTILEVER FABRICATION AND CHARACTERIZATION

3.1 Introduction

Magnetic resonance force microscopy requires the fabrication of ultrasensitive cantilevers with small magnets near the end. Previous reports have shown that fabricating attonewton-sensitive cantilever from silicon nitride [39] and silicon [16, 17, 39, 61] is viable. However, placing small magnets near the end of the cantilever is not simple. In previous magnet-on-cantilever MRFM experiments, the magnetic tips were either glued to the cantilever tip by hand and then shaped by ion beam milling, or they were deposited one at a time through a shadow mask [16, 31, 44]. In this chapter, we will detail the first batch fabrication procedure for fabrication of ultrasensitive silicon cantilevers with integrated submicron magnetic tips. In addition, this process streamlines the general process for fabricating thin silicon cantilevers developed by Stowe, *et al.* [16].

Methods for characterizing the spring constant, resonance frequency, and quality factor for these attonewton-sensitive cantilevers will be discussed in Section 3.3. In Section 3.4, results from cantilever magnetometry experiments will show that the nickel thin films deposited on the end of the cantilevers during fabrication are indeed magnetic. Finally, we will describe two additional procedures for fabricating cantilevers with sharp tips for dissipation studies (Section 3.5) and large oscillators for potential use in self-assembled monolayer MRFM (Section 3.6).

3.2 Fabrication Process

The starting point for cantilever fabrication is a commercially available 100 mm diameter $\langle 100 \rangle$ silicon-on-insulator (SOI) wafer [62] having a silicon thickness of 340 nm and a buried oxide thickness of 400 nm. These layers are supported by a 525 μm thick bulk Si layer. The top layer of silicon has a resistivity of $14 - 22 \Omega\text{cm}$, corresponding to boron doping at a concentration of $6 - 9 \times 10^{14} \text{ cm}^{-3}$. The cantilever will be eventually defined in the top layer of silicon, and the oxide will act as an etch stop during processing (Fig 3.1a). SOI wafers are ideal for this process since the top submicron Si layer and the buried oxide layer are fairly uniform over the entire wafer. The thickness uniformity is about 12.3 nm for the Si layer, and about 7.2 nm for the buried oxide. Uniformity of the Si layer is critical for interferometry and for the quality factor of the oscillator. Thinner cantilevers can be fabricated by using an oxide furnace to convert the silicon to oxide and subsequently removing the oxide with an HF etch.

Typically, the $\langle 111 \rangle$ Si surface orientation is preferred over the $\langle 100 \rangle$ orientation for oscillator fabrication because the $\langle 111 \rangle$ surface is smoother and better passivated chemically [43]. Aqueous hydrofluoric acid and ammonium fluoride passivate the surface of both $\langle 111 \rangle$ and $\langle 100 \rangle$ silicon with hydrogen atoms, slowing the onset of surface oxidation and contamination [63]. However, etching of the $\langle 111 \rangle$ surface with these chemicals results in atomically smooth surfaces [45], while etching of the $\langle 100 \rangle$ silicon is much rougher, promoting energy dissipation and lower Q [64]. Despite using the $\langle 100 \rangle$ orientation, our process produces cantilevers with high quality factors without the use of any chemical passivation or heat treatment steps.

Prior to any etching of the wafer, nickel or cobalt magnets are defined in resist

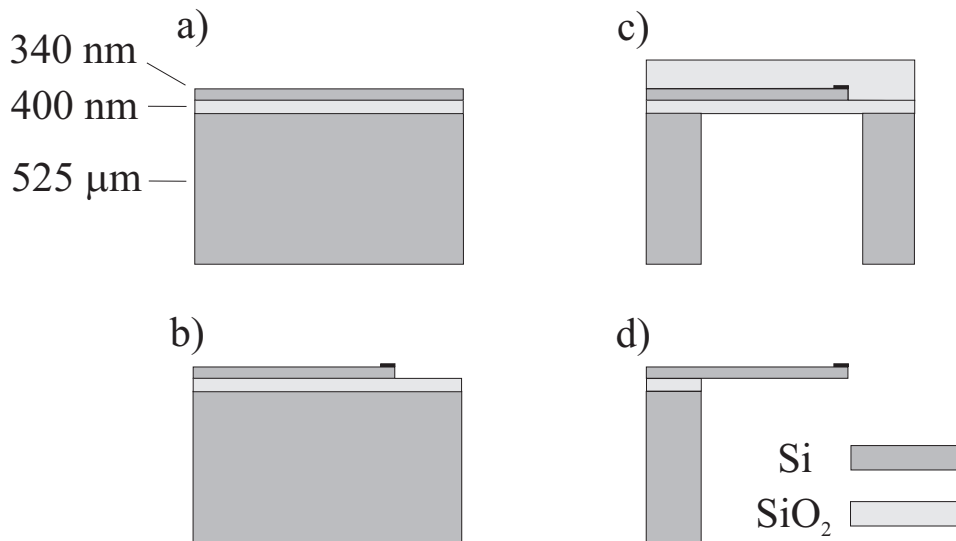


Figure 3.1: Process flow for fabricating ultrasensitive cantilevers with magnetic tips. See text for explanation of steps.

using contact lithography or electron beam lithography followed by deposition and lift-off. Contact lithography is faster and cheaper, but is unable to fabricate magnets with features smaller than $\sim 2 \mu\text{m}$. Large, micron-scale magnets were fabricated with typical lift-off techniques in standard photoresist. For smaller magnets, electron beam lithography is performed using a Leica/Cambridge EBMF 10.5/CS machine¹ (40 kV beam, 150 nm resolution) and a bilayer resist comprised of a 200 nm layer of polymethylmethacrylate (PMMA) on top of a 500 nm layer of the copolymer poly(methylmethacrylate-co-methacrylate acid) (P(MMA-MAA)).

A 125 – 200 nm thick layer of Ni or Co is evaporated onto a 5 nm thick layer of Cr; both layers are deposited at a rate of 0.1 nm/s. The Cr layer is added to promote adhesion of Ni and to inhibit formation of nickel silicides. [65, 66] When optically defined magnets were prepared, an additional 10 nm thick cap-

¹The Leica/Cambridge EBMF is no longer in service at the Cornell Nanoscale Facility. The JEOL 9300 is a suitable replacement tool for defining small magnets.

ping layer of Cr was immediately evaporated over the Ni or Co film to prevent the film from oxidizing during further processing and under ambient conditions later. For electron-beam defined magnets, both Cr capped and uncapped magnets were prepared; subsequent cantilever magnetometry studies showed no discernible difference in the saturation magnetization of the capped and uncapped magnets. The magnet studied in Section 3.4 was fabricated by electron beam lithography and did not have a capping layer. Magnet feature sizes range from $4 - 10 \mu\text{m}$ using contact lithography and as low as 200 nm using electron beam lithography. We find that Ni or Co films thicker than 200 nm are not uniform and appear cracked. If necessary, magnets thicker than 200 nm may be fabricated by sandwiching Cr adhesion layers between 200 nm thick magnetic layers.

After lift-off of the resist in solvent, rectangular cantilever beams with a blunt, rectangular end are defined in the top layer of silicon using contact lithography and an SF₆ plasma etch (Fig 3.1b). It is necessary to completely remove the exposed 340 nm Si layer and leave only the buried oxide etch stop in the etch pits. For this reason, the Unaxis 770 Bosch etcher was used to etch the Si layer for approximately 30 s to ensure complete etching to the buried oxide, rather than a slower etching tool. This process likely leaves a thin layer of fluorinated polymer on the sidewalls of the cantilever, but quality factors remain high despite the polymer's potential to dissipate energy. The remaining photoresist is removed via soaking in solvents (acetone and isopropyl alcohol) and oxygen plasma etching.

Approximately 1.25 μm of silicon oxide is deposited on the topside of the wafer to protect the cantilevers and magnets during backside processing, as well as to reduce stress over the wafer. The low stress oxide is deposited at a temperature of 275°C by plasma enhanced chemical vapor deposition (PECVD) using a SiH₄ and

N_2O plasma using the IPE PECVD tool. It is also possible to use the GSI PECVD tool to deposit the protective oxide at a rate of 250 nm/min, which is much faster than the IPE. No discernable difference has been noted between the two tools.

Free space below the cantilever (known as a “flophole”) is next defined in the bulk 525 μm thick Si backside using a 10 μm thick layer of photoresist as an etch mask, and etched at a rate of 2 $\mu\text{m}/\text{min}$ using the anisotropic Bosch deep reactive ion etch (DRIE) process. [67–70] The Bosch process uses alternating etch and passivation steps to etch deep, highly anisotropic pits in silicon. The exposed silicon is etched by the fluorine radicals and ions produced by a plasma of SF_6 . After a brief etch step, a protective fluorocarbon (Bosch polymer) is deposited onto the entire wafer, including the sidewalls of the etch pit. The subsequent etch step preferentially removes the fluorocarbon and silicon at the bottom of the etch pit via physical etching while little etching of the protected sidewalls occurs. The process repeats and produces trenches with high aspect ratios at an etch rate of about 2 $\mu\text{m}/\text{min}$. At the conclusion of this etch step, the cantilevers are sandwiched between the deposited oxide and the SOI buried oxide (Fig 3.1c). It is important to run a brief (~ 30 s) isotropic etch to remove the bulk of the fluorocarbon from the sidewalls, which can flake off of the sidewalls and damage cantilevers during the release step.

Uniform etching of the backside of the wafer is difficult, and it is important to end the etch when the optimal number of cantilever dies are etched. The outer dies of the wafer tend to etch faster than the inner dies, which can lead to several problems. Occasionally, the thin layers of buried oxide and protective deposited oxide will break. This interrupts the flow of helium gas used to cool the wafer and causes the etcher to end the etch process. Etching can continue past this stage if

the helium flow is switched off, but the wafer should be taken out of the etcher every 5-10 minutes to keep the wafer from getting too hot. Overetching results in a “ledge” of silicon attached to the cantilever that is not supported by the bulk silicon layer and has the potential to decrease the quality factor by promoting clamping losses from the beam to the silicon ledge.

A standard buffered oxide etch (BOE) is used to etch away the oxide layers and release the cantilevers (Fig 3.1d). The extremely fragile wafer is lowered into a beaker of BOE using a custom designed teflon holder and allowed to etch for about 10 minutes. After the oxide layers have been removed, the cantilevers cannot be dried in air since the surface meniscus forces will warp and break the thin cantilevers. Critical point drying is used to avoid this problem. The wafer is quickly transferred from BOE to water and then serially diluted from water to ethanol, which is miscible in liquid carbon dioxide. The teflon holders used in the serial dilution process are designed to keep the wafer submerged during the transfers. The wafer is placed into a critical point dryer (Tousimis Research Corp, Model Automegasamdry 915B) which slowly replaces the ethanol with liquid CO₂. The pressure and temperature inside the dryer are then increased to create a supercritical fluid of CO₂. Finally, the pressure and temperature are lowered to facilitate a phase change from a supercritical fluid to the gaseous state. This transition avoids the meniscus forces from the liquid to gas transition.

Cantilevers fabricated using this method were 340nm thick, with widths ranging from 2 – 50 μm and lengths from 80 – 500 μm. The yield is approximately 50 – 60% across an entire wafer. Figure 3.2 shows an array of 10 μm wide cantilevers and magnetic tips defined by photolithography (a) and by electron beam lithography (b). Apparent at the base of the cantilever is a ~ 10μm wide ledge of 340 nm

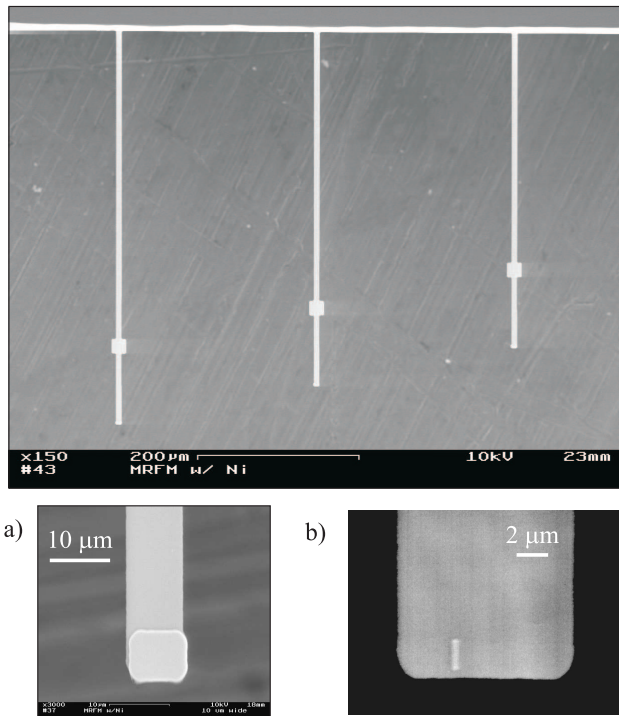


Figure 3.2: SEM images of 10 μm wide cantilevers of lengths 400 – 500 μm .

The Ni magnet in a) is 10 $\mu\text{m} \times 8 \mu\text{m} \times 125 \text{ nm}$ and was fabricated using contact lithography and is on the tip of the middle cantilever above. Electron beam lithography was used to define the 2 $\mu\text{m} \times 400 \text{ nm} \times 200 \text{ nm}$ Ni magnet in b).

thick silicon caused by overetching during the Bosch process. Both overetching and underetching of the underlying bulk silicon wafer was observed. Cantilevers for which the overetch or underetch exceeded 40 μm were rejected from further analysis. It should be noted that the quality factors of cantilevers with overetched ledges between 10 – 40 μm have a relatively high room temperature Q in the 10^4 range.

Magnetic tips fabricated using this method are close to the edge of the cantilever, but are not overhanging or centered exactly on the cantilever. Centering the magnetic tips requires greater control over the alignment steps in contact lithography. Alternate methods of aligning magnets to tips are currently being explored and include stepper-based lithography, which allows greater control of alignment.

3.3 Cantilever Characterization

3.3.1 Characterization apparatus and fiber-optic interferometry

Cantilever resonance frequency, spring constant, and quality factor were characterized in a vacuum of 10^{-6} torr to avoid air damping. Cryogenic experiments were carried out in a custom 1.5 inch diameter probe that could be inserted into either a liquid helium transfer dewar or a flowing helium gas variable temperature cryostat (custom, Janis). Room temperature experiments were performed in a simple four-way flange. The cantilever stage was designed to fit on a brass plate that connected to the flange in one opening, and electrical connections and optical interferometer fiber were inserted through two other openings. Vibrations from the vacuum pump, which oscillates at 1.5 kHz, were found to spuriously excite the

cantilever in most cases. To damp these vibrations, the vacuum hose was connected to the flange or probe through a home-built sandbox. Experiments were performed with the vacuum pump on to minimize any leaks to atmosphere through the probe. No difference in the cantilever Brownian motion was seen between experiments performed with the pump off (in the absence of leaks) and the pump on when using the sandbox to damp pump vibrations.

A custom built fiber optic interferometer [71] was used to detect cantilever displacements. The interferometer operates at a wavelength of 1310 nm, has a sensitivity of 10^{-3} nm Hz $^{-1/2}$, and uses active temperature tuning of the laser wavelength to calibrate the interferometer sensitivity and to lock onto the sensitive point of the interferometric fringe [72]. An interferometric cavity is created by positioning the cleaved end of the fiber approximately one fiber diameter (125 μm) from the cantilever beam. For cantilevers less than 20 μm wide, the fiber was aligned to a 20 μm wide square or octagonal pad located 100 μm from the tip (Figure 3.2). For cantilevers wider than 20 μm the fiber was aligned directly to the end of the cantilever.

The fiber is cleaved via numerous techniques, including an ultrasonic cleaving tool (PK Technologies FK II), a mechanical cleaving tool (Alcoa/Fujikura CT-04B), or by hand cleaving with a ruler and a diamond scribe (a method developed by Seppe Kuehn of the Marohn laboratory at Cornell University). Some of the laser light that propagates down the fiber reflects off of the flat, cleaved fiber surface and the rest reflects off of the cantilever beam and reenters the fiber core. These beams interfere with each other, creating a voltage output that is dependent on the cantilever position. The voltage output is sinusoidal with respect to the distance between the fiber cleave and the cantilever. To detect small changes

in displacement, the interferometer must be tuned to the nearly linear portion between the minimum and maximum of the sinusoid. This is achieved by adjusting the laser temperature, and thus the output wavelength, of the laser [73]. In most experiments, the temperature of the laser is set so that the voltage output is in the center of a fringe and then checked periodically for stability.

As the cantilever beam moves, the voltage of the interference signal changes and can be converted to a displacement in units of length. For a small change in the voltage output (δV) with the interferometer tuned to the center of a fringe, the change in distance for the cantilever will be [74]

$$\delta d \cong \frac{\lambda}{2\pi V_{pp}} \delta V \quad (3.1)$$

where $\lambda = 1310\text{ nm}$ is the wavelength of the laser used and V_{pp} is the peak-to-peak voltage amplitude of the interferometer fringe.

The peak-to-peak voltage amplitude is determined by one of several methods which drive the cantilever through at least one interferometric fringe while monitoring the interferometer output on an oscilloscope. The cantilever can be excited by striking the outside of the probe or by driving the cantilever with a piezo or a capacitive wire. The peak-to-peak amplitude is then measured on the oscilloscope. Dividing Eq. 3.1 by δV and plugging in λ and V_{pp} gives the interferometric sensitivity, reported in units of nanometers per volt. This is used to convert voltage readings from the oscilloscope or the lock-in amplifier into displacements. More details of the particular interferometer used in this work can be found in Ref. [74].

Aligning the cantilever to the fiber requires steady hands and quite a bit of practice. The fiber is first cleaved and inserted into a stainless steel tube (Small Parts) with an inner diameter of 0.020" and a length of approximately 2 cm so that only 0.5 – 1 mm of the fiber is protruding from the end of the tube. A small

amount of 5-minute epoxy is placed on the fiber near the cleaved end sticking out of the tube. The epoxy is spread into the tube by moving the fiber, resulting in a bubble of epoxy surrounding the fiber at the end of the tube. The fiber should extend about $300\text{ }\mu\text{m}$ above the epoxy so that the cantilever die is not too close to the bubble of epoxy that holds the fiber when aligned. If the fiber is extended too far, however, it is possible that the fiber will misalign when cooling to cryogenic temperatures. It is necessary to clean out the inside of the tube before inserting the fiber with Mitchell's abrasive cord (size 60S) and acetone to round the sharp inner edges of the tube and remove any metal spurs from the inside of the tube that can damage the fiber. The fiber is held in place on the cantilever stage using a set screw against the metal tube.

The cantilever is next placed near the edge of the stage to set the distance between the fiber and cantilever. The cantilever is roughly aligned to the fiber using an optical microscope, without glue, to check the interferometer fringe in atmosphere by inspecting the interferometer output on the lock-in amplifier or the oscilloscope. The fringe depth is determined by clapping near the lever, jumping up and down on the floor, or tapping the cantilever stage. If the depth of the fringe is greater than $\sim 1\text{ V}$ in atmosphere, then the fiber spacing is adequate. Typically, the fiber and cantilever should be about a fiber diameter apart or closer, depending on the quality of the cleave and the laser power.

When the height is adjusted to the satisfaction of the experimenter, a toothpick is used to put a small amount of 5-minute epoxy on the bottom of the cantilever die. The cantilever is then aligned to the fiber core. Alignment is made easier by shining incandescent light through the fiber, which illuminates the fiber core under the microscope. The cantilever is adjusted so that the light from the fiber core is

in the center of the cantilever's optical pad.

Since the cantilever motion is smaller at the optical pad than at the cantilever tip, it is important to note the distance from the end of the cantilever to the point of measurement to correct for this discrepancy [45]. This is necessary to calculate correct values of x_{rms} , and will affect the calculation of the spring constant. A scaling factor, c , is used to convert the measured displacement x_{meas} at the optical pad into the x_{rms} at the cantilever tip is used. This factor accounts for both the measurement position and the shape of the vibrational mode. For the fundamental mode of a rectangular cantilever, the scaling factor is given by

$$c = [0.500(\cosh \xi - \cos \xi) - 0.366(\sinh \xi - \sin \xi)]^{-1} \quad (3.2)$$

where $\xi = 1.876L_{\text{meas}}/L$, L_{meas} is the distance from the cantilever base to the measurement point, L is the cantilever length, and $x_{\text{rms}} = c x_{\text{meas}}$.

3.3.2 Characterization results

Measurements of the cantilever mean square displacement, $\langle x^2 \rangle$, were used to infer the cantilever spring constant, k [38]. Treating the cantilever as an ideal one-dimensional harmonic oscillator, we apply the equipartition theorem to predict

$$k = \frac{k_B T}{\langle x^2 \rangle} \quad (3.3)$$

Using a fiber interferometer allows us to measure x quantitatively and thereby infer k . Measuring $\langle x^2 \rangle$ as the area under the power spectrum of position fluctuations is problematic for our high- Q cantilevers because of the narrowness of the mechanical resonance. We instead used a lock-in amplifier to measure $\langle x^2 \rangle$ as follows. The lock-in center frequency was set to f_0 and the lock-in bandwidth was set to a few times the natural bandwidth of the cantilever, $\pi f_0 Q^{-1}$. The lock-in outputs were

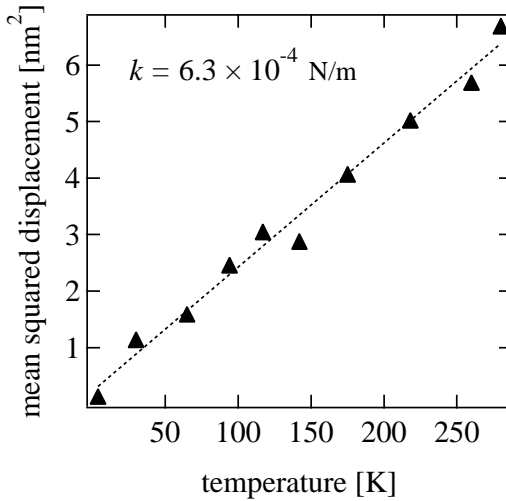


Figure 3.3: Graph of cantilever mean-squared displacement as a function of temperature. As the temperature approaches 0 K, $\langle x^2 \rangle$ approaches zero, confirming that we are observing position fluctuations due predominantly to thermo-mechanical Brownian motion. The spring constant of the cantilever inferred from the slope of the line is $k = 6.3 \times 10^{-4}$ N. The dimensions of the cantilever are $550 \mu\text{m} \times 45 \mu\text{m} \times 340 \text{ nm}$.

sampled for many cantilever correlation times, 30 – 60 s typically, and $\langle x^2 \rangle$ was calculated from the resulting time series data in a Labview program. This procedure serves to capture all but a few percent of the fluctuations, whose frequency content is centered at the cantilever frequency, while rejecting non-thermal sources of apparent displacement fluctuations such as low frequency acoustic and electronic noise.

Before applying Eq. 3.3, we performed an experiment to confirm that, in our apparatus, cantilever position noise was due solely to thermomechanical fluctuations. Cantilever fluctuations were observed as a function of temperature using our low temperature probe and flowing gas cryostat (Figure 3.3). The fluctuations were

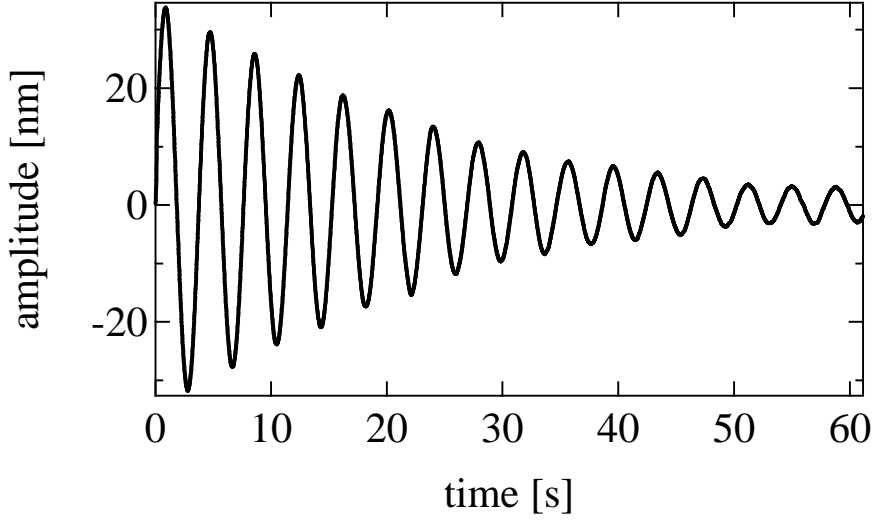


Figure 3.4: Lock-in demodulated ring-down of a $400\text{ }\mu\text{m} \times 7\text{ }\mu\text{m} \times 340\text{ nm}$ cantilever at 11 K. For this experiment, $f_{LI} = 2.18800\text{ kHz}$, and $f_0 = 2.18826\text{ kHz}$ and $Q = 182,000$ were determined by fitting the ring-down.

fit to $\langle x^2 \rangle = k_B(T + T_{\text{vib}})/k$, where T_{vib} is a temperature characterizing cantilever excitations due to extrathermal sources such as room and flowing-gas vibrations. We find $T_{\text{vib}} = 10.5 \pm 6.8\text{ K}$, from which we conclude that using Eq. 3.3 to infer k from $\langle x^2 \rangle$ observed at room temperature is accurate to better than 3%. The cantilever's k inferred from the slope of $\langle x^2 \rangle$ versus T agreed with the k calculated from the physical dimensions of the cantilever and Eq. 3.4 to within 10%.

Cantilever resonance frequency and quality factor were measured using a ring-down technique. To excite the cantilever for ringdown measurements, a wire was positioned approximately 1 – 2 mm above the cantilever, and a second grounding wire was affixed with silver paint to the cantilever die. The cantilever was capacitively driven to an amplitude of $\sim 50\text{ nm}$ in vacuum by applying an oscillating voltage of amplitude $0.1 – 1\text{ V}$ to the wire near resonance². The drive frequency

²Capacitive driving will be discussed in greater detail in Section 5.3.1.

was typically $0.5 - 3$ Hz less than f_0 , and the driving was abruptly stopped after the driving was greater than at least one interferometer fringe. The cantilever ring-down transient was recorded as a lock-in demodulated signal where the apparent frequency of the ring-down is the difference between the lock-in frequency (f_{LI}) and f_0 . The transient was fit to an exponentially decaying sinusoidal function to obtain the cantilever f_0 and decay time, τ , from which the quality factor was calculated using $Q = \pi f_0 \tau$ [39]. Figure 3.4 shows a ring-down transient lasting about thirty seconds for a cantilever at 11 K. Cantilever ring-downs have also been measured by exciting the cantilever amplitude with a piezoelectric stack and by striking the outside of the probe with a hard object.

The cantilevers at room temperature in air had Q 's of less than 10 typically, and would exhibit $10 - 100$ μm of motion in response to ambient air currents if not carefully shielded. In vacuum, the Q 's were observed to be in the range of 25,000–35,000, independent of length and width. At cryogenic temperatures, ≤ 11 K, Q 's as high as 200,000 were observed for cantilevers placed into vacuum within one day of release. The quality factor of cantilevers left out in atmosphere in the lab for longer than a few days exhibited high quality factors in the 10^4 range at room temperature, despite the likely onset of surface oxidation.

In addition to fitting the ring-down, cantilever resonance frequency can also be determined by scanning the drive frequency to the wire or piezoelectric stack through the resonance frequency. The drive frequency is produced by the lock-in amplifier as in the ring-down experiment, and the resulting cantilever magnitude and phase are plotted versus drive frequency. The center frequency of the magnitude peak is the resonance frequency, and the cantilever Q can be determined by fitting the resonance peak to the real part of the cantilever frequency response in

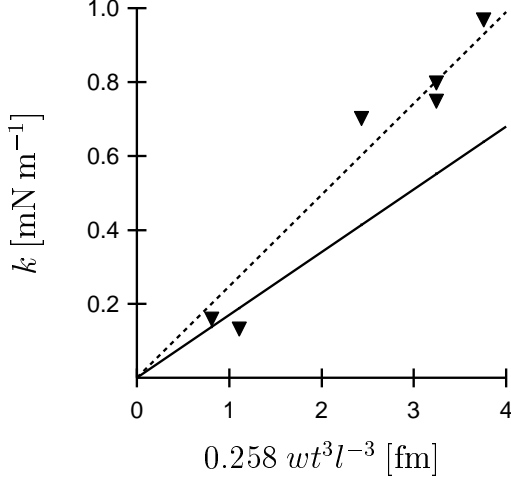


Figure 3.5: An across-wafer comparison of measured and expected spring constants. The solid line has a slope equal to the accepted Young’s modulus of silicon. The dashed line, a fit to Eq. 3.4, has slope $E_k = 2.7 \times 10^{11} \text{ N m}^{-1}$.

Section 2.1.1. This experiment typically takes longer to perform than a ring-down experiment since it is necessary to wait at least one τ , which can be as long as 30 s, between points for the cantilever to reach steady-state.

Across a given wafer, measured spring constants agreed reasonably well with the k calculated from measured dimensions using

$$k = 1.030 \frac{1}{4} \frac{Ewt^3}{l^3} \quad (3.4)$$

However, large discrepancies were observed. Figure 3.5 plots k versus $0.258 \text{ } wt^3 \text{ } l^{-3}$, in femtometers, for a group of cantilevers having spring constants in the range of $10^{-3} - 10^{-4} \text{ N m}^{-1}$, all drawn from the same wafer and processed in the same way. According to Eq. 3.4, the points should lie along the solid line whose slope is E , the bulk Young’s modulus for silicon. The expected trend is generally followed, but Eq. 3.4 consistently underestimates k . The dashed line of Fig. 3.5, with slope $E_k = 2.47 \pm 0.13 \times 10^{11} \text{ N m}^{-2}$, is a best fit of k_{meas} to Eq. 3.4 treating the Young’s

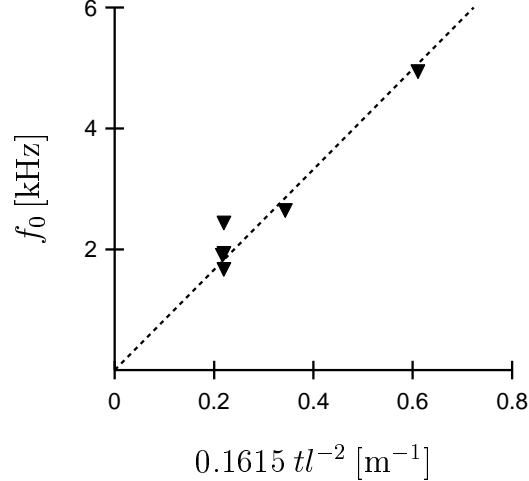


Figure 3.6: An across-wafer comparison of measured and expected resonance frequencies. The dashed line having slope $(E_f/\rho)^{1/2} = 8.3 \times 10^3 \text{ Hz m}$ is a fit to Eq. 3.5.

modulus as a free parameter. That E_k and E are not the same suggests that our process does noticeably damage the silicon of the cantilever.

Resonance frequencies were also in reasonable agreement with expectations. Fig. 3.6 plots f_0 versus $0.1615 tl^{-2}$, in $[\text{m}^{-1}]$, for the cantilevers of Fig. 3.5. The dashed line in the figure is a fit to

$$f_0 = \frac{3.518}{2\pi} \frac{t}{l^2} \left(\frac{E}{12\rho} \right)^{1/2} \quad (3.5)$$

The slope of the line, $(E_f/\rho)^{1/2} = 8.30 \pm 0.37 \times 10^3 \text{ Hz m}$, may be combined with the silicon density of $\rho = 2300 \text{ kg m}^{-3}$ to give an observed Young's modulus of $E_f = 1.58 \pm 0.07 \times 10^{11} \text{ N m}^{-2}$. This is in good agreement with the reported value of $E_{\langle 110 \rangle} = 1.69 \times 10^{11} \text{ N m}^{-2}$ [75, 76]. The relatively poor agreement between E_f and E_k is not fully understood. Young's moduli different from the bulk have been observed before, where the difference has been attributed to processing [77] and undercutting [78]. Here, the error is too large to be attributed to changes in l due

to undercutting or to uncertainties in thickness; an implausibly thick layer of oxide is required to explain the discrepancy. This leaves wafer damage or strain as likely candidates.

Additionally, we determined that the presence of the silicon ledge due to overetching did not deleteriously decrease force sensitivity. In the Stowe process, a thick polysilicon layer is deposited on the topside silicon to provide a more well defined cantilever length, and thus resonance frequency and spring constant. The polysilicon layer provides a stable support for the cantilever even if overetching occurs in the backside processing. While this may improve the agreement between the calculated and measured k and f_0 , our results show that at low temperature, even though no thick cantilever base is present, the Q is still high and allows for attonewton sensitivity. A useful figure of merit for comparing cantilevers is the loss factor [39]

$$\Gamma = \frac{k}{2\pi f_0 Q}, \quad (3.6)$$

from which the minimum detectable force can be calculated using

$$F_{\min} = (4\Gamma k_B T b)^{1/2} \quad (3.7)$$

Table 3.1 shows that our room temperature cantilever ($\Gamma = 2.5 \times 10^{-13} \text{ kg s}^{-1}$) compares well with Yasumura *et al.*'s much thinner and narrower cantilever ($1.5 \times 10^{-13} \text{ kg s}^{-1}$), corroborating that our ledge is not harming sensitivity. It should be noted that the force sensitivity of our cantilevers could be improved by including a thick silicon support in future fabrication processes, if it is deemed necessary.

Table 3.1 summarizes the measured properties of four representative cantilevers fabricated from different SOI wafers. Cantilever C1 was stored under ambient conditions for two weeks following release before being vacuum tested. Surprisingly,

Table 3.1: Cantilever parameters. The table lists A) physical dimensions, B) temperature T at which the cantilevers were characterized and measured properties, C) ringdown time τ and natural cantilever bandwidth δf , and D) loss factor γ , Eq. 3.6, and force fluctuation spectral density $S_F \equiv 4\gamma k_B T$.

		C1	C2	C3	C4	units
A.	l	400	400	200	400	μm
	w	7	7	10	20	μm
	t	0.34	0.34	0.34	0.34	μm
B.	T	300	11	4.2	115	K
	f_0	2,641	2,188	10,863	1,097	Hz
	k	130	830	5,800	600	$\mu\text{N m}^{-1}$
	Q	32,000	180,000	19,000	500	
C.	τ	3.8	26	0.56	0.15	s
	δf	260	38	1,800	6,600	mHz
D.	Γ	245	330	1,620	170,000	$10^{-15} \text{ kg s}^{-1}$
	$S_F^{1/2}$	64	14	19	1000	$\text{aN Hz}^{-1/2}$

this cantilever exhibited a high Q despite the fact that a native oxide had ample time to form. Cantilever C2 was placed into vacuum within one day of release. The cantilevers had nominally the same dimensions. The differences in spring constant and resonance frequency are due to differences in fabrication conditions. Cantilevers C3 and C4 were stored in air for many months. Cantilever C4 was used in ESR-MRFM experiments described in Ref. [19], has a sample of diphenylpicryl-hydrazyl glued to the tip, and was operated with gas in the probe to intentionally lower the Q .

3.4 Cantilever Magnetometry

The magnetic properties of the submicron nickel magnets were inferred by measuring cantilever frequency as a function of magnetic field applied parallel to the long axis of the cantilever [44, 60]. For the magnetometer measurements, performed at 4 K, the low temperature probe was backfilled with a few millitorr of helium gas to assure rapid equilibration of the cantilever temperature, resulting in a comparatively low Q . The cantilever was driven capacitively via positive feedback (Section 4.3.3) to peak-peak amplitudes of ~ 100 nm with a wire positioned near the cantilever (Figure 3.7). The frequency of cantilever self oscillation was recorded with a commercial frequency counter. Magnetometry results were obtained by Tse Nga Ng in Refs. [19] and [59] and will be summarized here.

Figure 3.8 is a plot of the fractional change of the resonance frequency for cantilever C3 as a function of magnetic field. The magnet's long axis was parallel to the cantilever length, as shown in Fig. 3.2(inset), and the cantilever's magnet was 680 nm wide and 1310 nm long (as measured by SEM) and 200 nm thick (as measured by a quartz crystal microbalance during evaporation). These and

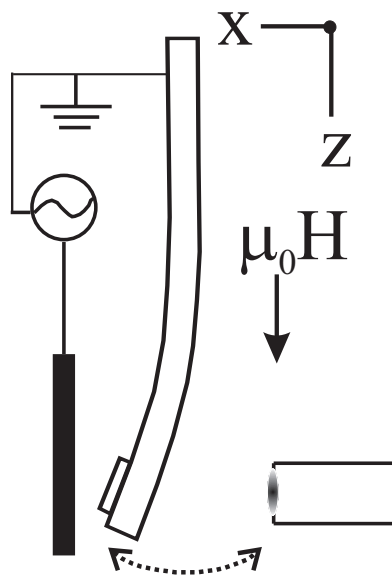
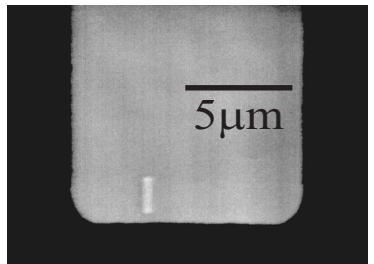


Figure 3.7: Setup for cantilever magnetometry. The magnet's long axis is situated parallel to the cantilever length and the external magnetic field. A wire positioned parallel to the cantilever is used to drive the cantilever capacitively with positive feedback. As the external field is increased, the cantilever stiffness changes due to an interaction between the magnet and the external field. This change in spring constant is measured as a change in resonance frequency. Cantilever displacement is measured with a fiber-optic interferometer.

other measured properties of cantilever C3 are summarized in Table 3.1. The magnetic field induced frequency shift of cantilever C3 is much larger than that of a blank cantilever, indicating qualitatively that the cantilever's nickel tip is indeed magnetic.

The tip's magnetic moment and magnetization can be inferred from an analysis of the f_0 versus B curve of Fig. 3.8. Using the tip-field interaction model of Ref. [60] discussed in Section 2.5, we would predict

$$f - f_0 \approx \Delta f \frac{B \Delta B}{B + \Delta B} \quad (3.8)$$

where

$$\Delta f = \frac{f_0}{2k} \left(\frac{\alpha}{l} \right)^2 \mu \quad (3.9)$$

$$\Delta B = \mu_0 \mu \frac{\Delta N}{V} \quad (3.10)$$

The approximation holds when $f/f_0 \approx 1$, which is the case here. In Eqs. 3.8–3.10, $l = 200 \mu\text{m}$ is the length of the cantilever, $\alpha = 1.377$ is a correction factor accounting for the curvature of a beam cantilever, V is the volume of the magnet, μ is the tip magnetization, and $\Delta N = N_t - N_l$ is the difference in the tip's demagnetization factors along the direction of the cantilever's thickness and length.

The f versus B curve can be analyzed to give the full hysteresis curve $\mu(B)$ for the submicron magnet using Eqs. 3.8–3.10. A more detailed description of the magnetometry measurements — including an examination of μ_s , M_s , coercive field, and magnetic fluctuations for tips of various sizes and aspect ratios — can be found in Ref. [59]. The saturation magnetic moment for the nickel magnet can be estimated by setting $\mu = \mu_s$ in Eqs. 3.9–3.10, and fitting the data of Figure 3.8 from 0 – 6 T to Eq. 3.8. Using the obtained values of Δf and ΔB , the saturation

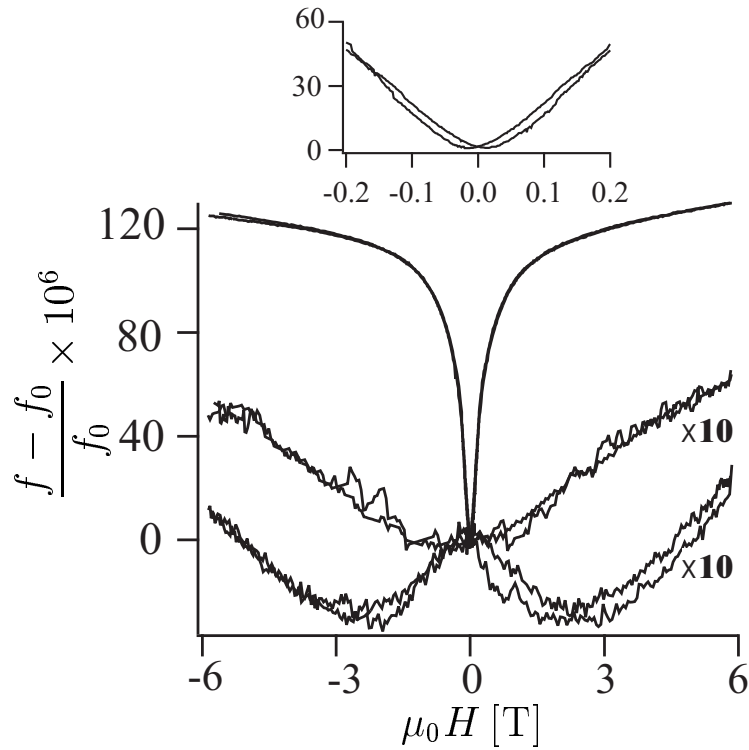


Figure 3.8: Cantilever frequency shift, in parts per million, versus applied magnetic field. Upper curve: cantilever with a $1310\text{ nm} \times 680\text{ nm} \times 200\text{ nm}$ Ni magnet. Middle curve: bare Si_3N_4 cantilever ($200\mu\text{m} \times 10\mu\text{m} \times 0.60\mu\text{m}$, $f_0 = 19198\text{ Hz}$, $k = 20\text{ mN m}^{-1}$, and $Q = 1000$). Lower curve: bare silicon cantilever ($200\mu\text{m} \times 10\mu\text{m} \times 0.34\mu\text{m}$, $f_0 = 8087\text{ Hz}$, $k = 1.6\text{ mN m}^{-1}$, and $Q = 11000$). Magnetic hysteresis in the frequency shift is clearly visible in the inset.

magnetization of the nickel is

$$\mu_0 M_s = \frac{\mu_0 \mu_s}{V} = 0.60 \pm 0.12 \text{ T} \quad (3.11)$$

where $V = 178 \times 10^{-21} \text{ m}^3$ calculated from SEM-measured dimensions. This agrees well with the value of 0.60 T expected for bulk nickel. The uncertainty in μ_s is set by the uncertainty in k , which we estimate could be as large as 20%.

Using Eq. 3.10, the measured μ_s , the measured V , and $\Delta N = 0.563$ calculated from measured dimensions [79], we estimate $\Delta B_{\text{calc}} = 0.32 \pm 0.06 \text{ T}$, approximately 15 – 20% smaller than the measured value. This possible discrepancy in ΔB cannot be explained as due to M_s since the saturation magnetization does not appear in Eq. 3.10, and must therefore be due to the magnetically active volume being smaller than the volume calculated from the measured dimensions. If we assume that the volume is smaller due to a uniform layer of antiferromagnetic oxide [80] on the tip, which will change both V and ΔB , then we can estimate a thickness for the oxide. If we adjust the thickness of the oxide until $\Delta N/V$ is consistent with the measured $\Delta B/\mu_s$ via Eq. 3.10, this gives an oxide thickness of no more than 28 nm, approximately 10% of the thickness of the magnet.

3.5 Sharp Cantilevers

In the most sensitive MRFM experiments, it is necessary to bring the cantilever's magnetic tip to within 100 nm or closer of the surface or closer to obtain a large gradient. Unfortunately, it is not possible to bring an ultrathin cantilever that close to a surface in the traditional scanned probe geometry where the cantilever length is parallel to the surface. Approaching in this geometry will cause the cantilever to snap down to the surface due to electrostatic van der Waals

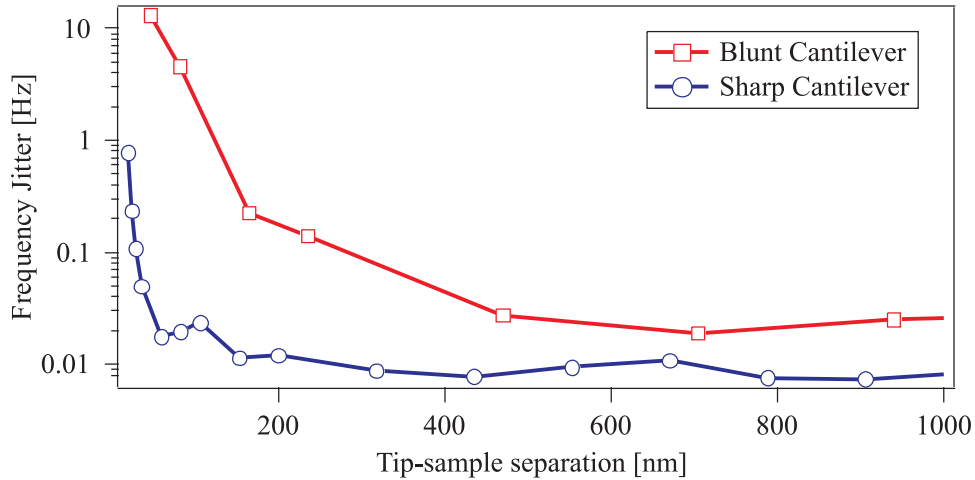


Figure 3.9: Dissipation of blunt and sharp cantilevers versus distance above an evaporated gold surface. Blunt cantilevers show an increase in frequency jitter, and thus dissipation, at distances less than 500 nm from the surface. Sharp cantilevers, fabricated using electron beam lithography, are able to approach the surface to within 50 nm before dissipation begins to limit sensitivity.

forces, which will destroy the cantilever. Closely approaching the surface requires a perpendicular geometry where the length is normal to the surface [16].

The perpendicular geometry introduces a new set of problems. As the cantilever tip is brought closer to the surface, noncontact friction between the tip and the sample enhances the dissipation of the cantilever and limits the sensitivity of the experiment. The origins of this noncontact friction are not well understood. It has been shown that noncontact friction over a polymer film is related to the dielectric fluctuations in the film that produce a time-varying electric field at the capacitively charged cantilever tip, resulting in a fluctuating, time-dependent force on the cantilever [51].

Dissipation due to noncontact friction has been shown by Seppe Kuehn to be dependent on the area of the tip exposed to the surface, as seen in Figure 3.9 where

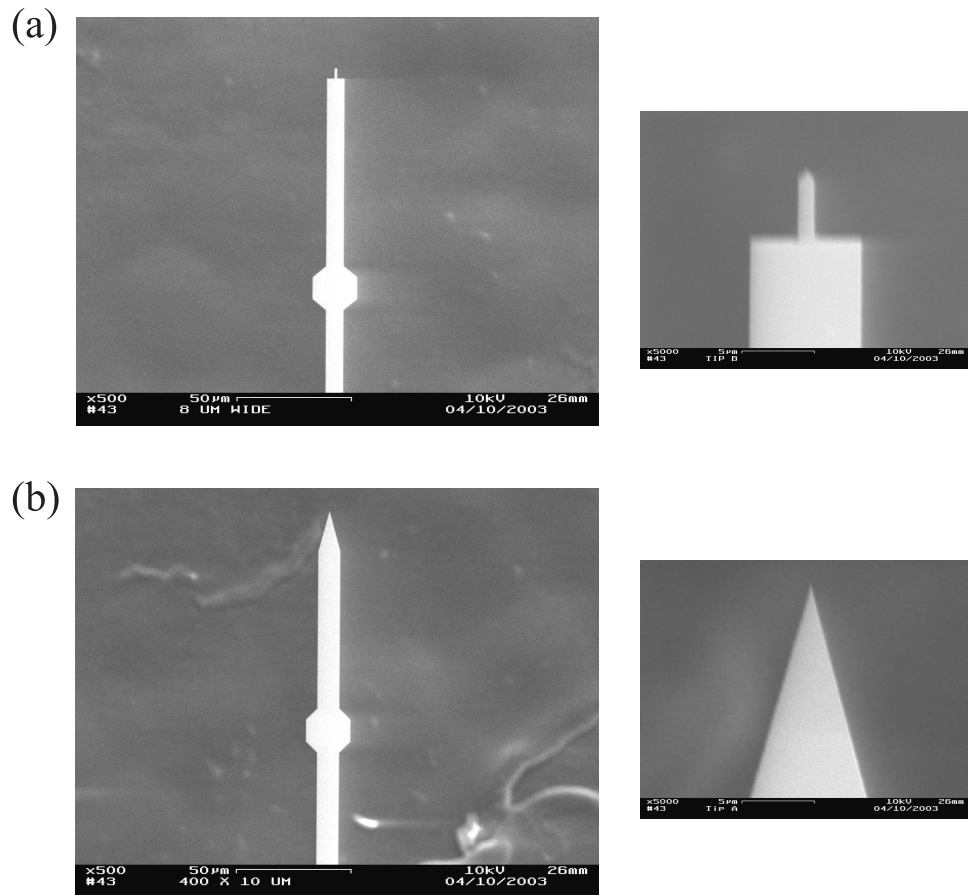


Figure 3.10: Sharp cantilevers fabricated using electron beam lithography.

A closeup of the cantilever tip is shown to the right of each cantilever. The cantilever in (a) is 8 μm wide with a 1 μm wide extended triangular tip. The cantilever in (b) is 10 μm wide with a triangular tip. The tip radii in each case is ~100 nm.

dissipation is measured as frequency jitter. When a blunt cantilever is brought near an evaporated gold surface in the perpendicular geometry, the frequency jitter begins to increase about 400nm from the surface. This increase in jitter corresponds to an increase in cantilever dissipation and a decrease in Q . To maintain a high quality factor close to a surface, cantilevers with sharp ends, and thus a smaller exposed area, should be fabricated.

Cantilevers with sharp tips were fabricated using electron beam lithography to define the cantilever in the top layer of silicon. In this technique, the cantilever shafts and tips are patterned into an electron beam resist (XP9947) using an electron beam, which allows a tip radius of much less than 400 nm to be formed. After the cantilever is patterned, the fabrication procedure continues in the normal method discussed in Section 3.2. Using this technique, several types of cantilever tips were developed, shown in Figure 3.10, with tip radii of ~ 100 nm. A cantilever like the one shown in Figure 3.10(b) was used to measure the dissipation versus tip-surface separation over the gold surface in Figure 3.9 and showed no change in dissipation at distances larger than 50nm of the sample surface, an improvement of nearly an order of magnitude over the rectangular tipped cantilevers. The tip area can be decreased even further by etching the cantilever thickness at the end of the cantilever before defining the cantilever tip and shaft. Cantilevers with thinned, sharp tips were used to approach to within tens of nanometers of a polymer surface before significantly limiting sensitivity [51].

3.6 Phatlevers

The cantilever fabrication procedure described in Section 3.2 has also been used to design two-legged oscillators with large rectangular paddles dubbed “phatlevers”.

These oscillators were designed to perform future MRFM measurements on vapor deposited self-assembled monolayers (SAMs) [81] in the sample-on-cantilever geometry as shown in Figure 3.11. In this example, a monolayer is formed on the square paddle, and a force is measured between the sample spins and the magnetic particle.

Suitable oscillators for SAM-MRFM should be wide to offer a large area for the SAM while maintaining the excellent force sensitivity seen in our ultrathin cantilevers. Recall that the spring constant of a cantilever beam increases linearly with width (Eq. 3.4), while the resonance frequency is independent of width (Eq. 3.5). If we fabricate wider cantilever beams to hold a SAM, the spring constant and F_{\min} would be expected to increase. Fabricating a large paddle with two legs connecting it to a support decreases the effective width of the cantilever, allowing for “wide” cantilevers with force sensitivities approaching that of a narrow cantilever. Using this design, oscillators with paddle areas of $100 \times 100 \mu\text{m}^2$ have been developed with spring constants as low as $3 \times 10^{-4} \text{ N/m}$ and $S_F = 140 \text{ aN/Hz}^{-1/2}$ at room temperature.

Samples used with phatlevers could include general self-assembled monolayers with many proton spins, such as octadecyltrichlorosilane (OTS), which forms on the native oxidized silicon surface of the oscillator [82], or thiol monolayers, which form on gold [83] that could be evaporated onto the oscillator. More complex monolayers with potential applications in quantum computing could be studied with this method, where the qubit is either an unpaired electron or a single proton [84]. For example, SAMs could be synthesized with TEMPO (2,2,6,6-tetramethylpiperidine 1-oxyl), a free radical, on the ends to study electron qubits [85]. Alternatively, a molecule could be synthesized in which all but one of the hydrogens would be

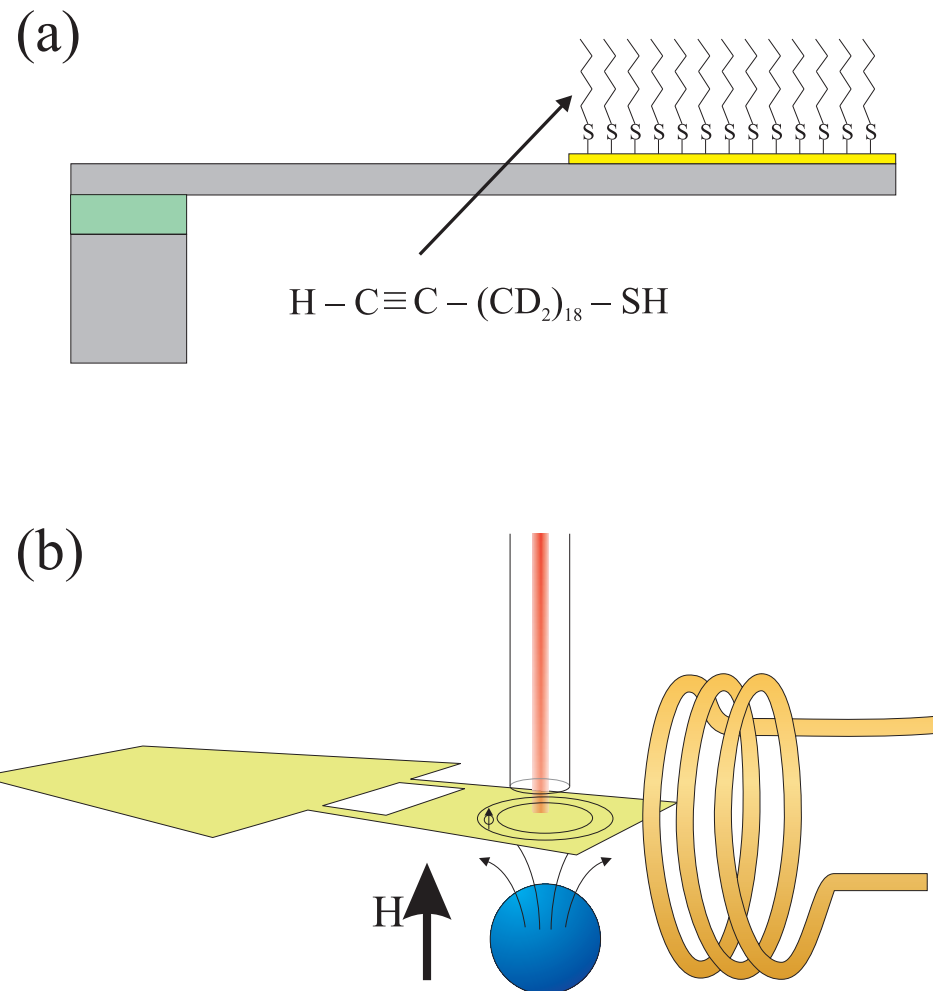


Figure 3.11: SAM-MRFM with Phatlevers. (a) A possible thiol SAM on a gold-patterned phatlever. The potential thiol is deuterated so that there is only one NMR-active proton on the sample. (b) A general sample-on-cantilever experimental setup for SAM-MRFM. The sample is a self-assembled monolayer deposited onto the paddle of the phatlever.

replaced by deuterium (^2H), which is not NMR active, as seen in Figure 3.11(a). Either of these molecules would form a monolayer where single spins would be spaced at even intervals depending on the length of the chain and the size of the side groups to be used in quantum computing applications. Initial MRFM data on these samples could be obtained by depositing the SAM on the large paddles of a phatlever. This would allow us to obtain relaxation times for the spins in the qubit SAM in the monolayer, rather than studying the bulk sample with conventional ESR or NMR. At single spin sensitivity, MRFM techniques could be used as a way to initialize and read-out the spin states in these qubits.

What is the size of the force that we could expect in a SAM-MRFM experiment? Let us assume that we are using a phatlever with a paddle area of $100 \times 100 \mu\text{m}^2$ that is covered with a thin layer of gold. A deuterated thiol monolayer is vapor deposited onto the gold and each thiol has a single, NMR-active proton on the end. The required area per molecule for a typical thiol at full coverage is 21.6 \AA^2 and the molecule-to-molecule spacing is approximately 5 \AA [81], and the paddle would contain 4.6×10^{10} spins. Based on the Boltzmann polarization of the spins at 4 K and a relatively conservative gradient estimate of 100 T/m, we would expect a force of 250 aN, assuming that the entire paddle is inside the sensitive slice (a good assumption with such a small gradient). This bulk signal is well within the limit of sensitivity based on our earlier work with ultrasensitive cantilevers. Approaching the single spin limit would likely require a much larger gradient.

The fabrication procedure for blank phatlevers is identical to the procedure discussed in Section 3.2. These phatlevers could be used with SAMs that form on the oxidized silicon surface. To study monolayers that form on gold or other metal films, a process was developed to evaporate a thin layer of metal on the

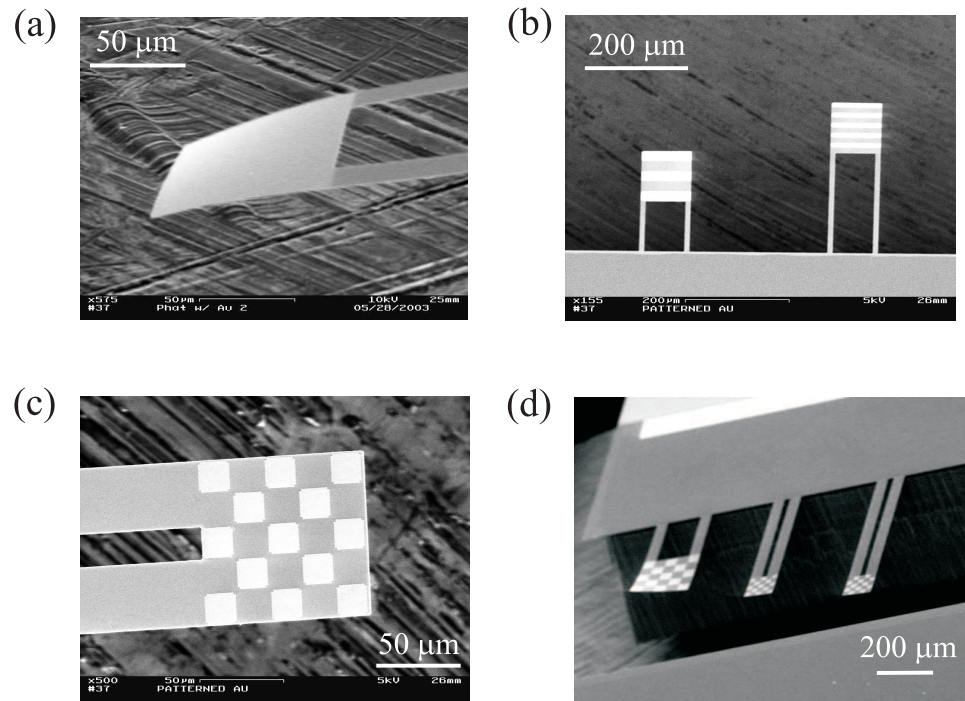


Figure 3.12: SEM micrographs of fabricated phatlevers. (a) $100 \times 100 \mu\text{m}^2$ paddle with an $\sim 20 \text{ nm}$ thick layer of Au covering the entire paddle. Notice that the end of the phatlever is curled. (b) Phatlevers with Au-patterned stripes to reduce stress on the paddle. Each paddle is $100 \times 100 \mu\text{m}^2$ with $10 \mu\text{m}$ wide legs. (c) Phatlever with a Au-patterned checkerboard. The paddle is $100 \times 100 \mu\text{m}^2$ with $40 \mu\text{m}$ wide legs. (d) Phatlevers with Au-patterned checkerboards. Notice that the largest phatlever ($200 \times 200 \mu\text{m}^2$ paddle) is curled.

phatlever paddle area using a lift-off process. This evaporation and lift-off step takes the place of the magnet evaporation step in the typical batch fabrication process for magnetic-tipped cantilevers. The first attempts patterned 15 – 25 nm gold on a 5 nm chromium adhesion layer over the entire paddle surface area, as seen in Figure 3.12(a). Unfortunately, covering the entire area with gold causes the paddle to curl due to the stress between the metal film and the silicon, rendering the phatlever useless. The total stress from the metal layers can be relieved by patterning the gold as stripes, Figure 3.12(b), or checkerboards, Figure 3.12(c) and (d), which cover half of the paddle area. A small amount of curling is still seen in larger paddles, i.e., the $200 \times 200 \mu\text{m}^2$ paddle in Figure 3.12(d). Reducing the area of gold by a factor of two halves the number of proton spins that would be present in a bulk SAM-MRFM experiment, but the expected force is still quite large (125 aN at 4 K).

The spring constant and resonance frequency for the phatlevers can be approximated by assuming that a portion of the paddle is an additional point mass on the end of a conventional cantilever, depicted in Figure 3.13. The resonance frequency of a cantilever with an extra mass M on the end of the cantilever is

$$f_0 = \frac{1}{2\pi} \sqrt{\frac{k}{m_{\text{eff}} + M}} \quad (3.12)$$

where $m_{\text{eff}} = 0.25m$ and m is the mass of the conventional cantilever. To determine a form for k and f_0 for phatlevers, we assume that the phatlever is a cantilever of length $l + l_0$, width $2w_0$, and thickness t with a point mass M on the end of the cantilever that is equal to the mass of the rectangular portion of the paddle not included in the conventional cantilever, between the legs with dimensions l , t , and

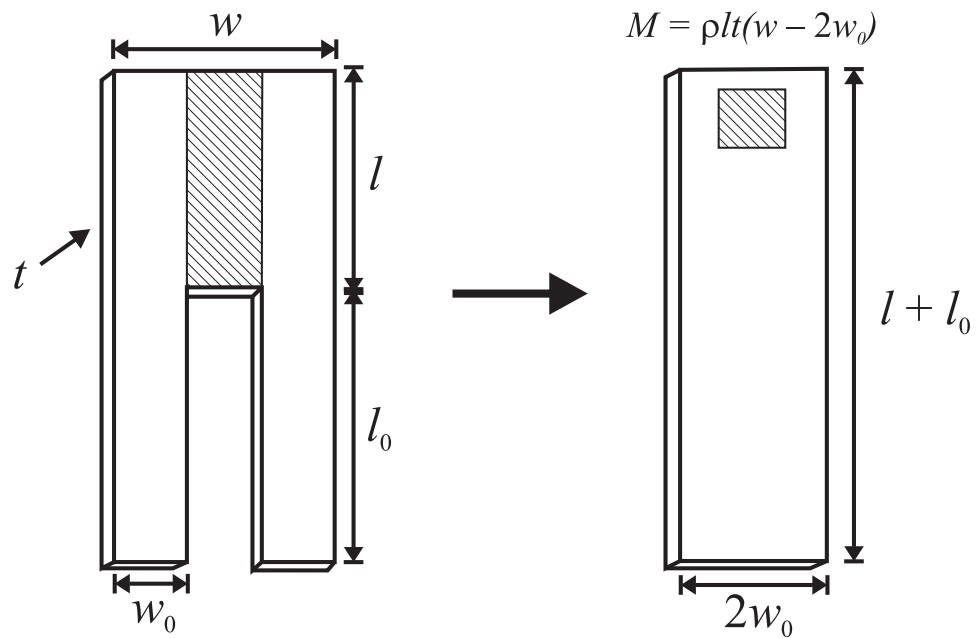


Figure 3.13: Dimensions for phatlevers used for k approximations. A typical phatlever is shown on the left. To approximate the k and f_0 , the phatlever is approximated as a cantilever of width $2w_0$, length $l + l_0$, and thickness t with an additional mass on the end of the cantilever M , which is equal to the mass of the phatlever paddle not included as a part of the approximated cantilever (hatched).

$w - 2w_0$. The mass of this portion is

$$M = \rho V = \rho l t (w - 2w_0) \quad (3.13)$$

Substituting the dimensions of the conventional cantilever into Eq. 3.4, the spring constant of the phatlever is approximately

$$k \sim 1.030 \frac{E(2w_0)t^3}{4(l + l_0)^3} \quad (3.14)$$

The resonance frequency of the phatlever is approximated by substituting M and k from Eq. 3.14 into Eq. 3.12

$$f_0 \sim \frac{2.486}{2\pi} \left(\frac{E}{12\rho} \right)^{1/2} \frac{t}{(l + l_0)^2} \left[0.48 + \frac{l(w - 2w_0)}{(l + l_0)w_0} \right]^{-1/2} \quad (3.15)$$

Comparisons of Eq. 3.15 with the experimental f_0 show agreement to within 5%, as long as the portion of the paddle used as the point mass is less than 50% of the entire paddle. Unsurprisingly, as the legs of the cantilever become narrow and M increases with respect to the total mass of the paddle, this approximation begins to break down. The experimental spring constant deviates significantly from Eq. 3.14, but is generally smaller than calculated, which is advantageous. These equations can be used to approximate the cantilever parameters prior to design, but are not extremely accurate. Methods to calculate the k and f_0 of these oscillators more precisely would require techniques such as finite element analysis and are beyond the scope of this work.

Characterization of the patterned gold and blank phatlevers was performed in the same manner as discussed in Section 3.3. Phatlever spring constants are consistently in the $10^{-3} - 10^{-4}$ N/m range with resonance frequencies between 1 – 10 kHz for blank and gold-patterned phatlevers. Blank phatlevers show large quality factors, as high as 30,000. For a 340nm-thick phatlever with a $100 \times 100 \mu\text{m}^2$

paddle and legs of length 300 μm and width 30 μm , the cantilever parameters were determined to be $k = 4 \times 10^{-4}$, $f_0 = 2.5\text{kHz}$, and $Q = 21,500$ at room temperature, resulting in a force sensitivity of 140 aN $\text{Hz}^{-1/2}$.

The determination of the quality factor for gold patterned phatlevers was made difficult by a fringe-dependent excitation of the cantilever by the laser interferometer. The interferometer laser can amplify or deamplify the quality factor and oscillation amplitude by heating [86]. Heating of the oscillator surface bends the phatlever by the bimetallic effect. As the phatlever bends farther away from the laser, the light intensity on the surface either increases or decreases depending on the sign of the slope of the interferometer fringe. Self-oscillation and quality factor enhancement occurs when the cantilever bending due to heating leads to a decrease in the intensity of the light, causing a decrease in the bending force. As in other forms of positive feedback, this is due to a phase difference between the drive and the response. Here, the drive (the bending due to heating) is out-of-phase with the response (the change in the bending force as a result of the changing intensity). On the opposite fringe, the effect is reversed. The cantilever amplitude will be damped and Q will decrease. Laser driving of oscillators has been seen in metal coated and non-metal coated cantilevers fabricated for the work presented in this dissertation. The effects of laser driving can be reduced by decreasing the laser power to the level where the Q on each interferometer fringe converges.

Patterned gold phatlevers have been shown to have a significantly lower quality factor than their blank counterparts. After correcting for laser driving, quality factors between 5,000–10,000 are observed. Unsurprisingly, the gold layer provides a source of dissipation for the oscillator, thereby lowering the Q . Despite the lower Q values, force sensitivities as low as 500 aN $\text{Hz}^{-1/2}$ have been observed

at room temperature. As the temperature is decreased, we expect the quality factor to improve, conservatively, by a factor of two. Taking this change in Q and the temperature scaling into effect, the expected force sensitivity at 4 K would be $40 \text{ aN Hz}^{-1/2}$, smaller than the expected force signal from a deuterated thiol monolayer on half of the area of a $100 \times 100 \mu\text{m}^2$ paddle.

3.7 Summary and Conclusions

In this chapter, we have discussed the fabrication procedure and characterization of attonewton sensitive cantilever with magnetic tips for use in magnetic resonance force microscopy experiments. This is the first batch fabrication procedure that incorporates submicron magnetic films onto the cantilever tips *in situ*, eliminating the need to attach magnets to cantilever tips one at a time. Our procedure streamlines the previous work of Stowe, *et al.* [16, 39, 43] by eliminating a polysilicon ledge to reduce clamping losses. Our results obtain force sensitivities comparable to other procedures, without surface modification or heat treatment of the cantilevers. This leaves considerable room for improvement of our cantilevers, if deemed necessary in the future.

Characterization has shown that our cantilevers have spring constants as low as 10^{-5} N/m with quality factors in the range of 25,000–35,000 and a force sensitivity as good as 64 aN in a 1 Hz bandwidth at room temperature in vacuum. At temperatures as low as 11 K, a force sensitivity of 14 aN in a 1 Hz bandwidth has been observed for a cantilever with $Q = 180,000$. Theoretically, force sensitivity should be improved by fabricating thinner cantilevers. However, the advantages gained by decreasing k may be outweighed by an expected decrease in the quality factor of thinner oscillators.

We are able to produce submicron nickel magnets near the ends of our cantilevers with essentially perfect magnetization, comparable to that of bulk nickel. Using cantilever magnetometry, we estimate that the magnets have no more than ~ 28 nm of nickel oxide. This is noteworthy because the magnets have been subjected to temperatures of up to 275°C during the PECVD silicon oxide growth step and have been exposed to air for over a month between fabrication and characterization by magnetometry.

Cantilevers with sharp tips have been fabricated for use in experiments where the cantilever approaches the surface with its length perpendicular to the sample. It has been shown that rectangular tipped cantilevers exhibit increased dissipation due to noncontact friction at distances greater than 400 nm from the surface. Sharp cantilevers mitigate this problem by reducing the area of the tip that is exposed to the surface. Future fabrication procedures will further reduce this area by thinning an area near the tip with reactive ion etching, allowing the cantilever to be tens of nanometers from the surface without a loss in force sensitivity.

Research is ongoing to produce cantilevers with magnets that extend approximately 100 nm from the cantilever tip. This will allow the magnetic particle to be positioned as close as possible to the sample spins, thereby maximizing the gradient while maintaining the intrinsic dissipation of the cantilever. The current method being developed by the Marohn research group is to use electron beam lithography to deposit a small magnet on a silicon $\langle 111 \rangle$ surface. This orientation of silicon will etch anisotropically when exposed to KOH (potassium hydroxide). A pit is defined at the edge of the magnet and etched with KOH, producing a magnet overhanging the pit. The cantilever is subsequently defined in the normal method.

If this silicon wet etching method proves difficult, two other methods could be attempted. For example, the etch pit could be defined in $\langle 111 \rangle$ or $\langle 100 \rangle$ silicon by dry etching prior to the magnet deposition. An oxide or nitride layer could then be deposited over the entire surface by PECVD and chemical mechanical polishing (CMP) could be used to remove the material not in the etched pit, exposing the top layer of silicon. The magnets would then be deposited so that part of it is overhanging the oxide or nitride. Removal of the oxide or nitride by wet etching would leave behind an overhanging magnet. Another technique could use technology developed by Harnett, *et al.*, who have patterned fluorescent beads as small as 20 nm onto the surface of silicon [87]. An inert self-assembled monolayer could be used to initially coat the entire cantilever surface. This inert SAM could then be removed near the tip by patterning with electron beam lithography and replaced with a backfilled, amine-terminated monolayer. This would create an active SAM, where a magnetic particle coated with a complimentary monolayer could self-assemble in solution onto the cantilever tip. This procedure could conceivably done in a batch process or in a one-by-one method. Additionally, the inert SAM used for coating the cantilever surface could be chosen to chemically increase and stabilize the quality factor.

Finally, we have developed oscillators with large surface area that could be used in initial bulk self-assembled monolayer MRFM experiments. The paddle surface can be modified with gold or other thin metal films to accommodate different types of monolayers. Blank phatlevers have force sensitivities similar to ultrathin cantilevers at room temperature. We have shown that evaporating thin metal films on the paddles of these oscillators leads to curling on the paddle and laser driving, but the observed force sensitivity remains well below the expected bulk signal from

a monolayer of deuterated thiols.

Ideally, vapor deposition would be used to form monolayers on the gold surface of the cantilevers to prepare MRFM samples. Sample preparation could also be performed by placing the cantilever in a solution of thiol molecules, followed by critical point drying to avoid meniscus forces. We imagine that the amount of curling of the paddle could increase at cryogenic temperatures due to the difference in thermal expansion between silicon and gold. In this case, thiol molecules could be studied by preparing a sample of gold nanoparticles with thiols attached to the surface [88]. These nanoparticles could then be deposited or adsorbed onto the surface of a blank phatlever, and bulk MRFM of the thiol sample could be measured in the absence of a gold film directly on the oscillator surface.

CHAPTER 4

FORCE GRADIENT DETECTED ELECTRON SPIN RESONANCE

4.1 Introduction

John Sidles imagined MRFM as a tool for imaging biological molecules with single nuclear spin sensitivity [8]. Sidles noted, “The missing structural information is a significant obstacle to the rational design of drugs and vaccines.” Single electron sensitivity could similarly be used to determine the structure of membrane-bound receptors, proteins, or nucleic acid complexes via spin labeling with nitroxides, such as TEMPO (2,2,6,6-tetramethylpiperidinyloxy), or other compounds containing unpaired electrons [6].

As detailed in Chapter 1, MRFM techniques have improved significantly in the last 15 years, moving from measuring ensembles of spins as a force on the cantilever to detecting and imaging the magnetic moment of a single electron as a change in the cantilever spring constant. Due to the engineering constraints involved with positioning thin cantilevers near a surface and limitations in detecting a homogeneous distribution of spins directly below the tip as a force, the most sensitive techniques to date detect spins as a spring constant shift, including OSCAR and CERMIT. Rugar, *et al.* detected a single electron spin in γ -irradiated silica as a frequency shift using the i-OSCAR protocol [10]. Garner, *et al.* detected 10^8 ^{71}Ga spins as a force gradient using the CERMIT technique, a record sensitivity for nuclei detection at the time [33]. However, each of these protocols place stringent requirements on the relaxation times of the sample. When used in conjunction with audio frequency cantilevers, OSCAR requires samples with a spin-lattice relaxation time in the rotating frame ($T_{1\rho}$) longer than about 10 ms and CERMIT

requires samples with T_1 generally longer than 10 ms.

Unfortunately, the relaxation times of typical biological spin labels may be too short to study using either OSCAR or CERMIT. Values for the electron spin-lattice relaxation times (T_{1e}) of nitroxide spin labels, such as TEMPO, range from $T_{1e} = 0.2\text{--}5.0\mu\text{s}$ at temperatures of 200K–330K [89–91]. The T_{1e} of 1mM 4-amino-TEMPO in a water/glycerol system is ~ 75 ms at 11 K and 139.50 GHz [92]. Since $T_1 \gg T_{1\rho}$ at cryogenic temperatures, we might expect that the OSCAR techniques would have difficulty detecting the unpaired electrons in these typical spin labels. In general, for a given spin label, the spin-lattice relaxation time increases as the temperature decreases. In solution, this is due to the freezing out of the rotational and translational motions of the molecules that cause relaxation [93]. The T_1 is also known to increase as the concentration of spins decreases, since spins are relaxed by the fluctuating magnetic fields from nearby spins. There is no way of knowing if the T_1 is large enough at 4 K to enable use of CERMIT or OSCAR without further experimental data. Very few measurements of the T_{1e} for spin labels and biological molecules have been performed at cryogenic temperatures.

In this chapter, we detail efforts to extend a force gradient approach to a sample with $T_1 < 10$ ms, which is too short for detection by OSCAR or CERMIT. Here, the unpaired electrons in a sample of diphenylpicrylhydrazyl (DPPH) are detected as a force gradient. Force gradient measurements are performed by exposing the electrons to an unmodulated radio frequency field and sweeping the external magnetic field while driving the cantilever with positive feedback. As the sensitive slice (Section 1.1) moves through the sample, the electrons, which were originally magnetized along the external magnetic field, become saturated by the transverse rf field causing the magnetization to saturate. This change in magnetization inter-

acts with the gradient and the derivative of the gradient (the second gradient) from a nearby magnetic particle, causing a change in the cantilever spring constant.

This chapter will begin with a detailed discussion of the three MRFM techniques related to this work, cyclic saturation force detected ESR, CERMIT, and OSCAR (Section 4.2). The expected signal in these experiments will be derived from first principles, and the limitations of the experiments will be discussed and used to motivate the force gradient technique. The experimental apparatus will then be discussed (Section 4.3), followed by an in-depth discussion of the experiment (Section 4.4). This chapter will conclude with a discussion of the results from the force and force gradient experiments (Section 4.5 and 4.6).

4.2 MRFM Techniques

4.2.1 Cyclic saturation ESR

As discussed in Section 1.1, the conventional magnetic resonance force microscopy experiments detect the spins in a sample as a force on the cantilever. In the sample-on-cantilever geometry, the dipole from the spins on the end of the cantilever interacts with the gradient from a nearby magnetic particle, producing a small force governed by

$$F = \mu_z \frac{\partial B_z}{\partial z} \quad (4.1)$$

where μ_z is the magnetic moment of the spins and $\partial B_z / \partial z$ is the gradient from the magnetic particle. The cantilever motion, the direction of the external field, and the polarized sample magnetization are along the z axis. This force produces a small deflection of the cantilever, which is difficult to detect. These deflections can be increased to a measurable level by modulating the sample magnetization at

some frequency f_{mod} , and thus the force on the cantilever, via the cyclic saturation method [94]. If f_{mod} is the cantilever resonance frequency, this will cause large, quality-factor-enhanced oscillations of the cantilever, which are detectable for large values of Q .

The force experiments discussed in this chapter were performed using amplitude modulated cyclic saturation. The sample is placed in an external magnetic field, and a magnetic moment is induced in the sample along this field. A nearby coil produces rf radiation at a specific frequency ω . When the sum of the external magnetic field and the tip field equal the frequency from the coil (known as the Larmor condition), the projection of the magnetization of the spins along the z axis becomes randomized in a bowl-shaped region of space known as the sensitive slice. This causes an instantaneous decrease in the magnetization in the slice and a decrease in the force.

This effect is known as saturation. Placing the spins in an external field creates an energy level splitting, where spins oriented against the field are higher in energy than those aligned with the field, and the energy difference is related to $\hbar\omega_0 = \hbar\gamma_e B_{\text{tot}}$, where γ_e is the electron gyromagnetic ratio. Due to Boltzmann statistics, there are more spins in the lower energy level. Turning on the rf promotes the excess spins from the lower level to the upper level and equalizes the number of spins in each energy level, saturating the system and destroying the net magnetization in the slice.

When the rf is turned off, the spins relax along the external magnetization in a time T_1 , the spin-lattice relaxation time, and the magnetization increases to its original value as polarization of the spins is reestablished. Therefore, modulating the rf creates an oscillating force at the modulation frequency. The spin-lattice

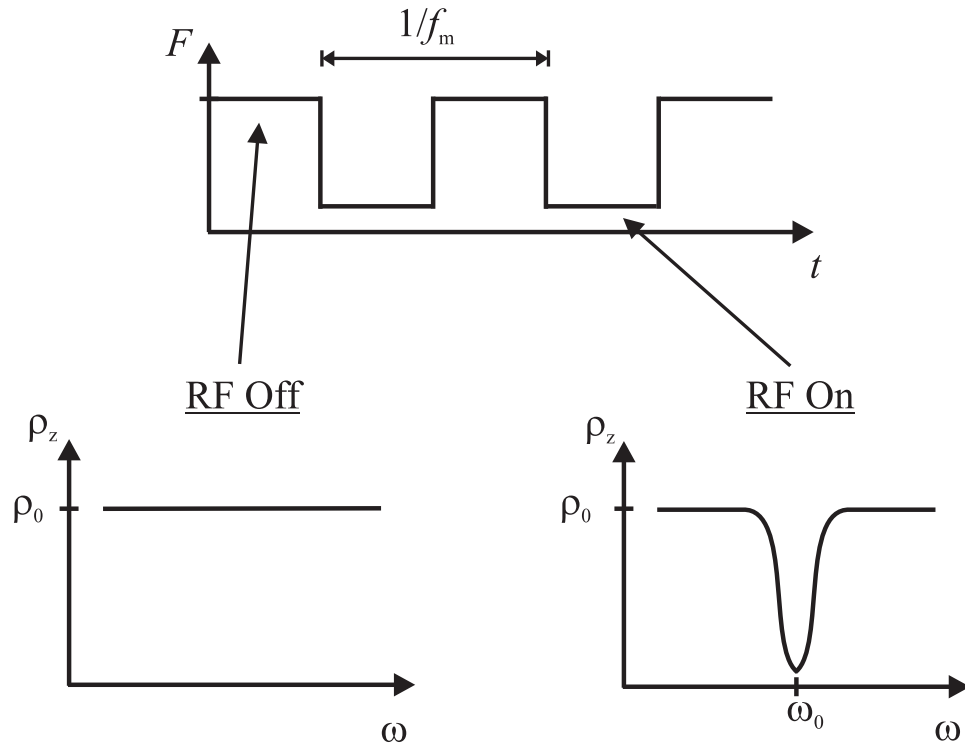


Figure 4.1: Magnetization behavior and the force in the cyclic saturation ESR experiment. The force between the magnetization in the slice and the gradient from the magnetic particle is modulated at a frequency f_m by amplitude modulating the rf field from a nearby coil. When the rf is off, the sample spins are aligned along the external field, and there is a gradient-dipole force on the cantilever. When the rf field is turned on and the resonance condition is satisfied, the spins become saturated and the spin magnetization density (ρ_0) decreases, causing the force to decrease. If $T_1 \ll 1/f_m$, the modulated force signal will be effectively square. If T_1 is on the order of the modulation period or larger, the spin magnetization along the z axis will not completely recover between saturations and the force will be smaller than expected.

relaxation time must be short compared to the period of the modulation frequency so that the magnetization has time to fully recover before becoming saturated again. In the experiments discussed here, $T_1 \ll 1/f_{\text{mod}}$, and the force modulation is nearly square, seen in Figure 4.1.

The saturation behavior for electrons is described by the steady-state solution of the Bloch equations [95]. The spin magnetization density along the z component of magnetization is

$$\rho_z = \rho_0 \frac{1 + (\omega - \omega_0)^2 T_1^2}{1 + (\gamma_e^2 B_1^2 + (\omega - \omega_0)^2) T_1^2} \quad (4.2)$$

where ρ_0 is the spin magnetization density of the thermal magnetization, B_1 is the amplitude of the applied oscillating transverse magnetic field and $\omega_0 = \gamma_e B_{\text{res}}$ is the Larmor frequency (not to be confused with the cantilever resonance frequency).

The approximation $T_1 = T_2$ has been made for our sample and will be justified in Section 4.3.5. Figure 4.1 depicts the spin magnetization density as a function of rf frequency. A minimum in the magnetization occurs at the resonance frequency, ω_0 , due to the random flipping of the spins that satisfy the Larmor condition. For spins where $\omega \neq \omega_0$, the magnetization is constant and along the external field. The depth of the peak is determined by the transverse magnetization B_1 , which is set by the power to the rf coil. As B_1 increases, the magnetization decreases as more of the spins become saturated. Eventually, all of the spins become saturated and no further decrease in magnetization will occur. Increasing the rf power further results in a wider resonance peak. This effect is known as power broadening.

4.2.2 OSCAR

OSCAR, or oscillating cantilever-driven adiabatic reversals, is a technique developed by Dan Rugar's group at IBM Almaden [31,32,34]. In OSCAR, the sample

spins are detected as a change in the cantilever spring constant as a distance-dependent force, not a force gradient. A variation of this technique has been used to detect a single electron spin in a silica sample [10].

The OSCAR technique uses the magnet-on-cantilever geometry, and the cantilever is brought close to a surface in either the parallel or perpendicular geometry. The latter geometry is depicted in Figure 4.2. The cantilever is oscillated with positive feedback, and the sample spins are allowed to polarize in the external magnetic field for a time longer than T_1 , if the sample is a large ensemble. The spins in a small ensemble will “self-polarize” and there is no need to wait T_1 . When polarization has occurred, the rf is turned on at a maximum of the cantilever oscillation to produce an in-phase force with the cantilever position. Since a single rf frequency is used, only the spins in the slice when the cantilever is at its equilibrium position are in resonance. When the cantilever is not at the equilibrium of its motion, the magnetic field at the resonant spins is either too large or too small to satisfy the resonance condition. This results in a resonance condition that is a function of the cantilever position. As the cantilever moves through the equilibrium position, the spins in the resonant slice are cyclically inverted by adiabatic rapid passage. This inversion occurs at the cantilever resonance frequency and is either in-phase or out-of-phase with the cantilever motion, depending on the initial state of the spins.

The oscillating inversion of the spins creates a gradient-dipole force on the cantilever that acts as a restoring force. The equation of motion for the cantilever in the presence of this in-phase restoring force can be written as

$$m\ddot{x} + \frac{m\omega_0}{Q}\dot{x} + kx = k'x \quad (4.3)$$

where $k'x$ is the in-phase force. Combining the spring constants results in an

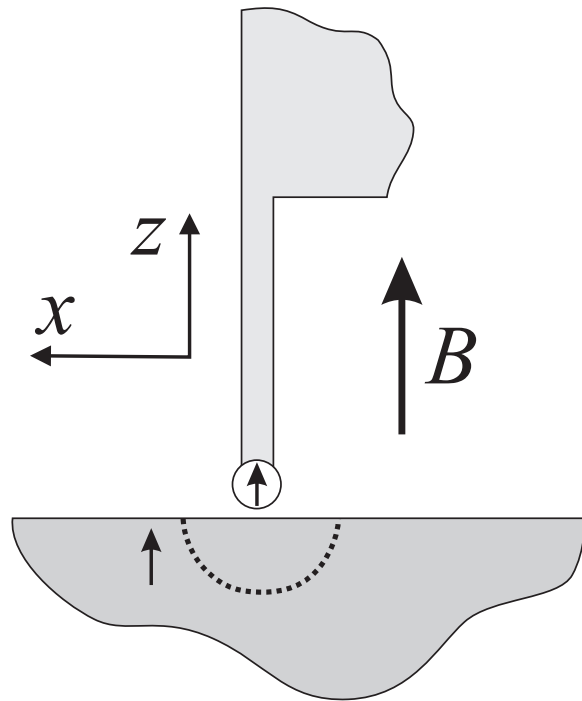


Figure 4.2: The OSCAR Experiment. The spin is located to the side of the cantilever tip. If the spin is directly below the tip, no signal will be recorded. The rf is turned on unmodulated, and the cantilever oscillation (from positive feedback) moves the sensitive slice in the x direction. This motion of the sensitive slice causes the spin to invert due to an adiabatic rapid passage, and this cyclic inversion occurs at the cantilever frequency. An oscillatory force is created that effectively modifies the restoring force of the cantilever, detected as a change in frequency.

effective change in the spring constant Δk which is equal to

$$\Delta k = \frac{F_{\text{spin}}}{\Delta x_c} \quad (4.4)$$

where F_{spin} is the rms amplitude of the oscillating force and Δx_c is the rms cantilever amplitude. This oscillating spring constant shift is measured as a change in the cantilever resonance frequency. Note carefully that the spring constant change in OSCAR is the result of a *force*, not a *force gradient*, which will be the case in the CERMIT technique. Additionally, the OSCAR protocol requires that the spin or spins being detected are not directly under the cantilever tip. This requires an imbalance in the sample spin distribution.

After the rf is on for some time, the spins no longer invert with the movement of the cantilever and the magnetization of the sample dies. Thus, the OSCAR experiment is limited by the length of time that the spins in the slice remain locked to the cantilever motion. This spin coherence time must be long compared to the cantilever resonance frequency. If not, the spins will only be inverted and produce signal in a small number of cantilever oscillations, and the spins will be undetectable. The spin coherence time is defined by τ_m and is a function of the transverse magnetic field from the coil (B_1), the adiabatic reversal rate, and the spin-lattice relaxation times in the lab frame (T_1) and the rotating frame ($T_{1\rho}$) [31]. If $T_{1\rho} \geq 10$ ms, the τ_m will be large enough to detect signal for OSCAR using a typical 1kHz cantilever. This τ_m for the single electron spin experiment was 760ms for the γ -irradiated silica sample, a highly specialized sample chosen for its long coherence time [10]. The τ_m restriction is highly limiting, and it is doubtful that the spin coherence times of biological samples or electron spin labels will be this long. This calls into question the applicability of OSCAR to many real world samples.

In some cases it is necessary to detect the signal in the presence of low-frequency noise. This can be achieved using interrupted-OSCAR (i-OSCAR), where the rf is periodically turned off and restarted at the opposite extreme [32]. This changes the phase of the cantilever response at the frequency of the interruption. The i-OSCAR method gives the signal a distinctive signature, making it easy to detect and characterize with a lock-in amplifier.

First Principles Derivation

The OSCAR effect can be derived from first principles, beginning with the Hamiltonian between one of the spins and the magnetic tip

$$\mathcal{H} = \boldsymbol{\mu}_{\text{spin}} \cdot \mathbf{B} \quad (4.5)$$

where $\boldsymbol{\mu}_{\text{spin}}$ is the magnetic moment of one spin and \mathbf{B} is the total field from the tip and the external field. In order to include all of the spins in the sensitive slice, we multiply $\boldsymbol{\rho}$, the spin magnetization density, by dV , which is the volume of the slice. This gives $\boldsymbol{\mu} = \boldsymbol{\rho} \cdot dV$. The classical energy is the integral over dV of all the spin-field interactions:

$$E = \int \boldsymbol{\rho} \cdot \mathbf{B} \, dV \quad (4.6)$$

Since we are only concerned with the spin magnetization in the z direction and since the contributions from the tip field in the x and y directions are small compared to the large static, external field, we can write the energy as

$$E = \int \rho_z \, B_z \, dV \quad (4.7)$$

It is now necessary to determine the forms of ρ_z and B_z during the OSCAR experiment. The field B_z represents the external field in the z direction plus the tip field at each spin. Since the cantilever is being driven, the field at a point \mathbf{r} will

change with the lever position, and the cantilever position x_c must be included in the field. Thus B_z will have the form $B_z(\mathbf{r} + x_c\mathbf{x})$ where \mathbf{x} represents the vector in the x-direction, i.e. the cantilever motion (Figure 4.2).

The spin magnetization density ρ_z is also dependent on the cantilever position. Recall that the spins are being modulated via the cantilever position x_c and are inverted adiabatically (the spin magnetization density must be normalized). Thus the spin density will have the form

$$\rho_z = \rho_m \frac{B_z(\mathbf{r} + x_c\mathbf{x}) - \omega/\gamma}{\sqrt{B_1^2 + (B_z(\mathbf{r} + x_c\mathbf{x}) - \omega/\gamma)^2}} \quad (4.8)$$

where B_1 is the transverse field from the rf coil, ρ_m is the spin magnetization density about the static field, ω is the Larmor frequency, and γ is the electron gyromagnetic ratio. When $B_z(\mathbf{r} + x_c\mathbf{x}) = \omega/\gamma$, the spins are on resonance, the magnetization is locked along the direction of the effective field, and $\rho_z = 0$.

The terms are now inserted into the energy integral in Eq. 4.7, and the integral is expanded using a Taylor series, assuming small oscillations of the cantilever x_c . It is useful to work in general terms where $\rho_z(B_z(\mathbf{r} + x_c\mathbf{x}))$ indicates that ρ_z is a function of B_z . This gives us

$$E = \int dV \{\rho_z(B_z(\mathbf{r} + x_c\mathbf{x})) \cdot B_z(\mathbf{r} + x_c\mathbf{x})\} \quad (4.9)$$

We expand $\rho_z B_z$ about \mathbf{r} :

$$\rho_z(\mathbf{r} + x_c\mathbf{x})B_z(\mathbf{r} + x_c\mathbf{x}) \simeq \rho_z B_z + x_c \frac{\partial}{\partial x}(\rho_z B_z) + \frac{1}{2}x_c^2 \frac{\partial^2}{\partial x^2}(\rho_z B_z) \quad (4.10)$$

When the chain rule is used to analyse these derivatives, the result will be partial derivatives such as $\partial B_z / \partial x$, the gradient, and $\partial \rho_z / \partial x$, which is not well described. For the partial derivatives of the spin density, it is easier to define them in terms

of the chain rule:

$$\frac{\partial \rho_z}{\partial x} = \frac{\partial \rho_z}{\partial B_z} \frac{\partial B_z}{\partial x} \quad (4.11)$$

The cross-term derivatives from the second-order terms can be manipulated in the same manner. After using the chain rule and combining terms, we are left with the following

$$E(x_c) = E_0 + x_c E_1 + \frac{1}{2} x_c^2 E_2 + \mathcal{O}(x_c^3) \quad (4.12)$$

where

$$E_0 = \int dV \{ \rho_z B_z \} \quad (4.13)$$

$$E_1 = \int dV \left\{ \rho_z \frac{\partial B_z}{\partial x} + \frac{\partial \rho_z}{\partial B_z} \frac{\partial B_z}{\partial x} B_z \right\} \quad (4.14)$$

$$E_2 = \int dV \left\{ \left(\rho_z + \frac{\partial \rho_z}{\partial B_z} B_z \right) \frac{\partial^2 B_z}{\partial x^2} + \left(2 \frac{\partial \rho_z}{\partial B_z} + \frac{\partial^2 \rho_z}{\partial B_z^2} B_z \right) \left(\frac{\partial B_z}{\partial x} \right)^2 \right\} \quad (4.15)$$

Now we must analyze the size of the various terms when the spins are on resonance. For simplicity, $\Delta B = B_z - \omega/\gamma$, which is zero on resonance.

$$\begin{aligned} \rho_z &= \rho_m \frac{\Delta B}{\sqrt{B_1^2 + \Delta B^2}} = 0 \\ \frac{\partial \rho_z}{\partial B_z} &= \rho_m \frac{B_1^2}{(B_1^2 + \Delta B^2)^{3/2}} = \rho_m \frac{1}{B_1} \\ \frac{\partial^2 \rho_z}{\partial B_z^2} &= -\rho_m \frac{3B_1^2 \Delta B^2}{(B_1^2 + \Delta B^2)^{5/2}} = 0 \end{aligned} \quad (4.16)$$

Since the OSCAR term will look like a spring constant, we focus on the terms in the third term of the energy (Eq. 4.15). When the spins are resonant, the only remaining non-zero terms are the second and third ones:

$$\left(\frac{\partial \rho_z}{\partial B_z} B_z \right) \frac{\partial^2 B_z}{\partial x^2} = \rho_m \frac{B_z}{B_1} \frac{\partial^2 B_z}{\partial x^2} \quad (4.17)$$

$$2 \frac{\partial \rho_z}{\partial B_z} \left(\frac{\partial B_z}{\partial x} \right)^2 = 2 \rho_m \frac{1}{B_1} \left(\frac{\partial B_z}{\partial x} \right)^2 \quad (4.18)$$

The question now becomes which of these two terms is responsible for the OSCAR effect, which is linear in the gradient. We will focus on the term described in Eq. 4.18 since it contains the gradient term.

Consider the form of $\partial\rho_z/\partial B_z$. It is Lorentzian with a peak at ρ_m/B_1 . The linewidth of this Lorentzian is $\Delta x = B_1/G$ where G is the gradient ($\partial B_z/\partial x$). If we approximate the gradient as constant over the sensitive slice and ignore the other terms in the third integral (a good assumption since they are either zero or small), then the classical energy is dominated by Eq. 4.18 (A in this derivation corresponds to the area of the slice):

$$\begin{aligned} E &= \dots + \frac{1}{2}x_c^2 \int dV \left\{ 2 \frac{\partial\rho_z}{\partial B_z} \left(\frac{\partial B_z}{\partial x} \right)^2 \right\} \\ E &\simeq \dots + \frac{1}{2}x_c^2 \underbrace{\int \int dy dz}_{A} \underbrace{\int 2 \frac{\partial\rho_z}{\partial B_z} G G dx}_{2 \frac{\rho_m}{B_1} G G \frac{B_1}{G} = 2\rho_m G} \\ E &\simeq \dots + \frac{1}{2}x_c^2 2\rho_m G A = x_c^2 \rho_m G A \end{aligned} \quad (4.19)$$

Now we have a term that is linear in the gradient! The term in Eq. 4.18 is proportional to G^2 , but one power of the gradient cancels when integrating over x .

Finally, we relate this result to the form of F_{spin} from the original OSCAR experiment [31]. Recall that the spring constant shift is described using Eq. 4.4, where $\Delta k \simeq F_{\text{spin}}/x_c$. According to Ref. [31], the force becomes

$$F_{\text{spin}} \simeq GN(\mu_B^2 B_0/k_B T)Ax_c \quad (4.20)$$

for small slice penetration depths, where N is the spin density (in units of m^{-3}).

Remember that, in general, $E = Fx$, and the spin magnetization density is

$$\rho = N \frac{\gamma_e^2 \hbar^2 B_0}{k_B T} \quad (4.21)$$

where B_0 is the resonance field. This means we can write Stipe, *et. al.*'s classical energy in terms of our variables as

$$E = F_{\text{spin}}x_c \simeq x_c^2\rho_mGA \quad (4.22)$$

which is the same as the energy we find from the first principles derivation. Therefore, we conclude that the OSCAR signal is dominated by

$$E(x_c) \simeq \frac{1}{2}x_c^2 \int dV \left\{ 2\frac{\partial\rho_z}{\partial B_z} \left(\frac{\partial B_z}{\partial x} \right)^2 \right\} \quad (4.23)$$

4.2.3 CERMIT

CERMIT, or cantilever enabled readout of magnetic inversion transients, was developed in the Marohn group as a way to detect a homogeneous distribution of spins in the perpendicular geometry [33]. If the spin distribution below a perpendicular cantilever tip is homogenous, the force on the cantilever would be zero, making prior MRFM techniques inapplicable. CERMIT breaks this symmetry and detects the spins as a force gradient, not a force.

In CERMIT, a low spring constant cantilever with a magnetic tip is brought close to a sample surface and driven with positive feedback. The nuclear spins in a sensitive slice below the tip are inverted once with an adiabatic rapid passage (ARP); the spin magnetization does not need to be inverted every cantilever cycle as in the OSCAR experiment. The spins in this slice have the opposite magnetization of the spins outside of the slice. The force is still zero by symmetry. Any force from the right side of the cantilever will be canceled by the force from the left side of the cantilever and vice versa. However, the spring constant has changed due to a force gradient. If the cantilever is driven to the right, the inverted spins below the tip “pull” the cantilever downward and make it stiffer. This spring constant

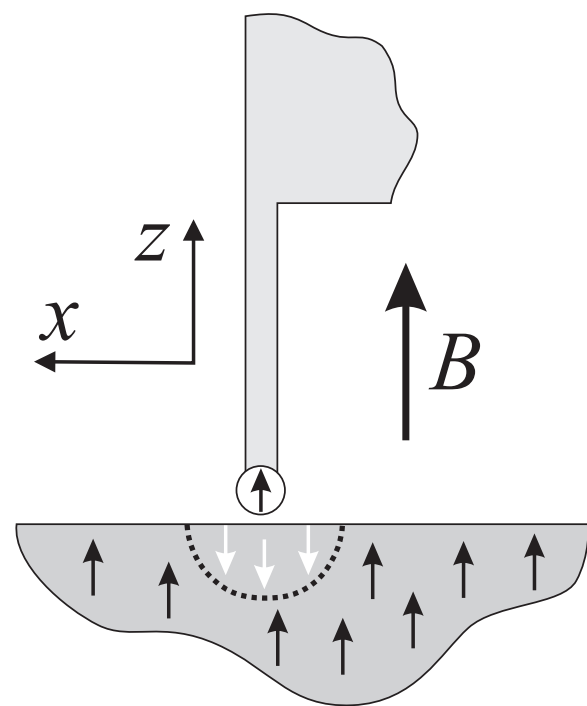


Figure 4.3: The CERMIT Experiment. The spins flipped via the adiabatic rapid passage (ARP) are the only spins that contribute to the signal.

change is proportional to the magnetization in the slice and to the derivative of the gradient from the particle, $\partial^2 B_z / \partial z^2$, which we will call the second gradient

$$\Delta k = \mu_z \frac{\partial^2 B_z}{\partial z^2} \quad (4.24)$$

The change in the cantilever spring constant is measured as a change in the cantilever resonance frequency via the positive feedback circuit and a commercial frequency counter. The frequency shift is converted to a spring constant shift using

$$\frac{\Delta f}{f_0} = \frac{\Delta k}{2k} \quad (4.25)$$

where k is the intrinsic cantilever spring constant.

The main limitation of CERMIT lies in the spin-lattice relaxation time of the spins being detected. After the spins are inverted by the ARP sweep, they will begin to relax back along the external field in a time T_1 . If the T_1 is short compared to the cantilever period ($1/f_0$), then the spins will recover faster than the time it takes to record the frequency shift. For a typical low spring constant cantilever, the resonance frequency will be around 1 kHz, so T_1 should be much larger than 1 ms, say 10 ms or longer, for spins detected by CERMIT. This restriction on sample relaxation rate is similar to the $T_{1\rho}$ limitation in OSCAR. However, since T_1 is generally larger than $T_{1\rho}$ at cryogenic temperatures, it is easier to find samples to use for CERMIT than for OSCAR. Unfortunately, it is possible that the T_1 for spin labels, biological samples, or other potential samples is below this threshold at cryogenic temperatures. This is difficult to gauge due to the lack of experimental data for T_1 at cryogenic temperatures and low rf fields.

First Principles Derivation

The CERMIT effect can be derived from first principles in a method similar to that used above for the OSCAR experiment. We again begin with the Hamiltonian of the interaction between the spin and the magnetic particle (Eq. 4.5), including only the spins in the sensitive slice (Eq. 4.6). As before, we are only concerned with the magnetization along z , so we have (Eq. 4.7)

$$E = \int \rho_z B_z dV$$

We now determine forms for ρ_z and B_z based on the CERMIT experiment. Unlike OSCAR, the spins that contribute to the signal are fixed by the ARP sweep, and ρ_z is not dependent on the cantilever position. It only depends on the vector \mathbf{r} that describes the spin position with respect to the magnetic particle. The cantilever is again driven using positive feedback, so the field at the spin will depend on the cantilever position x_c , which is identical to the OSCAR case. We can write the energy as

$$E = \int dV \{\rho_z(\mathbf{r}) \cdot B_z(\mathbf{r} + x_c \mathbf{x})\} \quad (4.26)$$

We now assume a small oscillation of the cantilever position (x_c), and expand only the field term in a Taylor series out to the second power. The Taylor series expansion (to three terms) results in

$$E \simeq \int dV \left\{ \rho_z B_z \right\} + x_c \underbrace{\int dV \left\{ \rho_z \frac{\partial B_z}{\partial x} \right\}}_{\text{Force} = 0} + \frac{1}{2} x_c^2 \underbrace{\int dV \left\{ \rho_z \frac{\partial^2 B_z}{\partial x^2} \right\}}_{\text{Spring Constant} \neq 0} \quad (4.27)$$

Now we can see the terms that give rise to the CERMIT signal. The second integral contains the force between the spins and the tip-field gradient $\partial B_z / \partial x$, which is zero by symmetry in a homogeneous spin distribution. The third integral contains the spring constant term which arises due to the force gradient $\partial^2 B_z / \partial x^2$ which is

nonzero. This term predicts a shift in the spring constant due to the force gradient known as the CERMIT effect.

4.2.4 Motivations

In the following sections, a new ESR-MRFM protocol is presented that allows detection of electron spins with T_1 below 10 ms, beyond the reach of OSCAR and CERMIT techniques using audio frequency cantilevers. The unpaired electrons in a sample of DPPH are detected as a change in the cantilever resonance frequency due to a force gradient interaction between the spins and a magnetic particle positioned near the sample in the presence of an unmodulated transverse magnetic field. This interaction is governed by the derivative of the force in the cyclic saturation experiment (Eq. 4.1)

$$\Delta k = \frac{\partial F}{\partial z} = \mu_z \frac{\partial^2 B_z}{\partial z^2} + \frac{\partial \mu_z}{\partial z} \frac{\partial B_z}{\partial z} \quad (4.28)$$

The first term in Eq. 4.28 is the dominant term in the CERMIT experiment. The second term is the change in the magnetic moment (μ_z) from the movement of the sensitive slice ($\partial \mu_z / \partial z$) multiplied by the gradient, a term similar to the one that governs the IBM Group's OSCAR experiment. In CERMIT, the rf is off during data acquisition and the magnetic moment in the sensitive slice does not change, resulting in $\partial \mu_z / \partial z = 0$. The spring constant shift in CERMIT is dominated by the first term. We will see that when the rf is on and the gradient from the magnetic particle is small, the majority of the spring constant shift comes from the second term.

Saturation of the spins by the rf field is instantaneous, and detection of the spins occurs while the rf field is irradiating, thereby removing any limitations on

the signal related to the relaxation rates of the sample. This effect has been observed in both a low-gradient ($\sim 50 \text{ T/m}$) and a slightly higher gradient ($\sim 300 \text{ T/m}$) and we find that the shape of the signal is unexpectedly observed to change with the size of the gradient. This force gradient method opens up the possibility of detecting electron spins in spin labels, biomolecules, or any other free radical sample, regardless of their relaxation rates at cryogenic temperatures. In addition, the physics of this effect are due to saturation of the spins, rather than spin inversion as in OSCAR and CERMIT. Therefore, we expect to see a distinct difference in the signal between this force gradient effect and previous force gradient measurements.

4.3 Experimental Apparatus and Sample

4.3.1 Overview

Experiments discussed in this chapter were performed using the high-vacuum, cryogenic probe built and designed by Sean Garner, which is described in his dissertation [74]. Cyclic saturation force and force gradient experiments are performed using the sample-on-cantilever geometry, shown in Figure 4.4. This simplifies our proof-of-concept experiments by removing the need for scanning instrumentation and allows the use of a relatively large magnetic particle. A sample of DPPH is glued to the end of a custom-fabricated cantilever which is positioned near the center of an rf coil. The coil produces the magnetic field (B_1) necessary to saturate the magnetization of the spins. A piece of samarium cobalt ($\text{Sm}_2\text{Co}_{17}$) is positioned near the end of the cantilever and provides the gradient that interacts with the sample magnetic moment in force and force gradient detected MRFM

experiments. Cantilever displacement is measured using a fiber-optic interferometer (Section 3.3), and the cantilever can be excited using a piezoelectric actuator glued to the stage. This section will discuss some of the highlights of the probe important to the work and some alterations made to the probe by the author.

4.3.2 RF coil and circuit

The rf coil is approximately 1 mm in diameter and was hand wound to approximately three turns using one lead of a $1/4 - \text{W}$ resistor [74]. A tank circuit is formed by placing the inductance from the coil in parallel with a capacitor, called the tuning capacitor C_T , which creates a resonant LC circuit. This is in series with a second capacitor, the matching capacitor C_M . In order to make sure that all of the power that is transmitted through the line makes it to the coil, the impedance of the tank circuit must be the same as the impedance of the BNC used to transmit the rf down the probe, which is 50Ω . The tank impedance is adjusted by using a variable capacitor as the C_M . When matched, approximately 100% of the power that is sent down the line is transferred to the coil. The resonant frequency of the circuit (i.e., the rf frequency used in the ESR experiments) and the matching of the circuit is verified using an rf sweeper (Morris Instruments, model 505NV+). The rf frequency and degree of matching can be adjusted independently using the variable capacitor tuning pins on top of the probe. It should be noted that the properties of the tank circuit change with temperature, so it is important to check the circuit resonance and matching at room temperature and at cryogenic temperatures.

Since the tunable capacitors used in this probe are large, it would be inconvenient to place them near the rf coil and cantilever setup. This problem is solved using a half-wave line. If a transmission line with a length half as long as the

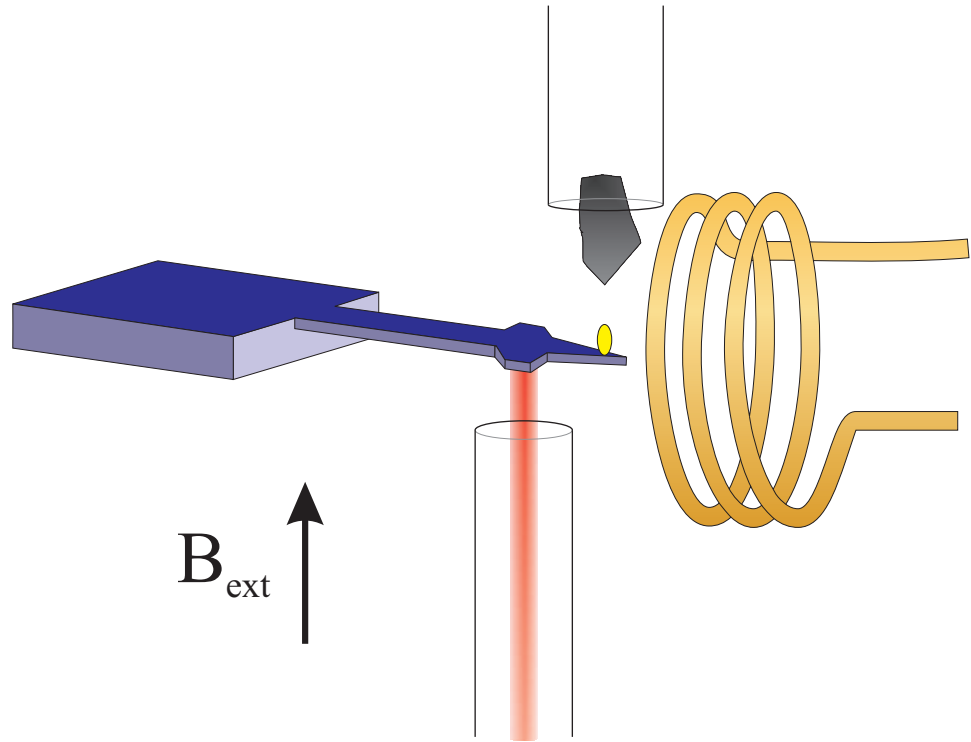


Figure 4.4: The setup for the force gradient electron spin resonance experiment. An ellipsoidal piece of diphenylpicrylhydrazyl (DPPH) is glued to the end of the cantilever. A shard of samarium cobalt provides the magnetic gradient necessary to produce a force on the cantilever. The cantilever is positioned near the center of an rf coil, which produces the transverse magnetic field necessary to saturate the sample spins. The movement of the cantilever is detected using a fiber-optic interferometer.

wavelength of the frequency used in the experiment is placed between the capacitors and the coil, the tank circuit will behave as if the coil is directly beside the capacitors. The capacitors are placed in the main body of the probe, several inches above the coil and cantilever.

The rf used in these experiments is generated by an HP signal generator (model number HP8657A). In the cyclic saturation ESR experiments, the rf is amplitude modulated at a frequency f_{mod} . This frequency can be set to the cantilever resonance frequency if quality factor enhancement of the resulting force is required, or it can be set to some convenient off-resonance frequency. Modulation of the rf is provided by a home-built TTL-controlled rf switching circuit. This circuit uses the TTL output generated by the lock-in amplifier (Stanford SR830) at the lock-in reference frequency. The rf output of the HP generator is sent to the switch, which turns the rf on and off at the TTL frequency to allow amplitude modulation of the rf signal. This modulated signal is amplified by +44 dBm using a Kalmus amplifier (model number 320FCP-CE, 10 – 400 MHz) and sent to the rf coil.

In the force gradient ESR experiments, the rf is on constantly and is not sent through the switch. The output from the HP generator is sent directly to the amplifier and then to the coil. This unmodulated rf heats the cantilever, resulting in a decrease of the resonance frequency of the cantilever due to a lowering of the Young's modulus of silicon at higher temperature [43].

4.3.3 Positive feedback

During the force gradient ESR experiment, the cantilever is driven using positive feedback [43, 96]. In this circuit (Figure 4.5), the interferometer voltage, which is proportional to the cantilever displacement, is the input of a feedback loop. This

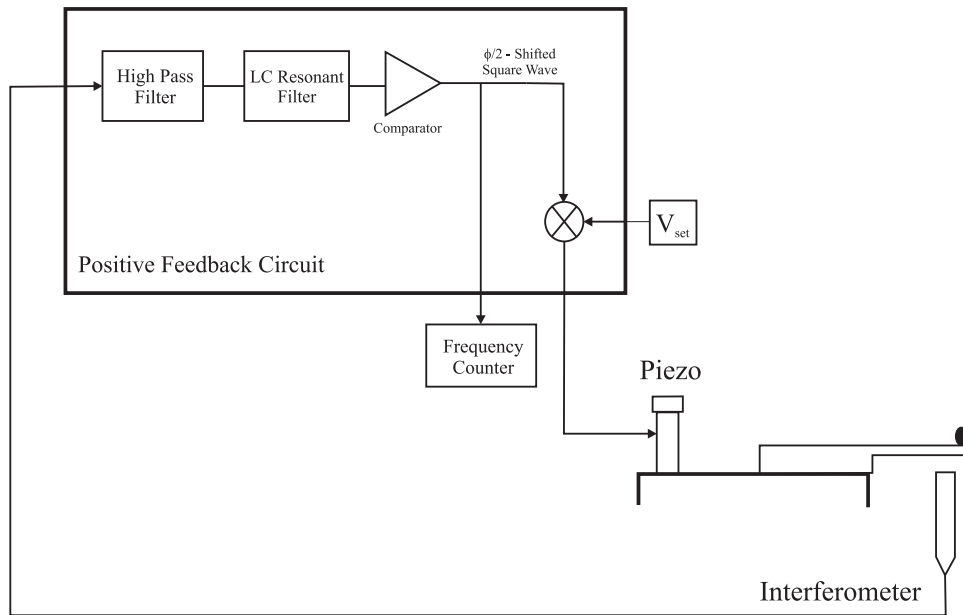


Figure 4.5: The positive feedback circuit. The cantilever is driven by base shaking from the piezo glued to the stage. A capacitive drive wire can also be used to drive the cantilever.

signal is high-pass filtered and sent through a resonant LC filter. The LC filter should have a circuit resonance near the cantilever resonance frequency in order to filter out background oscillations from higher cantilever modes or piezoelectric modes. Experience has shown that there is a great deal of latitude in setting the circuit resonance. These two filters produce a sinusoid centered at zero volts and phase shifted by $\pi/2$.

This sinusoid is sent to a commercial frequency counter (Stanford SR620), and to a comparator. The comparator outputs 0 V when the sinusoidal signal is negative and 5 V when the signal is positive, resulting in a phase-shifted square wave at the cantilever frequency. This square wave output is multiplied by a set point voltage from one of the lock-in amplifier outputs and is sent to a piezoelectric actuator glued to the cantilever stage (Thorlabs, 5 mm tall). This piezo excites

the cantilever at the resonance frequency. The set point voltage (V_{set}) is adjusted to set the cantilever amplitude. The cantilever can also be driven into positive feedback with a capacitive drive wire. One advantage of this technique is that the change in the cantilever frequency due to a force gradient can be measured instantaneously. We are not required to wait a characteristic cantilever ring down time (which can be very long, 30 – 60 s, with high quality factors) to see a change from a force gradient as we would if we were measuring a change in amplitude.

The piezoelectric stack is glued to the cantilever stage with epoxy and is positioned behind and to the side of the cantilever. A small piece of brass about 0.5 cm thick is glued to the top of the stack to add extra force to the piezo's oscillations. Base shaking of the cantilever using this method has proven to be reliable and effective at temperatures from 4 K to 300 K in vacuum. Furthermore, set point voltages required from the lock-in amplifier to drive the cantilever nearly a full fringe are typically between 1 – 2 V.

4.3.4 Magnetic particle

Magnet parameters used in the following discussions include the tip field, gradient, and second gradient. These values are calculated from the force signals, estimates of the particle size, and the distance from the magnet to the sample. The relevant equations for determining these parameters for a spherical magnetic

particle are

$$B_{\text{tip}} = \frac{2}{3} B_s \frac{r^3}{(r+d)^3} \quad (4.29)$$

$$\nabla B = \frac{\partial B_z}{\partial z} = -2 B_s \frac{r^3}{(r+d)^4} \quad (4.30)$$

$$\nabla^2 B = \frac{\partial^2 B_z}{\partial z^2} = 8 B_s \frac{r^3}{(r+d)^5} \quad (4.31)$$

$$(4.32)$$

where B_{tip} is the z component of the magnetic field from the tip along the z -axis, $B_s = \mu_0 M$ is the particle saturation, r is the radius of the (assumed) spherical magnetic particle, and d is the distance from the tip of the magnet to the sample. To maximize the gradient and the second gradient produced by the magnetic particle, it is necessary to saturate the particle by maximizing B_s and placing the particle as close as possible to the sample to minimize the tip-sample distance d .

The magnetic particle is aligned to the sample on the end of the cantilever using the magnetic particle mount. The mount consists of a cylinder which passes through three plates. A 2-56 screw passes through the center of the cylinder, and a glass capillary tube of outer diameter ~ 0.5 mm is glued to the end of the screw. The magnetic particle is glued onto the end of this capillary, and the capillary is long enough to allow room for the piezoelectric glued to the cantilever stage. Three screws and springs hold the cylinder tight during the experiment. The screws are loosened when aligning and the cylinder can be adjusted in x and y . The height above the sample can be set roughly by moving the entire particle mount, while some fine tuning of the height can be achieved by turning the 2-56 screw. Aspects of this setup can be seen in Figure 4.7.

Previous cyclic saturation ESR experiments performed in this lab by the author and others used Alnico for the magnetic particle, which requires a small field of

300mT to saturate the particle. Typically, the Alnico particle is positioned onto the end of the capillary with five-minute epoxy. While the epoxy is drying, a magnet with a surface magnetization of 0.4 T is brought near the magnet in order to align the easy axis of the particle along the length of the capillary and to nominally saturate the particle. Experiments are performed using a resistive electromagnet with a coil constant of 18.6 G/A, formed by winding two layers of 16-gauge Cu magnet wire on a lathe around a Cu spool which was designed to fit outside of the probe. Experiments using this magnet were performed at 77 K with relatively low magnetic fields (the range of the magnet is approximately 300 G).

Unfortunately, the Alnico particles used in these experiments were never completely saturated, and could not provide the assumed gradients necessary to see a force gradient signal. Gradients in early ESR experiments using Alnico ranged from 10 – 50 T/m). To completely saturate the Alinco particles, it would be necessary to use a superconducting magnet which can provide fields of 6 T or higher. However, this increases the tip field and the field required to see resonance, and Alnico cannot be used in these high fields due to its low coercivity (0.06 T).

Samarium cobalt ($\text{Sm}_2\text{Co}_{17}$, or SmCo) was chosen as a suitable material for use in our force gradient experiments (Arnold Magnetics, S3/225 Sintered, Die Pressed) [97]. SmCo has a higher coercivity (0.95 T) than Alnico, well within the range of the external field sweeps from -0.2 T to $+0.2$ T and produces a larger gradient due to its higher B_s . For purposes of calculating the tip field, gradient, and second gradient, the magnetic particle used in the following experiments is assumed to be spherical with a radius of 300 μm . In reality, the particle is shaped more like a shard (depicted in Figure 4.4), with approximate particle dimensions 700 μm wide, 400 μm thick, and 800 μm tall. The spherical radius value was determined by

calculating the volume of the particle, assuming that it is cylindrical, then setting this volume equal to the volume of a sphere and solving for the radius.

The switch to SmCo required a change in the normal saturation protocol due to the high (5.5 T) saturation field required to saturate the particle. This field is reached using the 6 T superconducting magnet previously used in cantilever magnetometry experiments [59]. The particle is magnetized *in situ* prior to performing the cyclic saturation and force gradient experiments. The probe is placed into the magnet dewar so that the magnetic particle and cantilever are in the center of the 6 T magnet (Figure 4.6(a)), and the magnetic field is ramped slowly to +5.8 T or -5.8 T and allowed to stay there for about half an hour. The field is then ramped back to zero.

Two aspects of the experiment should be noted at this point. First, the sign of the saturation field affects the magnitudes of the tip field, gradient, and second gradient during the experiments, producing strikingly different results. This could be due to improper resetting of the magnetic hysteresis between experiments or incomplete saturation of the particle. The particle's shape may require saturation fields greater than the 5.8 T used for saturation. There is also some evidence for incomplete saturation in the experimental results themselves, where it appears that the external field is changing the saturation of the particle.

Secondly, because the coil constant in the center of the magnet is rather large (1.392 kG/A), experiments cannot be performed in the center of the superconducting magnet. Small changes in current (0.1 A) produce field steps that are larger than the resonance widths seen in these experiments, which are typically between 20 – 120 G. For this reason, it was necessary to raise the probe so that the magnetic particle and cantilever are about 14 cm above the center of the mag-

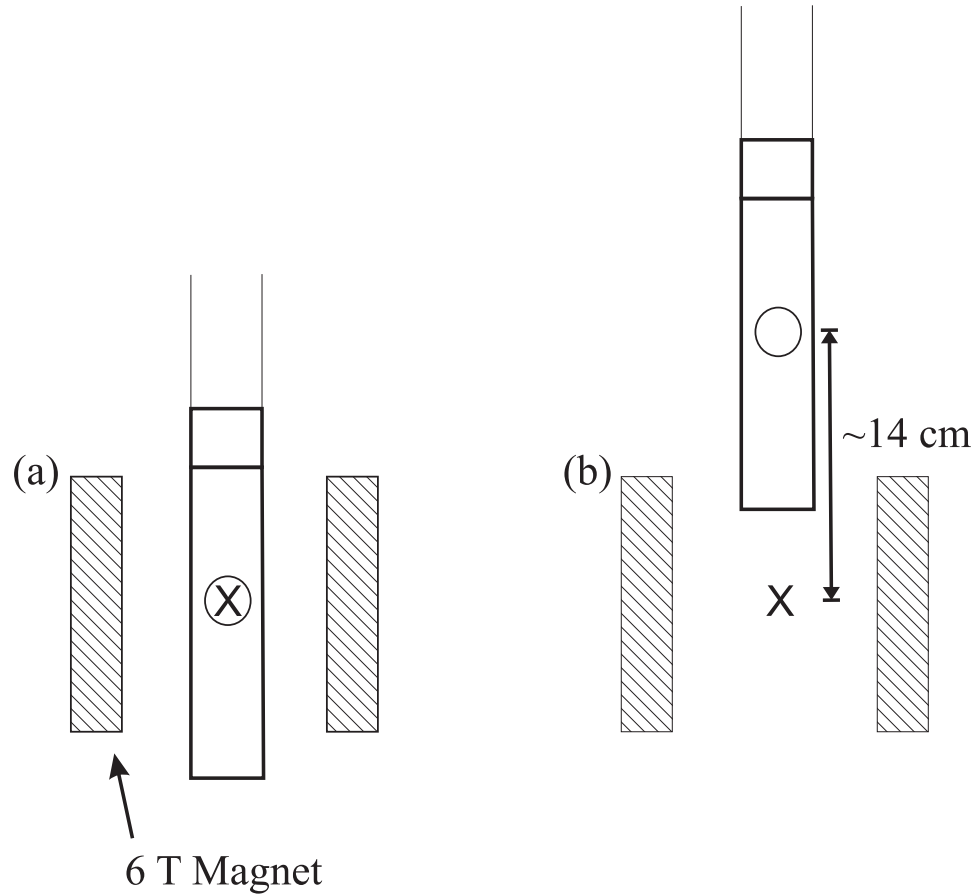


Figure 4.6: Positioning of the probe for particle saturation and experiments.

The center of the 6 T superconducting magnet is represented by the X, and the circle represents the position of the magnetic particle, cantilever, and sample in the probe. In (a), the probe is positioned so that the magnetic particle is positioned in the center of the magnet to saturate the particle. In (b), the particle and cantilever are raised approximately 14 cm above the center of the magnet. The force and force gradient experiments are performed in the smaller inhomogeneous field of the magnet. Note that the probe and magnet are not to scale.

net (Figure 4.6(b)). This places the experiment in the inhomogeneous field of the magnet where the coil constant at this height is 43 G/A, determined using the computer simulations provided by American Magnetics. A proportional relationship with the coil constant in the center of the magnet is used to determine the coil constant above the magnet center. Any error in the measurement of the height above the magnet center, which may be as much as 1 cm, will affect the value of the external field used in experiment. Errors in the coil constant are discussed in Appendix A.

4.3.5 Sample preparation

The sample used in the following experiments is diphenylpicrylhydrazyl, or DPPH. DPPH is an organic nitroxide radical, seen in Figure 4.7(f), that is ubiquitous in the ESR community as a “tune-up” sample. DPPH readily forms a solid, providing a high density of electron spins ($\rho_{\text{DPPH}} = 2.3 \times 10^{27} \text{ spins/m}^3$) [98]. The sample used in this experiment was purchased from Sigma Aldrich (Sigma, 1,1-Diphenyl-2-picrylhydrazyl radical, item number D9132). It is important to store the samples in a cold, dark environment when not being used as it will only last for about a month in ambient light and room temperature.

DPPH was chosen as a test sample for this force gradient technique due to its short T_{1e} relative to the ~ 10 ms lower limit of the CERMIT technique. Early work by Singer, *et al.* determined that the linewidth of powder and single-crystal DPPH samples remains relatively constant within an order of magnitude as the temperature is decreased from 300 K to 4.2 K at MHz and GHz ranges [99, 100]. It was also determined that $T_1 = T_2$ for DPPH in this temperature range at GHz field, due to the spin exchange interaction [101–103]. Based on the steady-state Bloch

equation for the z -magnetization with $T_1 = T_2$ (Eq. 4.2), the squared linewidth of the Lorentzian saturation curve is¹

$$\frac{1}{(\gamma T_1)^2} = (5 \text{ G})^2 \quad (4.33)$$

for DPPH at 4 K [100]. This gives $T_1 \approx 70$ ns for DPPH at 4 K. Values close to this have been used for DPPH samples in past MRFM experiments [21, 104]. It should also be noted that $T_1 \neq T_2$ for dilute DPPH in polystyrene. In this system, T_1 is ~ 20 μ s at 77 K and ~ 200 μ s at 4 K, whereas $T_2 = 20$ ns and is essentially independent of temperature [105, 106].

The sample was glued to the end of the cantilever as follows. The procedure required two Exacto knives with small pieces of double-stick tape on the ends and, of course, a microscope. One knife held the cantilever die and the other held a hair or small wire for spreading glue. The cantilever die was placed on the end of one Exacto knife and this was used to find a piece of DPPH small enough to place onto the end of the cantilever. Next, the hair is dipped into a small amount of epoxy and a streak of epoxy (Hardman, 5 minute drying time) is made near the DPPH sample. The cantilever is turned upside down and lowered into the end of the streak. This ensured that the least amount of epoxy is on the end of the cantilever as possible. Finally, the tip was gently touched to a small piece of sample and plenty of time was allowed for the epoxy to dry. In the author's experience, the sample will remain on the end of the cantilever through many cold cycles.

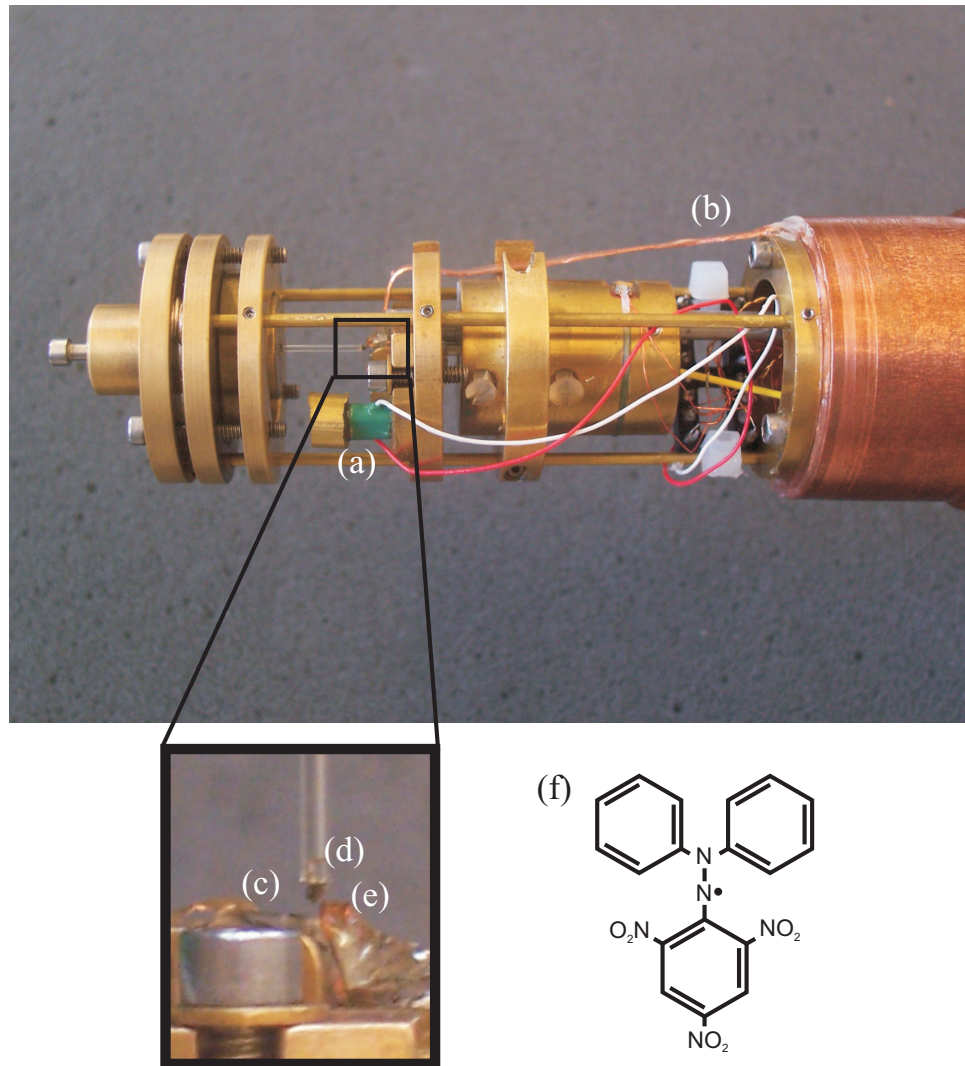


Figure 4.7: Photograph of the ESR probe used in the cyclic saturation and force gradient experiments. The piezo (a) used to excite the cantilever is glued behind the cantilever die. Heat sinking of the stage to the copper of the probe is provided by a long piece of high purity copper (b). In the inset, the cantilever die (c), the magnetic particle on the end of the glass capillary (d), and the rf coil (e) are all visible. The chemical structure of the sample used in these experiments, diphenylpicrylhydrazyl or DPPH, is pictured in (f).

4.4 Experimental Details

A $\sim 40 \mu\text{m}$ tall, $\sim 20 \mu\text{m}$ wide ellipsoidal, crystalline sample of DPPH was glued to the end of a custom fabricated single-crystal silicon cantilever 340 nm thick, 275 μm long, and 8 μm wide with a spring constant of $1 \times 10^{-3} \text{ N/m}$ and a resonance frequency of 1460 Hz (Table 4.1). The DPPH sample was positioned on the cantilever as depicted in Figure 4.4, and the height of 40 μm , which is the distance that the sensitive slice must traverse during the scan, will be referred to as the sample thickness. 40 μm is an estimate of the sample thickness measured using an optical microscope, and can be assumed to have an error of about 10 μm .

The spring constant value was determined by analyzing the Brownian motion of the cantilever, as described in Section 3.3. The cantilever was positioned approximately 400 μm from the 1 mm-diameter coil. The coil was tuned to $\sim 350 \text{ MHz}$ and driven with powers from 4 to 2000 mW. According to power broadening data, the coil produced approximately $6 \text{ G}/\sqrt{\text{W}}$, resulting in a magnetic field of $B_1 \sim 0.5 \text{ mT}$ at higher rf powers. The SmCo magnetic particle (assumed spherical with $r \sim 300 \mu\text{m}$) was positioned above the cantilever and sample. The distance from the tip of the magnetic particle to the sample was $d \sim 250 \mu\text{m}$. A photograph of the probe head, with all of the components properly aligned for the experiment, is located in Figure 4.7. These parameters are summarized in Table 4.2.

The experiments were performed at cryogenic temperatures, around 20 K. No thermometer was present in the probe to measure the exact temperature. This temperature was determined by analysis of the high gradient force experiment that follows in Section 4.6.2 and is an estimate. The cantilever and sample are

¹When $T_1 \neq T_2$, the ESR linewidth is approximately $1/(\gamma\sqrt{T_1T_2})$. This makes the independent determination of T_1 and T_2 in traditional ESR experiments very difficult due to inhomogeneous line broadening.

Table 4.1: Cantilever Parameters for the DPPH-loaded cantilever used in the force and force gradient detected ESR experiments.

Length (l)	275 μm
Width (w)	8 μm
Thickness (t)	0.34 μm
Spring Constant (k)	$1 \times 10^{-3} \text{ N/m}$
Resonance Frequency (f_0)	1460 Hz
Quality Factor (Q)	25,000

Table 4.2: Experimental parameters for the force and force gradient experiments.

Temperature (T)	$\sim 20 \text{ K}$
DPPH Thickness (est.)	$40 \pm 10 \mu\text{m}$
$\text{Sm}_2\text{Co}_{17}$ Radius (r , est.)	300 μm
Tip-Sample Distance (d , est.)	250 μm
Larmor Frequency (ω_{rf})	348 MHz
Resonance Field (B_{res})	124 G

heated above 4 K by the rf, complicating the temperature estimate. The actual temperature of the cantilever and sample during unmodulated rf experiments are likely higher than 20 K.

For cooling, a small amount of Helium gas was used as an exchange medium and was pumped out after the temperature in the probe had settled. This was determined by monitoring the interferometer drift on the oscilloscope without temperature tuning. Heat sinking was provided by a 2" long by 3 mm by 0.5 mm thick piece of high-purity copper foil (Alfa Aesar) linking the copper on the 1-degree seal to the brass stage, seen in Figure 4.7(b). A thinner piece of high-purity copper foil (0.05 mm thick, 1.3 mm wide) sinks the brass stage to the cantilever die. The copper heat sinks are connected using tin-lead solder. Prior force gradient experiments without the copper heat sinking did not show signal under identical conditions, indicating that the sample and probe were likely too warm.

In addition, all experiments were performed at high vacuum. To ensure high-vacuum conditions throughout the experiments, the vacuum pump continually pumped on the probe, and vibrations from the pump were damped using a home-made sandbox. Turning off the pump allowed atmospheric gas to enter the probe through a small leak, which subsequently decreased the quality factor during the experiment.

As mentioned previously, the cantilever displacement was measured using a fiber-optic interferometer with a wavelength of 1310 nm. It should be noted that laser driving (Section 3.6) affected the cantilever Q and amplitude during the experiment, but did not cause a change in the positive feedback frequency, nor did it change the results from either experiment. The laser power was decreased until the Q on each side of the interferometer fringe was nearly the same. Additionally,

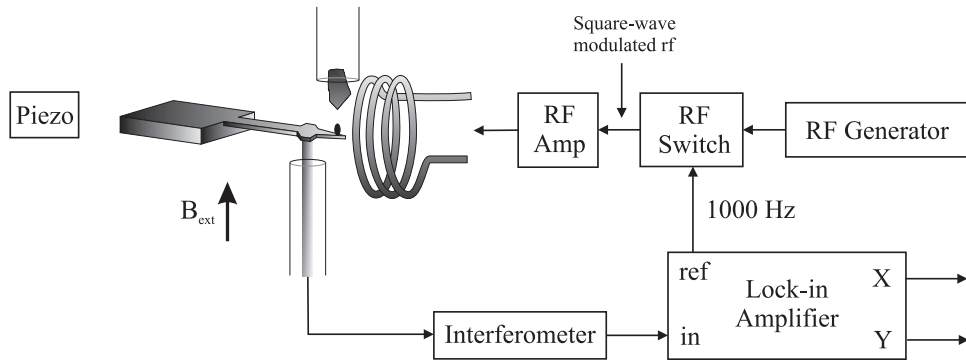


Figure 4.8: Block diagram of the cyclic saturation ESR experiment, where the electron spins in the sample are detected as a force.

the force and force gradient experiments were performed on each interferometer fringe and the results were identical. The quality factor quoted in Table 4.1 is the convergence point from the positive and negative feedback fringes.

The electron spins in the DPPH sample were first detected as a force using the off-resonance cyclic saturation method (Section 4.2.1). On-resonance modulation of the force resulted in cantilever displacements that were larger than 100 nm, the peak-to-peak interferometer limit. To prevent driving the cantilever over an interferometer fringe, the force was modulated at 1 kHz, and the cantilever amplitude is not magnified by a factor of Q as would be the case in an on-resonance experiment. Note that even though the measurement is being made off-resonance and Q has no effect on the amplitude, a higher Q is preferred since it results in a lower thermal noise floor (Eq. 2.51). Brownian motion, the source of thermal noise, is larger than the detector noise when on-resonance, making the experiment thermally limited. In an off-resonance experiment, the Brownian motion noise is smaller than the detector noise, and the dominant source of noise becomes the interferometer.

The frequency of the rf is fixed at around 350 MHz and amplitude modulated at 1000 Hz as the external field was swept through resonance. The B_1 from the

coil saturated the magnetization in the slice. When the rf was off, the spins quickly realign along the external field. If the sample T_1 is short compared with the cantilever period, as is the case with DPPH, the recovery is assumed to be instantaneous, resulting in an oscillating force that is closely approximated as a square wave. The oscillating sample magnetization interacts with the gradient from the nearby magnetic particle, resulting in a modulated force on the cantilever governed by Eq. 4.1. Due to the presence of the gradient, different sections of spins were in resonance at different external fields. Changing the eternal field moved the sensitive slice through the sample, essentially plotting the one-dimensional spin density.

The deflection of the cantilever due to this interaction was converted to a force using Hooke's Law ($F = -kx$). A lock-in amplifier was used to detect the rms deflection of the cantilever at the first Fourier component of the square wave

$$F(t) = \frac{F_0}{2} + \frac{F_0}{2} \frac{4}{\pi} \sin(2\pi f_{\text{mod}} t) + \dots \quad (4.34)$$

It is necessary to convert the rms force (F_{rms}) to the zero-to-peak value using

$$F_0 = 2\sqrt{2} \frac{\pi}{4} F_{\text{rms}} = 2.2 F_{\text{rms}} \quad (4.35)$$

The resulting peak is typically Gaussian, with a width that depends on the thicknesses of the sample and sensitive slice.

The DPPH spins were also detected as a force gradient. In this experiment, the cantilever was driven with the piezoelectric stack to a large oscillation (typically 100 nm or a full fringe) via positive feedback, and the cantilever resonance frequency was measured with the commercial frequency counter as discussed in Section 4.3.3. The rf from the coil was turned on, unmodulated, while the cantilever was being driven. This caused an immediate decrease in the resonance frequency

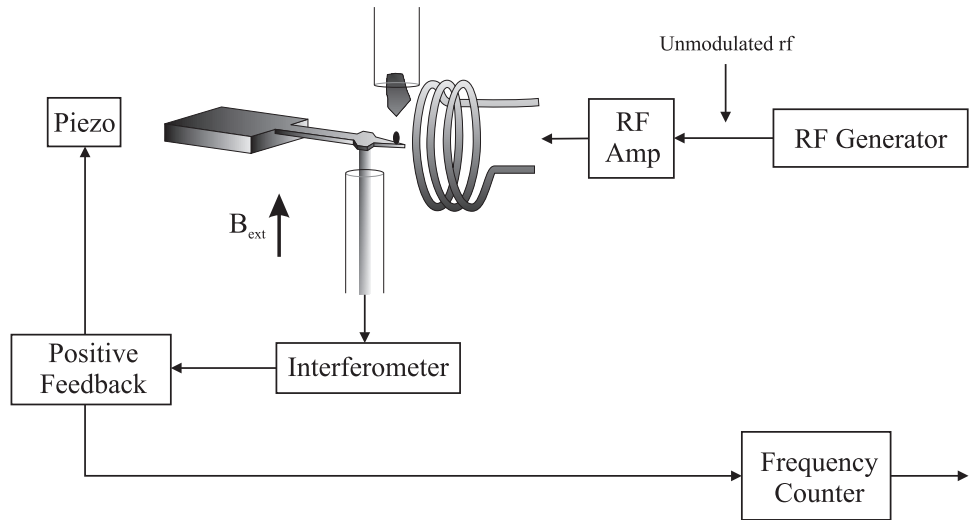


Figure 4.9: Block diagram of the force gradient ESR experiment, where the electron spins in the sample are detected as a change in the resonance frequency of the cantilever.

due to heating of the cantilever. After the drift in f_0 stabilizes, the resonant slice was swept through the sample as in the force experiment. The frequency of the cantilever changed via a force gradient effect as the sensitive slice saturated spins in the sample. This change in spring constant is, at least partially, governed by the derivative of the force as seen in Eq 4.28. The systematic frequency drift was subtracted out of the signal using a fitting protocol in Matlab and was converted to a spring constant change by

$$\Delta k = 2k \frac{\Delta f}{f_0} \quad (4.36)$$

where k is the spring constant of the cantilever. Each data point acquisition took approximately 10 s, and a full length scan was about 15 minutes in length.

Surprisingly, we find that the shape of the force gradient signal varies with the magnitude of the gradient produced by the magnetic particle. A -6 T saturation field gave a lower magnitude tip field and lower gradient than a $+6$ T saturation

field. When saturating the particle at -6 T (referred to hereafter as the low gradient case), the force gradient signal was approximately the derivative of the force signal. This signal shows two narrow peaks 350 G apart. The first peak in the force signal is taller than the second, implying that the tip field (B_{tip}), and thus the gradient, are being changed by the external field (B_{ext}).

If the saturation field is reversed to $+6\text{ T}$ (referred to as the high gradient case), one wide peak was seen in the force and force gradient experiments. The force gradient signal in the high gradient regime was quite different from the previous result. Here the spring constant shift has an absorptive component, in contrast with the purely dispersive signal seen in the low gradient case². Results of force and force gradient experiments in the low and high gradient cases will be described in Section 4.5 and analyzed in detail in Section 4.6.

4.5 Results

4.5.1 The low gradient case

In the low gradient case, the magnetic particle was saturated with a field of approximately -6 T . Results from force and force gradient experiments are shown in Figure 4.10 for an rf power of 125 mW . The two peaks shown are for the two possible resonance conditions of the sample. Sample spins are in resonance when the vector sum of the tip field and the external field is

$$B_{\text{res}} = \frac{\omega_{\text{rf}}}{\gamma_e} = \frac{348\text{ MHz}}{2.8\text{ MHz/G}} = \pm 124\text{ G} \quad (4.37)$$

²This chapter refers to high and low gradients in terms relative to this experiment. The high gradient in these experiments is $\sim 300\text{ T/m}$, which is orders of magnitude below the gradients used in much of Rugar's OSCAR work and our CERMIT experiment ($\sim 10^5\text{ T/m}$) [31, 33].

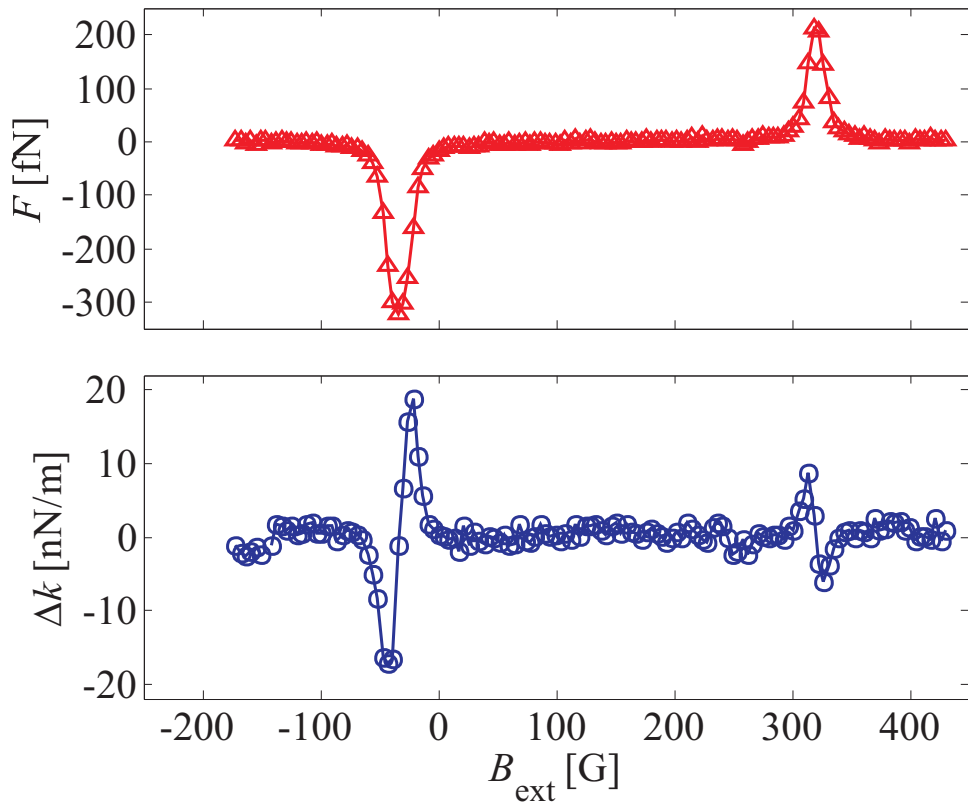


Figure 4.10: Force (top) and force gradient (bottom) results for the low gradient case. The force signal is based on the in-phase channel from the lock-in and includes the corrective factors (Eq. 3.2) to convert from the lock-in value to the peak-to-peak force. The first peak occurs at -33 G and the second peak is at 320 G. The rf power in each of these experiments was 125 mW.

Table 4.3: Results of the low gradient force and force gradient experiments.

The value of B_{tip} is an average of the tip field from the two peaks and was used to calculate the gradient and second gradient.

Tip Field (B_{tip})	$-100 \text{ G} = -0.01 \text{ T}$
Gradient (G or ∇B)	$0.50 \text{ G}/\mu\text{m} = 50 \text{ T/m}$
Second Gradient ($\nabla^2 B$)	$-3.4 \times 10^5 \text{ T/m}^2$
Sensitive Slice Thickness (Δz)	$10 \mu\text{m}$
Data, Peak 1:	
F_{max}	-320 fN
Δk_{max}	19 nN/m
Peak Width (F)	20 G
Peak Center (F)	-33.7 G
Data, Peak 2:	
F_{max}	+210 fN
Δk_{max}	9 nN/m
Peak Width (F)	16 G
Peak Center (F)	320 G
Noise:	
$F_{\text{min}} @ 20 \text{ K}$	$70 \text{ aN}/\text{Hz}^{1/2}$
$\Delta k_{\text{min}} @ x_{\text{rms}} = 130 \text{ nm}$	$0.55 \text{ nN}/\text{mHz}^{1/2}$
Observed Force Noise	4000 aN
Observed Δk Noise	4 nN/m

The tip field, B_{tip} was small enough in this case to see two peaks. The value of B_{tip} will be calculated and used with the particle dimensions and tip-sample distance to calculate the saturation field (B_s), the gradient (∇B), and the second gradient ($\nabla^2 B$) in Section 4.6.1. As expected, the force signal is Gaussian, and the two force peaks have opposite sign due to the sign of the magnetic moment in the slice in the different resonance conditions.

The force gradient signal appears to be the derivative of the force signal. Prior to scanning the external magnetic field, the rf was allowed to bake the cantilever until the frequency drift became linear, which took about 30 minutes at powers less than 500mW. RF powers above 500mW caused large frequency drifts that typically did not settle even after two hours of exposure to rf. This amount of heating also led to unpredictable cantilever behavior, ranging from quality factor degradation to odd interactions with the interferometer. Use of the Matlab program to remove the drift and isolate the frequency shift also proved difficult at higher powers.

4.5.2 The high gradient case

The high gradient experiments were performed after resaturating the magnetic particle at a field of +6 T, which surprisingly changed not only the sign of the particle B_s , but also resulted in a considerably higher magnitude tip field, gradient, and second gradient. The difference in the behavior of the magnetic particle in different saturation fields is likely related to the shape of the particle and an improper saturation procedure. Normally, when saturating a magnet, the hysteresis loop should be repeated several times to erase the previous magnetic memory. This was not done in this case, and it appears that neglecting this procedure opened the door to an extremely intriguing result.

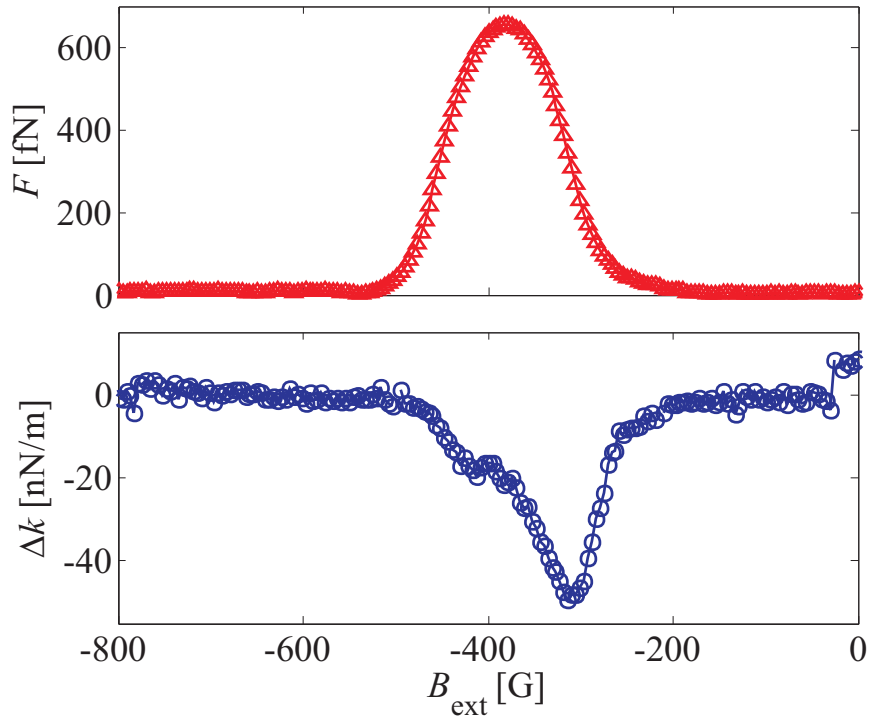


Figure 4.11: Force (top) and force gradient (bottom) results for the high gradient case. The force signal is based on the magnitude (R) from the lock-in and includes the corrective factors to convert from the lock-in value to the peak-to-peak force. The rf power in each of these experiments was 500 mW.

Results from the force and force gradient experiments in the high gradient case can be seen in Figure 4.11. Each experiment was performed at an rf power of 500 mW and only one peak is observed, as opposed to the two peaks seen in the Figure 4.10. In this case, B_{tip} is so large that only one of the two possible resonance conditions can be met, resulting in a single peak. Also, the width of the peak is considerably larger in this case, indicating a larger gradient, and thus a thinner resonant slice than in the low gradient case. A thin slice leads to a wider peak because more field steps are required to move the slice through the particle.

The force gradient signal in the high gradient case is starkly different than the signal in the low gradient case. The zero-to-peak spring constant shift (approximately 50 nN/m) is more than twice as large as the peak shift in the low gradient case, despite evidence that both signals are nearly saturated. The sign of the frequency shift stays constant throughout the scan, which is what we would expect if the spring constant shift was dominated by the CERMIT term. However, the high gradient Δk also appears to have a dispersive contribution. The minimum of the high gradient spring constant shift occurs at approximately the halfway point of the force signal, which is similar to the derivative characteristics from the OSCAR term. It appears that the high gradient signal is either a combination of the two terms in Eq. 4.28 or the result of some new, unexpected physics which may be attributed to a combination of spin diffusion and dynamic nuclear polarization.

Experiments with rf powers above 500mW were attempted in the force gradient experiment but these experienced similar problems to those seen in the low gradient case. The frequency drift did not settle after two hours or more, and the cantilever behavior changed drastically, presumably due to heating. After trying 2 W of rf power, helium gas was introduced into the probe to cool the lever.

Table 4.4: Results of the high gradient force and force gradient experiments.

Tip Field (B_{tip})	$500 \text{ G} = 0.05 \text{ T}$
Gradient (G or ∇B)	$-2.80 \text{ G}/\mu\text{m} = -280 \text{ T/m}$
Second Gradient ($\nabla^2 B$)	$2.0 \times 10^6 \text{ T/m}^2$
Sensitive Slice Thickness (Δz)	$2 \mu\text{m}$
Data:	
F_{max}	690 fN
Δk_{max}	-50 nN/m
Peak Width (F)	110 G
Peak Center (F)	-381 G
Noise:	
$F_{\text{min}} @ 20 \text{ K}$	$70 \text{ aN/Hz}^{1/2}$
$\Delta k_{\text{min}} @ x_{\text{rms}} = 130 \text{ nm}$	$0.55 \text{ nN/mHz}^{1/2}$
Observed Force Noise	4 000 aN
Observed Δk Noise	4 nN/m

4.6 Discussion

In this section, the results of the low and high gradient cases will be described. The force signals will be discussed first, and the observed signal will be compared to the expected values. The force results will place a maximum value on the possible spin-lattice relaxation time, T_1 . Next, the saturation behavior of the force and force gradient signals at increasing rf powers will be described and different saturation behaviors are observed in the different experiments. Finally, the force gradient experiments will be discussed in terms of the derivative of the force, which will motivate methods to simulate the spring constant shift based on the observed signals. The force signal will be used to predict the spring constant shift in the force gradient experiment with no free parameters.

4.6.1 The low gradient force signal

The first thing to notice is that the peaks in the low gradient force and force gradient experiments are not 248 G apart (Fig. 4.10), as would be expected based on the resonance condition set by the rf frequency and the gyromagnetic ratio of the electron. The peaks are actually closer to 350 G apart. We can say with some certainty that this discrepancy is not related to the sample. This identical piece of DPPH was used in previous cyclic saturation ESR experiments at 77 K with Alnico as the magnetic particle and the external field provided by the resistive hand-coiled magnet. These force detected experiments resulted in two ESR peaks approximately 250 G apart, as expected. The error in the peak separation must be the result of an error in the coil constant in the inhomogeneous magnetic field outside of the superconducting coil or from some extraneous magnetic fields. This

will be discussed further in Appendix A.

It is also obvious that the peaks are not the same size as would be expected in the presence of a constant gradient, suggesting that the gradient is changing during the external field scan. This is most likely due to an incomplete saturation of the particle magnetization, which leads to a low tip field and gradient that can be influenced by the external field during scanning. As the external field is scanned and made more positive, the second resonance condition experiences a smaller gradient and a smaller force. This phenomenon will be explored further in Section 4.6.4.

For now, we can estimate a tip field for the magnetic particle based on the first peak in Fig. 4.10. Since the magnetic particle was saturated in a -6T field, the B_{tip} should be negative, resulting in a positive gradient. The tip field is approximately -100 G based on the first peak:

$$B_{\text{res}} = -124\text{ G} = B_{\text{tip}} + B_{\text{ext}} \quad (4.38)$$

where $B_{\text{ext}} = -24\text{ G}$. The particle radius and the tip-sample distance estimates are used to determine the gradient and the second gradient using Eqs. 4.29-4.31. We find a rough estimate for the gradient of 50 T/m , using a magnet radius of $300\text{ }\mu\text{m}$ and a tip-sample distance of $250\text{ }\mu\text{m}$, both measured by eye using the optical microscope. The gradient for each peak will be calculated based on a simulation in Section 4.6.4.

This gradient can be checked independently using the full width at half max (FWHM) of the signal (in tesla)

$$\text{FWHM} = (\nabla B)(\text{Sample Thickness}) \quad (4.39)$$

If the gradient is 50 T/m and we use the low estimate for the sample thickness of

40 μm , we calculate a peak width of 20 G, which is in good agreement with the observed value for both peaks (see Table 4.3).

The thickness of the sensitive slice is related to the gradient (∇B) by

$$\Delta z = \frac{\Gamma}{\nabla B} \quad (4.40)$$

where Γ is the rf field strength³ (generally $B_1 \sim 5$ G) or the intrinsic linewidth of the sample, whichever is larger; for DPPH, we typically use B_1 . If the slice is thicker in space than the sample, the FWHM of the force peak will be narrow in field because fewer field steps will be required to move the slice through the sample. When the slice is thinner in space than the sample, the FWHM of the force peak will be wider in field. Recall also that if the B_1 is larger than the intrinsic sample linewidth, the peak will be wider due to power broadening, which is discussed in Section 4.2.1.

In the low gradient case, the sensitive slice thickness is

$$\Delta z = \frac{B_1}{\nabla B} = \frac{5.0 \text{ G}}{0.50 \text{ G}/\mu\text{m}} = 10 \mu\text{m} \quad (4.41)$$

Note that this is on the order of the sample thickness. Multiple factors could make this term larger or smaller, including incorrect estimates of the particle radius, tip-sample distance, and tip field. Also, the particle is not very spherical, so the values of the tip field, gradient, and second gradient based on Eq. 4.29-4.31 are approximate. Furthermore, the actual sample thickness is difficult to measure accurately by eye, thus the estimate of $40 \pm 10 \mu\text{m}$. For these reasons, we consider the comparison of the sample thickness to Δz to be only within an order of magnitude.

³The B_1 of the coil depends on the power, where B_1 is the product of the coil constant, determined by power broadening data [74] to be approximately $6 \text{ G}/\sqrt{\text{W}}$, and the square root of the output rf power. The value used here is an approximation which holds for most of our rf powers within a factor of two.

To estimate the size of the force, recall that the force is the product of the sample magnetization and the gradient from the magnetic particle (Eq. 4.1). If the sensitive slice is thinner than the sample, we can write a scaling law that shows that the force is independent of the gradient.

$$\begin{aligned}
 F &= \mu_z \nabla B \\
 &= \rho_m V \nabla B \\
 &= \rho_m (A \Delta z) \nabla B \\
 &= \rho_m \left(A \frac{\Gamma}{\nabla B} \right) \nabla B \\
 &= \rho_m \Gamma A
 \end{aligned} \tag{4.42}$$

where ρ_m is the spin magnetization density, V is the volume of the slice, and A is the area of the slice. If the slice thickness increases to approximately the sample thickness, this scaling law will begin to break down. Additionally, at the ends of the sample, the volume of the slice will not be equivalent to the volume of the spins and the scaling law would overestimate the number of spins in resonance. The scaling law is most applicable in the center of the sample and fails completely if the slice is thicker than the sample.

Let us first assume that the scaling law holds in the force experiment shown in Figure 4.10. The cross-sectional area of the DPPH particle is measured by eye using an optical microscope to be $20 \times 20 \mu\text{m}^2$. If the temperature in the probe is assumed to be 20K based on incomplete heat sinking of the cantilever and heating from the rf radiation, then the spin magnetization density of DPPH will be

$$\rho_m = \frac{\rho_{\text{DPPH}} \mu_e^2 B_{\text{res}}}{k_B T} = 9 \text{ N m}^{-2} \text{T}^{-1} \tag{4.43}$$

resulting in an expected force of 1800 fN. This is nearly a factor of six larger than the observed force for the first peak, and a factor of nine larger than the second

peak. Error can be attributed to an accurate measure of the cantilever and sample temperature and to the estimate of the area. It should also be noted that the spins in the slice are not completely saturated at this low rf power of 125 mW, as will be discussed in Section 4.6.3, accounting for a smaller than expected observed force. Finally, the slice thickness is approaching the sample thickness (Eq. 4.41) and we can expect that the theoretical force based on the scaling law would begin to deviate from the observed force. Each of these contributions will make the observed force smaller than 1800 fN, and we can conclude that the signal is in good agreement with our expectations.

4.6.2 The high gradient force signal

The tip field in the high gradient force signal (Figure 4.11) can be determined based on the center of the peak. At this point, it is unclear whether the resonance at -381 G occurs at $+124\text{ G}$ or -124 G . Using $B_{\text{res}} = B_{\text{tip}} + B_{\text{ext}}$ and each possible value of B_{res} , we determine that $B_{\text{tip}} = +505\text{ G}$ or $+257\text{ G}$. The sign for each of these possibilities is most likely correct since saturation occurred in a positive field.

The correct magnitude of B_{tip} can be ascertained from the peak width. Each value of B_{tip} can be used to calculate a gradient, which can in turn be used to obtain an expected peak width from the estimated sample thickness. The correct value of the tip field will be the one that gives the best agreement to the observed peak width. If the tip field is 505 G , then the gradient will be $2.80\text{ G}/\mu\text{m}$ (assuming values of particle radius and tip sample distance from table 4.4). Assuming that the sample is $40\text{ }\mu\text{m}$ thick, the peak width will be

$$(2.80\text{ G}/\mu\text{m})(40\text{ }\mu\text{m}) = 112\text{ G} \quad (4.44)$$

in very good agreement with the actual peak width of 110 G. Using the second possibility of $B_{\text{tip}} = +257$ G, we obtain a gradient of $1.40 \text{ G}/\mu\text{m}$. This gradient predicts a FWHM of 56 G if the sample is $40 \mu\text{m}$ thick, smaller than the observed value by a factor of two. Therefore, the correct B_{tip} should be $+505$ G and the gradient in this case is 280 T/m . Using this value, the saturation field B_s is determined using B_{tip} and Eq. 4.29. The gradient and second gradient are calculated using Eqs. 4.30 and 4.31, and the dimension r and d from the table. These parameters are located in Table 4.4.

Equation 4.40 can be used to calculate a sensitive slice thickness of $2 \mu\text{m}$, which is now much less than the estimated sample thickness. Consequently, the expected force based on the scaling law (Eq. 4.42) should be a better indicator of the observed force than in the low gradient experiment. Recall that $\rho_m = 9 \text{ Nm}^{-2}\text{T}^{-1}$ at 20 K from Eq. 4.43, resulting in a peak force of 1800 fN . This is now only 2.6 times larger than the observed peak force of 690 fN , a better agreement than the low gradient case. The small error between the observed and predicted signals can easily be attributed to a sample temperature higher than 20 K due to rf heating, a smaller than estimated sample area, and incomplete saturation of the sample spins by the rf.

Since the scaling law is a better indicator of the actual force in the high gradient case, let us estimate the sample temperature by setting the expected force equal to the force from the scaling law. Using our estimate of the particle area and Eq. 4.42, the spin magnetization density at 690 fN would be $\rho_m = 3.45 \text{ Nm}^{-2}\text{T}^{-1}$. This corresponds to a reasonable sample temperature of 51 K which is certainly possible considering that the rf is heating the sample during the experiment. Furthermore, if the temperature is actually 20 K, the area would only have to be $150 \mu\text{m}^2$, or

$\sim 12 \times 12 \mu\text{m}^2$ to match the predicted force value. Most likely, there is some combination of errors in the temperature and area estimates that can reasonably account for the difference in the theoretical and observed forces. Based on these calculations, we are justified for estimating the temperature of the experiment as 20 K.

The good agreement between the observed force and the scaling law in the high gradient case places a maximum value on the spin-lattice relaxation time T_1 of the DPPH spins in this experiment. Recall from the discussion of the cyclic saturation experiment (Section 4.2.1) that the spins are randomized when the rf is turned on and the magnetization approaches zero. When the rf is turned off, the spins relax back along the external field in a time T_1 and regain their polarization and magnetization. Our scaling law assumes that the spins completely repolarize faster than the period of the rf modulation ($1/f_m$). If the T_1 was on the order of $1/f_m$, then the spins would not completely remagnetize before being saturated again, and the observed force would be much smaller than the force from the scaling law. Thus, an upper bound of 1 ms can be assigned to the sample T_1 . In fact, the sample T_1 is likely orders of magnitude less than 1 ms so the force can be approximated as a square wave.

4.6.3 Saturation of the force and force gradient signals

The force and force gradient experiments were performed at several rf powers in order to study the saturation behavior of the signals. As the rf power is increased, more spins are saturated in a particular slice, providing a larger force signal. When the rf power is large enough that the spins become saturated, increasing the rf power broadens the signal, but the peak force should remain constant. The spin

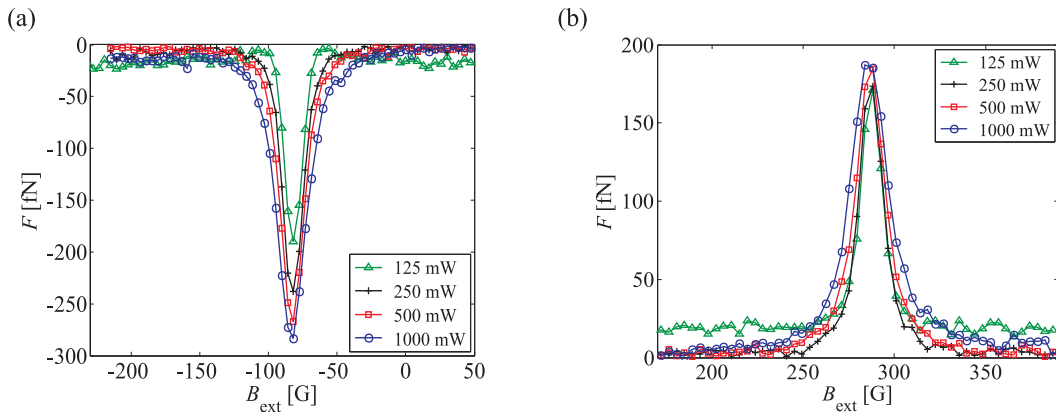


Figure 4.12: Power broadening in the first peak (a) and the second peak (b) of the low gradient cyclic saturation force experiment. RF powers range from 125 mW to 1 W. The data present here was taken during a separate liquid helium run than the force experiment in Fig 4.10.

magnetization density ρ_m does not increase with rf power past the saturation point, and the force is governed by Eq. 4.42, as long as the sensitive slice thickness is much less than the sample thickness. It was found that, in general, the force gradient experiments saturate at lower rf powers than the corresponding force experiments.

Saturation in the Low Gradient Case

In the low gradient case, force experiments were performed at rf powers from 125 – 1000 mW during a liquid helium run on a different date than the data shown in Figure 4.10. The magnetic particle was remagnetized at -6T for this experiment and the resulting B_s was changed. This accounts for the observed differences in peak force and Δk , as well as a slight shift of the peaks in field when compared with the data from Figure 4.10. The power broadening of the force gradient signal in the low gradient regime were not examined due to difficulty in removing the frequency drift from the data for rf powers larger than 125 mW.

Figure 4.12(a) shows the broadening for the force data in the negative external field (ie, Peak 1) and Figure 4.12(b) shows the broadening for the force data in the positive external field (ie, Peak 2). As expected, increasing the rf power results in an increased saturation and a higher force in both peaks. Since the difference in the force signal between the two highest rf powers is small, we are close to the saturation limit at an rf power of 1 W. The force scaling law discussed in Section 4.6.1 assumed full saturation of the signal. The force signals discussed in Figure 4.10 were taken at 125 mW and thus not fully saturated. Since the force scaling law assumes full saturation of the spins in the slice, we note that the expected force should be about 1.5 times smaller than that calculated, improving the agreement between the observed force and the scaling law.

It was mentioned earlier that the difference in the size of the force in Peaks 1 and 2 was most likely due to the gradient decreasing as the external field is made more positive. However, inspection of the force scaling law in Eq. 4.42 shows that the force should be independent of the gradient. At first glance, these two things are contradictory: a changing gradient should not result in a changing force if the sensitive slice thickness ($\sim 10 \mu\text{m}$) is less than the sample thickness (40 μm). Since these values are within an order of magnitude, we believe that the force scaling law is beginning to break down as it approaches the limit of its applicability. It was previously noted that the breaking down of the scaling law in the low gradient case is partly responsible for the smaller than expected peak force at each individual peak. We now point out that it is also explains the difference in the size of the peak force from Peak 1 to Peak 2, where the gradient at Peak 1 is larger than the gradient at Peak 2. The actual decrease in the gradient will be calculated in Section 4.6.4.

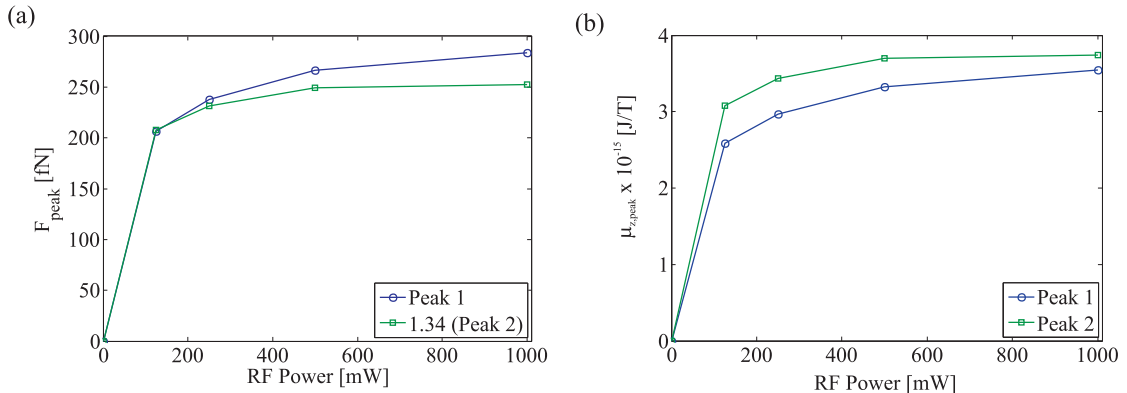


Figure 4.13: Force (a) and magnetic moment saturation (b) curves for the low gradient case. Peak 1 (circles) corresponds to the absolute value of the peak forces and magnetic moment in the slice from Fig 4.12(a). Peak 2 (squares) corresponds to the data from Fig 4.12(b). In (a), Peak 2 is scaled by a factor of 1.34 to compare the saturation behavior of the two curves.

Does this changing gradient, and thus sensitive slice thickness, affect the relative saturation behavior of the two peaks? Since the gradient at Peak 2 is smaller, the sensitive slice will be larger and more spins will be present in the slice. It is thus conceivable that the saturation behavior between the two peaks will be different. In order to test this, the peak force is graphed versus the rf power in Figure 4.13(a) for both peaks. It is necessary to scale Peak 2 by a factor of 1.34 to allow comparison of to the data in Peak 1. The scaled data for Peak 2 shows that the two peaks are saturating differently. The curve for Peak 2 has a substantially different slope than Peak 1, and appears to saturate earlier than Peak 1.

To determine whether or not the difference in the saturation is related to a difference in the gradient between the two peaks, we divide the peak force by the gradient at each peak to isolate the peak value of μ_z , which is the total magnetic moment in the slice in the center of the sample and is proportional to the number

of spins in the slice. We expect that the peak μ_z should be larger in the Peak 2 data since the sensitive slice will be larger. This is confirmed in Figure 4.13(b), where the gradient at Peak 1 is assumed to be 80 T/m and the gradient at Peak 2 is assumed to be 50 T/m (these gradient values will be validated in Section 4.6.4). Therefore, since the gradient and the number of spins in the sensitive slice at each peak are different, we expect that the saturation profiles will be different.

Saturation in the High Gradient Case

The force and force gradient experiments in the high gradient regime were performed at powers ranging from 4 mW to 2 W. It was not feasible to perform experiments at rf powers higher than 2 W due to the spurious effects associated with increased heating of the cantilever. The saturation behavior of the force signal can be seen in Figure 4.14(a), and the peak force is graphed versus the power in Figure 4.14(b), which shows that the force signal is nearly saturated at 2 W of rf power. As in the low gradient case, the force experiment in the high gradient case (Figure 4.11) was performed at 500 mW. Comparison of the observed force at 500 mW and the nearly saturated force at 2 W shows that the expected force should be about a factor of 1.25 smaller than calculated, improving the agreement between the observed and expected forces.

The effects of increasing power were also measured in the force gradient experiment in the high gradient regime, seen in Figure 4.15(a). As the rf power is increased, the features of the high gradient Δk signal, notably the peak shift and the knee in the signal at the field where the maximum force occurs, begin to appear as more and more spins become saturated in the slice. The peak frequency shift⁴

⁴The peak frequency shift is chosen to compare the saturation for convenience. Both μ_z and $\partial\mu_z/\partial z$ scale together with rf power, and any point on the curve can

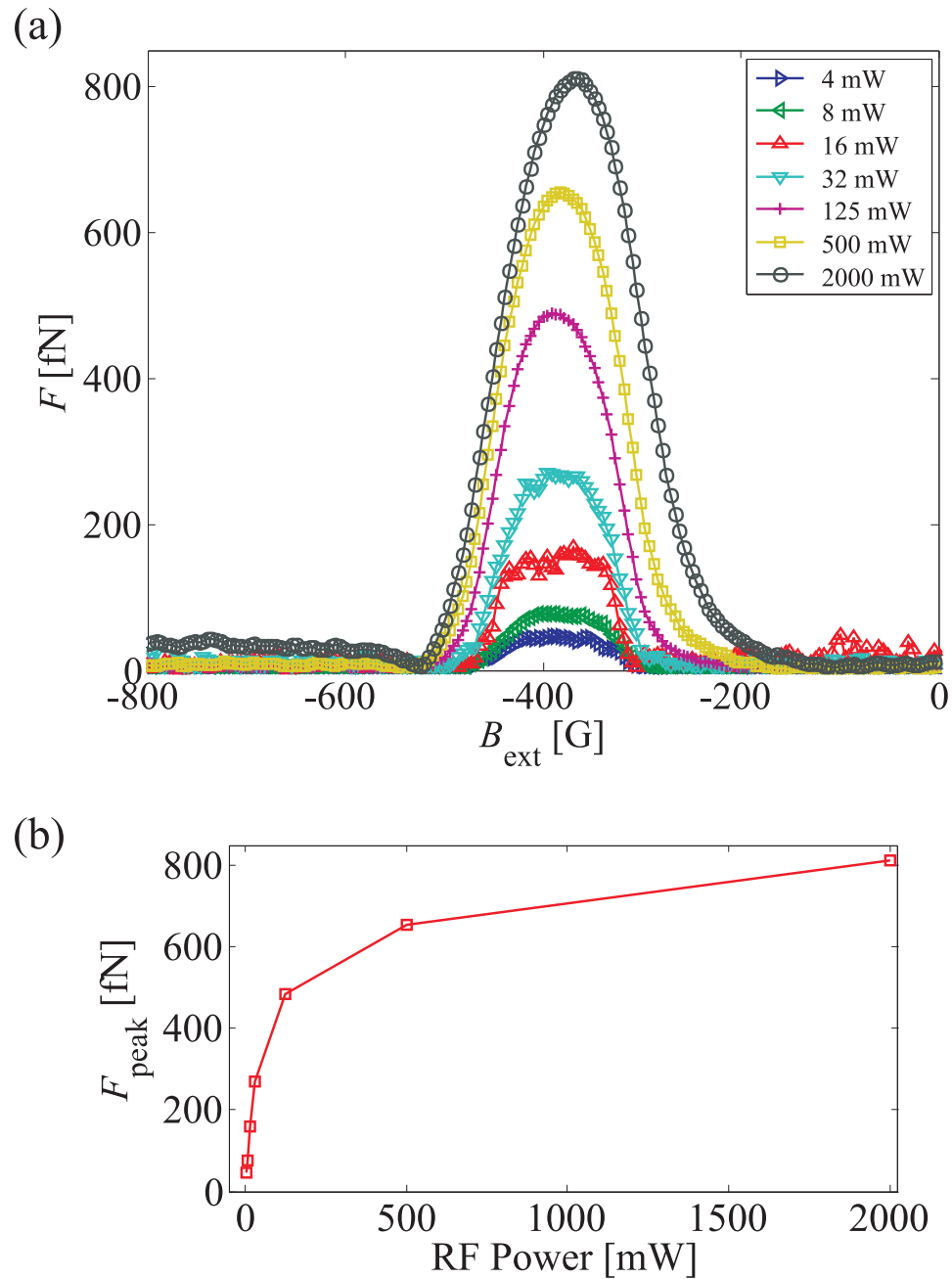


Figure 4.14: (a) Power broadening in the high gradient cyclic saturation force experiment. RF powers range from 4 mW to 2 W. (b) Peak force versus rf power in the high gradient cyclic saturation force experiment from Fig 4.14. The signal is nearly saturated at 2 W.

is plotted versus rf power in Figure 4.15(b). Force gradient signals at rf powers above 500 mW could not be separated from the overlying cantilever drift and are not included in this analysis.

Interestingly, the force gradient signal appears to saturate at much lower powers than the force signal, between 125 – 500 mW. This effect could be explained by considering the average power at the sample during each experiment rather than the peak power. In the force experiment, the rf is modulated and spends half of the experiment on and half of it off – a duty cycle of 50%. The average power from the coil is a factor of two smaller than the peak output power. In the force gradient experiment, the rf is unmodulated, and the average power from the coil is equal to the output power. Therefore, it is conceivable that the sample in the unmodulated experiment would be heated more than the sample in the force experiment.

These effects can be observed by comparing the integral of the force (i.e., the total area under the force signal) in a modulated force experiment to the integral of the force gradient versus the average rf power. The integral of the signal is a measure of the total number of spins that are saturated in the sample. To do this, we calculate the area under the force signal and the force gradient signal at a particular output power. The areas are then plotted versus the output powers used in the experiments in the top graph of Figure 4.16, where $\int F$ has been scaled by a factor of $\alpha = 1.25 \times 10^5$ to make comparison of the two signals possible. This shows poor agreement for output powers above 100 mW, indicating that the amount of saturation is different in the two experiments at equivalent powers. When we account for the average power experienced by the cantilever and sample in the experiment, the curves for the two experiments, seen in the bottom graph of

 be chosen as long as the point appears at the same external field.

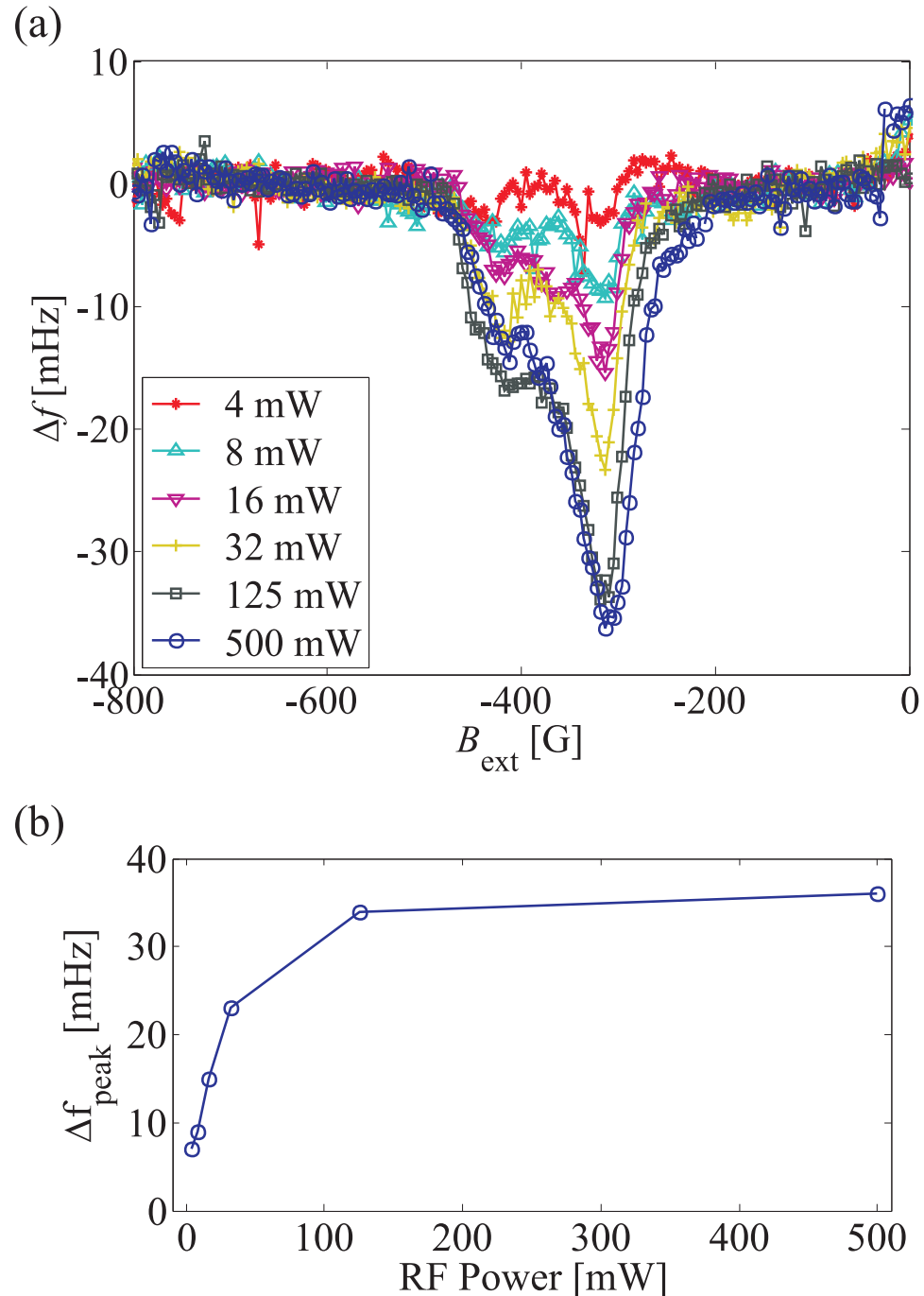


Figure 4.15: (a) Power broadening in the high gradient force gradient experiment. RF powers range from 4 mW to 500 mW. Note that the y -axis on this figure is frequency shift in mHz, not spring constant shift. (b) Peak frequency shift versus rf power in the high gradient force gradient experiment. The signal is saturated between 125 mW and 500 mW, well before the saturation in the force experiment.

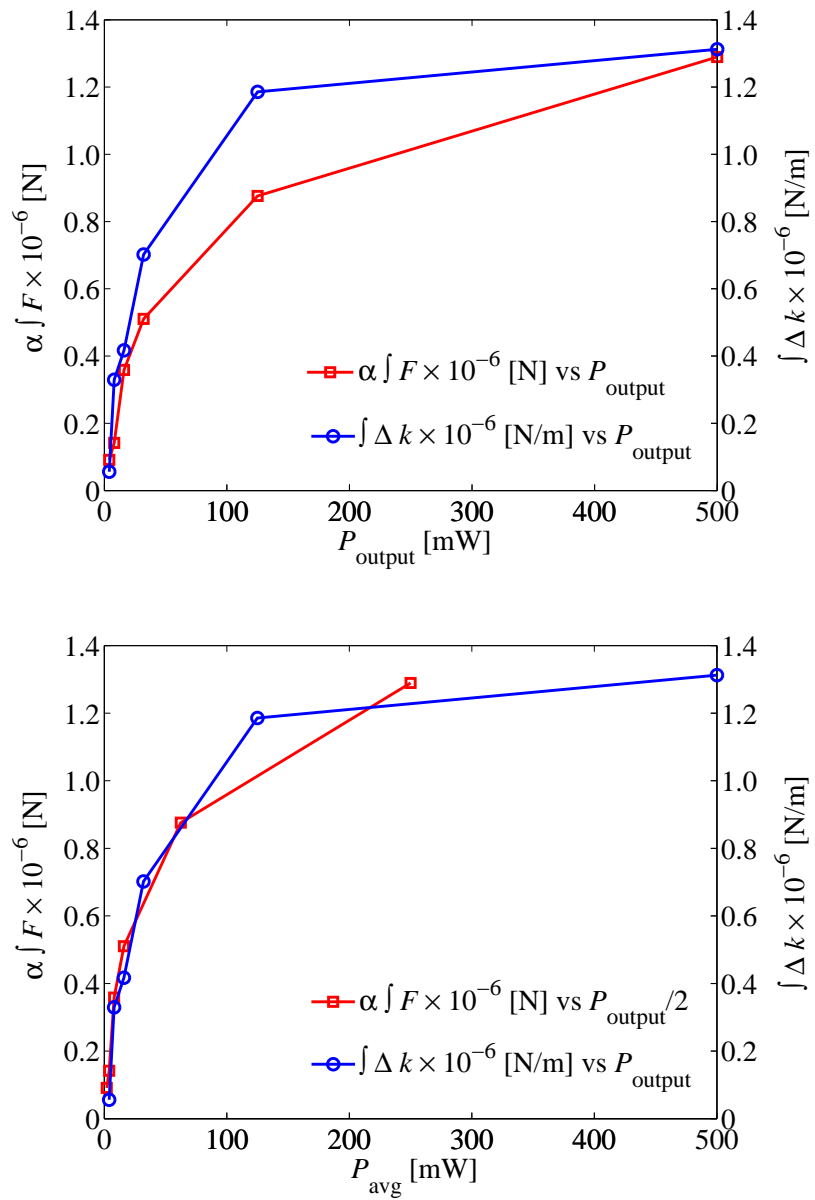


Figure 4.16: Comparison of the saturation behavior with respect to output and average power. The area under the force signal ($\int F$, squares) and the area under the force gradient signal ($\int \Delta k$, circles) are graphed versus the output power (top) and the average power (bottom) for each curve. $\int F$ has been scaled by a factor of $\alpha = 1.25 \times 10^5$ to make comparison of the two signals possible.

Figure 4.16, are very similar, especially at low average power. This indicates that the saturation behavior is indeed linked to the average power experienced by the sample, not the total output power.

Based on this comparison, we expect that the unmodulated rf in the force gradient experiment would heat the sample more than the modulated rf in the force experiment. The difference in the saturation behavior between the force and force gradient profiles may actually be due to a temperature difference, and not some other physical effect. The Curie Law predicts the spin polarization and the spin magnetization density (Eq. 4.43) in the sample. At the higher temperatures experienced in the force gradient experiment, the spin magnetization density, ρ_m , would be smaller than the ρ_m in the force experiment. This difference causes saturation to occur at lower powers in the force gradient experiment than in the force experiment, as observed.

4.6.4 The low gradient Δk signal: simulations

We now turn our attention to the force gradient signal from Figure 4.10. Originally, the spring constant shift in this experiment was expected to have a form identical to the CERMIT experiment, in which a force gradient arises by an interaction between the sample magnetization and the second gradient of the magnetic particle

$$\Delta k = \mu_z \frac{\partial^2 B_z}{\partial z^2} \quad (4.45)$$

In this case, the signal would have the same general shape as the force since both the gradient and the second gradient are essentially constant over the sample thickness. However, Figure 4.10 shows that this is not the case. The force gradient signal appears to be the derivative of the force signal. The answer to this puzzle

lies in the complete derivative of the force.

If we use the chain rule and write out the full force derivative, the spring constant shift becomes

$$\Delta k = \frac{\partial F}{\partial z} = \mu_z \frac{\partial^2 B_z}{\partial z^2} + \frac{\partial \mu_z}{\partial z} \frac{\partial B_z}{\partial z} \quad (4.46)$$

The second term is the derivative of the magnetic moment in the slice with respect to the movement of the sensitive slice, multiplied by the gradient. This term is nonzero only when the rf is on and the magnetization in the slice is changing with the cantilever position. This term is dropped in CERMIT because the rf is off during the signal acquisition phase and the slice is fixed with respect to the lever. It was originally assumed that this term would be small in the force gradient ESR experiment, but in fact, it is the dominant term in the low gradient case, and should be the dominant term in most cases.

In this section, the force signal will be used to simulate the force gradient signal using Eq 4.46. The simulated signal will be compared to the observed force gradient data at the same power. In the low gradient case, we find that Eq. 4.46 adequately describes the observed peaks. In addition, the simulations in this section will be used to determine the gradient at each peak, and we will validate these gradients using several different calculations.

We have established that the gradient must be changing during the external field scan based on results from the force data. In order to simulate the spring constant shift, we will assume that the gradient is constant over the sample for each resonance condition, but that the gradient at the first peak is different from the gradient at the second peak. The peak heights and widths show that the gradient at the second peak will be smaller than the gradient at the first peak. We can determine approximate values for these gradients using the simulations, and these

gradients can be used to calculate the tip field and the second gradient at each peak.

We must first isolate the magnetic moment in the sensitive slice, μ_z , from the force data. Recall that the force in this experiment is the product of the magnetic moment and the gradient produced by the magnetic particle. If we assume that the gradient is constant over the width of the sample, the force data can be divided by the gradient to determine μ_z at each point. Initially, we guess a gradient value, and a second gradient is calculated based on this guess. The first term in Eq. 4.46 (the CERMIT term) is determined by multiplying the μ_z obtained from the assumed gradient and the force by the calculated second gradient. The second term (known as the OSCAR term) is slightly more difficult to simulate.

The first step in calculating the OSCAR term is to take the numerical derivative of μ_z in Matlab by calculating the difference between each successive μ_z point and dividing that difference by the difference in field between the two points. This gives us $\partial\mu_z/\partial B_{\text{ext}}$, not $\partial\mu_z/\partial z$. We can use the chain rule to convert the result of the numerical derivative to the proper derivative in the OSCAR term

$$\frac{\partial\mu_z}{\partial z} = \frac{\partial\mu_z}{\partial B_{\text{ext}}} \frac{\partial B_z}{\partial z} \quad (4.47)$$

Eq. 4.47 is substituted into the OSCAR term to give

$$\frac{\partial\mu_z}{\partial z} \frac{\partial B_z}{\partial z} = \frac{\partial\mu_z}{\partial B_{\text{ext}}} \left(\frac{\partial B_z}{\partial z} \right)^2 \quad (4.48)$$

The force gradient becomes

$$\Delta k = \mu_z \frac{\partial^2 B_z}{\partial z^2} + \frac{\partial\mu_z}{\partial B_{\text{ext}}} \left(\frac{\partial B_z}{\partial z} \right)^2 \quad (4.49)$$

This equation allows us to estimate the spring constant shift from μ_z and $\partial\mu_z/\partial B_{\text{ext}}$. The magnetic moment μ_z is obtained by dividing the force by an assumed gradient, and $\partial\mu_z/\partial B_{\text{ext}}$ is determined by numerically differentiating the derived μ_z .

It will be shown that the OSCAR term dominates the spring constant shift, and the gradient is the only parameter needed to simulate the spring constant. The CERMIT term will always be significantly smaller than the OSCAR term due to the values of the second gradient allowed by the tip-sample spacing.

Figure 4.17(a) shows a comparison of the simulated force gradient from the force experiment at 125 mW to the force gradient data at 125 mW. The assumed gradient used in this comparison is 50 T/m, the gradient calculated in Table 4.3. The second gradient, calculated based on the assumed gradient, is $-3.4 \times 10^5 \text{ T/m}^2$. We see that the simulation (line) agrees relatively well with the experiment (circles) for the second peak. Based on this, the gradient at the second peak must be approximately 50 T/m. Note that the simulated spring constant shift is calculated from the force signal using essentially no free parameters. Also, it is important to pay close attention to the sign of the gradient and second gradient in order to correctly determine the shape of the signal.

Comparing the magnitudes of the OSCAR and CERMIT terms in this particular simulation reveals that the first term in Eq. 4.49 is very small and only adds about 1 – 2 nN/m to the total spring constant change. In fact, the contribution from the second gradient is constant and independent of the gradient, resulting in a spring constant shift that is dominated by the OSCAR term, especially at gradients larger than about 10 T/m. The gradient can be written in terms of the second gradient as

$$\nabla B = \nabla^2 B \frac{r + d}{4} \quad (4.50)$$

The simulated spring constant (Eq. 4.49) can be rewritten in terms of ∇B , using Eq. 4.50 as

$$\Delta k = \mu_z \nabla B \frac{4}{r + d} + \frac{\partial \mu_z}{\partial B_{\text{ext}}} (\nabla B)^2 \quad (4.51)$$

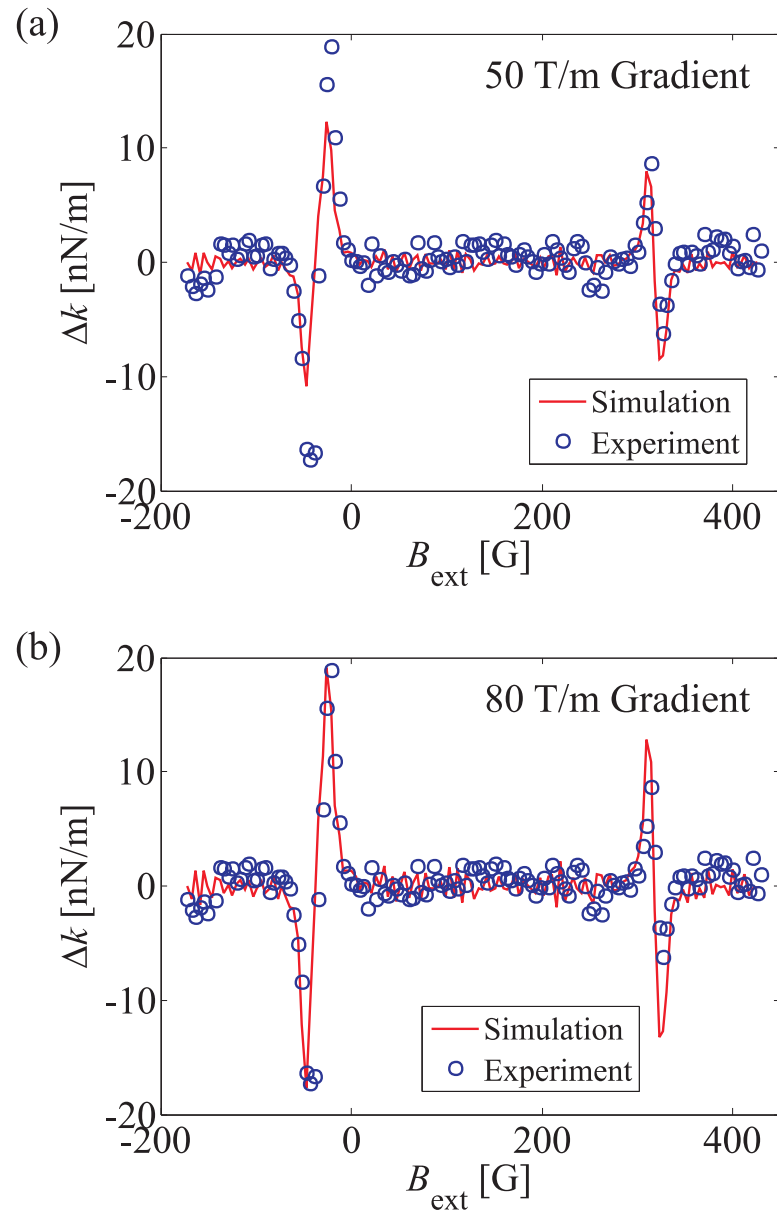


Figure 4.17: Comparison of the simulated spring constant shift based on the force (line) with the experimental Δk signal (circles) in Figure 4.10. The gradient and second gradient were chosen based on the values in Table 4.3. (a) The fit with $\nabla B = 50 \text{ T/m}$, which fits the second peak. (b) The fit with $\nabla B = 80 \text{ T/m}$, which fits to the first peak.

Table 4.5: Magnetic particle parameters inferred from comparing simulations to the data in Figures 4.17. The parameters listed below were used in the simulation that best corresponded to the experimental data for the listed peak.

Parameter	Peak 1	Peak 2
B_s	-0.14 T	-0.092 T
B_{tip}	-0.015 T	-0.010 T
∇B	80 T/m	50 T/m
Δz	6 μm	10 μm

Recall that in the simulation, $\mu_z = F/\nabla B$ and the gradient is assumed to be constant. We can now put Eq. 4.51 in terms of force, which results in

$$\Delta k = F \frac{4}{r+d} + \frac{\partial F}{\partial B_{\text{ext}}} \nabla B \quad (4.52)$$

The first term in Eq. 4.52 is small compared to the second term, and it is independent of the gradient and second gradient. This means that the simulation of the force gradient signal only needs the gradient as a free parameter. The second gradient can subsequently be calculated from the gradient that provides the best fit. For the purposes of this low gradient case, the second term in the total force derivative is responsible for the majority of the change in the spring constant, and the spring constant shift is

$$\Delta k \approx \frac{\partial \mu_z}{\partial z} \frac{\partial B_z}{\partial z} = \frac{\partial \mu_z}{\partial B_{\text{ext}}} \left(\frac{\partial B_z}{\partial z} \right)^2 \quad (4.53)$$

Now that we have approximated the gradient at the second peak, we can determine the gradient at the first peak using the same method. We guess a new

gradient value that is larger than 50 T/m and use the force data to simulate the spring constant shift. Through several attempts, it was found that a gradient of 80 T/m resulted in a good agreement to the first peak as seen in Fig. 4.17(b). The second gradient, which is calculated from the assumed gradient, is $-6 \times 10^5 \text{ T/m}^2$. These values correspond to a saturation field of $B_s = -0.14 \text{ T}$ and a $B_{\text{tip}} = -150 \text{ G}$, assuming a particle diameter of $300 \mu\text{m}$ and a tip-sample distance of $250 \mu\text{m}$. As expected, the gradient decreases during the external field scan.

The gradients from these simulations, along with the estimation of the sample thickness, can be used to predict the width of the peaks. The observed peak widths are located in Table 4.3. If the sample thickness is assumed to be $40 \mu\text{m}$, we calculate peak widths for the first and second peaks of 32 G and 20 G , respectively, using Eq 4.39, in good agreement with the observed values of 20 G and 16 G . If the sample is instead assumed to be $30 \mu\text{m}$ thick (a very reasonable assumption since the sample thickness is determined using an optical microscope), the gradient values will predict the peak widths exactly.

Can the observed decrease in the magnitude of the gradient be explained in terms of the magnetic particle saturation? A typical magnetic hysteresis curve is depicted in Figure 4.18. In the low gradient case, the particle was saturated with a negative field, so we assume that the particle has a negative value of B_s at the beginning of the field sweep (point (a) in Figure 4.18). The field sweep in this experiment was from negative to positive, through zero field. If we follow the hysteresis curve far enough in the positive field, the magnitude of the particle magnetization will begin to decrease in magnitude (point (b) in Figure 4.18), which would decrease the gradient. This is the behavior we observe in the experiment. The shape of our particle affects the demagnetization factor, which in turn distorts

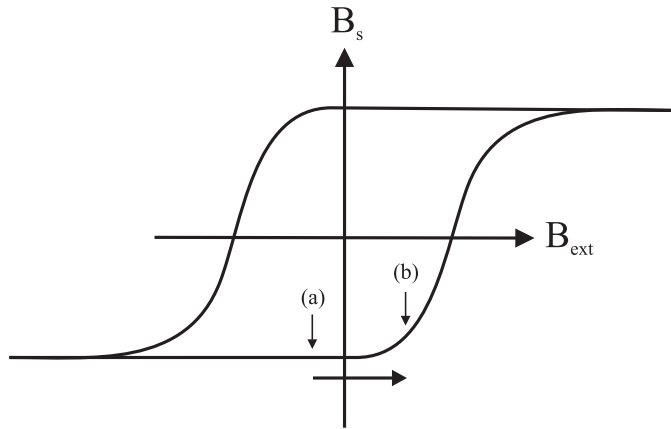


Figure 4.18: Typical hysteresis curve for the magnetic particle. The sweep in the low gradient case is from a negative external field to a positive external field and is represented by the arrow above. Points (a) and (b) represent the saturation of the particle (B_s) with respect to the external field.

the observed hysteresis loop. Changing the shape of the particle will affect the residual field of the magnet at zero applied field and change the field necessary to saturate the particle, but the ultimate saturation of the particle and the coercive field do not change with shape. It is possible that the field required to achieve complete saturation of the particle was not reached in this experiment due to the shape of the magnet.

In summary, comparisons of the observed force gradient signal with simulations based on the force data confirm that the force gradient is governed by Eq. 4.28 in the low gradient case. The simulations have been used to determine the gradient at each peak and the changing gradient agrees with the possible magnet hysteresis. Now that we have good agreement between our experiment and the mathematics, can the data be understood in terms of the sensitive slice as it moves through the sample?

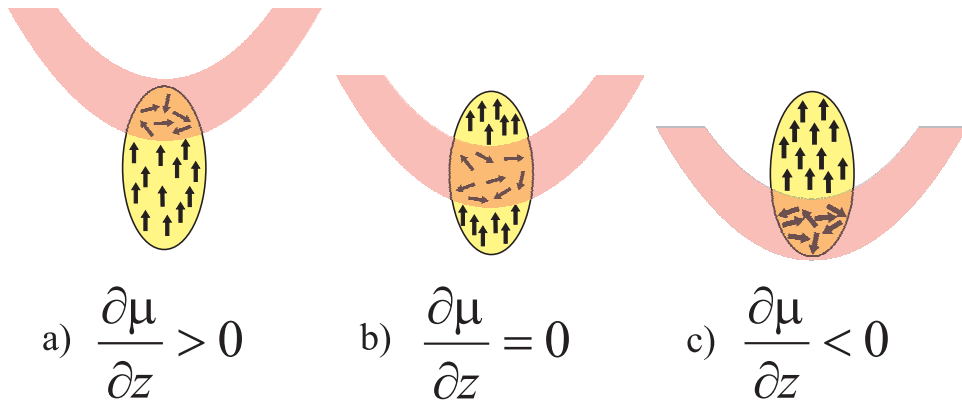


Figure 4.19: Pictorial representation of the sensitive slice as it moves through the DPPH sample, along with the sign of the $\partial\mu_z/\partial z$ for each case. The three cases are a) a slice entering the sample, b) a slice fully inside of the sample, and c) a slice exiting the sample.

4.6.5 The low gradient Δk signal: physical picture

Comparison of the force and spring constant shift signals in Figure 4.10 indicate that the spring constant change is the derivative of the force signal. In this section, we show that the motion of the sensitive slice through the sample, along with Eq. 4.53, completely explains the shape and the negative and positive signs of the derivative signal in Figure 4.10.

Based on the calculation of the sensitive slice in Eq. 4.41, the slice thickness is on the order of the sample thickness (the sensitive slice thickness is between $6 - 10 \mu\text{m}$, and the sample thickness is approximately $40 \mu\text{m}$). When the slice is in the sample and the rf is on, electrons in the slice will become saturated, decreasing their magnetization. How does $\partial\mu_z/\partial z$ change when the slice is moving through the sample?

Recall that this term is the change in μ_z with the movement of the sensitive slice. When the slice is entering the sample, $\partial\mu_z/\partial z$ is positive as more spins are

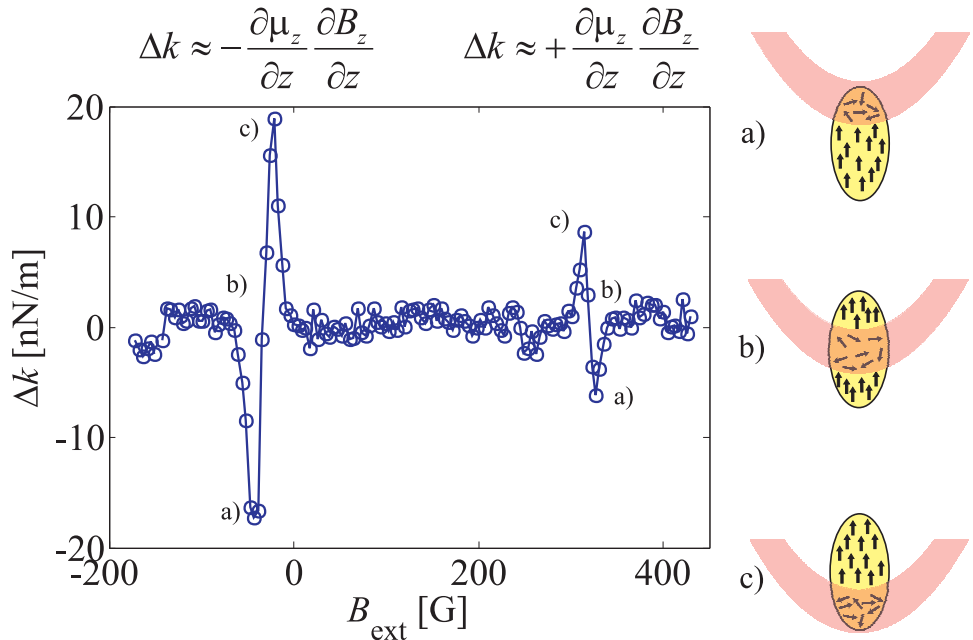


Figure 4.20: Direction of movement for the sensitive slice compared to the sign of the force gradient.

becoming saturated by the slice as it enters the sample. When the slice is fully inside the sample, μ_z does not change as the slice moves because the same number of spins are being affected in each slice, and $\partial\mu_z/\partial z = 0$. As the slice begins to leave the sample fewer spins are randomized as the slice moves and $\partial\mu_z/\partial z$ will be negative. These three cases are depicted in Figure 4.19.

Now that we understand the sign of $\partial\mu_z/\partial z$ in Eq. 4.53, we need to determine the sign of μ_z at each peak to explain the shape of the force gradient. The sign of μ_z determines the resonance condition (+124 G or -124 G) and the sign of the force at each peak. The magnetic particle is magnetized at -6 T and the resulting tip field is assumed to be negative. The vector sum of the negative tip field and the negative external field at the first peak will result in a negative B_{res} , which must correspond to a negative μ_z . Since the gradient is positive when the tip field

is negative in our sample geometry, the first peak is the result of a negative force. The sum of the external field and the tip field at the second peak must be positive, resulting in a positive B_{res} , a positive μ_z , and a positive force. We use the signs of μ_z and $\partial\mu_z/\partial z$ to justify the force gradient signal in Figure 4.20.

Based on the sign of the tip field (negative) and the scanning direction (from negative external field to a positive external field), we determine that the slice starts close to the magnetic particle at the beginning of the scan. As the magnetic field is scanned towards the positive field, the slice enters the sample, represented by the first peak with $-\mu_z$. The sign of the spring constant shift for the first peak is determined using Eq. 4.53 where

$$\Delta k = \frac{\partial(-\mu_z)}{\partial z} \frac{\partial B_z}{\partial z} = -\frac{\partial\mu_z}{\partial z} \frac{\partial B_z}{\partial z} \quad (4.54)$$

Since $\partial\mu_z/\partial z$ and the gradient are positive, we predict a decrease in the spring constant as the slice enters the sample for this resonance condition. In the middle of the sample, $\partial\mu_z/\partial z = 0$, and $\Delta k = 0$. As the slice leaves the sample, $\partial\mu_z/\partial z$ is negative, the gradient remains positive, and Δk increases. This agrees with the observed data.

We also see the correct behavior for the second peak for the second peak with $+\mu_z$. The sign of Δk for the second peak is determined using

$$\Delta k = \frac{\partial(+\mu_z)}{\partial z} \frac{\partial B_z}{\partial z} = +\frac{\partial\mu_z}{\partial z} \frac{\partial B_z}{\partial z} \quad (4.55)$$

As the slice enters the sample, Δk is positive, zero in the middle of the sample, and negative as the magnetization in the slice decreases. Therefore, our intuition and physical pictures of the slice inside the sample agrees with the experimental data.

4.6.6 The high gradient Δk signal: simulations

In order to investigate the character of the force gradient signal in the high gradient case, calculations similar to those discussed in Section 4.6.4 will be used to simulate the force gradient signal from the force signal. Signals will be compared at the same powers and at different powers to determine if the rf duty cycle affects the signal. Finally, the contribution to the frequency shift from the OSCAR term will be subtracted from the observed frequency shift for several powers using the simulations to investigate the spring constant shift that is related solely to the CERMIT term. The absorptive nature of the high gradient signal is unexpected, and not fully explainable with the model developed for the low gradient signal.

We begin by returning to the derivative of the force (Eq. 4.46), which was shown in Section 4.6.4 to be independent of the second gradient. The conclusion, based on Eq. 4.52, was that as the gradient increased, the derivative nature of the OSCAR term dominated the small, constant contribution from the CERMIT term when both terms are present. This is also the case in the high gradient regime. The force signal in Figure 4.11 at 500 mW is divided by a constant gradient (-300 T/m , approximated from the tip field in Section 4.6.2) to isolate the magnetization in the slice (μ_z). The force gradient signal is calculated using these derived variables and Eq. 4.52 and compared to the force gradient signal at 500 mW. The result is a derivative lineshape, just as in the low gradient case. The OSCAR term in the force gradient equation dominates, and the force gradient signal is the derivative of the force signal. Thus, equation 4.46 alone does not describe the observed high gradient behavior.

It has been previously noted that the force gradient signal in Figure 4.11 has some absorptive character, which could be due to an unexpected increase in the

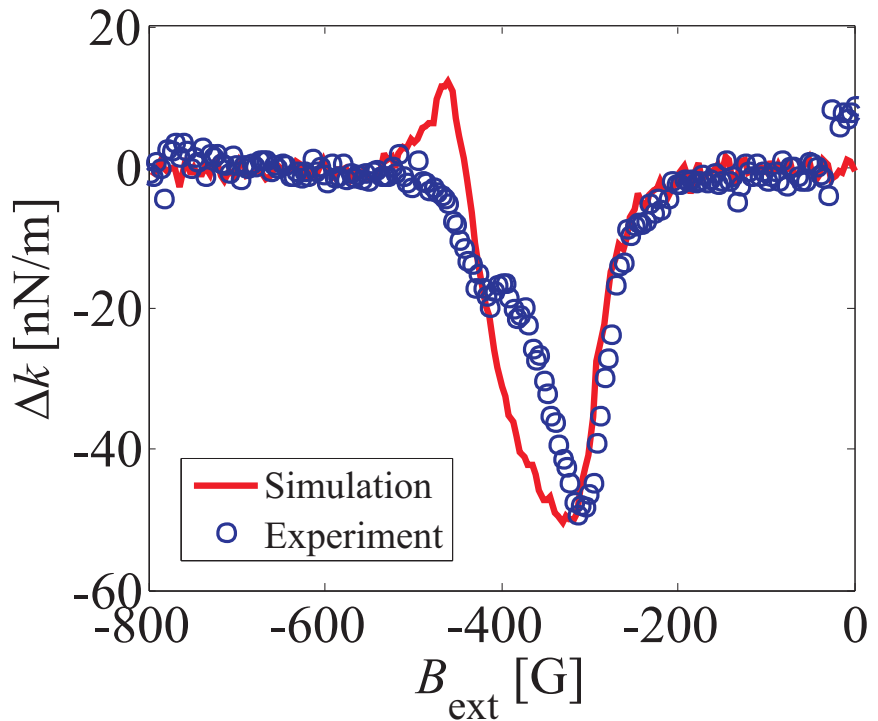


Figure 4.21: Comparison of the simulated spring constant shift (line) based on the force and the experimental Δk signal (circles). The gradient ($\nabla B = -300$ T/m) and the second gradient ($\nabla^2 B = 2 \times 10^6$ T/m²) are assumed to be constant over the sample thickness, and the first term in Eq. 4.46 is multiplied by a factor of 9 to achieve qualitative agreement with the experimental force gradient signal.

CERMIT term. We expect this term to have a Gaussian lineshape, just like the force, as long as the second gradient is constant over the sample thickness (which is a good assumption). Let us assume that more of the absorptive CERMIT character from the first term in Eq. 4.46 is being introduced in this case than expected by an unknown mechanism. This should have the effect of nulling the derivative character on one side of the signal while enhancing it on the other, making the overall signal more absorptive. If the force gradient signal is calculated with the first term multiplied by nine, ie

$$\Delta k = 9\mu_z \frac{\partial^2 B_z}{\partial z^2} + \frac{\partial \mu_z}{\partial z} \frac{\partial B_z}{\partial z} \quad (4.56)$$

we see qualitative agreement between the simulated and observed signals, depicted in Figure 4.21. The larger than expected CERMIT term cannot be a function of the second gradient since this term remains relatively constant throughout the scan. Thus, the magnetization μ_z in the sample would have to be nearly an order of magnitude larger than the value calculated from the thickness of the sensitive slice to achieve the qualitative agreement.

4.6.7 The anomalous CERMIT signal

We can say with certainty that we understand the nature of the force gradient when the gradient is low. In this regime, the OSCAR term explains the signal both qualitatively and quantitatively and we understand the small contribution from the CERMIT term. However, the high gradient signal cannot be explained so simply. In the following sections, we will assume that the shape of the high gradient signal is due to a large, anomalous spring constant shift that adds to and dominates the well-understood contribution from the force gradient in Eq. 4.28. We will use

the simulation protocol to determine the contribution to the signal from the force gradient in Eq. 4.52 and subtract it from the observed spring constant shift, thus isolating the large, oddly shaped signal that we do not understand. This part of the signal will be called the anomalous CERMIT signal due to its absorptive lineshape.

The total observed spring constant shift can be written as

$$\Delta k_{\text{obs}} = \Delta k_{\text{CERMIT}} + \Delta k_{\text{OSCAR}} \quad (4.57)$$

We will assume, based on the low gradient experiments, that the simulation accurately reflects the contribution of the OSCAR signal to the total signal in the high gradient case as well as the small contribution from the CERMIT term. This simulated signal can be subtracted from the observed signal to isolate the anomalous CERMIT contribution

$$\Delta k_{\text{CERMIT}} = \Delta k_{\text{obs}} - \Delta k_{\text{OSCAR, sim}} \quad (4.58)$$

Here, Δk_{CERMIT} will account for the anomalous spring constant shift in the experiment that is not well understood.

The anomalous spring constant shift for the force gradient signal at 500 mW is shown in Figure 4.22. In (a), we see the observed Δk and the simulated OSCAR contribution from the associated force signal. The difference in the two signals is seen in (b) and represents the anomalous spring constant shift that would need to be added to the known contribution from the force gradient to obtain the observed signal. Recall that the slice enters the sample at approximately -250 G, and moves through the sample as the external field is scanned to -800 G. Inspection of this figure shows that the contribution from Δk_{CERMIT} is roughly constant at approximately -20 nN/m in the first half of the sample, then suddenly increases

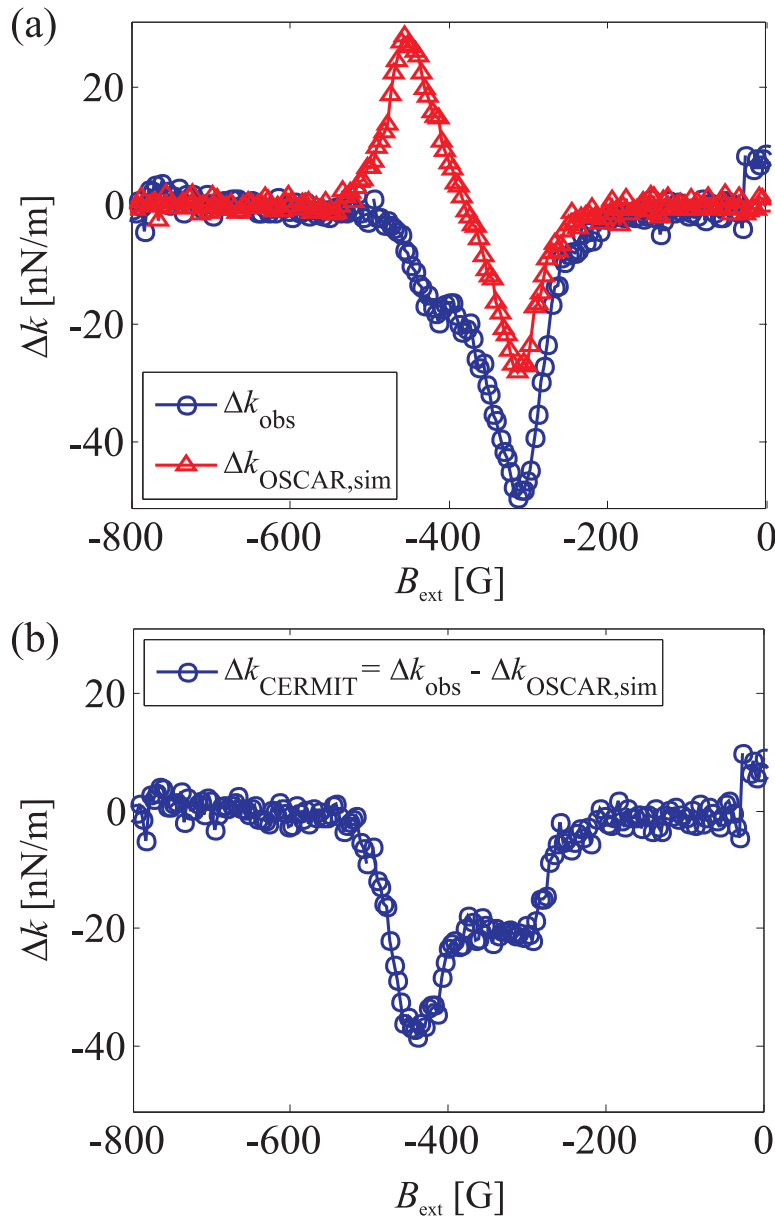


Figure 4.22: The contribution from the anomalous spring constant shift in the high gradient case at 500 mW. The observed spring constant shift and the simulated spring constant shift for the 500 mW case are shown in (a). The anomalous spring constant shift, resulting from the difference of the two signals above, is plotted in (b).

to a value that is nearly twice as large as the first shift.

If the signal in Figure 4.22(b) is described by the spring constant shift from a CERMIT effect, $\mu_z(\partial^2 B_z / \partial z^2)$, and the second gradient is considered constant over the sample thickness, the plot would be considered a one-dimensional image of the spin density in the sample. The anomalous CERMIT signal would imply that the bottom half of the sample is twice as large as the top half of the sample, which is highly unlikely. The particle appears to be an ellipsoid by inspection with an optical microscope and the force signal is Gaussian, as we would expect for an ellipsoidal sample. This suggests that the anomalous spring constant shift is governed by something more complex than the CERMIT spring constant shift from electrons. It should be noted that all but one of the scans was performed from 0 G to -800 G. The single scan in the opposite direction (from -800 G to 0 G) shows the same shape and behavior of all previous scans. This indicates that the shape of the anomalous CERMIT signal is not due to a build up of spin magnetization over the time of the scan. Thus, the larger portion of the spring constant shift is actually confined to the second half of the sample, which is attached to the cantilever.

The same general behavior is also seen at lower rf powers. Figure 4.23 plots the anomalous CERMIT signals for rf powers from 16 – 500 mW. The behavior of the low power runs (16 – 32 mW) show a general trend of an sudden, increasing spring constant shift in the center of the sample. As the power is increased to 125 – 500 mW, the signal appears to have two plateaus: a constant shift in the first half of the sample, and a sudden jump to a shift twice as large in the center.

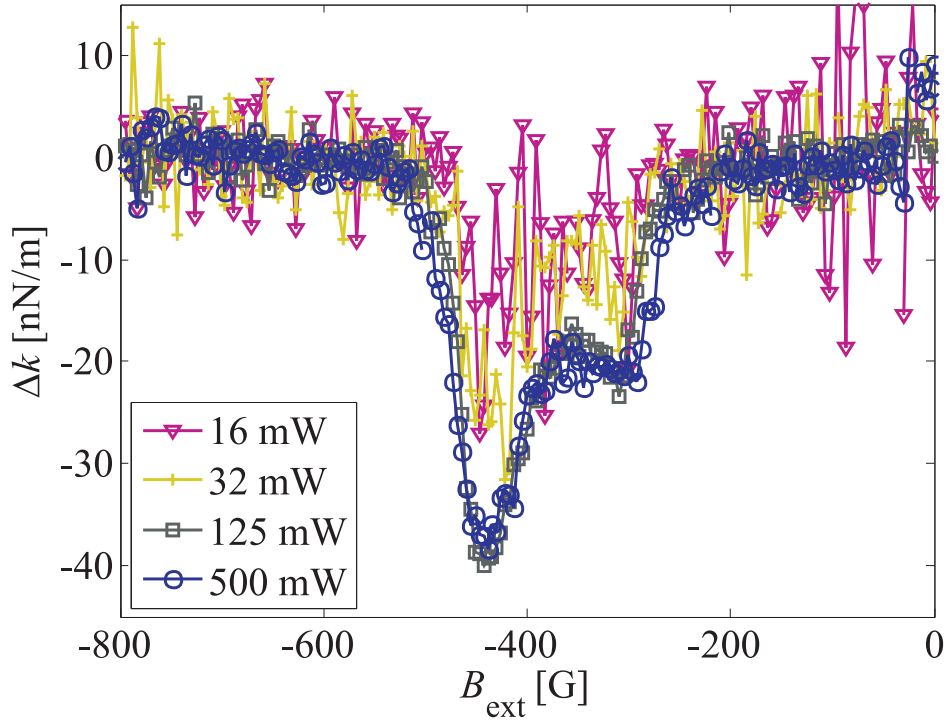


Figure 4.23: Anomalous Δk at several rf powers. The amount of noise in the lower power data sets is due to the lower signal-to-noise ratios in the force and force gradient signals at those powers. The anomalous Δk appears to be saturated at 125 mW.

4.6.8 Investigating the anomaly: The spin diffusion paradox

As shown in Figure 4.21, qualitative agreement between the observed and simulated signals is reached only if the CERMIT contribution is nine times larger than expected. One possible way to justify the larger than expected spring constant shift from the CERMIT term, which must come from an increase in μ_z and not the second gradient, is to assume that the sensitive slice has become thicker due to spin diffusion.

Spin diffusion is the entropic drive towards spatially uniform magnetization by transference of magnetization in the presence of a spin temperature gradient, which occurs via flip-flop interactions between fixed, neighboring spins [107, 108]. It was first used by Bloembergen to explain the faster-than-expected nuclear spin-lattice relaxation times in CaF_2 [109]. Electron spins at paramagnetic impurities in a sample cause nearby nuclear spins to have fast relaxation times. These fast relaxing nuclear spins transfer their magnetization to far away slower relaxing nuclear spins via spin flip-flops, lowering the average relaxation time of the nuclear spins in the sample. This interaction conserves magnetization, and there is typically no energy cost in going from one state to another. For example, if two spins are near each other in the configuration $\uparrow\downarrow$ and a spin flip-flop occurs, resulting in $\downarrow\uparrow$, the energy of the first state is equal to the energy of the second state if the magnetic field is the same at both spins. The effects of spin diffusion can be reversed, increasing the spin relaxation time of the system, using a sequence of strong rf fields [110]. Spin diffusion can also be used to determine the distances between nuclei and angular distribution functions [111–113]. Cory, *et al.* have measured the spin diffusion rate in a single-crystal CaF_2 sample directly with a pulsed gradient spin

echo method [114].

Budakian, *et al.* have shown suppression of spin diffusion in γ -irradiated silica in the presence of large gradients, resulting in longer spin-lattice relaxation times as the gradient is increased using MRFM techniques [115, 116]. In this experiment, the presence of the gradient from a magnetic particle changes the magnetic field across the sample, and the fast relaxing spin (from the previous example) is at a different field than the slow relaxing spin. This creates an energy cost associated with the spin flip-flop, even though the magnetization and angular momentum of the system are still conserved. If the difference in field, and thus energy, is large enough, no interaction between the spins will occur. The spin diffusion will be suppressed (the relaxation rate will decrease) and the T_1 of the sample will increase to a value closer to that of the slow relaxing spins. Increasing the gradient from 10 T/m to 36,000 T/m resulted in an increase of the spin T_1 from 6 s to 25 s.

Budakian states that the the relaxation rate T_1^{-1} will decrease if the field between the adjacent spins is larger than the homogeneous linewidth of the spins, which is the result of microscopic random magnetic fields from other spins [117]. We will now calculate the difference in the magnetic fields between adjacent electron spins to show that while spin diffusion is suppressed in Budakian's work, the gradient in our experiment is not large enough to suppress spin diffusion.

For spin diffusion to be suppressed, the following must be true

$$\delta z \nabla B > \Delta B_h \quad (4.59)$$

where $\delta z = \rho^{-1/3}/2$ is the average spacing between spins in the sample and ρ is the spin density [115]. The homogeneous linewidth is $\Delta B_h = 3.8\mu_0\gamma_e\hbar\rho/4\pi$, which has been converted from CGS units in Ref. [118] to SI units. In their experiment, $\rho = 2 \times 10^{24} \text{ m}^{-3}$, resulting in $\Delta B_h = 1.4 \times 10^{-5} \text{ T}$. This is compared to the

product of the gradient, $\nabla B = 36,000 \text{ T/m}$ and the average spacing between spins $\delta z = 4 \text{ nm}$, $\delta z \nabla B = 1.44 \times 10^{-4} \text{ T}$. This product is larger than ΔB_h , and the T_1 of the system increases due to suppression of spin diffusion.

In our case, the spins are more concentrated ($\rho = 2.3 \times 10^{27} \text{ m}^{-3}$) and the gradient is lower ($\nabla B = 300 \text{ T/m}$). The distance between spins is $\delta z = 0.38 \text{ nm}$, and $\delta z \nabla B = 1.1 \times 10^{-7} \text{ T}$. The homogenous linewidth is calculated to be $\Delta B_h = 0.016 \text{ T}$, and $\delta z \nabla B \ll \Delta B_h$. Therefore, the energy difference is low enough for spin flip-flops to occur and we expect that spin magnetization could diffuse outside of the slice, effectively increasing the size of μ_z . The physics operative in the Budakian experiment must be different than what we see in the high gradient Δk experiment, even though both experiments are taking place in the presence of a gradient. Now that we have established that spin diffusion could occur in our sample, we will explore the possibility that our anomalous force gradient is caused by an increased μ_z due to spin diffusion.

Spin diffusion could effectively increase the thickness of the sensitive slice and thereby increase the contribution of the CERMIT term to the total spring constant shift. Since the spins in the slice have a saturated magnetization close to zero, the initial 2 μm -thick slice may be acting as a magnetization sink. The spins adjacent to this slice would begin to saturate and lose their magnetization, which would continue to spread out and encompass a volume that is larger than the original volume, as long as the rf is on. This situation is depicted in Figure 4.24. To match the qualitative agreement in Section 4.6.6 where μ_z was assumed to be nine times larger than expected, the sensitive slice would need to increase from 2 μm thick to 18 μm . This would require a diffusion length of 9 μm on each side of the slice. Additionally, the diffusion outside of the slice must be faster than the time it takes

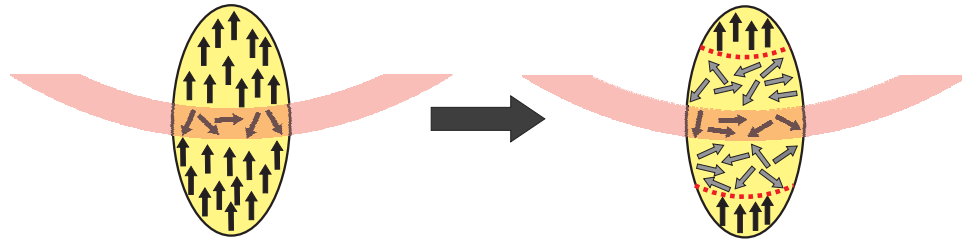


Figure 4.24: Spin diffusion outside of the sensitive slice. On the left is the slice inside the sample without spin diffusion, where only the spins inside the slice are saturated. If spin diffusion is invoked, the original slice will act as a magnetization sink and cause spins near the slice to randomize, making the volume of spins affected by the rf larger than expected.

for the slice to move through the sample, which takes roughly fifteen minutes for a typical scan. Note that spin diffusion would presumably not be operative in the low gradient case because the slice is much larger and covers a larger percentage of the sample, leaving fewer spins available to diffuse.

Is it possible for the electron spins to diffuse over the necessary sample volume? The distance L that spins can diffuse is determined using $L = \sqrt{DT_1}$, where D is the spin diffusion constant and T_1 is the spin-lattice relaxation time of the electrons. This expression is derived in Appendix B, assuming that the slice is infinitely thin and remains saturated during the experiment. The diffusion constant for a pure sample of DPPH has been estimated using [106]

$$D = \frac{\mu_0 \hbar \gamma_e^2 \rho^{1/3}}{4\pi} = 4.3 \times 10^{-10} \text{ m}^2/\text{s} \quad (4.60)$$

where $\rho = 2.3 \times 10^{27} \text{ m}^{-3}$ is the spin density of pure DPPH. If the spin-lattice relaxation time is $T_1 = 100 \text{ ns}$, which is close to the $50 - 80 \text{ ns}$ reported in the literature (Section 4.3.5), the diffusion length would be only 7 nm . This is one thousand times smaller than the necessary $9 \mu\text{m}$ diffusion length necessary to agree with the

simulation. Based on this particular diffusion constant, the T_1 of the sample spins would have to be 190 ms to achieve a diffusion length of 9 μm . Alternatively, if the sample T_1 was 100 ns, as assumed above, the diffusion constant D would have to be $8 \times 10^{-4} \text{ m}^2/\text{s}$ to give a diffusion length of 9 μm , nearly six orders of magnitude larger than that calculated in Eq. 4.60.

A DPPH T_1 longer than 1 ms cannot be correct based on the fact that the off-resonance force experiment results agree well with the the force scaling law, as stated in Section 4.6.2. The force experiments shown throughout this chapter were performed at a modulation frequency of 1 kHz, which places an upper bound on the T_1 of the electrons in DPPH of 1 ms. If the spins recovered from saturation slower than 1 ms, the spins would be resaturated by the modulated rf before fully recovering, and the resulting force signal would be smaller than calculated or observed. The fact that a force signal with a value close to the expected value from the scaling law is seen at 1 kHz requires a T_1 less than 1 ms. This leads to a paradox. Spin diffusion requires a long T_1 based on this value of D to justify our simulations of the force gradient signal in the high gradient case. However, we cannot have a long T_1 because the results of the modulated force experiment agrees with the scaling law.

In this section, we have shown that it is possible for our system to exhibit spin diffusion, based on the gradient and the distance between the spins in the sample. However, only those spins approximately 7 nm outside of the slice would be saturated and contribute to the spring constant shift based on a reasonable value of T_1 , a spin diffusion length orders of magnitude smaller than required.

4.6.9 Investigating the anomaly: Dynamic nuclear polarization

The larger-than-expected spring constant shift in the high gradient experiment cannot be fully explained by the diffusion of electron magnetization outside of the slice. Could it be due to *nuclear* spin diffusion? In the mechanism known as dynamic nuclear polarization (DNP), the electrons in a sample polarize nuclei to the level of the Boltzmann polarization of the electrons (assuming 100% DNP efficiency), which is much larger than the thermal nuclear polarization. The Boltzmann polarization for a spin system is defined as

$$\frac{N_{\uparrow} - N_{\downarrow}}{N_{\uparrow} + N_{\downarrow}} = e^{\mu B_{\text{res}} / k_B T} \quad (4.61)$$

In most magnetic resonance experiments, the temperature is high and the field is low and the resulting fraction $\mu B_{\text{res}} / k_B T$ is much less than one. Thus, the polarization factor can be approximated using a linear expansion to the form

$$\frac{N_{\uparrow} - N_{\downarrow}}{N_{\uparrow} + N_{\downarrow}} = P_B = \frac{\mu B_{\text{res}}}{k_B T} \quad (4.62)$$

This fraction is multiplied by the total number of spins under study to determine how many of them are polarized along the external field, where μ is the magnetic moment of the electrons or the protons, depending on the sample.

Using Eq. 4.62, we can calculate the polarization of the electron spins in our experiments. At a temperature of 20 K and $B_{\text{res}} = 0.012$ T, the polarization would be

$$P_{B,e} = 4 \times 10^{-4} \quad (4.63)$$

using the electron magnetic moment of $\mu_e = 9.28 \times 10^{-24}$ J/T. Typically, the polarization factor for electrons is 650 times larger than the nuclear polarization due to the difference in the magnetic moment of the electron and the proton.

DNP occurs through electron-nuclear cross relaxation when the electrons in a sample are irradiated by a continuous microwave field at the electron Larmor frequency, which is exactly the case in the force gradient experiment. DNP was proposed by Albert Overhauser [119, 120] and first verified experimentally by Carver and Slichter [121, 122]. DNP of protons has been previously observed in dilute DPPH samples [105]. If the resonant electrons in the force gradient ESR experiment increase the nuclear polarization of the protons in DPPH to the level of the electron polarization via DNP, the resulting nuclear spin magnetization could diffuse quite far outside of the slice and account for the anomalous spring constant shift. The calculated diffusion length in this case requires the diffusion constant D and T_1 of the nuclei, not the electrons, as before.

Let us assume that the anomalous spring constant shift in the high gradient case at 500 mW (Figure 4.22) is entirely a result of the protons, not the electrons, in the DPPH sample. We can calculate the polarization of the protons needed to cause this spring constant shift and compare it to the polarization of the electrons in the experiment. If the calculated polarizations are similar, then the nuclear spins could be polarized by DNP. In this assumption, the magnetic moment associated with the anomalous CERMIT signal, μ_{anom} would be

$$\mu_{\text{anom}} = \rho_p V_{\text{sample}} \mu_p P_{B,p} \quad (4.64)$$

where ρ_p is the spin density of the protons in the sample, μ_p is the proton magnetic moment, and $P_{B,p}$ is the Boltzmann polarization of the protons. DPPH has 12 hydrogens, so we assume that $\rho_p = 12\rho_e = 2.76 \times 10^{28} \text{ m}^{-3}$. For simplicity, we assume that the DPPH particle is shaped like a box with dimensions $25 \times 25 \times 40 \mu\text{m}^3$ and slightly overestimate V_{sample} . To determine μ_{anom} , we assume that the frequency shift is due to a CERMIT effect only and divide it by $\nabla^2 B =$

$$2 \times 10^6 \text{ T/m}^2.$$

We now assume that the maximum spring constant shift in Figure 4.22(b) occurs when the sensitive slice is approximately in the center of the sample. The electrons in the slice are saturated and polarize the DPPH nuclei in the slice. This nuclear magnetization then diffuses 20 μm above and below the slice, encompassing the full sample thickness. At the peak spring constant shift, $\Delta k = 40 \text{ nN/m}$ and $\mu_{\text{anom}} = 2 \times 10^{-14} \text{ J/m}$. In order for the μ_{anom} to be from all of the nuclei in the sample, the nuclear polarization, calculated using Eq. 4.64, would have to be

$$P_{B,p} = \frac{\mu_{\text{anom}}}{\rho_p V_{\text{sample}} \mu_p} = 2 \times 10^{-3} \quad (4.65)$$

where the volume is the total DPPH volume $V_{\text{sample}} = 2.5 \times 10^{-14} \text{ m}^3$. This is compared to the Boltzmann polarization for the electrons, calculated in Eq. 4.63 as 4×10^{-4} , smaller than the nuclear polarization by a factor of five. These polarizations are in good agreement when the uncertainties in the estimates of the sample volume and temperature are taken into account. Thus, the electron polarization and the nuclear polarization necessary to give rise to the observed spring constant shift are similar, a unique signature of dynamic nuclear polarization.

To calculate the required nuclear polarization, it was assumed that the diffusion length for the nuclear magnetization was 20 μm in order to polarize all of the nuclei in the sample. To check this hypothesis, the nuclear T_1 for the DPPH protons can be calculated using this spin diffusion length $L = \sqrt{DT_1}$, where the nuclear spin diffusion constant is assumed to be $D \sim 10^{-16} \text{ m}^2/\text{s}$ based on the work of Cory on CaF₂ samples⁵ [114]. A diffusion length of $L = 20 \text{ } \mu\text{m}$ would require a nuclear

⁵Note that the diffusion constant for the nuclei in CaF₂ depends on the density of the spins in the lattice and will be different for the nuclei in DPPH. However, it can be imagined that the difference in ρ between the nuclei in DPPH and in CaF₂ is not large enough to change the D by more than an order of magnitude.

relaxation time of

$$T_1 = \frac{L^2}{D} = 4 \times 10^6 \text{ s} \quad (4.66)$$

or about 1,100 hours. This is unreasonably long based on the fact that subsequent high gradient spring constant shift experiments appear to be unpolarized. If the relaxation time was this long, we would expect that the nuclear spins would remain polarized between scans and the resulting spring constant shift would be constant across the sample. Based on the scan times, which take about 15 minutes to perform and are spaced about 15 minutes apart, we could expect that the nuclear T_1 could be as long as 300 s, which corresponds to diffusion constants on the order of $10^{-12} \text{ m}^2/\text{s}$. Based on the abrupt change in the size of the signal which occurs over the span of seconds, it may be more reasonable to assume a T_1 of 4 s and a $D = 10^{-10} \text{ m}^2/\text{s}$.

However, it is conceivable that the sample T_1 could decrease dramatically when the total field at the sample ($B_{\text{tot}} = B_{\text{tip}} + B_{\text{ext}}$) approaches zero, as follows. If the total field at the sample was zero, the Larmor precession frequency of the sample spins would also approach zero since $\omega_L = \gamma_p B_{\text{tot}}$. The spectral density of magnetic fluctuations near zero frequency is large due to slow motions that come from many different sources in the lattice. These low frequency fluctuations cause the proton T_1 to decrease according to BPP (Bloembergen, Purcell, and Pound) theory, where T_1 is inversely proportional to the spectral density of the magnetic fluctuations in the local field at the Larmor frequency [74, 123]. For the nuclei in the DPPH sample, the Larmor frequency at low fields (100 – 500 G) is in the range of 0.5 – 2 MHz, a correlation time $\tau_c = 0.5 – 2 \mu\text{s}$. Therefore, any fluctuating magnetic field in the kilohertz range or lower will relax the proton spins and reduce T_1 . Recall from Table 4.4 that the tip field for the particle in

this case is $B_{\text{tip}} = 500 \text{ G}$, and the external field required to make the total field at the particle zero would thus be -500 G . Surprisingly, $B_{\text{ext}} = -500 \text{ G}$ occurs near the end of the sample scan where the spring constant shift is approximately zero, as seen in Figure 4.22(b), indicating that the T_1 may be decreasing rapidly at this point. This may explain why the nuclear spins appear unpolarized in subsequent scans.

Our calculations of the nuclear and electron Boltzmann polarizations show that dynamic nuclear polarization at 100% efficiency, in tandem with diffusion of the nuclear magnetization outside of the sensitive slice, may account for a small portion of our anomalous spring constant shift in the high gradient case. However in order for DNP and nuclear spin diffusion to completely account for the anomalous signal, the nuclear spin diffusion constant for DPPH would have to be orders of magnitude larger than known nuclear diffusion constants or nuclear spin-lattice relaxation times would need to be unreasonably large. These facts prevent us from fully attributing the signal to a DNP effect. We do not expect DNP to play a role in the low gradient signal since the sensitive slice thickness is on the order of the sample thickness and no additional sample outside of the slice is available to polarize. Additionally, the low gradient experiments were performed at lower rf powers than the high gradient experiments. The electrons in the low gradient case are thus not as saturated and are less likely to polarize the nuclei.

4.7 Investigating the anomaly: Comparing average rf power

So far, we have only considered the anomalous signal in experiments where the force and force gradient measurements were taken at equal output rf powers. Recall from Section 4.6.3 that the heating of the sample is lower in the force experiment

than in the force gradient experiment for equivalent rf output powers. Based on this, it is possible that we should be comparing the force and force gradient experiments at equal average powers, not equal output powers. In this section, we will investigate the anomalous signal when comparing signals with equivalent average rf powers.

The force gradient will be simulated from a force signal at an output rf power of 32mW, graphed in Figure 4.25(a). This force signal is divided by $\nabla B = -300\text{T/m}$ to isolate the magnetization in the slice. The numerical derivative is determined as in previous simulations. These are substituted into Eq. 4.52 and the result is graphed in Figure 4.25(b) and compared to the force gradient experiment at 16 mW, which has the same average power as the force experiment at 32 mW.

As expected, the simulated signal is dominated by the OSCAR term and has a dispersive lineshape. The large noise in the simulation is a result of the lower signal-to-noise in the 32 mW force experiment when compared to the higher power results. The contribution from the CERMIT signal is small, approximately 2nN/m at its peak. Unlike the previous high gradient simulation of signals at the same output power in Figure 4.21, the CERMIT contribution to the simulated signal has not been multiplied by a scaling factor. The simulation is in very good agreement with the 16 mW signal from -300 G to -400 G . However, this simulation does not explain the behavior from -400 G to -500 G , indicating that we still observe an anomalous signal.

We can determine the anomalous CERMIT in this comparison by subtracting the simulated signal from the observed signal, seen in Figure 4.26. Now, the anomalous signal appears concentrated in the second half of the sample. The anomalous signal from -300 G to -400 G is zero within the noise, indicating that

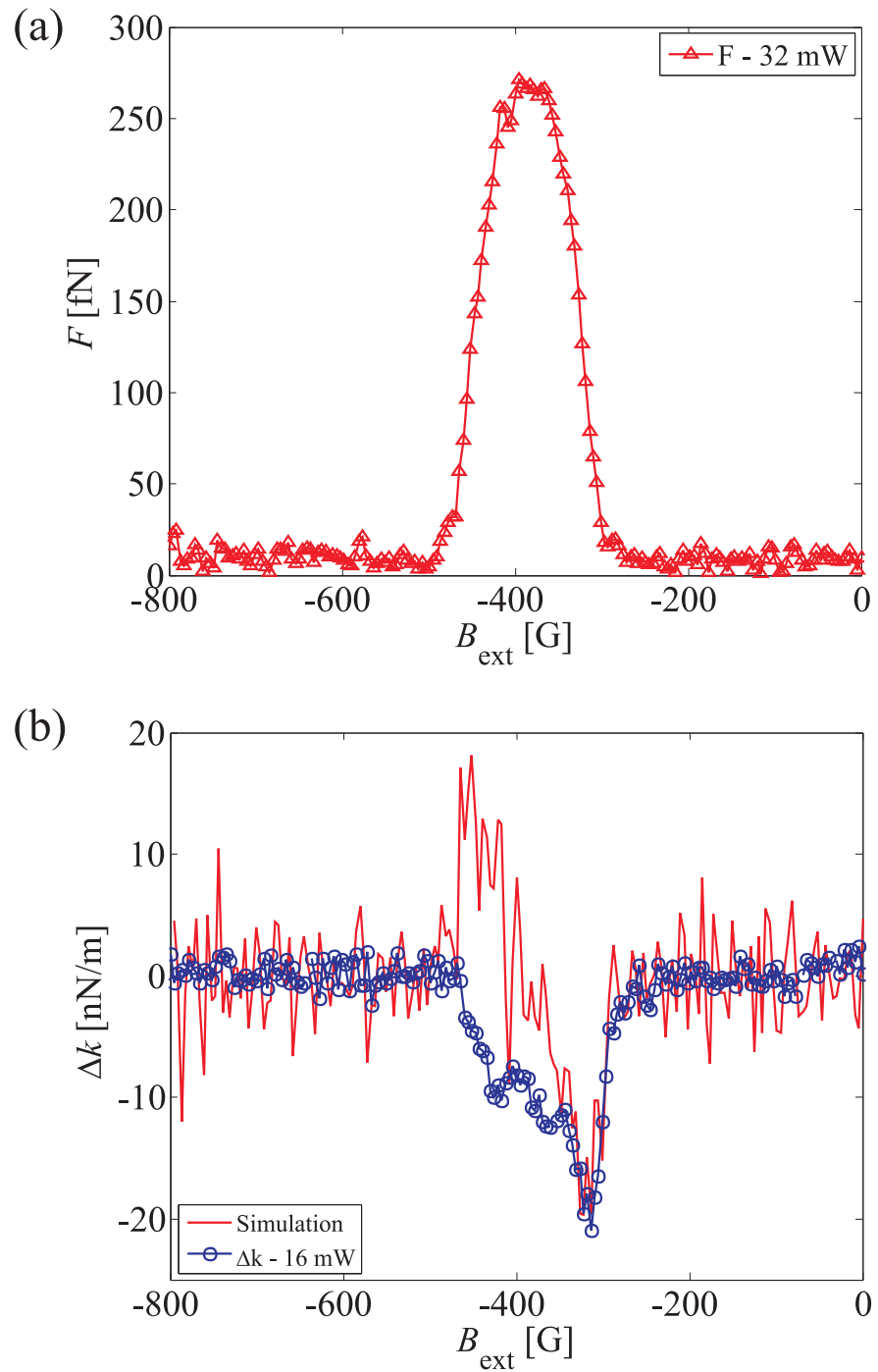


Figure 4.25: Comparison of the force signal at 32 mW to the force gradient signal at 16 mW. A comparison between the force gradient signal at 16 mW (circles) to the simulated spring constant shift (solid line) based and the force signal in (a) is shown in (b).

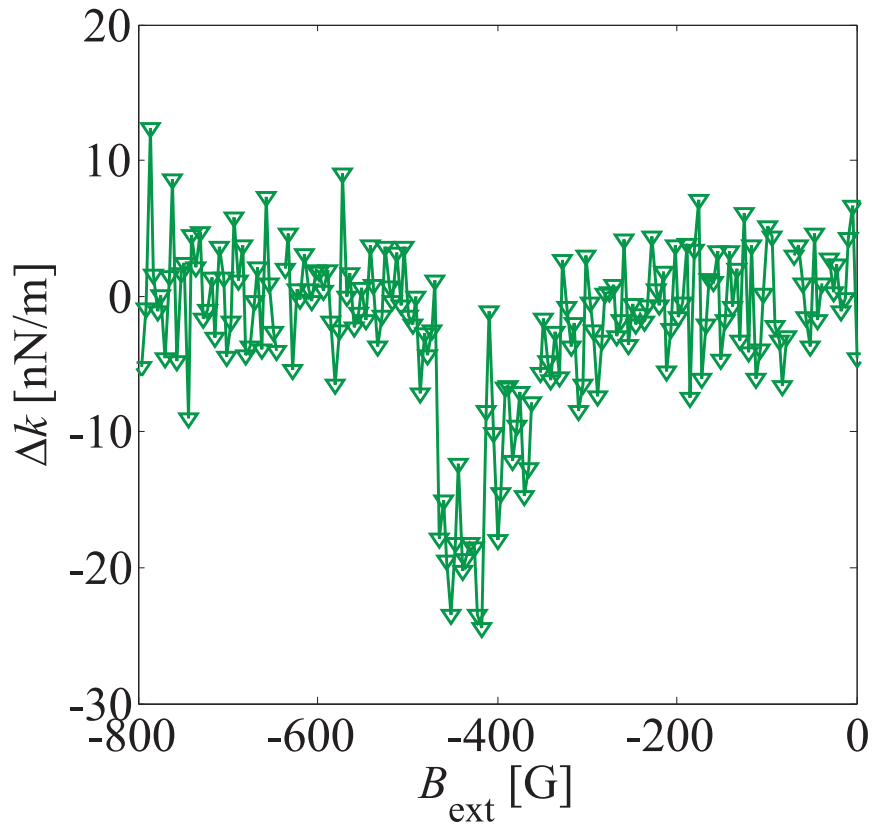


Figure 4.26: Anomalous CERMAT signal based on the comparison of force and force gradient experiments performed at different powers. The Δk_{obs} is from the force gradient experiment at 16 mW and the $\Delta k_{\text{OSCAR,sim}}$ is determined from the force data at 32 mW. The relevant signals used to make this plot are seen in Figure 4.25.

the first half of the sample is fully understood by Eq. 4.52 where we include the small CERMIT contribution. Thus, when comparing identical average powers, the anomalous signal is confined to the second half of the sample only.

Can we attribute this anomaly to electron spin diffusion? Assuming that the peak in Figure 4.26 of approximately -20 nN/m is due to electrons, the slice thickness would have to increase from $2 \mu\text{m}$ to approximately $5 \mu\text{m}$ using

$$\mu_{\text{anom}} = \frac{\Delta k}{\nabla^2 B} = \rho_e \Delta z A \mu_e P_{B,e} \quad (4.67)$$

and solving for the slice thickness, Δz . Here, we have used an area of $A = 20 \times 20 \mu\text{m}$ and $P_{B,e} = 4 \times 10^{-4}$. If the peak is due to the diffusion of electrons outside of the slice, the diffusion length would be $L = 1.5 \mu\text{m}$ and the corresponding T_{1e} would be 5 ms. Although the T_{1e} is much shorter than the one needed in the previous electron spin diffusion calculation, it is still too long based on the force signal where $1/f_{\text{mod}} = 1 \text{ ms}$. Thus, the anomalous peak is not likely due to DPPH electron magnetization diffusing outside of the slice.

The main difference between the first and second halves of the sample is that the second half is the part of the sample that is epoxied to the cantilever. The particle appears to be symmetrical by eye, ruling out any changes in the particle shape. Based on this, we believe that the anomalous signal is most likely due to electrons from the DPPH diffusing into the epoxy. This could occur via reactions between the DPPH molecules and the epoxy while the epoxy is hardening. The hardening is an exothermic process, and the heat produced by the epoxy could activate a reaction. It is then conceivable that unpaired electrons from the DPPH could diffuse farther into the epoxy. DPPH particles could also diffuse into the epoxy without reacting via physical mechanisms, such as small flecks of DPPH mixing into the epoxy during the adhesion procedure.

If this is the case, why would these extra electrons in the epoxy give a signal in the force gradient experiment but not in the force experiment? If there are electrons in the epoxy, it is reasonable to assume that they would have a much lower concentration than the electrons in the solid DPPH sample. This lower concentration would lead to a T_1 of the epoxy spins that is longer than the T_1 of the concentrated electrons in the DPPH sample due to a decrease in the fluctuating magnetic fields available to relax the epoxy spins. This T_1 could conceivably be much longer than the modulation frequency in the force experiment, and these spins would not be detected in the force signal. Thus the force signal would underestimate the total number of electrons in the sample and epoxy. This results in an anomalous signal in the force gradient experiment, which detects the spins nearly independent of the relaxation time. The difference in the force and force gradient signals would be due to a difference in the T_1 's of the electron spins, and we would be obtaining T_1 imaging contrast. Additionally, the anomalous signal is constrained to the high gradient signal and not seen in the low gradient signal. This could be due to the differences in spatial resolution between the two experiments. The thick sensitive slice in the low gradient signal may not be able to resolve the electrons in the epoxy, whereas in the high gradient case, the slice is thin enough to resolve the epoxy spins.

4.8 Summary and Conclusions

For the first time, a force gradient effect has been extended to a sample with a short spin-lattice relaxation time. Previous frequency shift detection techniques have required T_1 , $T_{1\rho}$, or τ_m to be longer than several cantilever cycles, typically longer than 10ms. This new technique extends the reach of force gradient methods

to electron spin samples with $T_1 < 10$ ms, which, we envision, will enable the imaging of biological samples and spin labels with short relaxation times. This technique can be combined with the CERMIT technique to image electron samples with T_1 's ranging from $10^{-9} - 10^3$ s. Additionally, the force gradient observed using this technique is due to saturation of electron spins, rather than the inversion mechanisms used in OSCAR and CERMIT. This is the first time that a force gradient has been observed due to a saturation effect.

The force signals observed at high and low gradients agree well with expectations. The observed force in the low gradient regime is smaller than the expected force from the scaling law, which can be accounted for by considering the uncertainties in sample heating, estimates of the sample dimensions, and incomplete saturation of the spins in the slice. In the low gradient case, the sensitive slice thickness is on the order of the sample thickness and the scaling law is expected to begin to break down in this regime. By contrast, in the high gradient case, the slice thickness is much thinner than the sample thickness, and the expected force from the MRFM scaling law agrees well with the observed force. Estimates of the gradients and the sample thickness based on the force experiments show excellent agreement with the observed peak widths. These results place a maximum on the T_1 value of the sample at cryogenic temperatures of approximately 10 ms.

The low gradient spring constant shift due to the force gradient is understood and agrees extremely well with the theoretical model. Comparisons of the force gradient signal to the force signal closely predict the shape and size of the change in the spring constant with no free parameters required, and the value of the gradient at each peak can be determined using these simulations. A physical picture of the slice moving through the sample has been proposed and also agrees

with expectations.

In the high gradient regime, a spring constant shift was observed, but could not be so straightforwardly explained. The signal appears to have both absorptive and dispersive characteristics, which is unexpected at high gradients where the dispersive nature of the signal is expected to dominate. We believe that the dispersive spring constant shift seen in the low gradient case is present in the high gradient case, but is dominated by an anomalous spring constant shift. Efforts to explain the anomalous spring constant shift using diffusion of electron magnetization were unsuccessful. The sample T_1 required for the spin diffusion hypothesis to explain the anomalous signal would have to be 230 ms, which is inconsistent with the maximum value of $T_1 = 1$ ms placed on the sample spins by the force experiment. Alternatively, the diffusion constant required for the spins to diffuse over 10 μm would have to be seven orders of magnitude larger than the D calculated in Eq. 4.60. We have also attempted to explain the anomalous signal in terms of dynamic nuclear polarization. Calculations of the nuclear and electron polarization factors show that it is reasonable, though unlikely, that the anomalous spring constant shift could be due to the nuclei in the DPPH sample, and not the electrons. Without knowledge of the nuclear spin-diffusion constant of DPPH, we are unable to attribute the bulk of the anomalous signal to the nuclei. Finally, comparisons of force and force gradient signals at equal average rf powers show that the anomalous signal is confined to the second half of the sample. This indicates that the anomalous signal may be due to the epoxy used to glue the sample to the end of the cantilever.

The only discernable difference between our two experiments is a change in the thickness of the sensitive slice, from a regime where the slice is on the order of the

sample thickness to one where it is an order of magnitude smaller. The change in slice thickness relative to the sample thickness may be related to the differences in the signals, and it suggests several experiments to attempt to explain these new effects. First and foremost, force gradient experiments should be performed with even larger gradients. The dependence of the signal on the slice thickness could also be explored by changing the distance between the magnetic particle and the sample via scanning. Increasing the tip-sample distance results in a smaller gradient at the sample, and a thicker slice. Experiments such as these would allow one to explore the crossover from a well-behaved signal in the low gradient to one that is not well understood.

The absorptive nature of the force gradient signal suggests that the magnetic moment μ is the dominant feature of the signal, not the $\partial\mu/\partial z$ term. Since $\nabla^2 B$ has a different distance dependence than ∇B , the high gradient signal could be plotted versus the tip-sample distance, and the crossover from a dispersive signal, like that in the low gradient signal, to an absorptive signal can be determined. We expect that the anomalous CERMIT effect would grow larger as the tip-sample distance is decreased and the sample thickness is kept constant.

The effects of sample thickness could also be explored by moving to the magnet-on-tip geometry and varying the thickness of the sample below the tip. It would also be advantageous to study low concentrations of electron spin labels, such as those used in bulk ESR measurements. Samples could include common spin labels such as 4-amino TEMPO (4-amino-2,2,6,6-tetramethyl-piperidine-1-oxyl) or BDPA (α - γ -bisdiphenylene- β -phenylallyl). These future experiments could illuminate the effect of dynamic nuclear polarization on these biologically relevant samples since a decreasing spin density should lead to a decreasing diffusion constant and a smaller

DNP effect.

Several experiments can be imagined to explore the dependence of the signal on the epoxy. First and foremost, a different adhesive that does not heat up during hardening (such as superglue) could be used to affix the sample to the cantilever. Sample-on-cantilever experiments could also be attempted where the sample is attached to the cantilever via electrostatic forces, but care would need to be taken to avoid bumping the probe, which could knock the sample off of the cantilever. The most promising method would be to study a piece of DPPH in the magnet-on-cantilever geometry in the absence of an adhesive. This would allow one to change the gradient and probe the signal shape, as mentioned previously. In this geometry, the sample could be held down with metal clips, and it may be the case that high gradient spring constant shifts are no longer anomalous in the absence of epoxy.

Finally, let us consider possible small ensemble and single spin measurements using this technique. It will first be necessary to move to the magnet-on-tip geometry in order to use small magnets with larger ∇B and $\nabla^2 B$ at small tip-sample distance. At the current field and temperature, the Boltzmann polarization (Eq. 4.62) is quite small, around 4×10^{-4} . As the number of spins decreases, this polarization factor will cause magnetization in the slice to decrease greatly, making detection difficult. The polarization factor can be improved to 0.1 by increasing the field to 18 GHz with a stripline rf resonator and by going to 4 K. When studying single spins, the position of the spin underneath the tip will be critical. If the single spin case is governed by the low gradient results, it will be necessary to study a spin that is not directly beneath the tip as in the OSCAR experiment. This is because the gradient ∇B is zero directly below the tip, so the spin must be off center in a

non-zero gradient. In contrast, a CERMIT signal may be seen if the spin is directly below the tip since the second gradient is non-zero in this case. If the single spin is in the high gradient regime, there is less of a restriction on the spin placement since the signal is more dependent on the second gradient, which is a maximum directly beneath the tip.

CHAPTER 5

PARAMETRIC AMPLIFICATION OF ULTRASENSITIVE CANTILEVERS

5.1 Introduction

The CERMIT and force gradient detected ESR techniques measure the magnetic moment of the sample as a small (millihertz) change in the cantilever resonance frequency, which has a resonance frequency of a few kilohertz. However, as the number of spins in the sample decreases, the size of the frequency shift will decrease greatly and grow increasingly difficult to detect with conventional techniques.

As an example, consider a CERMIT experiment where the magnetic moment from a relatively small number of net spins, say 3×10^5 protons, is detected. The magnetic moment of these spins would be $\mu_z = 4 \times 10^{-21} \text{ J/T}$, which is equivalent to the magnetic moment of about 400 electrons, where we have used the standard values of the proton and electron magnetic moment. Using the experimental parameters from Garner, *et al.* in Ref. [33], this magnetic moment would result in a spring constant shift of

$$\Delta k = \mu_z \frac{\partial^2 B_z}{\partial x^2} = 8 \times 10^{-11} \text{ N/m} \quad (5.1)$$

where the second gradient is $2 \times 10^{10} \text{ T/m}^2$. The frequency shift would be

$$\Delta f = \frac{f_0}{2k} \Delta k = 0.57 \text{ mHz} \quad (5.2)$$

where $k = 6 \times 10^{-5} \text{ N/m}$ and $f_0 = 854 \text{ Hz}$. This is well below the reported frequency jitter of 2 mHz, resulting in a signal-to-noise ratio of approximately 0.25. It would be possible to increase this ratio by averaging for long periods of

time, but it would be more useful for imaging applications to measure the change quickly. This problem will only increase as smaller spin ensembles are studied with cantilevers brought closer and closer to sample surfaces.

Most scanned probe microscopy experiments, including the MRFM experiments discussed in Chapters 1 and 4 of this thesis, employ audio-frequency cantilevers. The dominant source of noise in these experiments is the thermomechanical Brownian motion of the cantilever. In studies of submicron radio frequency cantilevers, however, the amplitude of the thermomechanical motion is so small that it is difficult to observe, even with a fiber-optic interferometer. In this situation, where the detector is the dominant source of the noise, it is advantageous to introduce a modulation of the cantilever spring constant at $2f_0$ in order to parametrically amplify the thermomechanical motion to a detectable amplitude [124].

In this chapter, we introduce a potential new way to employ parametric amplification to measure small spring constant shifts in MRFM experiments. In the proposed technique, we will excite the cantilever with a force at f_0 and use the sample spins, whose magnetization is modulated at $2f_0$, to parametrically amplify the forced oscillation at f_0 . Essentially, we are proposing to detect the spins by using them as an *amplifier*. In Section 5.2, the theory of parametric amplification and the potential MRFM application will be described in detail. In Sections 5.3 and 5.4, control experiments will be discussed where we show that small changes in cantilever amplitudes by parametric amplification can be measured using the cantilevers fabricated in Chapter 3.

5.2 Parametric Amplification: Background and Theory

Degenerate parametric amplification occurs in oscillators when the spring constant, length, or mass is changed at twice the resonance frequency. The classic example of parametric amplification is a child on a swing, which is essentially a pendulum. The child is able to change their center of gravity up and down by kicking, which changes the effective length of the pendulum and modulates the resonance frequency of the swing [125]. If the child kicks their legs at the extremes of motion, the amplitude of the swing's oscillations will be amplified. In 1831, Faraday first observed a parametric excitation in the ripples on the surface of water in a glass oscillating up and down [126]. This system was first treated theoretically by Rayleigh in the 1880s [127]. In most experiments where a signal is amplified, the amplification takes place after the signal has been transduced into an electrical signal. Parametric amplification is unique in that the signal is amplified prior to being transduced and measured. Mechanical parametric amplifiers are noise-free down to the quantum-mechanical level [128] and can be used to improve sensitivity when the system is limited by detection noise.

Typically, a parametrically amplified system consists of three modes [129]. In our case, a cantilever is driven at its resonance frequency, f_0 , which is known as the driven mode. The spring constant is also modulated, or pumped, at a frequency that is the sum or difference of the driven mode frequency and the frequency of an idler mode. If the frequency of the idler mode is the same as the frequency of the driven mode then the frequency of the pumping mode is $2f_0$. This is known as degenerate parametric amplification and is the technique used in this work.

Mechanical parametric amplification using cantilevers was first described by Rugar and Grutter [128]. In this experiment, the spring constant of an atomic

force microscope cantilever was modulated electrostatically at $2f_0$ by a capacitor plate. This effect was used to amplify the subangstrom mechanical signals and to perform thermomechanical noise squeezing. The experimental setup in our control experiment is similar to the one discussed in this paper. Furthermore, parametric amplification has also been observed in a torsional oscillator using an applied voltage to modulate the spring constant [124]. Dougherty, *et al.* used an AC magnetic field to parametrically amplify a magnetic tipped cantilever [129]. The spring constant of the cantilever was modulated by an amount $\Delta k \simeq \mu B(t)/l^2$ where μ was the tip magnetic moment, $B(t)$ is the time dependent field at $2f_0$, and l was the length of the cantilever. Finally, the Craighead research group at Cornell University has performed parametric amplification on several small oscillators by modulating the spring constant with the interferometer laser via laser heating-induced thermal stress [130–132].

5.2.1 Derivation of Parametric Amplification in a Simple Harmonic Oscillator

To derive the parametric amplification effect for a simple harmonic oscillator, we begin with the equation of motion for a cantilever (Chapter 2)

$$\ddot{x} + \frac{\omega_0}{Q}\dot{x} + \frac{k(t)}{m}x = \frac{F(t)}{m} \quad (5.3)$$

where the cantilever is driven on resonance by a time-dependent force, $F(t) = F \sin \omega_0 t$, and the intrinsic spring constant k is modulated at twice the resonance frequency $2\omega_0$ by an amount Δk

$$k(t) = k + \Delta k \sin [2\omega_0 t + \phi] \quad (5.4)$$

The phase between the driving force (the drive) and the spring constant modulation (the pump) is ϕ . We now assume a solution of the equation of motion of the form

$$x(t) = X \cos \omega_0 t + Y \sin \omega_0 t \quad (5.5)$$

where X is the in-phase cantilever response and Y is the out-of-phase response, which are identical to the lock-in amplifier outputs during the experiment.

X and Y are determined by substituting Eq. 5.5 and its time derivatives into Eq. 5.3. The expression is simplified with the use of several trigonometric identities, and all resulting $3\omega_0$ components are eliminated since the signal will be lock-in demodulated at ω_0 . We are left with an expression that must be separated into two equations and solved simultaneously. The first equation is multiplied by $\cos \omega_0 t$ and must be equal to zero

$$\frac{\omega_0^2}{Q} Y + \frac{\Delta k}{2m} X \sin \phi + \frac{\Delta k}{2m} Y \cos \phi = 0 \quad (5.6)$$

and the second equation is multiplied by $\sin \omega_0 t$ and must equal F/m

$$-\frac{\omega_0^2}{Q} X + \frac{\Delta k}{2m} X \cos \phi - \frac{\Delta k}{2m} Y \sin \phi = \frac{F}{m} \quad (5.7)$$

These equations are further simplified by multiplying each by Q/ω_0^2 and using $m\omega_0^2 = k$. In matrix form, the simultaneous equations become

$$\begin{pmatrix} g \sin \phi & 1 + g \cos \phi \\ -1 + g \cos \phi & -g \sin \phi \end{pmatrix} \begin{pmatrix} X \\ Y \end{pmatrix} = \begin{pmatrix} 0 \\ QF/k \end{pmatrix} \quad (5.8)$$

where we have defined the gain factor g as

$$g = \frac{Q\Delta k}{2k} \quad (5.9)$$

To solve for X and Y , Eq. 5.8 is multiplied by the inverse of the 2×2 matrix, resulting in

$$\begin{pmatrix} X \\ Y \end{pmatrix} = \frac{QF}{k} \frac{1}{1 - g^2} \begin{pmatrix} -1 - g \cos 2\phi \\ -g \sin 2\phi \end{pmatrix} \quad (5.10)$$

where we have made the change of variables¹ $\phi \rightarrow -2\phi$. The components of the complex lock-in signal $Z = X + iY$ are thus

$$X = -\frac{QF}{k} \left(\frac{1 + g \cos 2\phi}{1 - g^2} \right) \quad (5.11)$$

$$Y = -\frac{QF}{k} \left(\frac{g \sin 2\phi}{1 - g^2} \right) \quad (5.12)$$

Modulating the spring constant at $2\omega_0$ has the effect of multiplying the in-phase and out-of-phase components of the driven cantilever amplitude by terms that are a function of the phase between the drive and the pump, as well as the gain factor.

When there is no parametric amplification, Δk and g will be zero. This leads to the expected results for the on-resonance cantilever amplitude response

$$X_{\text{off}} = -\frac{QF}{k} \quad (5.13)$$

$$Y_{\text{off}} = 0 \quad (5.14)$$

where the cantilever amplitude is out-of-phase with the driving force and is Q -enhanced. The subscript “off” indicates that the spring constant modulation is set to zero. This is a slightly different result from the case derived in Chapter 2 where the driving force was sinusoidal and the on-resonance response was in the Y channel of the lock-in. Ultimately, the two cases are equivalent.

When the spring constant is modulated, the cantilever response depends on the phase between the drive and the pump. If the phase difference is zero ($2\phi = 0$)

$$X_{\text{on}} = -\frac{QF}{k} \left(\frac{1}{1 - g} \right) \quad (5.15)$$

$$Y_{\text{on}} = 0 \quad (5.16)$$

¹This change of variables is a convention used to equate this case of parametric amplification to a derivation of the Quantum Harmonic Oscillator by John Marohn (unpublished). In addition, the phase difference measured by the lock-in in the experiment is 2ϕ , not ϕ , due to a quirk in the experimental setup which will be explained in Section 5.3.2.

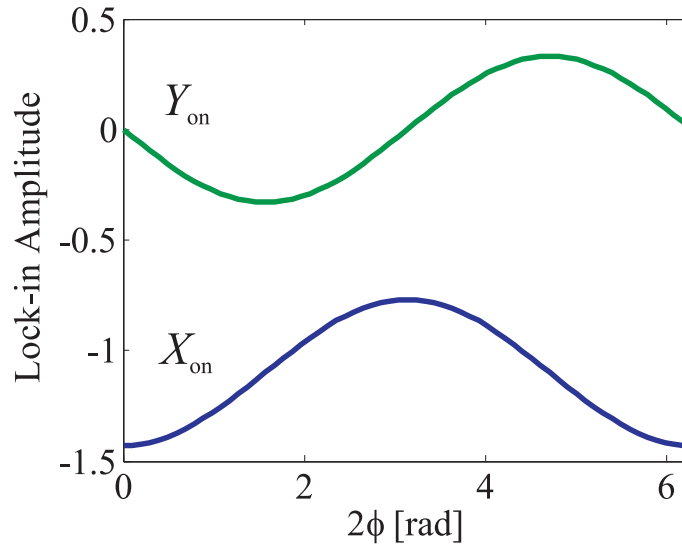


Figure 5.1: General behavior of X_{on} (bottom) and Y_{on} (top) versus phase for parametric amplification. For simplicity, QF/k is set to 1 nm and $g = 0.30$.

where “on” indicates that $g \neq 0$. We expect no change in the out-of-phase cantilever response when the phase between the drive and the pump are equal. When the phase difference between the two drives is $2\phi = \pi/2$

$$X_{\text{on}} = -\frac{QF}{k} \left(\frac{1}{1-g^2} \right) \quad (5.17)$$

$$Y_{\text{on}} = -\frac{QF}{k} \left(\frac{g}{1-g^2} \right) \quad (5.18)$$

Therefore the Y response is at an extreme that is dependent on g . X_{on} and Y_{on} are plotted versus the phase difference in Figure 5.1. The cantilever amplitude QF/k has been set to 1 nm for simplicity.

Another factor of merit in parametric amplification experiments is the Gain (not to be confused with the gain factor), which is the ratio of the cantilever magnitude with the amplification on to the magnitude with the amplification off,

$R_{\text{on}}/R_{\text{off}}$, where $R^2 = X^2 + Y^2$. The Gain, therefore, is

$$\text{Gain} = \frac{1}{1 - g^2} [(1 + g \cos 2\phi)^2 + (g \sin 2\phi)^2]^{1/2} \quad (5.19)$$

In later sections, the Gain, X_{on} , and Y_{on} will be graphed versus the phase difference in order to prove that our cantilever is being parametrically amplified. As g approaches one, the amplification becomes quite large.

In the experiments, the lock-in phase is set so that the Y response is zero prior to parametric amplification. When the parametric amplification is turned on with the phase difference set to $2\phi = \pi/2$, we expect to see a change in the Y amplitude that can be used to calculate Δk with Eq. 5.9. Theoretically, g can be calculated from this change using

$$g = \frac{1}{2} \left(1 \pm \sqrt{1 - 4 \frac{Y_{\text{on}}}{QF/k}} \right) \quad (5.20)$$

If the g from this calculation is ambiguous due to the sign of Y_{on} , it can be calculated from a ratio of the X signals before and after amplification with $2\phi = 0$

$$\frac{X_{\text{on}}}{X_{\text{off}}} = \frac{1}{1 - g} \quad (5.21)$$

Furthermore, g can be determined by fitting Gain versus phase data using Eq. 5.19. The last two approaches will be used in Section 5.4 to compare the observed g factor in our control experiments to the theoretical g .

5.2.2 Parametric amplification and MRFM

As discussed in Section 5.1, the spring constant shift from 3×10^5 net protons or 400 net electrons produces a spring constant shift which would be difficult to detect using conventional methods due to the small signal-to-noise ratio. However,

we may be able to detect this spring constant shift using parametric amplification, where the spins are the amplifier.

In this proposed parametric amplification MRFM experiment, the spins below the magnetic-tipped cantilever need to be modulated at $2f_0$ while the cantilever is driven at $1/f_0$. For electrons with short T_1 , modulation at $2f_0$ can be performed using saturation techniques. For electron and nuclear spins with long relaxation times compared with f_0 , it would be necessary to use adiabatic rapid passages to perform the modulation. This would require that the adiabatic condition be met and that the spins have a favorable $T_{1\rho}$ [133]. The interaction between the spin magnetization and the second gradient of the magnetic particle will cause a change in the spring constant $\Delta k = \mu(\partial^2 B_z / \partial x^2)$ due to the CERMIT effect, which is now modulated at $2f_0$. This modulation of the spring constant will change the cantilever amplitude due to the parametric effect with a gain factor of $g = Q\Delta k / 2k$. To determine the size of the spring constant shift, the phase between the drive and the pump (the spin modulation frequency) is set to maximize the change in the out-of-phase cantilever amplitude (monitored using a lock-in amplifier). The difference between the amplitude before and after amplification is a function of g , and can be used to determine the Δk of the spins in resonance. In most parametric amplification techniques, the cantilever motion is amplified independent of the system being studied. In this proposed experiment, we would like to change the spring constant using the system under study, the spins.

How small is the change in cantilever amplitude from this effect? Based on the $\Delta k = 8 \times 10^{-11} \text{ N/m}$ calculated in Section 5.1 and using the cantilever parameters from Ref. [33], the parametric amplification gain factor would be $g = 0.03$. The rms driving amplitude of the cantilever in that experiment was set to $QF/k = 176 \text{ nm}$.

This would produce a parametrically amplified out-of-phase response of

$$Y_{\text{on}} = \frac{QF}{k} \left(\frac{g}{1 - g^2} \right) = 5 \text{ nm} \quad (5.22)$$

which should easily be detectable. In the case that the change in the out-of-phase response is too small, the driving force could be increased.

Let us briefly compare the sensitivity of the parametric amplification technique to CERMIT. Recall from Eq. 5.18 that at the maximum phase response of the cantilever, the out-of-phase cantilever amplitude response will depend on g . If g is small, the out-of-phase response will be

$$Y_{\text{on}} = -\frac{QF}{k} \frac{Q\Delta k}{2k} \quad (5.23)$$

where we have substituted the gain factor with Eq. 5.9. If the spring constant shift is due to a CERMIT effect and the drive amplitude is $QF/k = x_0$, then the measured amplitude can be written as

$$Y_{\text{on}} = x_0 \frac{Q}{2k} \mu \frac{\partial^2 B_z}{\partial x^2} \quad (5.24)$$

This can be compared to the CERMIT signal, written in terms of the force where $F = x_0 \Delta k$. The amplitude due to a CERMIT experiment would be $Y = QF/k$ which is

$$Y_{\text{on}} = x_0 \frac{Q}{k} \mu \frac{\partial^2 B_z}{\partial x^2} \quad (5.25)$$

This is essentially the same as Eq. 5.24, indicating that there does not seem to be a sensitivity advantage to using parametric amplification over CERMIT. The two techniques appear to be formally equivalent. However, parametric amplification does hold a practical advantage in that the amplitude is measured at the cantilever frequency. In CERMIT, the detection of spins by a frequency shift is limited by surface frequency noise [51, 134].

We can also compare the parametric amplification experiment to the conventional force experiment. The amplitude measured in the force experiment is $Y = QF/k$ or

$$Y \sim \frac{Q}{k} \mu \frac{B_{\text{tip}}}{r} \quad (5.26)$$

where r is the radius of the magnetic particle and we have approximated the gradient as B_{tip}/r . The second gradient can be written, using the same analysis, as B_{tip}/r^2 . Using this, the amplitude from the parametric amplification measurement (Eq. 5.24) can be written as

$$Y_{\text{on}} \sim \left(\frac{Q}{k} \mu \frac{B_{\text{tip}}}{r} \right) \times \frac{x_0}{2r} \quad (5.27)$$

The expression in the parenthesis is Eq. 5.26, indicating that parametric amplification will improve the amplitude in the force experiment by a factor of $x_0/2r$. Unfortunately, this improvement must be small or close to unity in most cases. Increasing this ratio requires driving the cantilever to an amplitude much larger than the radius of the magnetic particle. A large x_0 causes the gradient and second gradient at the sample spins to change and these scaling law expressions will begin to break down. For the drive amplitudes used in these experiments, the amplitude in the parametric amplification experiment will be roughly equivalent to the amplitude from the force experiment. As in the case of CERMIT, however, parametric amplification holds a practical advantage over force detection. Since the parametric amplification effect is dependent on the spring constant shift from the second gradient, this technique could be used to detect homogeneously distributed spins or a single spin directly below the cantilever tip. This is not possible in the force experiment since the gradient directly below the tip would be zero.

In the following section, results from control experiments will be discussed where a thin, attonewton-sensitive cantilever is parametrically amplified. The

cantilever spring constant will be modulated electrostatically by a wire, and the size of the spring constant shift will be set so that $g = 0.03$. We will show that it is possible to measure a change in the spring constant corresponding to this gain factor, indicating that parametric amplification could be used to detect the spring constant shift from a small number of spins. Additionally, it will be shown that driving the cantilever with positive feedback produces changes in amplitude that cannot be predicted by parametric amplification. We conclude that the f_0 must be produced from an external source that is independent of the cantilever.

5.3 Experimental Aspects

In this section, capacitive driving will be discussed and the spring constant shift due to a capacitive force will be derived. The experimental apparatus and conditions for performing parametric amplification will be described.

5.3.1 Changing the spring constant by a capacitive force

A capacitive force and an associated force gradient can be applied to a cantilever by positioning a thin wire near the cantilever and applying an AC or DC voltage between it and a second wire that is silver painted to the cantilever die. The wire can be positioned perpendicular to the cantilever length near the tip (as in this experiment) or parallel to the cantilever length, depending on the constraints of the experimental setup.

To determine the change in spring constant due to a capacitive force, the wire and cantilever are modeled as the plates in a parallel plate capacitor [135]. The

energy stored in a capacitor is related to the voltage and the capacitance by

$$E = -\frac{1}{2}C(V - \varphi)^2 \quad (5.28)$$

where φ is the contact potential difference between the wire and the cantilever. The capacitance is defined as the ratio of the charge on the plates, q , to the applied voltage between the plates, $C = q/V$. For a parallel plate capacitor, the capacitance is $C = \epsilon_0 A/z$ where A is the area of the plate and z is the distance between the plates.

The force between the wire and the cantilever is the derivative of the energy

$$F = -\frac{\partial E}{\partial z} = \frac{1}{2} \frac{\partial C}{\partial z} (V - \varphi)^2 \quad (5.29)$$

This applied force causes a change in the spring constant of

$$\Delta k = \frac{\partial F}{\partial z} = \frac{1}{2} \frac{\partial^2 C}{\partial z^2} (V - \varphi)^2 \quad (5.30)$$

It is advantageous for the wire to be close to the cantilever since the spring constant shift will increase with the cube of the distance between the cantilever and the wire, $\partial^2 C / \partial z^2 = \epsilon_0 A / z^3$. The spring constant shift is measured as a frequency change using a commercial frequency counter, where $\Delta f = \Delta k(f_0/2k)$.

The applied voltage can have an AC component, a DC component, or both

$$V = V_{DC} + V_{AC} \cos \omega t \quad (5.31)$$

The spring constant shift from this voltage is derived by substituting this voltage into $(V - \varphi)^2$ from Eq. 5.30. After some simplification, the spring constant shift becomes

$$\Delta k = \frac{1}{2} \frac{\partial^2 C}{\partial z^2} \left[(V_{DC} - \varphi)^2 + \frac{1}{2} V_{AC}^2 + \frac{1}{2} V_{AC}^2 \cos 2\omega t + 2(V_{DC} - \varphi)V_{AC} \cos \omega t \right] \quad (5.32)$$

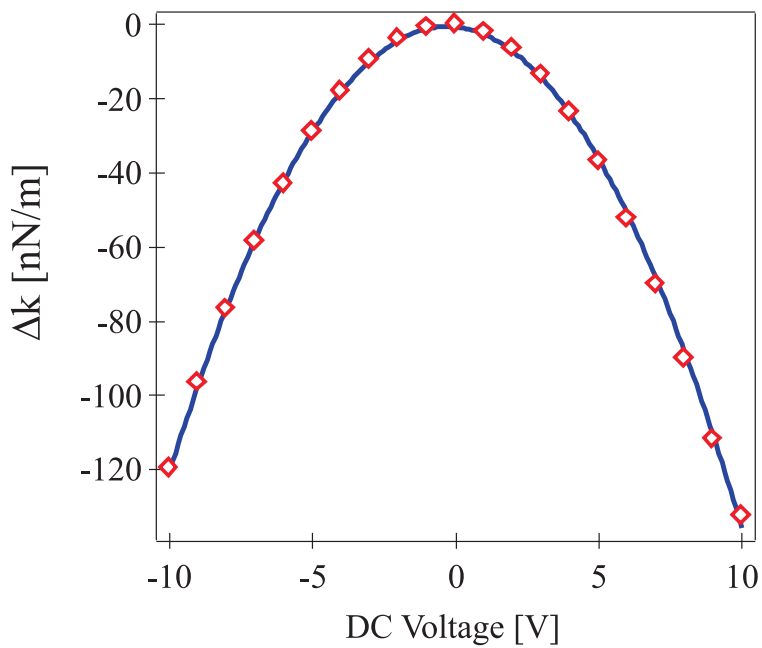


Figure 5.2: Spring constant shift versus DC voltage for a capacitive driving force. Based on the fit of this data, the contact potential difference between the wire and the cantilever is $\varphi = -0.3\text{V}$ and $\partial^2C/\partial z^2 = -2.55 \times 10^{-9}\text{C/Vm}^2$.

The contact potential and the second derivative of the capacitance are determined by applying a DC voltage to the wire and measuring the associated spring constant shift. If there is no AC voltage component on the wire, Eq. 5.32 becomes

$$\Delta k = \frac{1}{2} \frac{\partial^2 C}{\partial z^2} (V_{DC} - \varphi)^2 \quad (5.33)$$

Thus, we expect a parabolic change in cantilever stiffness with respect to an applied DC voltage. The change in cantilever spring constant is plotted versus the DC voltage for the cantilever and wire arrangement used in the following experiments in Figure 5.2. Based on a fit of the data to Eq. 5.33, we find $\varphi = -0.3$ V and $\partial^2 C / \partial z^2 = -2.55 \times 10^{-9}$ C/Vm². These values are specific to the cantilever-wire distance in this experiment and will be used to approximate the expected spring constant shifts in the parametric amplification control experiments. It should be noted that the contact potential difference between the cantilever and wire is known to change by as much as 0.1 V from day to day due to surface adsorbates, such as water [135].

5.3.2 Description of the experiment

Parametric amplification experiments are performed at high vacuum and room temperature in the probe discussed in Section 4.3. The rf coil and the magnetic particle are positioned far from the cantilever to prevent any interference. Cantilever motion is detected using a fiber-optic laser interferometer. The cantilever used in this experiment was custom-fabricated using the same procedure discussed in Chapter 3 with dimensions 300 μm long, 12 μm wide, and 340 nm thick and a $Q \sim 25,000$. The intrinsic spring constant $k = 3 \times 10^{-4}$ N/m was measured using the Brownian motion method. The resonance frequency was ~ 5.2 kHz, measured using positive feedback and frequency sweeps. A piezoelectric stack was epoxied onto

Table 5.1: Cantilever and experimental parameters for parametric amplification control experiments.

Length (l)	300 μm
Width (w)	12 μm
Thickness (t)	0.34 μm
Spring Constant (k)	$3 \times 10^{-4} \text{ N/m}$
Resonance Frequency (f_0)	5.2 kHz
Quality Factor (Q)	25,000
Contact Potential (φ)	-0.3 V
$\partial^2 C / \partial z^2$	$-2.55 \times 10^{-9} \text{ C/Vm}^2$

the stage behind the cantilever to provide the driving force. A thin copper wire was positioned $\sim 500 \mu\text{m}$ above the cantilever, aligned perpendicular to the end. A second wire was silver painted to the cantilever die to provide a voltage between the wire and cantilever. We measured the demodulated in-phase (X) and out-of-phase (Y) cantilever amplitudes using the lock-in amplifier with the reference frequency set to f_0 . A block diagram for the parametric amplification experiment is shown in Figure 5.3 and the experimental parameters are summarized in Table 5.1.

To perform parametric amplification, the cantilever is driven near f_0 with the piezoelectric stack while the cantilever spring constant is modulated by the capacitive drive wire at $2f_0$. Each of these drive voltages originate from a variable amplitude sine wave from the lock-in amplifier (Stanford Research 830). The lock-in output is routed to the piezo for on-resonance cantilever driving (the drive) and to a phase shifter and a frequency doubler to synthesize a sine wave with frequency

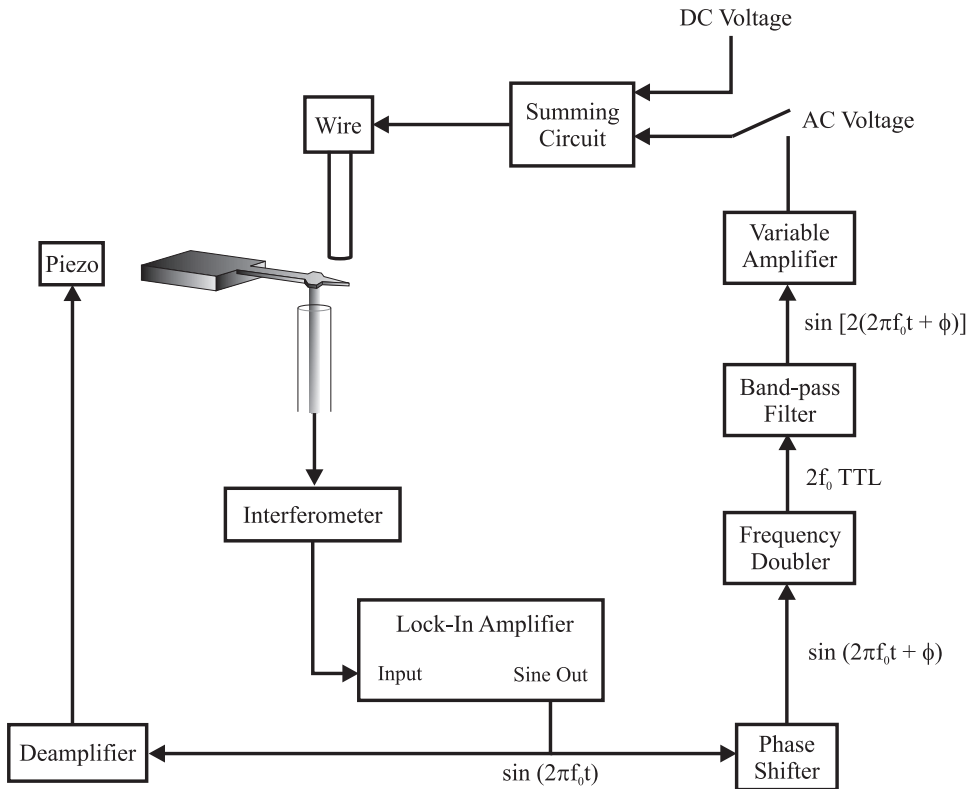


Figure 5.3: Block diagram for the parametric amplification experiment. The cantilever is driven at f_0 by a piezo, and the spring constant is modulated at $2f_0$ by a wire positioned above the cantilever tip. The AC voltage from the lock-in sine out is used to drive the cantilever and to produce an AC voltage at $2f_0$ where the phase between the drive and the pump can be adjusted.

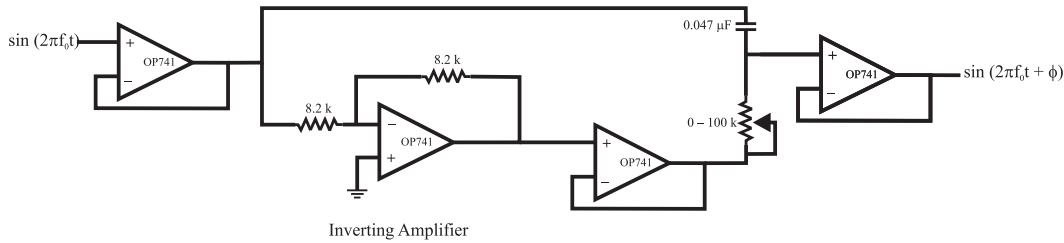


Figure 5.4: Circuit diagram for the custom-built phase shifter.

$2f_0$ and variable phase with respect to the drive (the pump). The voltage amplitude of the lock-in sine output must be larger than ~ 100 mV for the frequency doubler to output the necessary signal. Voltages this large, however, overdrive the cantilever and thus must be deamplified to ~ 6 mV before reaching the piezo. The zero-to-peak amplitude of the cantilever is set to approximately 50 nm.

The lock-in reference frequency (f_{LI}), which determines the lock-in demodulation and the cantilever driving frequency, is set so that f_{LI} is as close as possible to f_0 (i.e., f_{LI} is chosen to maximize the resulting cantilever oscillations). Precise on-resonance driving is not possible using the output sine wave of the lock-in due to limitations on the number of significant digits for the reference frequency. For this particular lock-in, the value of f_{LI} is limited to five digits or 0.0001 Hz, whichever is greater. This means that for cantilever frequencies in the kilohertz range, the smallest change we can make in f_{LI} is 1 Hz. Frequency steps of 0.1 Hz or smaller can be made using a National Instruments Frequency Generator (NIFGEN) board to drive the cantilever, but this requires an external lock-in reference, greatly complicating the experimental setup. Future parametric amplification experiments with high quality factor cantilevers may require an external driving source.

The $2f_0$ pump signal is synthesized as follows. The sine wave from the lock-in is sent to a custom-built phase shifter [136], which uses a variable resistor to

change the phase (ϕ) of the incoming signal. A circuit diagram for the phase shifter is shown in Figure 5.4. The output from the lock-in is a sine wave of the form $\sin(2\pi f_0 t)$, where $2\pi f_0 = \omega_0$. An inverted copy of the input sine wave, which is 180° out of phase with the input, is synthesized in the circuit by an inverting amplifier. The output signal is the phasor sum of the input sine wave and the inverted sine wave. The amount of the inverted sine wave added to the original input is controlled by the variable resistor. The circuit is able to change the phase of the incoming signal by a maximum of π radians.

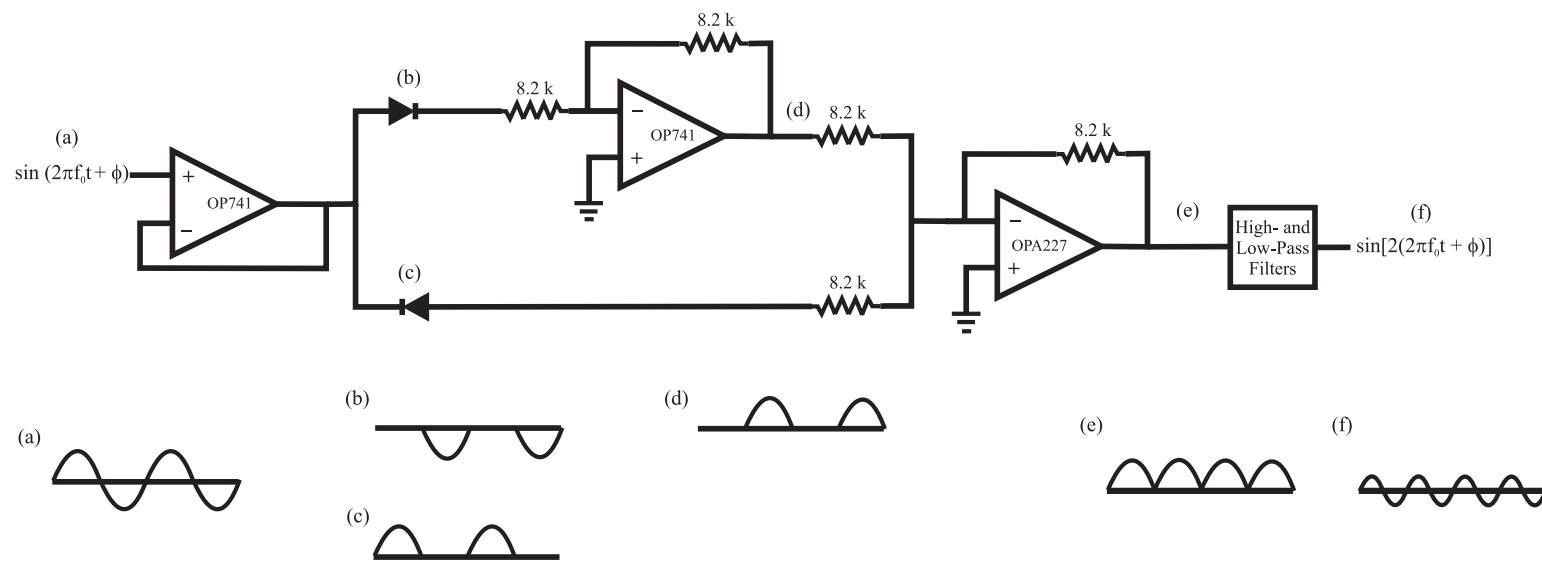


Figure 5.5: Circuit diagram for the custom-built frequency doubler.

The phase shifted signal, $\sin(2\pi f_0 t + \phi)$, is next sent to a custom-built frequency doubler. A circuit diagram and depiction of the sine wave at several points in the circuit is shown in Figure 5.5. The input ((a) in Figure 5.5) is sent to two separate diodes, one of which outputs only the parts of the sine wave with a negative amplitude (b) and the other outputs only the positive part of the sine wave (c). The negative output is inverted (d), and the two signals are combined by a summing circuit, creating a fully rectified copy of the input, essentially at $2f_0$ due to the rectification (e). The DC of the rectified wave is removed by high-pass filtering (with a cutoff frequency of 200 Hz), and subsequent low-pass filtering (with a cutoff frequency of 25 kHz) removes the higher order signal modes. The output of the filters is a sine wave at $2f_0$, (f). This is converted to a TTL signal (a square wave from 0 V to 5 V) using a standard comparator circuit and band-pass filtered at $2f_0$ with a Krohn-Hite Dual Channel Filter (Model 3940). This band-pass filter is very important because it removes any signal components at the resonance frequency which can spuriously drive the cantilever capacitively on-resonance. The output of the filter is sinusoidal and is sent to a variable amplifier, which sets the applied AC voltage to the wire (typically between 0.01 – 1 V). Notice that the phase of the output from the doubler is 2ϕ , not ϕ . This is the source of the change in variables described in the derivation in Section 5.2.1 and explains why the data will show phase differences of 2π rad, twice as large as the maximum from the phase shifter.

The phase between the drive and pump is set using the phase shifter and measured using the lock-in amplifier. To do this, the phase-shifted sine wave from the band-pass filter with frequency $2f_0$ and phase 2ϕ is set as the input of the lock-in. The lock-in must be set to measure the second harmonic of the reference

frequency, which remains set at f_0 . The phase between the two signals can be adjusted using the phase shifter and read on the display.

Before modulating the spring constant at a certain phase, the cantilever amplitude is set to approximately 50 nm by adjusting the amplitude of the sine wave from the lock-in. Recall that we would like to visualize the parametric amplification as a change in the out-of-phase cantilever amplitude from zero to non-zero. To do this, we set the lock-in phase (ϕ_{LI}) between the input cantilever signal and the lock-in reference so that the Y signal is zero.

This is complicated by the fact that the spring constant shift from parametric amplification will cause a frequency shift. If the frequency shift from the parametric amplification is a significant fraction of the cantilever resonance width (the intrinsic bandwidth of the cantilever), the cantilever will no longer be driven exactly on resonance, and the X and Y measured by the lock-in will not correspond to the expected on-resonance response. This could introduce significant error in the lock-in detection technique and is of particular concern with high- Q cantilevers which are quite narrow in frequency. For example, the cantilever resonance in these experiments is approximately 200 mHz wide, and we expect to measure frequency shifts of approximately 30 mHz.

This problem is circumvented by applying a DC spring constant shift prior to performing parametric amplification, the magnitude of which should be similar to the shift expected in the parametric amplification experiment. The X and Y will change as they would due to the Δk experienced during the parametric amplification experiment, and the lock-in phase is set to make the Y signal zero in the presence of this DC Δk . This prepares the lock-in for the expected frequency change and removes a source of error from the experiment.

After setting the lock-in phase using a DC voltage, we perform parametric amplification by adding the $2f_0$ voltage to the drive wire. The resulting modulated spring constant shift on the lever is due to both a DC voltage and an AC voltage at $2f_0$ and is calculated using Eq. 5.32. The spring constant is modulated at twice the resonance frequency by

$$\Delta k \approx \frac{1}{2} \frac{\partial^2 C}{\partial z^2} [2(V_{DC} - \varphi)V_{AC}] \quad (5.34)$$

The contributions to Δk from DC and $2f_0$ terms have been eliminated since the measured signal is lock-in demodulated at f_0 . When the phase between the drive and the pump is $2\phi = \pi/2$, the change in the out-of-phase cantilever amplitude will be maximized. When $2\phi = 0$, we expect no change in the out-of-phase amplitude.

5.4 Results

In this section, results from several parametric amplification experiments will be discussed. Parametric amplification will be confirmed by observing the in-phase and out-of-phase cantilever response with respect to the phase between the drive and the pump, and it will be shown that our cantilevers can be used to measure gain factors similar to those necessary to detect small spin ensembles. Finally, positive feedback will be used to produce the drive mode. This produces cantilever amplitude changes that are larger than predicted by parametric amplification. We conclude that the driven mode must instead come from a frequency source that is independent of the cantilever oscillation.

5.4.1 Confirming parametric amplification

As stated in Section 5.2.2, our goal is to measure a parametric gain factor of 0.03 using our cantilevers. We begin in this section by measuring a larger gain factor to verify the parametric effect. The cantilever is driven to an amplitude of approximately 58 nm by the piezo near f_0 and the phase between the drive and pump is set as described in Section 5.3.2. A DC voltage of -2 V is applied to the wire to shift the cantilever spring constant by an amount close to that expected in the parametric amplification experiment, and the lock-in phase is set to minimize the signal in the Y channel of the lock-in. According to Eq. 5.33 and the values of φ and $\partial^2C/\partial z^2$ from Table 5.1, we expect a $\Delta k = 3.7$ nN/m from the DC voltage. The voltage is momentarily turned off prior to data collection.

Figure 5.6 depicts the in-phase (X) and out-of-phase (Y) lock-in demodulated amplitudes of the cantilever during a parametric amplification experiment for several different phase settings (for clarity, not all values of the phase used in the experiment are shown). In the first 20 s of data acquisition, no voltage is applied to the wire. At approximately 20 s, $V_{DC} = -2$ V is applied to the wire and the measured X and Y amplitudes change to minimize the Y amplitude due to the resonance frequency shift set prior to data collection. The slow change in the cantilever signal is due to the high cantilever quality factor. The average of the data between $\sim 20 - 30$ s is used to determine X_{off} , Y_{off} , and R_{off} . After 40 s, an AC voltage at $2f_0$ of 1 V is sent to the wire in addition to V_{DC} , and a sudden change in the cantilever amplitude is observed. The addition of an AC voltage causes a modulated change in the spring constant of $\Delta k = 4.3$ nN/m, calculated using Eq. 5.34. As expected, this value is approximately equal to the Δk from the V_{DC} only. Based on the cantilever parameters in Table 5.1, we expect a parametric

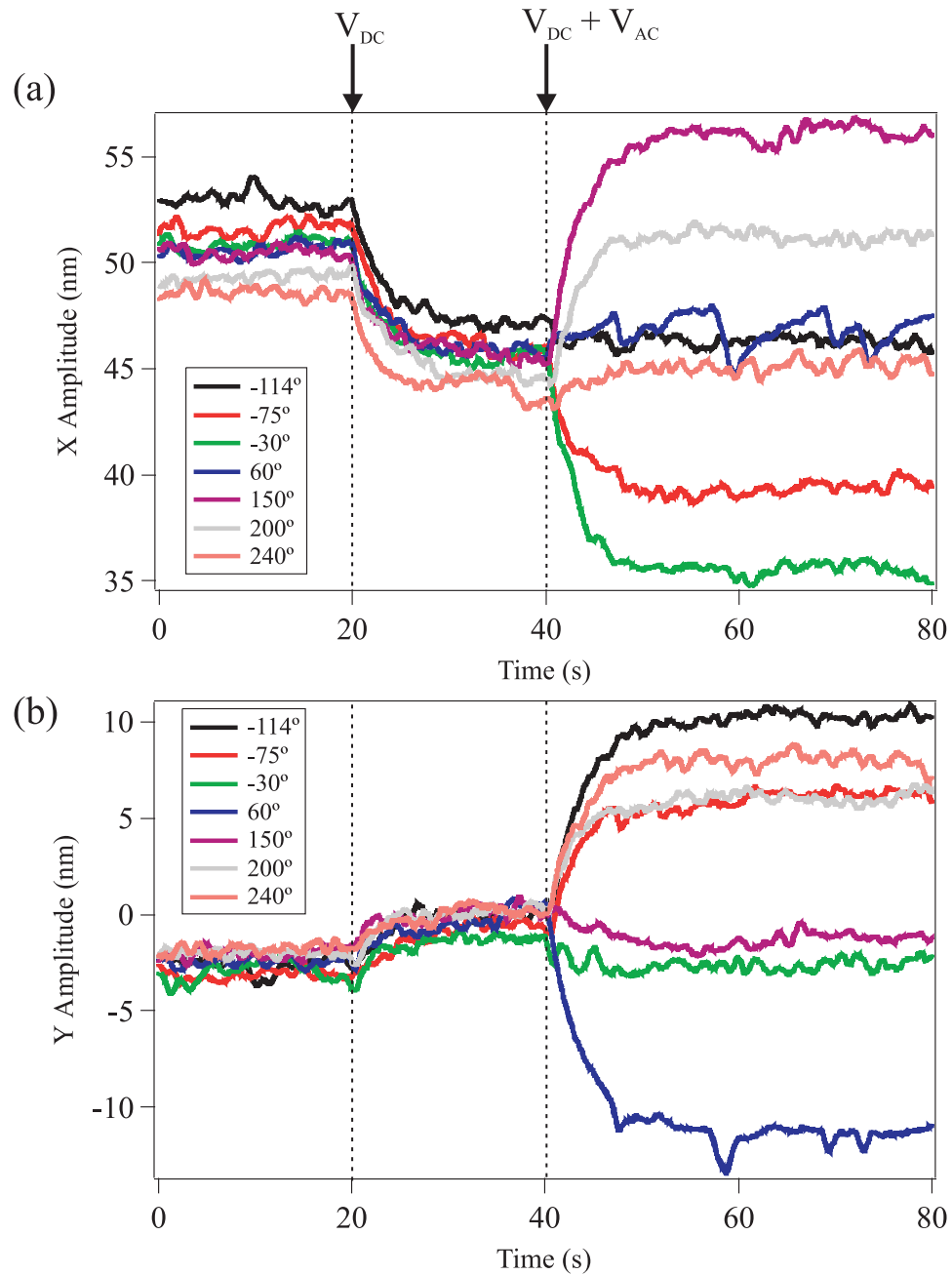


Figure 5.6: Lock-in in-phase (a) and out-of-phase (b) response versus time in the parametric amplification experiment for different phase angles between the drive and the pump. The cantilever is driven to an amplitude of 58 nm prior to modulating the spring constant.

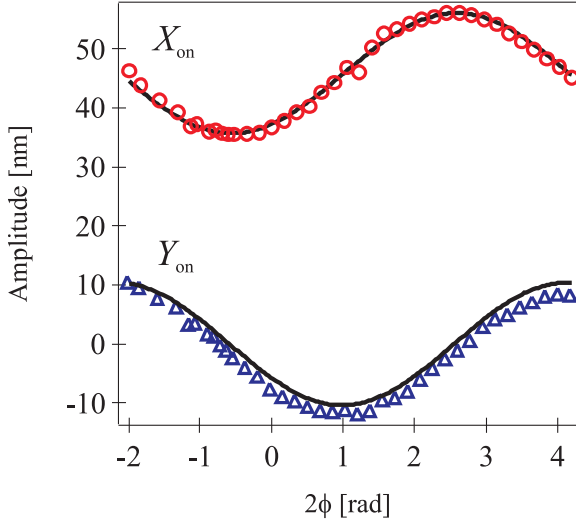


Figure 5.7: X_{on} and Y_{on} versus phase for the parametric amplification experiment. X_{on} (circles) is fit to Eq. 5.11 and Y_{on} (triangles) is fit to Eq. 5.12. The lines represent fits for $g = 0.22$ and a phase shift of $2\phi = -2.5 \text{ rad}$.

amplification gain factor of $g = Q\Delta k/2k = 0.18$. It is obvious from the figure that modulating the voltage on the wire has an effect on the cantilever amplitude that is a function of the phase between the drive and the pump, a defining feature of parametric amplification.

The X and Y cantilever amplitudes during the spring constant modulation ($\sim 50 \text{ s}$ to the end of the data set) are averaged for each phase setting and graphed in Figure 5.7. Fitting X_{on} to Eq. 5.11 and Y_{on} to Eq. 5.12 indicates that we are indeed seeing parametric amplification. The fits shown in the figure correspond to a gain factor of $g = 0.22$, in excellent agreement to the calculated g of 0.18. Additionally, X_{on} and Y_{on} are $\pi/2$ out of phase with each other, as expected and seen in Figure 5.1. The gain factor can also be determined by plotting the Gain, $R_{\text{on}}/R_{\text{off}}$, which is calculated using the appropriate average X and Y values when the amplification is on and off. The Gain is graphed in Figure 5.8 and fit using

Eq. 5.19 with $g = 0.20$. It appears that the observed deamplification that occurs between 0 and -1rad is slightly larger than predicted by Eq. 5.19. This may be due to the imprecise on-resonance drive frequency from the lock-in amplifier or from a drift of the cantilever signal off of the most sensitive part of the interferometer fringe.

Inspection of Y_{on} in Figure 5.7 shows that the first extremum occurs at $2\phi = -2\text{ rad}$ or -114° (the minimum possible phase change from the variable resistor) and a minimum occurs at $1.04\text{ rad} = 60^\circ$. These extrema are approximately π radians apart, but do not occur at $\pi/2$ and $3\pi/2$ as predicted. This is due to a large phase shift of -2.5 rad in the circuitry and the probe, determined by fitting X_{on} , Y_{on} , or the gain to a function with a phase offset. The phase shift due to the circuitry up to the band-pass filter is -2 rad , the initial offset measured when the phase shifter is not changing the phase. Thus, the circuitry after this point and the probe account for roughly 0.5 rad of phase shifting. These phase shifts are difficult to predict and control precisely from day to day, and it is necessary to account for the phase shift by performing a range of phase points and finding the overall phase shift. This shift is then used to determine the phase at which the maximum out-of-phase amplitude change occurs.

Finally, the maximum change in the in-phase amplitude can be used to measure the gain factor. The maximum displacement due to parametric amplification in X occurs at

$$X_{\text{on, max}} = -\frac{QF}{k} \frac{1}{1-g} \quad (5.35)$$

and the X amplitude when the parametric amplification is off is $X_{\text{off}} = -QF/k$. The gain factor can be determined by taking the ratio of these two values and

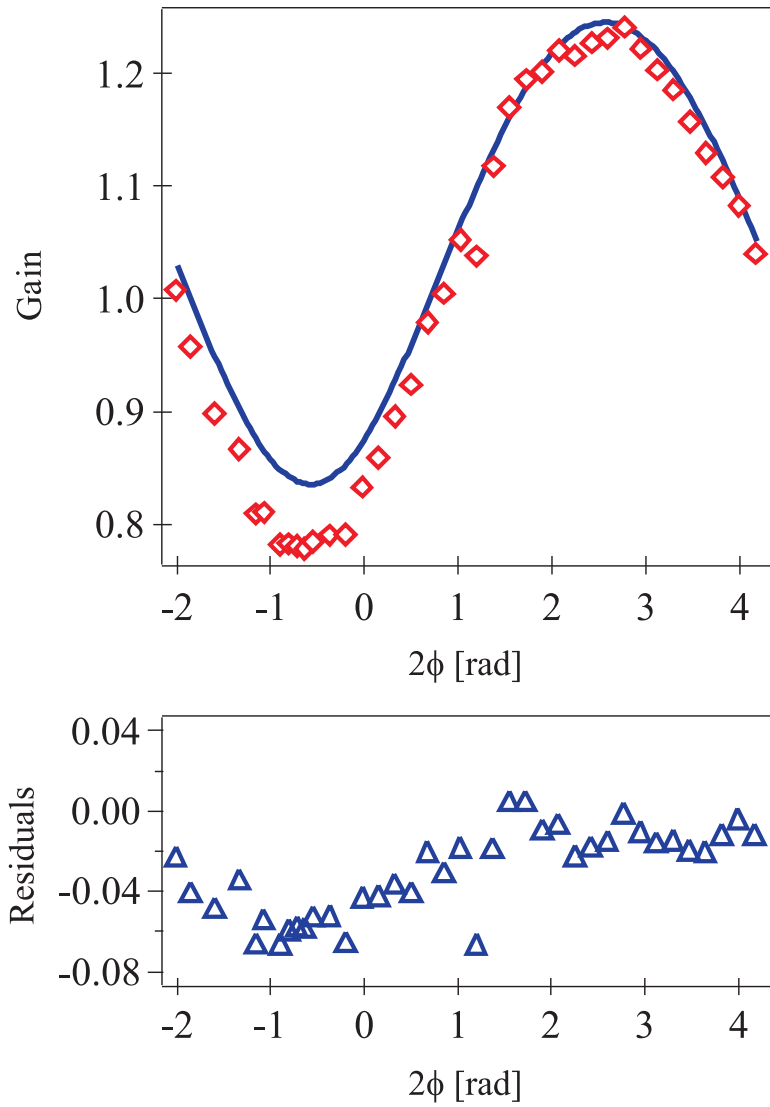


Figure 5.8: Gain and residuals versus phase for data from Figure 5.7. The line is a fit of the data to Eq. 5.19 with $g = 0.20$ and an overall phase shift of $2\phi = -2.5$ rad.

solving for g .

$$g = 1 - \frac{X_{\text{off}}}{X_{\text{on, max}}} \quad (5.36)$$

Based on Figure 5.7, where $X_{\text{on, max}} \sim 55 \text{ nm}$, $X_{\text{off}} \sim 45 \text{ nm}$, and we find that the gain factor is 0.18, in excellent agreement with the expected gain factor.

5.4.2 Measuring a small gain factor

Now that parametric amplification has been observed, the gain factor is decreased to a value on the order of 0.03 by decreasing the applied AC voltage. These experiments were performed approximately one week after the previous experiments using the same cantilever, which remained in vacuum in the interim. The cantilever drive amplitude was set to approximately 66 nm.

Initially, the AC voltage is set to 1V and a gain factor of 0.18 is expected, as in the previous experiment. The Gain ($R_{\text{on}}/R_{\text{off}}$) is plotted versus phase for $V_{\text{AC}} = 1\text{V}$ in Figure 5.9(a). A fit of the data to Eq. 5.19 finds that the gain factor is 0.37 and the overall phase shift is -3 rad . This gain factor is approximately twice as large as the expected g and the g previously measured under the identical conditions. This difference can be attributed to fluctuations in the contact potential (which can change by as much as 0.1 V from day to day), $\partial^2 C/\partial z^2$, spring constant, and quality factor. The k and Q used to calculate the theoretical g are based on averages of the cantilever parameters over several days.

In Figure 5.9(b), the AC voltage is reduced to 0.1V, and we expect the observed g to decrease by a factor of ten from the previous results. A fit of the Gain in Figure 5.9(b) results in $g = 0.045$, in excellent agreement with our expectations, and approximately twice as large as the gain factor calculated using the contact potential, $\partial^2 C/\partial z^2$, and the cantilever parameters.

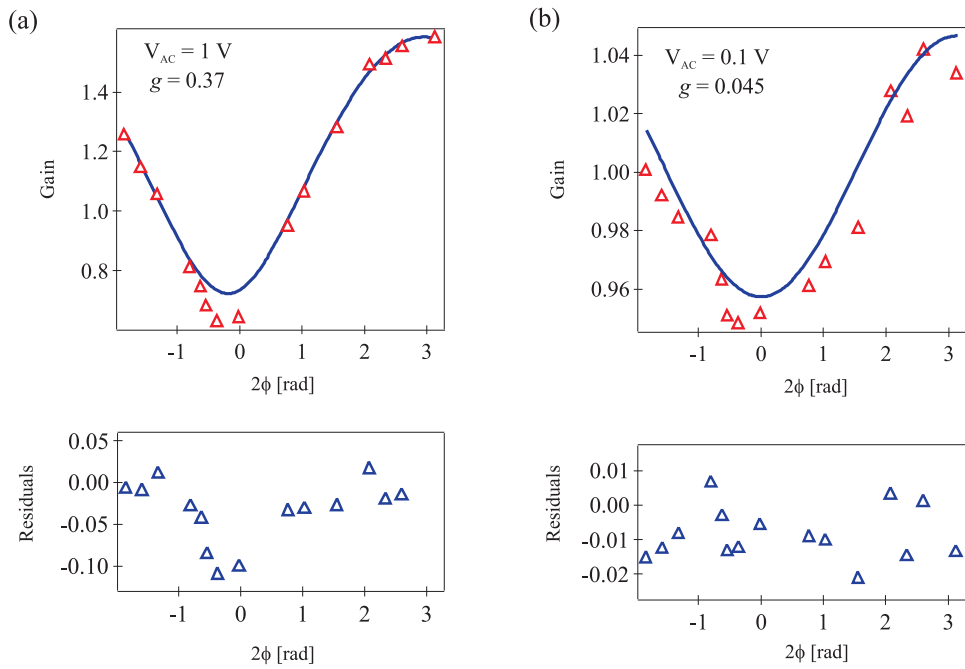


Figure 5.9: Gain and residuals versus phase at $V_{AC} = 1 \text{ V}$ (a) and $V_{AC} = 0.1 \text{ V}$ (b). In (a), the data is fit to Eq. 5.19 with a $g = 0.37$ and an overall phase of $2\phi = -3 \text{ rad}$. In (b), the AC voltage is decreased by a factor of ten. Fitting the data results in a $g = 0.045$ and an overall phase shift of $2\phi = -3.1 \text{ rad}$.

This small gain factor is the result of a spring constant shift of

$$\Delta k = \frac{2k}{Q}g = 1.1 \times 10^{-9} \text{ N/m} \quad (5.37)$$

If this cantilever was used in a CERMIT experiment with the magnetic tip in Ref. [33] ($\partial^2 B_z / \partial x^2 = 2 \times 10^{10} \text{ T/m}$), this Δk would correspond to the magnetic moment corresponding to 4×10^6 protons or 6,000 electrons, a factor of ten smaller than the corresponding magnetic moment measured in the CERMIT experiment. The cantilever used by Garner, *et al.* would be capable of measuring the spring constant shift from 3×10^5 protons or 300 electrons at this g , our original goal from Section 5.1. Thus, we conclude that parametric amplification can be used to measure the small spring constant shifts that would be experienced in a CERMIT experiment with few spins.

Although the amplitude shift is small from a g of 0.03, it is still easily measurable using a lock-in amplifier. The maximum gain is ~ 1.04 , which is a change in the magnitude of the cantilever amplitude of $1.04 \times 66 \text{ nm} = 2.6 \text{ nm}$. If this amplitude change is too small to measure with the lock-in, X_{on} and Y_{on} can be increased by increasing the driving amplitude.

5.4.3 Parametric amplification with positive feedback

In both CERMIT and force gradient detected ESR experiments, the cantilever is driven at f_0 with positive feedback in order to detect changes in the cantilever resonance frequency. In this section, we detail results where the drive in the parametric amplification experiment is replaced with positive feedback.

The experimental setup is nearly identical to that discussed in Section 5.3.2 and Figure 5.3. In this experiment, the cantilever is driven on-resonance with a positive

feedback circuit (discussed in Section 4.3.3), rather than using the sine out of the lock-in. The output of the interferometer determines the drive frequency in the positive feedback circuit and is also the input of the lock-in amplifier. Synthesizing the $2f_0$ signal is more difficult in this case because the output of the positive feedback circuit is a square wave, which is not compatible with the frequency doubler. This square wave at f_0 is converted to a sine wave at f_0 by setting the square wave as the external reference of the lock-in, and f_{LI} is precisely f_0 . The lock-in sine out now provides a sine wave at f_0 which is used to make $2f_0$ as before. In this setup, the lock-in is referenced to the cantilever signal via the positive feedback circuit and changes when a Δk is applied. Initially, it was believed that this would be advantageous since the spring constant shift would no longer be able to move the cantilever resonance outside of the lock-in bandwidth, as is possible in the previous experimental setup.

Experiments were performed using the methods discussed previously. The cantilever was driven to an amplitude of 69 nm using positive feedback. The spring constant of the cantilever was modulated at $2f_0$ using $V_{\text{DC}} = -2 \text{ V}$ and $V_{\text{AC}} = 1 \text{ V}$, and the phase between the drive and the pump was set to several different values. A phase-dependent amplitude change is observed and plotted in Figure 5.10(a). The line shown is the best fit of the data to Eq. 5.19, resulting in $g = 0.34$ and an overall phase shift of -2.5 rad . However, the amplification and deamplification are larger than in previous experiments. We also note that the observed Gain does not follow the shape of the sinusoid as we saw in the earlier case, and the residuals of the fit are twice as large in this case as the residuals seen in the previous examples without positive feedback.

The X_{on} and Y_{on} , plotted in Figure 5.10(b) do not behave as expected when

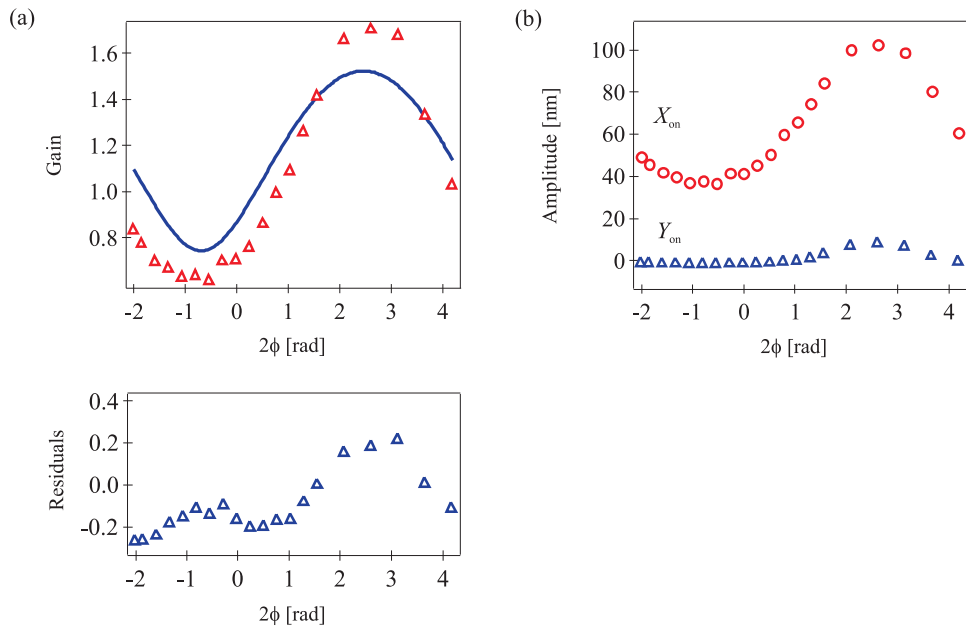


Figure 5.10: Gain, X_{on} , and Y_{on} versus phase with positive feedback. (a) The gain (triangles) versus phase for the cantilever amplitude change when driving the cantilever with positive feedback. The line is a plot of Eq. 5.19 with $g = 0.34$ and a phase shift of -2.5 rad. The amplification and deamplification seen in the experiment are larger than expected. (b) X_{on} and Y_{on} versus phase. The phase between the X and Y amplitudes are different than that seen in parametric amplification.

modulating the spring constant at $2f_0$. The phase difference between the two signals deviates from normal parametric amplification as depicted in Figure 5.1 where X_{on} and Y_{on} are $2\phi = \pi/2$ rad out-of-phase. In fact, Y_{on} is relatively constant until it begins to increase around 1 rad and does not appear to be sinusoidal at all. Based on the behavior of X_{on} and Y_{on} , it is likely that some effect other than parametric amplification is causing a phase dependent amplitude change.

This is possibly the result of the constantly changing drive frequency produced by the positive feedback circuit creating a feedback loop. As the spring constant is modulated at $2f_0$, the resonance frequency is also modulated at $2f_0$. This changing frequency at $2f_0$ is registered by the positive feedback circuit, and the circuit produces a constantly changing drive signal. This, in turn, affects both the lock-in reference frequency and the $2f_0$ pump signal, creating a type of feedback circuit that changes the magnitude of the amplification and deamplification that we expect in a parametric amplification experiment. It is possible that parametric amplification is occurring, but we observe a more complex behavior than expected due to additional phase modulations. We conclude that it is important to use a drive frequency that does not change during the experiment, even if that frequency is slightly off resonance.

5.5 Summary and Conclusions

In this chapter, a possible MRFM experiment has been identified which would use parametric amplification as a method for detecting spring constant shifts from small ensembles of spins. Control experiments indicate that modulating spring constant shifts as small as 1.1×10^{-9} N/m at twice the cantilever frequency can easily be detected as a change in cantilever amplitude using lock-in techniques.

It can be imagined that cantilevers with higher quality factors and lower spring constants could be used to detect fewer than 3×10^5 net protons or 300 net electrons with CERMIT techniques.

It has also been determined that driving the cantilever with positive feedback in parametric amplification experiments results in larger than expected changes in magnitude and phase behavior inconsistent with parametric amplification. Positive feedback introduces several issues with respect to the phase of the drive and pump signals, and ultimately changes the in-phase and out-of-phase cantilever amplitude response with respect to the phase between the drive and the pump. Therefore, we are limited to frequency sources that are independent of the changing cantilever frequency.

In future experiments, care should be taken to ensure that the resulting frequency shifts from parametric amplification do not affect the measurement of the cantilever amplitude by lock-in detection techniques. If the cantilever frequency shift is a significant portion of the lock-in bandwidth or larger, the measured signal will deviate from the expected signal. For high Q cantilevers with narrow resonance peaks, it may be necessary to drive with a frequency source that can be controlled more precisely at millihertz frequencies, such as the NIFGEN.

Finally, the use of analog electronics resulted in several complications regarding the phase between the drive and the pump. Precise control of the phase difference between the drive and the pump using the variable resistor was very difficult. This could be simplified greatly by using a digital delay generator, which creates a precise phase-shifted copy of the input. This phase shifted signal could then easily be doubled using the current method. The time required to perform parametric amplification experiments could also be greatly reduced by controlling the digital

delay generator with a Labview program. Finally, it may also be possible to create the drive frequency and a phase-shifted pump frequency with a digital signal processor, eliminating most of the overall phase shifts from the analog electronics.

APPENDIX A

PEAK SEPARATION IN THE LOW GRADIENT REGIME

In the low gradient force and force gradient experiments, it was observed in Figure 4.10 that the peaks were located approximately 350 G apart, not 248G as expected. Since we are working at an rf frequency of 348 MHz, we expect the resonance for electrons to occur at a field of 124G (see Eq. 4.37) and, in the absence of the tip field from the magnetic particle, we would expect to see the resonance peaks at external fields of +124 G and -124 G. The presence of the tip field has the effect of shifting the peaks more positive or negative in field, but they should remain 248 G apart if the tip field is independent of the external field.

As mentioned in Section 4.5.1, the discrepancy in the peak separation is not a function of the sample. Experiments with this identical sample at 77 K and an Alnico particle show peaks that are 248 G apart. What could cause the distance between the peaks to be larger than expected? The most obvious culprit is the value of the coil constant, but this cannot account for the difference alone.

The external magnetic field is controlled by changing the current that is sent to the magnetic leads. The current is converted to a field using the given coil constant. Thus, the coil constant sets the x axis of the experiment. If the coil constant used in the conversion is larger than the actual coil constant, the peaks will be farther apart on the graph than they should be. In the center of the magnet, the coil constant is well known based on data and information provided by the manufacturer. We are forced to work above the magnet center in order to have a coil constant that is small enough to see our resonance peak. This introduces a great deal of error.

The coil constant above the magnet was determined using the computer sim-

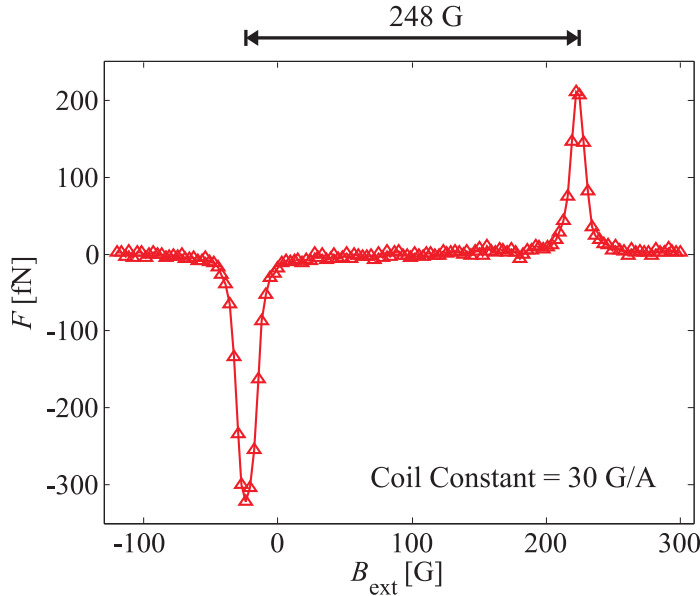


Figure A.1: Low gradient force data plotted against the external field with the coil constant set to make the distance between the peaks 248 G.

ulated values provided by the manufacturer. Based on a proportionality, the coil constant 14 cm above the magnet is 43 G/A, and this is the coil constant used to determine the x axis in Figure 4.10. What would the coil constant be if we set the distance between the peaks to be 248 G apart? Using the current in amperes as the x axis the coil constant would have to be 30 G/A in order to have the peaks separated by the proper distance. This corresponds to a distance above the magnet center of 16 cm. Based on measurements of distances inside the probe and the dewar and the opportunities for error in setting the distance, it would be reasonable to assume that the error in the distance above the magnet center is about 1 – 2 cm. Thus some of the error in the peak separation can be ascribed to error in the coil constant.

If the x axis is converted to field using 30 G/A, will this resolve our problems? Changing the coil constant results in the first peak moving to an external field of

-24G and the second peak shifting to $+222\text{G}$, and the peaks are now 246G apart as seen in Fig A.1. Note that changing the x axis alters the gradient values obtained from the low gradient simulations in Section 4.6.4 (changing the distance between the points in field changes the calculated numerical derivative). Performing the simulations with the new field values, we find that the first peak would have a gradient of 50T/m and a $B_{\text{tip}} = -100\text{ G}$. The second peak would have a gradient of 30T/m and a $B_{\text{tip}} = -50\text{ G}$.

Interestingly, the resonance values based on these simulations do not agree with the known resonance values. The resonance field at the first peak is determined using

$$B_{\text{res}} = -100\text{ G} + (-24\text{ G}) = -124\text{ G} \quad (\text{A.1})$$

which agrees with what we expect. However, the resonance field at the second peak is

$$B_{\text{res}} = -50\text{ G} + 222\text{ G} = +172\text{ G} \quad (\text{A.2})$$

which disagrees significantly with the expected value of $+124\text{ G}$. Therefore, errors associated with the coil constant alone cannot completely explain our peak separation problems.

Another factor to consider is the effect of the changing tip field on the distance between the peaks. If the magnitude of the tip field is decreasing during the external field sweep, which is the case in this experiment when the field is being swept from negative to positive, the distance between the peaks would decrease and our peaks should be closer together than 248 G . Unfortunately, it is not possible to determine how close they should be since we cannot determine the tip fields without some knowledge of the coil constant. The method of determining the coil constant based on the data depends on knowing the distance between the peaks

and it is impossible to say for sure how close the peaks actually are. In any case, this error would be small (in the tens of gauss), and does not change the fact that a force gradient effect is being detected.

An additional source of error could be due to the presence of a diamagnetic material or a material that is superconducting (like solder). A magnetic field created by either of these materials would add to the tip field and the external field and would have the effect of bringing the peaks closer together. A fractional change of two-thirds would be sufficient to make the peaks 240 G apart, assuming a coil constant of 43 G/A. These extraneous fields would not be a problem if we were working in the homogenous fields at the center of the magnet. Since we are working in the outer edges of the magnetic fields, we are susceptible to weak external fields.

Luckily, the important information in the signal is only weakly dependent on the x axis. Changes in the x axis to compensate for error in the coil constant do not have a large effect on the spring constant shifts, nor do they alter our central conclusion that the signal in Figure 4.10 is due to a force gradient effect governed by the OSCAR term in the derivative of the force. In future experiments, care should be taken to determine the correct coil constant and to saturate the magnetic particle completely to avoid a changing tip field.

APPENDIX B

DERIVATION OF THE SPIN DIFFUSION LENGTH

When the magnetization in the slice becomes saturated by an rf field in an electron spin resonance experiment, an entropic drive towards thermodynamic equilibrium occurs. Spins outside of the slice begin to saturate in order to maximize the entropy in the system. However, these newly saturated spins are outside of the sensitive slice and off-resonance, and the spins will begin to relax along the external field in a time T_1 . This competition between relaxation and saturation outside of the slice can be described by a differential equation, and solving this equation at steady state (ie, when the relaxation and saturation mechanisms are at equilibrium) will allow us to determine the maximum distance that spins may diffuse.

The diffusion length in a spin system at equilibrium can be derived for a classical ensemble of spins based on the diffusion equation used in conventional statistical thermodynamics to describe heat flow and other diffusion related phenomena [137]

$$\frac{\partial \rho_m}{\partial t} = D \frac{\partial^2 \rho_m}{\partial x^2} \quad (\text{B.1})$$

where ρ_m is the spin magnetization density and D is the diffusion constant in units of meters squared per second. The diffusion constant is equal to Wa^2 where a is the distance between spins (~ 1 nm) and W is the probability of a spin flip-flop between nearest neighbors [118]. Typical values of D and W for nuclei are on the order of 10^{-17} m 2 /s and 10^3 s $^{-1}$, respectively.

To account for the relaxation of the off-resonance spins outside of the slice, another term is added to the right hand side of Eq. B.1

$$\frac{\partial \Delta \rho_m}{\partial t} = D \frac{\partial^2 \Delta \rho_m}{\partial x^2} - \frac{1}{T_1} \Delta \rho_m \quad (\text{B.2})$$

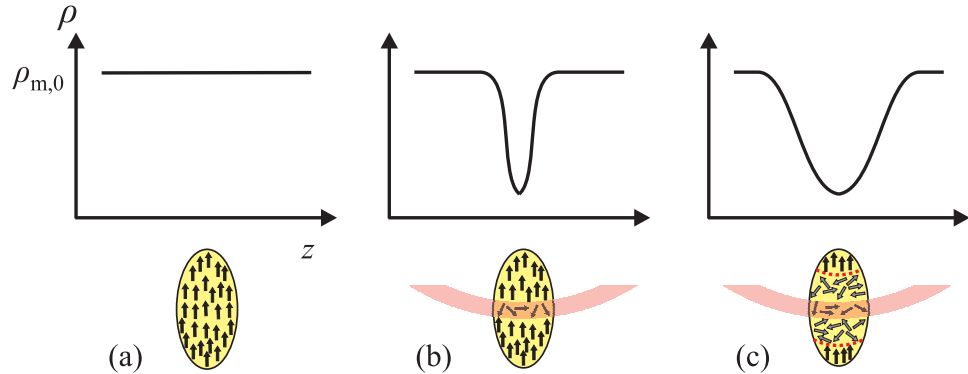


Figure B.1: Spin magnetization density at steady state with spin diffusion.

Initially in (a), the spin magnetization density is at a value of $\rho_{m,0}$. When the spins are initially saturated in (b), the slice is about $2 \mu\text{m}$ thick. As the steady-state is reached in (c), the affected magnetization diffuses out to a larger effective slice.

where $\Delta\rho_m = \rho_m - \rho_{m,0}$, and $\rho_{m,0}$ is the initial spin magnetization density before the spins are randomized. This is the familiar relaxation term for the longitudinal relaxation of the spins, developed by Bloch. We want to solve this differential equation at steady-state ($\partial\Delta\rho_m/\partial t = 0$) after the spin magnetization has had time to diffuse and come to equilibrium, as shown in Figure B.1(c). This derivation assumes that the slice stays saturated during the experiment while the rf is on and that the slice is infinitely thin. Even though our slice is “thick”, it is still thinner than the sample when in the center of the sample, validating this approximation.

At steady-state, we can write Eq. B.2 as

$$DT_1 \frac{\partial^2 \Delta\rho_m}{\partial x^2} = \Delta\rho_m \quad (\text{B.3})$$

To solve this differential equation, we will assume that the solution has the form

$$\Delta\rho_m(x) = \Delta\rho_m(0)e^{-kx} \quad (\text{B.4})$$

where $\Delta\rho_m(0)$ is the initial $\Delta\rho_m$ immediately after saturation of the spins and before any diffusion can take place, assuming that the slice defined by $\Delta\rho_m(0)$ is thin compared to the sample thickness. Inserting the solution into Eq. B.3 results in $k = (DT_1)^{-1/2}$ and the change in the spin magnetization density as a function of distance is

$$\Delta\rho_m(x) = \Delta\rho_m(0)e^{-x/\sqrt{DT_1}} \quad (\text{B.5})$$

At a distance $x = L = \sqrt{DT_1}$, the $\Delta\rho_m$ has decreased from its original value by a factor of $1/e$. Therefore, the maximum distance outside of the slice that the spin magnetization will diffuse is on the order of $L = \sqrt{DT_1}$.

It should also be noted that this is the limit of the diffusion length when the rf modulation is zero. If the modulation frequency increases, it can be imagined that the diffusion length would be less than the unmodulated case. When the rf is on, spins could diffuse outside of the slice. When the rf is off, the spin diffusion would stop since the thermodynamic drive to equilibrium is no longer present. If this modulation is fast, the diffusing spins would not have time to reach equilibrium before the rf is turned off and the diffusion length would be less than $\sqrt{DT_1}$. The more general case for the spin diffusion length including the modulation frequency is

$$L = \sqrt{D \frac{T_1}{1 + \omega_m T_1}} \quad (\text{B.6})$$

where ω_m is the rf modulation frequency. When $\omega_m = 0$, L becomes $\sqrt{DT_1}$, as expected. When the modulation frequency is large compared to T_1 , as in a typical cyclic saturation force experiment, the spin diffusion length becomes $L = (D/\omega_m)^{1/2}$. This diffusion length limit is observed and discussed for a cyclic saturation force experiment in Ref. [106].

REFERENCES

- [1] K. Wuthrich, Acc. Chem. Res. **22**, 36 (1989).
- [2] K. Wuthrich, Angew. Chem. Intl. Ed. **42**, 3340 (2003), Kinetic aspects;.
- [3] J. Aguayo, S. Blackband, J. Schoeniger, M. Mattingly, and M. Hintermann, Nature **322**, 190 (1986).
- [4] L. Ciobanu, D. Seeber, and C. Pennington, J. Magn. Reson. **158**, 178 (2002).
- [5] <http://www.rcsb.org/pdb/home/home.do>.
- [6] J. A. Sidles, J. L. Garbini, K. J. Bruland, and D. Rugar, Rev. Mod. Phys. **67**, 249 (1995).
- [7] N. Darby and T. Creighton, *Protein Structure*, IRL Press at Oxford University Press, 1993.
- [8] J. Sidles, Appl. Phys. Lett. **58**, 2854 (1991).
- [9] J. Sidles, Phys. Rev. Lett. **68**, 1124 (1992).
- [10] D. Rugar, R. Budaklan, H. Mamin, and B. Chui, Nature **430**, 329 (2004).
- [11] D. Rugar, Nuclear spin magnetic resonance force microscopy: Progress, challenges and prospects, in *Magnetic Resonance Force Microscopy: Routes to Three-Dimensional Imaging of Single Molecules*, Kavli Institute at Cornell Summer School in MRFM, 2006.
- [12] D. Weishaupt, V. Kochli, and B. Marincek, *How does MRI work?: An Introduction to the Physics and Function of Magnetic Resonance Imaging*, Springer, 2003.
- [13] M. Grandbois, M. Beyer, M. Rief, H. Clausen-Schaumann, and H. Gaub, Science **283**, 1727 (1999).
- [14] J. Finer, R. Simmons, and J. Sputlich, Nature **368**, 113 (1994).
- [15] J. Marohn, R. Fainchtein, and D. Smith, J. Appl. Phys. **86**, 4619 (1999).
- [16] T. Stowe et al., Appl. Phys. Lett. **71**, 288 (1997).
- [17] P. Streckeisen et al., Appl. Phys. A-Mater. Sci. Process. **66**, S341 (1998).
- [18] H. Mamin and D. Rugar, Appl. Phys. Lett. **79**, 3358 (2001).
- [19] N. Jenkins et al., J. Vac. Sci. Technol. B **22**, 909 (2004).

- [20] J. Sidles and J. Garbini, Program for achieving single nuclear spin detection, <http://courses.washington.edu/goodall/MRFM>, 2005.
- [21] D. Rugar, C. Yannoni, and J. Sidles, *Nature* **360**, 563 (1992).
- [22] O. Zuger and D. Rugar, *Appl. Phys. Lett.* **63**, 2496 (1993).
- [23] O. Zuger and D. Rugar, *J. Appl. Phys.* **75**, 6211 (1994).
- [24] D. Rugar et al., *Science* **264**, 1560 (1994).
- [25] O. Zuger, S. Hoen, C. Yannoni, and D. Rugar, *J. Appl. Phys.* **79**, 1881 (1996).
- [26] Z. Zhang, P. Hammel, and P. Wigen, *Appl. Phys. Lett.* **68**, 2005 (1996).
- [27] K. Wago, O. Zuger, R. Kendrick, C. S. Yannoni, and D. Rugar, *J. Vac. Sci. Technol. B* **14**, 1197 (1996).
- [28] K. Wago, D. Botkin, C. Yannoni, and D. Rugar, *Phys. Rev. B* **57**, 1108 (1998).
- [29] K. Wago, D. Botkin, C. Yannoni, and D. Rugar, *Appl. Phys. Lett.* **72**, 2757 (1998).
- [30] K. Bruland, W. Dougherty, J. Garbini, J. Sidles, and S. Chao, *Appl. Phys. Lett.* **73**, 3159 (1998).
- [31] B. Stipe et al., *Phys. Rev. Lett.* **87**, 277602 (2001).
- [32] H. Mamin, R. Budakian, B. Chui, and D. Rugar, *Phys. Rev. Lett.* **91**, 207604 (2003).
- [33] S. Garner, S. Kuehn, J. Dawlaty, N. Jenkins, and J. Marohn, *Appl. Phys. Lett.* **84**, 5091 (2004).
- [34] H. Mamin, R. Budakian, B. Chui, and D. Rugar, *Phys. Rev. B: Condens. Matter Mater. Phys.* **72**, 24413 (2005).
- [35] R. Weeks and C. Nelson, *J. Appl. Phys.* **31**, 1555 (1960).
- [36] J. Castle, J.G. and D. Feldman, *J. Appl. Phys.* **36**, 127 (1965).
- [37] L. E. Kinsler, A. R. Frey, A. B. Coppens, and J. V. Sanders, *Fundamentals of Acoustics, 4th Edition*, Wiley & Sons, 2000.
- [38] J. Hutter and J. Bechhoefer, *Rev. Sci. Instrum.* **64**, 1868 (1993).
- [39] K. Yasumura et al., *J. Microelectromech. Syst.* **9**, 117 (2000).

- [40] Y. Wang, J. A. Henry, A. T. Zehnder, and M. A. Hines, *J. Phys. Chem. B* **107**, 14270 (2003).
- [41] J. A. Henry, Y. Wang, and M. A. Hines, *Appl. Phys. Lett.* **84**, 1765 (2004).
- [42] Y. Wang, J. A. Henry, D. Sengupta, and M. A. Hines, *Appl. Phys. Lett.* **85**, 5736 (2004).
- [43] T. D. D. Stowe, *Extending the limits of force sensitivity using micromachined silicon cantilevers*, PhD thesis, Stanford University, 2000.
- [44] B. Stipe, H. Mamin, T. Stowe, T. Kenny, and D. Rugar, *Phys. Rev. Lett.* **86**, 2874 (2001).
- [45] D. Rugar et al., *Appl. Phys. A* **72**, S3 (2001).
- [46] S. Mouaziz et al., *Microelectron. Eng.* **83**, 1306 (2006).
- [47] J. Arlett, J. Maloney, B. Gudlewski, M. Muluneh, and M. Roukes, *Nano Lett.* **6**, 1000 (2006).
- [48] V. Sazonova et al., *Nature* **431**, 284 (2004).
- [49] M. LaHaye, O. Buu, B. Camarota, and K. Schwab, *Science* **304**, 74 (2004).
- [50] J. Sidles, J. Garbini, and G. Drobny, *Rev. Sci. Instrum.* **63**, 3881 (1992).
- [51] S. Kuehn, R. Loring, and J. Marohn, *Phys. Rev. Lett.* **96**, 156103 (2006).
- [52] D. Carr, S. Evoy, L. Sekaric, H. Craighead, and J. Parpia, *Appl. Phys. Lett.* **75**, 920 (1999).
- [53] S. Verbridge, J. Parpia, R. Reichenbach, L. Bellan, and H. Craighead, *J. Appl. Phys.* **99**, 124304 (2006).
- [54] S. Evoy et al., *Appl. Phys. Lett.* **77**, 2397 (2000).
- [55] R. G. Knobel and A. N. Cleland, *Nature* **424**, 291 (2003).
- [56] K. Ekinci and M. Roukes, *Rev. Sci. Instrum.* **76**, 061101 (2005).
- [57] K. Schwab, Direct detection of small numbers of nuclear spins, in *Magnetic Resonance Force Microscopy: Routes to Three-Dimensional Imaging of Single Molecules*, Kavli Institute at Cornell Summer School in MRFM, 2006.
- [58] K. C. Schwab and M. L. Roukes, *Physics Today* **58**, 36 (2005).
- [59] T. N. Ng, N. Jenkins, and J. Marohn, *IEEE Trans. Mag.* **42**, 378 (2006).
- [60] J. Marohn, R. Fainchtein, and D. Smith, *Appl. Phys. Lett.* **73**, 3778 (1998).

- [61] J. L. Yang, T. Ono, and M. Esashi, *Sens. Actuator A-Phys.* **82**, 102 (2000).
- [62] SOITEC, Part 40008P.
- [63] G. Higashi, Y. Chabal, G. Trucks, and K. Raghavachari, *Appl. Phys. Lett.* **56**, 656 (1990).
- [64] M. Houston and R. Maboudian, *J. Appl. Phys.* **78**, 3801 (1995).
- [65] K. N. Tu, *Appl. Phys. Lett.* **27**, 221 (1975).
- [66] J. M. Poate, K. N. Tu, and J. W. Mayer, editors, *Thin Films – Interdiffusion and Reactions*, chapter by K. N. Tu and J. W. Mayer, page 359, Wiley, New York, 1982.
- [67] M. A. Douglas, Trench etch process for a single-wafer RIE dry etcher reactor, U.S. Patent US4855017, Texas Instruments Inc., 1998.
- [68] F. Lärmer and A. Schilp, Verfahren zum anisotropen ätzen von Silicium, German Patent DE4241045, Robert Bosch GmbH, 1994.
- [69] A. A. Ayon, R. Braff, C. C. Lin, H. H. Sawin, and M. A. Schmidt, *J. Electrochem. Soc.* **146**, 339 (1999).
- [70] A. A. Ayon, R. L. Bayt, and K. S. Breuer, *Smart Mater. Struct.* **10**, 1135 (2001).
- [71] T. Albrecht, P. Grutter, D. Rugar, and D. Smith, *Ultramicroscopy* **42-44**, 1638 (1992).
- [72] K. Bruland et al., *Rev. Sci. Instrum.* **70**, 3542 (1999).
- [73] K. Bruland, J. Krzystek, J. Garbini, and J. Sidles, *Rev. Sci. Instrum.* **66**, 2853 (1995).
- [74] S. Garner, *Force-gradient Detection of Nuclear Magnetic Resonance*, PhD thesis, Cornell University, 2005.
- [75] D. E. Gray, editor, *American Institute of Physics Handbook*, chapter 2, McGraw Hill, third edition, 1972.
- [76] K. E. Petersen, *Proc. IEEE* **70**, 420 (1982).
- [77] S. Evoy et al., *J. Appl. Phys.* **86**, 6072 (1999).
- [78] L. Sekaric et al., *Appl. Phys. Lett.* **81**, 4455 (2002).
- [79] A. Aharoni, *J. Appl. Phys.* **83**, 3432 (1998).

- [80] R. H. Kodama, S. A. Makhlof, and A. E. Berkowitz, Phys. Rev. Lett. **79**, 1393 (1997).
- [81] F. Schreiber, Prog. Surf. Sci. **65**, 151 (2000).
- [82] D. L. Allara, Biosensors & Bioelectronics **10**, 771 (1995).
- [83] A. Ulman, *Thin Films (Volume 24): Self-Assembled Monolayers of Thiols*, Academic Press, 1998.
- [84] G. Berman, G. Doolen, P. Hammel, and V. Tsifrinovich, Phys. Rev. B **61**, 14694 (2000).
- [85] G. Berman, V. Tsifrinovich, and D. Allara, Phys. Rev. B **66**, 193406 (2002).
- [86] K. Kim and S. Lee, J. Appl. Phys. **91**, 4715 (2002).
- [87] C. K. Harnett, K. M. Satyalakshmi, and H. G. Craighead, Langmuir **17**, 178 (2001).
- [88] L. Reven and L. Dickinson, *Thin Films (Volume 24): Self-Assembled Monolayers of Thiols*, Academic Press, 1998.
- [89] D. Marsh, T. Pali, and L. Horvath, *Progressive saturation and saturation transfer EPR for measuring exchange processes and proximity relations in membranes*, volume 14, Spin Labelling: The Next Millenium of Biological Magnetic Resonance, Plenum Press, New York, 1998.
- [90] D. Marsh and D. Livshits, Phys. Med. Biol. **43**, 1977 (1998).
- [91] P. Percival and J. Hyde, J. Magn. Reson. **23**, 249 (1976).
- [92] C. Farrar, D. Hall, G. Gerfen, S. Inati, and R. Griffin, J. Chem. Phys. **114**, 4922 (2001).
- [93] B. Robinson, D. Haas, and C. Mailer, Science **263**, 490 (1994).
- [94] K. Wago et al., Rev. Sci. Instrum. **68**, 1823 (1997).
- [95] M. Goldman, *Quantum Description of High-Resolution NMR in Liquids*, Oxford Science Publications, 1991.
- [96] T. Albrecht, P. Grutter, D. Horne, and D. Rugar, J. Appl. Phys. **69**, 668 (1991).
- [97] <http://www.arnoldmagnetics.com/products/samarium/pdf/slmsam.pdf>.
- [98] G. Pake, *Paramagnetic Resonance*, W.A. Benjamin, Inc., New York, 1962.
- [99] L. Singer and E. Spencer, J. Chem. Phys. **21**, 939 (1953).

- [100] L. Singer and C. Kikuchi, J. Chem. Phys. **23**, 1738 (1955).
- [101] G. Whitfield and A. Redfield, Phys. Rev. **106**, 918 (1957).
- [102] Goldsborough, M. J.P., Mandel, and G. Pake, Phys. Rev. Lett. **4**, 13 (1960).
- [103] J. Burg and P. Grobet, J. Magn. Magn. Mater. **31-34**, 655 (1983).
- [104] A. Suter, D. Pelekhov, M. Roukes, and P. Hammel, J. Magn. Reson. **154**, 210 (2002).
- [105] J. Turkevich, J. Soria, and M. Che, J. Chem. Phys. **56**, 1463 (1972).
- [106] W. Dougherty et al., J. Magn. Reson. **143**, 106 (2000).
- [107] D. Suter and R. Ernst, Phys. Rev. B **32**, 5608 (1985).
- [108] C. Tang and J. Waugh, Phys. Rev. B **45**, 748 (1992).
- [109] N. Bloembergen, Physica **15**, 386 (1949).
- [110] W.-K. Rhim, A. Pines, and J. Waugh, Phys. Rev. B **3**, 684 (1971).
- [111] P. Caravatti, J. Deli, G. Bodenhausen, and R. Ernst, J. Am. Chem. Soc. **104**, 5506 (1982).
- [112] P. Henrichs and M. Linder, J. Magn. Reson. **58**, 458 (1984).
- [113] P. Robyr, B. Meier, and R. Ernst, Chem. Phys. Lett. **187**, 471 (1991).
- [114] W. Zhang and D. Cory, Phys. Rev. Lett. **80**, 1324 (1998).
- [115] R. Budakian, H. Mamin, and D. Rugar, Phys. Rev. Lett. **92**, 037205 (2004).
- [116] G. Berman, B. Chernobrod, V. Gorshkov, and V. Tsifrinovich, Phys. Rev. B **71**, 184409 (2005).
- [117] M. Levitt, *Spin Dynamics: Basics of Nuclear Magnetic Resonance*, John Wiley & Sons, 2001.
- [118] A. Abragam, *Principles of Nuclear Magnetism*, Oxford, 1961.
- [119] A. Overhauser, Phys. Rev. **89**, 689 (1953).
- [120] A. Overhauser, Phys. Rev. **92**, 411 (1953).
- [121] T. Carver and C. Slichter, Phys. Rev. **92**, 212 (1953).
- [122] T. Carver and C. Slichter, Phys. Rev. **102**, 975 (1956).
- [123] N. Bloembergen, E. Purcell, and R. Pound, Phys. Rev. **73**, 679 (1948).

- [124] D. W. Carr, S. Evoy, L. Sekaric, H. G. Craighead, and J. M. Parpia, Appl. Phys. Lett. **77**, 1545 (2000).
- [125] L. Adler and M. Breazeale, Amer. J. of Phys. **39**, 1522 (1971).
- [126] M. Faraday, Phil. Trans. Roy. Soc. (London) **121**, 299 (1831).
- [127] L. Rayleigh, Phil. Mag. **24**, 145 (1887).
- [128] D. Rugar and P. Grutter, Phys. Rev. Lett. **67**, 699 (1991).
- [129] W. Dougherty, K. Bruland, J. Garbini, and J. Sidles, Meas. Sci. & Tech. **7**, 1733 (1996).
- [130] M. Zalalutdinov et al., Appl. Phys. Lett. **78**, 3142 (2001).
- [131] M. Zalalutdinov et al., Appl. Phys. Lett. **79**, 695 (2001).
- [132] L. Sekaric et al., Appl. Phys. Lett. **80**, 3617 (2002).
- [133] K. Thurber, L. Harrell, R. Fainchtein, and D. Smith, Appl. Phys. Lett. **80**, 1794 (2002).
- [134] B. C. Stipe, H. J. Mamin, T. D. Stowe, T. W. Kenny, and D. Rugar, Phys. Rev. Lett. **87**, 096801 (2001).
- [135] W. Silveira, *Microscopic View of Charge Injection in a Model Organic Semiconductor*, PhD thesis, Cornell University, 2005.
- [136] P. Horowitz and W. Hill, *The Art of Electronics*, Cambridge University Press, 2nd edition, 1989.
- [137] D. A. McQuarrie, *Statistical Mechanics*, University Science Books, 2000.